Hydrodynamic Design of Multi-Rotor Tidal Array

Bowen Cao

St Edmund Hall

University of Oxford

A thesis submitted for the degree of

Doctor of Philosophy

Michaelmas 2020

Abstract

This thesis adopts a blade element actuator disc method, embedded in a Reynolds Average Navier-Stokes (RANS) solver, to design multi-rotor tidal arrays. The constructive interference effect is taken into account in the design process to maximize the hydrodynamic efficiency. The design process considers rotor arrays in a fence arrangement, investigating the relative merits of in-situ and uniform rotor designs. The designed rotor is fabricated and tested experimentally. The experimental results show that the rotor achieved superior power efficiency and substantial performance benefits are possible through the fence arrangement.

High-fidelity blade-resolved computations are conducted to evaluate the design process and to reveal detailed flow physics. The blade loading distributions in the mid-span region from the design model shows good agreement with the those from the blade-resolved model. Discrepancies are observed in the blade root and tip regions, primarily due to the three-dimensional flow effects that are not fully resolved in the RANS-BE model.

To increase the modelling accuracy of the reduced order design model, a theoretically derived blade loading correction model is developed to account for three-dimensional spanwise flow effects along the rotating blades. The correction formulation, based on inviscid flow assumptions and the radial component of the governing equations, relates the spanwise pressure gradient on the blade surface to the shedding of bound circulation to form the blade's trailing vortex sheet. The new model corrects for spanwise flow induced pressure effects, which cannot be simply accounted for by manipulation of the inflow to two-dimensional aerofoils modelling through sectional lift and drag data. The analytic model, closed with appropriately calibrated empirical coefficients, is used to anisotropically modify the lift and drag forces on blade sections within the framework of the Blade Element Momentum model. With the new correction model applied, in addition to the Glauert tip correction to account for finite blade number, the new model is found to significantly improve the prediction of the thrust and torque on outboard sections of the blade where spanwise flow effects are significant. The empirical coefficients in the model only show a slight dependence on the operating tip-speed-ratio and the flow blockage. However, the sensitivity of the empirical coefficients on different blade geometries are not examined in this thesis.

Acknowledgments

First and foremost, I would like to thank my supervisor Prof. Richard Willden for his consistent support and patient guidance over the past four years. I am very grateful to have been able to work with him during my time at Oxford. I would also like to thank Prof. Thomas Adcock, Dr Christopher Vogel, Dr James McNaughton and Dr Takafumi Nishino for their insightful advice and valuable feedbacks.

I am extremely grateful to my parents, who provide funding to support my entire DPhil study. With your strong support, I can freely pursue whatever I am interested in without any financial concerns. I also would like to thank China Oxford Scholarship Fund (COSF) for the scholarship provided and St Edmund Hall for providing financial support to attend conferences.

I would also like to thank my lovely friends in the tidal research group. In particular I would like to thank Aidan Wimshurst, Steven Ettema, Federico Zilic de Arcos and Mohamad Bin Osman for many interesting discussions and valuable feedbacks.

Table of Contents

Nomenclature

Symbol	**Unit**	**Definition**
a	-	Azimuthally-averaged axial induction factor
a'	-	Azimuthally-averaged Tangential induction factor
a_B	-	Axial induction factor local to the blade
a'_B	-	Tangential Induction factor local to the blade
A	m^2	Rotor swept area
B	-	Blockage ratio
c	m	Chord length
c_x	-	Local thrust coefficient
C_D	-	Drag coefficient
C_L	-	Lift coefficient
C_P	-	Power coefficient
C_{pre}	-	Static pressure coefficient
C_T	-	Thrust coefficient
C_μ	-	Model constant of 0.09 in turbulence viscosity formulation
d	m	Rotor diameter
d_{nac}	m	Nacelle diameter
D	N	Drag force
F	-	Prandtl correction factor
g_L, g_D	-	Closure parameters in the correction model

h	m	Height of the domain
I	-	Turbulence intensity
k	m^2/s^2	Turbulence kinetic energy
L	N	Lift force
N	-	Number of blades
p		Pressure
P	W	Power
Q	$\mathrm{N}\cdot\mathrm{m}$	Torque
r	m	Radial position along the blade
R	m	Rotor radius
R_0	m	Radius of the outer domain
Re	-	Reynolds number
Re_c	-	Chord-based Reynolds number
Re_T	-	Reynolds number for turbulence
Re_θ	-	Momentum-thickness Reynolds number
T	N	Thrust force
T_u	-	100 times turbulence intensity, I.
u_c	$\mathrm{m/s}$	Radial velocity resulted from centrifugal force
u_i, u_j	$\mathrm{m/s}$	Reynolds averaged/Mean velocity components ($i, j = 1{,}2{,}3$)
u_i', u_j'	$\mathrm{m/s}$	Fluctuating velocity components
u_I	$\mathrm{m/s}$	Absolute velocity in inertial frame
u_R	$\mathrm{m/s}$	Relative velocity in the rotating frame

u_Γ	$\mathrm{m/s}$	Radial velocity induced by shedding of bound circulation
U_∞	$\mathrm{m/s}$	Freestream velocity
U_{ref}	$\mathrm{m/s}$	Reference velocity
u_θ	$\mathrm{m/s}$	Swirl velocity local to the blade
w	m	Width of the domain
W	$\mathrm{m/s}$	Relative velocity approaching the blade
y^+	-	Dimensionless wall normal distance
x, y, z	m	Cartesian coordinates
δ	m	Wall unit
δ_0	m	Thickness of hydrofoil trailing edge
δ_{ij}	-	Kronecker delta
α	o	Angle of attack
β	o	Twist angle of the blade section
Γ	$\mathrm{m^2/s}$	Bound circulation
γ	-	Turbulence transition intermittency
λ	-	Tip speed ratio
μ	$\mathrm{N \cdot s/m^2}$	Dynamic viscosity
ν	$\mathrm{m^2/s}$	Kinematic viscosity
ν_T	$\mathrm{m^2/s}$	Kinematic eddy viscosity
ϕ	o	Flow angle local to the blade
ρ	$\mathrm{kg/m^3}$	Fluid density
σ	-	Rotor solidity

τ_w	$\mathrm{N/m^2}$	Wall shear stress
ε	$\mathrm{m^2/s^3}$	Turbulence dissipation rate
ω	$\mathrm{s^{-1}}$	Specific turbulence dissipation rate
$\mathcal{L}$	m	Turbulence length scale
Ω	rad/s	Rotational speed

List of Figures

Chapter 1

Introduction and Literature Review

1.1 Tidal Stream Energy

Renewable and sustainable energy resources are being largely exploited worldwide to cut greenhouse gases emissions, mitigate against global warming, and meet increased energy demand. Coastal countries with appreciable tidal stream flow speeds, principally UK, China, France, Canada, Australia and USA, have been developing technologies for extracting tidal stream power and planning large scale deployments. The world's largest planned next phase of deployment is for a 398MW tidal stream farm (MeyGen Project) in the UK. However, compared to other forms of renewable sources such as wind and hydropower, the exploitation of tidal stream power is still in its infancy.

The oceanic tides are mainly caused by the astronomical gravitational influence of the Moon and the Sun and the rotation of the Earth and are often magnified by the effect of local land topologies such as a coastal inlet (e.g. the Bristol Channel) and a channel between large basins (e.g. the Pentland Firth). The gravitational interaction between the moon and surface water on the Earth makes the major contribution towards tidal flows. The gravitational force of the moon causes bulges in the water level directed towards the closet and furthest regions from the moon. Each bulge moves around the Earth each 24.834 h. This period is slightly longer than 24 h due to the relative direction of the orbit of the moon and the earth's rotation. Another significant contribution to tidal flows is due to the influence of the sun. The relative locations of the earth-moon-sun system lead to a spring-neap tidal cycle, whereby the tides exhibit maxima when the sun, Earth and moon are aligned, namely spring tides, and minima when the sun, earth and moon form a right angle, namely neap tides. Further detailed discussions about tidal behaviour are given by Pugh (1996).

There are typically two methods to harvest tidal power. One is to store the tidal flow behind a barrage, such as the La Rance plant in France constructed in the 1960s. Although a tidal barrage can achieve a higher power capacity, it usually requires a long construction time and high capital costs and has a significant influence on the surrounding ecosystem (Bryden and Melville, 2004). The alternative method is to deploy in-stream tidal devices to exploit the energy from the tidal current. This method is more favourable due to its lower environmental impact and will be discussed in details in following sections.

1.1.1 Tidal Stream Devices

Most commonly the tidal energy technologies that have been developed can be classified into two main groups: axial-flow turbines and cross-flow turbines. Axial-flow turbines, which are broadly similar to submerged wind turbines, extract energy from the moving water. The tidal stream causes the rotors of the turbines to rotate around its horizontal axis and produce power. This type of turbine has been most widely developed and installed by the current tidal industry (examples shown in Fig. 1.1). Examples include: Marine Current Turbines Ltd.(2013) designed a 1.2 MW SeaGen-S commercial-scale axial flow device which has been field-proven since installation in Strangford Lough, North Ireland in 2008 and further developed a 2MW tidal system consisting of twin power trains; OpenHydro Group Ltd. (2017) in collaboration with Emera Inc. developed the Cape Sharp Tidal which is a novel open-centre turbine with a duct surrounding the rotor. The device has a diameter of 16m and is rated at 2MW and has been deployed in the Bay of Fundy, Canada in 2016; Orbital Marine Power Ltd (2020) launched a 2MW SR2000 floating tidal turbine based on its success of the pre-tested model. As a floating device, the turbine can be towed to and from the site with low-cost vessels; SIMEC Atlantis Energy (2017) owns a 1.5-MW AR1500 horizontal-axis turbine system designed in conjunction with Lockheed Martin. The turbine is of 18 m diameter and has triple redundancy built in all key operational systems to ensure reliability offshore. The AR1500 has been deployed in MeyGen project phase 1a and demonstrated levels of performance above the contractual baseline required.

A common drawback of the axial flow device is that the rotor diameter cannot be increased significantly due to limited depth of flow at most sites, the likelihood of cavitation inception and high structure strength requirement (see e.g. Bryden *et al.*, 1998 and Molland *et al.*, 2004). To achieve a farm of hundreds of megawatts power capacity using axial flow devices, the tidal array would have to be deployed.

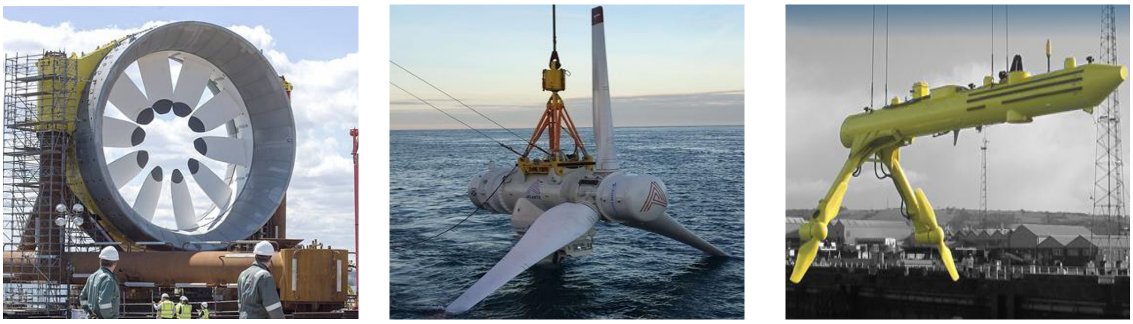

Fig. 1. 1 Examples of axial-flow tidal turbines. Left: Cape Sharp Tidal from OpenHydro Group Ltd. (2017); middle: AR1500 from SIMEC Atlantis Energy (2017); right: SR2000 from Orbital Marine Power Ltd (2020).

The cross-flow devices have rotational axes that are perpendicular to the flow, which could be extended horizontally across a tidal flow and thus have potential to achieve a significant scale of power generation by using a single device. Examples of such devices include the Transverse Horizontal Axis Water Turbine developed by McAdam *et al.* (2013a and 2013b) and the TidGen Power system designed by Ocean Renewable Power Company.

There are also manufacturers that are pursuing novel tidal energy concepts. For example, EEL Energy (2017) developed an idea of undulating membrane. The operation of which is such that the membrane oscillates under moving fluid pressure and this periodic motion drives an electromechanical system to generate electrical power; Flumill (2012) developed the Flumill Power Tower which is a central cylindrical shaft surrounded by a helical surface structure. As the tidal flow moves up and through the spiral, the cylindrical shaft rotates and thus turns the turbine; Vortex Hydro Energy (2013) invented a converter that utilises the physical phenomenon of vortex-induced-vibration to harness tidal current energy. The device is of a box shape with several cylinders installed inside it. As the tidal flow passes over the cylinders it creates vortices that cause cylinders to vibrate, which drives a generator to create electrical power.

Above all, a broad range of tidal concepts has been investigated and studied. Different full-scale devices and scaled prototypes are currently being developed in commercial tidal plants or tested in marine laboratories. However, possible final solutions are yet to emerge. As one might expect, much of the technology has been derived or imported from the wind industry and is not optimized for the harsh and constraining tidal environment. In this thesis, the main focus will be on the axial-flow tidal turbines.

1.2 Modelling of Tidal Flow

One simple method, which has been widely used in the analytical analysis of the wind and tidal power extraction (see e.g. Burton *et al.*, 2001 and Garrett and Cummins, 2007), is the momentum conservation. The force and torque exerted by the turbine to the flow are related to the rate of change of axial momentum and the rate of change of angular momentum respectively.

Three-dimensional Computational Fluid Dynamics (CFD) has become a powerful tool in studying tidal stream power production in both array and device scales. The numerical approach allows complex flow conditions such as turbulent, shear and yawed flows and flow constraints resulted from seabed, sea surface and neighbouring turbines to be modelled. The governing Navier-Stokes (NS) equations can be numerically solved directly, or the so-called Direct Numerical Simulation (DNS) method. However, the computational and data storage costs of the DNS method, resulted from resolving all the spatial and temporal scales of turbulence, are extremely high, which limits its application only to simple flow problems with relatively low Reynolds number. Instead, the Reynolds-Averaged Navier-Stokes (RANS) simulation which applies statistical averages to the NS equations and the Large Eddy Simulation (LES) which resolve the turbulence to a certain scale have been widely used to investigate the turbine performance and flow physics around the turbine. It is noted that even though the choice of turbulence model is important for both LES and RANS methods, it is generally more important in RANS than LES.

For the investigation of energy extractions in large basin scale and/or long-time tide period, the high computational cost of the RANS and LES makes these methods infeasible. The Shallow Water Equations (SWEs), also known as long wave equations, are widely used to model basin-scale tidal flows and to quantify an upper bound for power extraction (Adcock *et al.* , 2013; Walters, *et al.* , 2013 and Coles *et al.* , 2017). The main assumption of the SWEs is that the horizontal scale of flow is much larger than the vertical scale and hence the vertical motions are depth-averaged. The water depth of the tidal channel, often in the range of 25-50 m, compared to the wavelength of the tide is often a very small number, which makes the SWEs a reasonable approximation of tidal dynamics. However, it is well-known that the depth-averaged scheme does not correctly capture the turbulence mixing when the sheared flow (large vertical velocity gradient) is significant (see e.g. Stansby, 2006).

1.3 Hydrodynamic Modelling of Tidal Rotor

This section discusses several methods that have been used to represent tidal turbines and rotors in analytical, numerical and experimental studies to understand the downstream wake and flow interactions on the tidal device.

1.3.1 Bed friction

One simple method is to model the tidal turbine as an additional bed shear stress. Garrett and Cummins (2005) assumed that depth-averaged drag force imparted by the turbines is proportional to the square of the flow rate and have shown that the quadratic drag law is sufficient to obtain a good estimate of the maximum power. Therefore, it is reasonable to model the turbines as an additional friction coefficient to the natural bed friction coefficient. This method is easy to apply and gives realistic upper-bound power estimations if the friction coefficient is accurately calibrated (Serhadlioglu, 2014).

Several studies have been conducted to access the real-site power potential using the bed friction model. Sutherland *et al.* (2007) and Karsten *et al.* (2008) used the model to access the mean power potential of the Johnstone Strait, Canada (1320 MW) and Minas Passage of the Bay of Fundy, Canada (7GW), respectively. Coles *et al.* (2017) experimentally determined a drag coefficient of 0.8 based on their previous study (Coles *et al.* , 2016) as a realistic representation of turbine drag coefficient and used it in the SWEs model to access the power potential at tidal sites around the Channel Islands. Even though the bed friction model is easy to apply, it is difficult to relate the friction coefficient to different tidal array configurations and different operating conditions. In addition, without relating the friction to real turbine performance, the information about the 'available power', which is the power extracted by the turbine, remains unknown.

Another application of the bed friction model is to investigate the optimal arrangement of turbine positions in the array configuration. The optimisation of turbine positions within an array requires many iterations, which could lead to a high computational cost especially when the number of turbines is large. Low-order flow modelling and turbine representation thus become a feasible and attractive approach. Funke, *et al*. (2014) introduced a gradient-based adjoint approach with an objective function to optimize the time-averaged extracted power from tidal turbine array. In their study, the tidal flow is modelled by the steady shallow water equations and the turbine is parameterized as the additional bed friction in the SWEs, with a smooth function to avoid the non-differentiable problem in the gradient-based optimization algorithm. They used the model to optimize turbine array configurations for four idealized scenarios and found a significant power increase. They also demonstrated a case of optimization of 256 turbines in Inner Sound of the Pentland Firth, Scotland. Jacobs *et al*. (2016) compared the optimisation result from the SWE model of Funke, *et al.* (2014) with the LES model of Divett *et al.* (2013) and they found that even though the SWE model overpredicted the power production it produced a similar trend in the power curve. Furthermore, Culley *et al.* (2016) integrated the cost over the lifespan of the array into the optimisation process.

1.3.2 Uniform Actuator Disc

The uniform Actuator Disc (AD) is a concept that the tidal turbine is approximated by a disc that takes axial momentum from the fluid flow. Due to its simplicity, the AD approach has been widely used in analytical models and low-order numerical models to understand how tidal energy devices interact with the tidal flow.

A well-known method to determine the limit of power extraction in a fluid is the simple Linear Momentum Actuator Disc Theory (LMADT) introduced by Betz (Burton *et al.* , 2001). The method shows that the upper limit of the energy extraction is 16/27 times the undisturbed kinetic energy flux passing through the swept area of the turbine. The method assumes a uniform core-flow stream-tube that passes through the disc and a bypass stream-tube that surrounds the core-flow region. More importantly, the model considers an infinite volume of fluid, whilst for tidal energy extraction, the flow is constrained by the fluid's density and physical boundaries such as the channel/seabed and the water surface.

Garrett and Cummins (2007) developed an extended model that considers the constrained flow condition (i.e. finite volume of fluid), achieved by applying LMADT in a finite flow bounded by a non-deformable tube, described as a rigid-lid LMADT model, as shown in Fig. 1.2. Analyses of these models show that the maximum power coefficient of a single turbine is increased by a factor of $(1-B)^{-2}$, where B is the blockage ratio defined as the ratio of the cross-section area of the turbine to that of the channel, or termed as global blockage ratio in many studies (see e.g. Nishino and Willden, 2013). As core-flow stream-tube expands, the bypass stream-tube is contracted due to the presence of rigid-lid, which subsequently leads to an increase of the flow velocity and a reduction of the static pressure in the bypass region. At the station 4 as shown in Fig. 1.2, the pressure is equalised at a lower level than that in the conventional LMADT model. If the pressure recovery process in the core-flow stream-tube is assumed as the same for both the infinite and finite volume of fluid, the lower level of pressure at the station 4 will result in a lower pressure downstream of the turbine (at the station 3) and a greater pressure gradient across the disc; hence the turbine is able to exert a higher resistance to the flow and to achieve a higher power. Moreover, the additional mixing process, from station 4 to station 5 as shown in Fig. 1.2, which is not considered in the conventional LMADT model, considers the loss of energy in the mixing of the downstream wake. At the station 5, in addition to the pressure, the velocity is also equalized. One limitation of the rigid-lid model is that the rigid-lid assumption does not allow for the change of fluid depth along the channel and thus contradicts the spatial variation in hydrostatic pressure (Houlsby *et al.*, 2008). Hence, in order for the model to be accurate, the rigid-lid LMADT model requires a sufficiently low Froude number.

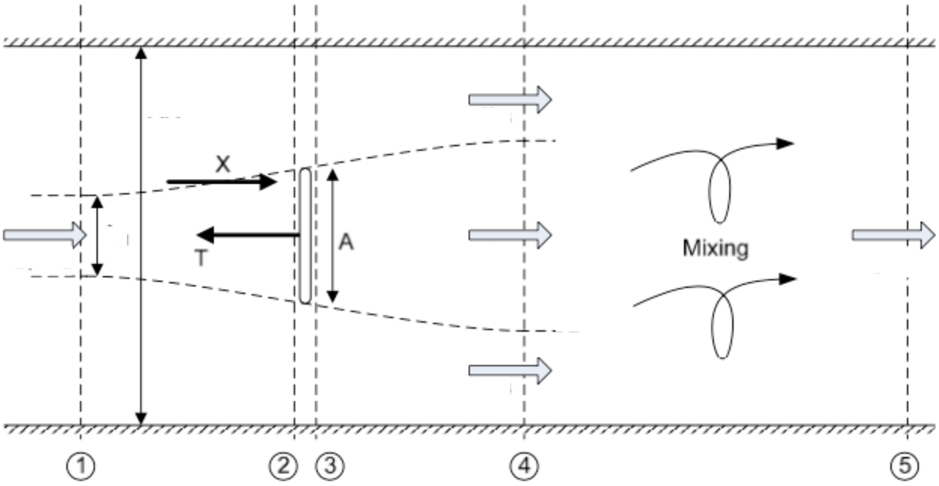

Fig. 1. 2 Schematic diagram of the rigid-lid linear momentum actuator disc theory by Garret and Cummins (2007), reproduced from Houlsby *et al.* (2008). X is the force resulted from stream-tube expansion, T is the thrust exerted by the turbine and A is the swept area of the turbine.

Alternatively, Whelan *et al.* (2007) considered the constrained flow condition by applying a constant pressure boundary to the LMADT model. The model allows the free surface to deform through the pressure drop across the rotor. Moreover, Houlsby *et al.* (2008) combined the approach of the rigid and the pressure boundary and developed the open-channel LMADT, allowing both the downstream mixing and the free surface deformation to be modelled.

Draper (2011) adopted the rigid-lid LMADT as a sub-grid model in the numerical SWE solver, in which the tidal turbine is parameterized by the blockage ratio and wake velocity coefficient. Serhadlioglu (2014) used the open channel flow LMADT as the sub-grid model in the numerical SWE solver. The model takes into account the change of flow height along the channel and parametrize the tidal turbine with an additional parameter – Froude number. She used the model to assess an upper limit for tidal stream power resources of Anglesey Skerries and the Bristol Channel and showed that the maximum mean available power values are 301.2 MW and 233.9 MW respectively. Adcock *et al.* (2013) adopted this model to assess an upper bound for tidal stream potential of the Pentland Firth and they showed that the numerical results from the study agreed reasonably with field data at various locations within the Firth. Furthermore, Bonar *et al.* (2018) utilized this model to explore the optimal turbine arrangements when flow conditions change from frictionless and steady to rough and oscillatory. They discovered the ‘reversal boost’ effect which is due to the phase shift between the array-scale core and bypass flows and suggested that the tidal turbines can be deployed in a compact configuration to maximize the power production.

Nishino and Willden (2012b) further extended the work of Garrett and Cummins to consider the two-scale flow dynamics for the tidal array. The device scale considers the flow around each turbine and the array scale considers the flow surrounds the entire array. They pointed out that when the turbine array is placed such that it blocks only a small portion of the cross-section of the channel, the array efficiency increases as the intra-turbine spacing reduces to an optimal value, but then decreases as the spacing is further reduced due to the array-scale choking effect, which means the flow through the entire array is significantly reduced. Nishino and Willden (2012b) also introduced the local blockage ratio, which is defined as the single device projected area to the cross-sectional area of the local flow passage, in contrast to the global blockage ratio, which is defined as the total device projected area to the cross-sectional area of the entire flow channel.

Numerically, the Actuator Disc model is often combined with RANS solver, known as RANS-AD model, when the large-scale flow effects are of interest. The turbine is often represented as a thin actuator disc which is a sink that takes momentum from the fluid flow passing through it as:

$$M = \frac{1}{2} K \rho u_d^2. \tag{1.1}$$

where K is the momentum loss coefficient, ρ is fluid density and u_d is the velocity through the rotor disc. Belloni and Willden (2011), Fleming *et al.* (2011) and Fleming and Willden (2016) utilized the RANS-AD model to examine ducted tidal turbine performance. Nishino and Willden (2012a) used the RANS-AD model to investigate the effect of turbulence mixing behind the disc, as well as the effects of channel blockage ratio and aspect ratio on wake mixing and the limit of power extraction. They showed that the limit of power extraction increases as the strength of turbulent mixing behind the disc increases. Nishino and Willden (2012a) also demonstrated that the channel blockage ratio has significant effect on the limit of power extraction but can be satisfactorily estimated using the LMADT while the effect of aspect ratio is minor.

In order to extract a significant amount of power, tidal turbines are commonly deployed in an array configuration. Hence, in order to maximize the power production it is important to understand the flow phenomena in both device and array scales, their interactions and their effects on the turbine performance. Nishino and Willden (2013) used the RANS-AD model to simulate a fence of 8 rotors (4 rotors with a symmetry plane), as shown in Fig. 1.3. The computational result showed good agreement with the analytical model of Nishino and Willden (2012b). The contour of the streamwise velocity, as shown in Fig. 1.3, shows that the device-scale wake mixing occurs at a much shorter length scale than the array-scale wake mixing, which indicates that the two-scale mixing process may occur independently.

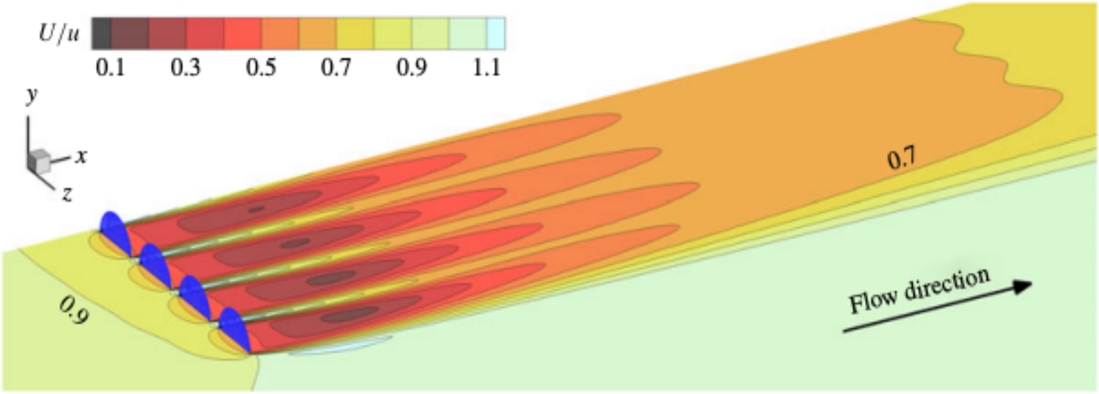

Fig. 1. 3 Contour of streamwise velocity from the simulation of Nishino and Willden (2013) of a fence of 4 actuator discs with a symmetry plane (to simulate a fence of 8 actuator discs), with an intra-disc spacing of 1/4 of the disc diameter.

In addition, the simplicity of the uniform actuator disc offers an efficient way of numerically investigating the effects of different array configurations and a large number of arrangement parameters, which could be infeasible for other numerical models. Bai, *et al.* , (2009) used the RANS-AD model to investigate 7 different array configurations of up to 7 turbines and found that benefit can be obtained by adding turbines in the cross-section direction while the streamwise spacing of the array can be a parameter to optimise. Hunter *et al*. (2015) used the RANS-AD to investigate the array of 7 turbines and its staggered variations along with the adjustment of individual turbine thrust. They found that the non-staggered array with uniform turbine thrust across the entire array gives the optimal power extraction. Abolghasemi *et al*. (2016) embedded the dynamically adaptive mesh optimisation techniques into the RANS-AD model, which allows dynamic mesh refinement only in the locations required and hence improves the computational efficiency of modelling turbine arrays. Gebreslassie, *et al*. (2015) combined the AD model with LES to study the performance of a staggered array of seven turbines and the wake interactions. They pointed out that the laterally closed configuration can achieve higher performance for this row of turbines, but it will affect the downstream rows and hence the global optimising of the turbine locations is challenging.

1.3.3 Blade Element Model

The blade element (BE) theory discretises the uniform actuator disc into azimuthally averaged concentric annular rings and introduces rotational source term, as depicted in Fig. 1.4. The forces on each ring are determined by incoming flow velocity and turbine parameters including rotational speed, pitch angle, blade twist profile and two-dimensional sectional lift and drag coefficients. This method relates the disc to realistic tidal turbine characteristics and operating conditions and allows for variation of flow velocities and blade forces across the disc. One key assumption of the BE model is that the forces on a blade element are based on the two-dimensional lift and drag data and incident resultant flow velocity. The radial velocity component, i.e., the component along the spanwise direction, is ignored. Hence, the three-dimensional flow effects are largely ignored. A number of corrections have been implemented to improve the accuracy of the blade element model, which will be discussed in details later in section 1.4.

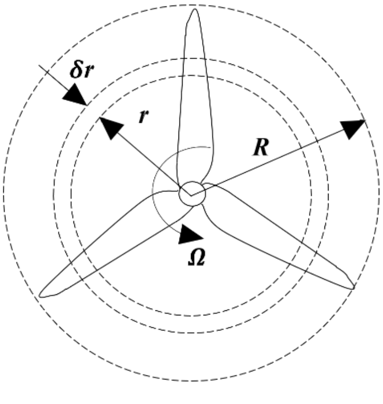

Fig. 1. 4 Schematic diagram of the blade element with width δr sweeping out an annular ring at radius r. The rotor is of radius R, rotating at angular velocity of Ω.

Vogel *et al*. (2018) developed a blockage-corrected semi-analytical BEM model, which combines the blade element theory with the rigid-lid momentum conservation of Garrett and Cummins (2007), namely, replacing the actuator disc with the blade element model. The hydrodynamic characteristics of the blade and the geometry of the rotor are the inputs to the model. Vogel *et al*. (2018) showed that the model offers a rapid way of investigating the rotor performance under different channel blockage ratios and operational tip-speed-ratios.

Numerically, the BE method is often combined with the RANS solver for ambient flow field modelling and thus the RANS-BE method. Batten *et al*. (2013) and Lavaroni *et al*. (2014) found that the wake characterises from the RANS-BE method showed a higher level of agreement with experimental measurements against the uniform disc model. Masters *et al*. (2013) adopted the RANS-BE method to study the performance of tidal turbine in the domain with a range of slopes and found that the accelerated flow facilitates the downstream wake recovery while has negligible effect on the rotor power coefficient. Allsop *et al*. (2017) and Belloni *et al*. (2017) used the RANS-BE method to conduct a hydrodynamic analysis of the ducted and open-centre tidal turbines. McIntosh *et al*. (2011) developed a design tool based on the RANS-BE method for hydrodynamic design of the blades of the tidal rotor. Schluntz and Willden (2015) utilized the method to design and analyse tidal rotors in channels with different blockages. Furthermore, Cao *et al*. (2018) utilized the method to analyse the effect of turbulence intensity on the tidal rotor design and performance

Compared to the uniform disc, the BE model incorporates real turbine characteristics and rotational source terms. This enables a higher order of accuracy in modelling near wake mixing, which plays an important role in determining downstream turbine array power. However, without detailed and transient representation of turbine blades and its induced vortices, the discrepancy in predicting wake characteristics may be amplified when flow passes through multiple downstream turbine arrays. For example, Olczak *et al*. (2016) studied multi-row array configurations of up to 3 rows of 12 turbines. They found that for a single row of turbines, the thrust and wake predicted by the RANS-BE showed good agreement with experimental study while for arrays of two and three rows, the difference of the thrust between the two methods is around 20% for the second row and 38% for the third row. Nevertheless, the BE method provides an efficient way to study turbine array arrangement and turbine operations. Turnock *et al*. (2011) used the RANS-BE method to investigate the lateral and longitudinal spacings of multi-row turbine array and showed that power production is maximized when the array is laterally packed and longitudinally as far-apart as the practical. Malki *et al*. (2014) also investigated the lateral and longitudinal spacings of the different array configurations using the RANS-BE method. Furthermore, they proposed a new 14-turbine arrangement based on the result from their array spacing studies and found a 10.7% power output increase compared to a regular 14-turbine arrangement. Schluntz (2014) used the RANS-BE method to investigate a fence (a single row of turbines) of 8 turbines and found an optimal intra-array spacing of 0.25 diameter. Vogel and Willden (2017) used the RANS-BE to study the performance of a fence of 4 turbines using the turbines optimally designed for power production for different blockage ratios. They found that the turbines designed for the moderate blockage maximized the entire fence power coefficient as a result of the balance between the device-scale and array-scale bypass flows around tidal arrays. Furthermore, Vogel and Willden (2018) showed that the fence power could be improved by adopting a blade pitch strategy to optimize the angle of attack distribution on blades of individual turbine.

1.3.4 Actuator Line Model

Sorensen and Shen (2002) introduced the actuator line (AL) method to represent the axial turbine by modelling the blade forces as momentum source terms along lines rotating with time. Similar to that in the blade element method, viscous effects on the blade surfaces are captured through 2D lift and drag coefficients. Compared to the blade element methods, the actuator line method resolves some unsteady flow effects such as tip vortices and hence predicts a better near wake flow field (Wimshurst and Willden, 2016). Baba-Ahmadi and Dong (2017) and Ouro *et al.* (2019) combined the AL model with the LES solver to predict the power production and the wake profiles of the tidal turbine. The result showed good agreements with the experimental data. Baratchi *et al.* (2017) demonstrated that the AL model combined with the LES gave a good prediction of tidal turbine performance in straight and yawed flows. Similar to that in the blade element model, the forces on the blade section are solely based on the two-dimensional lift and drag data and the incident resultant velocity and hence the three-dimensional flow effects are largely ignored. Wimshurst and Willden (2017b) developed a correction model based on the formulation from Shen *et al.* (2005) to increase the accuracy of predicting blade loadings in the tip region, by correcting the torque producing force and the thrust producing force in an anisotropic way. In addition, the AL does not account for unsteady effects such as dynamic stall and load hysteresis.

The actuator line method has been widely used in studying near wake interactions in tidal arrays. Churchfield *et al*. (2013) used the AL method combined with LES to study array power production in staggered and non-staggered configurations and found that the performance of downstream turbines was better in the staggered configuration due to the accelerated upstream bypass flows. Apsley *et al.* (2018) validated their actuator-line embedded LES against the experimental studies and used it for modelling up to 12 turbines in three-row array configuration. They also pointed out the choice of turbulence models was an important factor in reproducing the wake behaviour in the region affected by tip vortices.

1.3.5 Three-Dimensional Blade Model

Blade-Resolved (BR) model directly resolves the complete blade and rotor geometries, as an example shown in Fig. 1.5. Compared to the blade element and actuator line models where the blade force is highly dependent on the two-dimensional lift and drag coefficients, the blade-resolved model directly computes the blade force in the three-dimensional flow field and hence it accounts for three-dimensional flow effects that are significant in the blade tip and root regions, which lead to more accurate blade loading predictions (see e.g. Wimshurst and Willden, 2017a). Even though several studies have been conducted to parameterise these three-dimensional effects as corrections to the blade element and actuator line models (see e.g. Shen *et al.* , 2005 and Wimshurst and Willden, 2017b), generalised models have not been achieved yet since these three-dimensional effects can be very geometric specific.

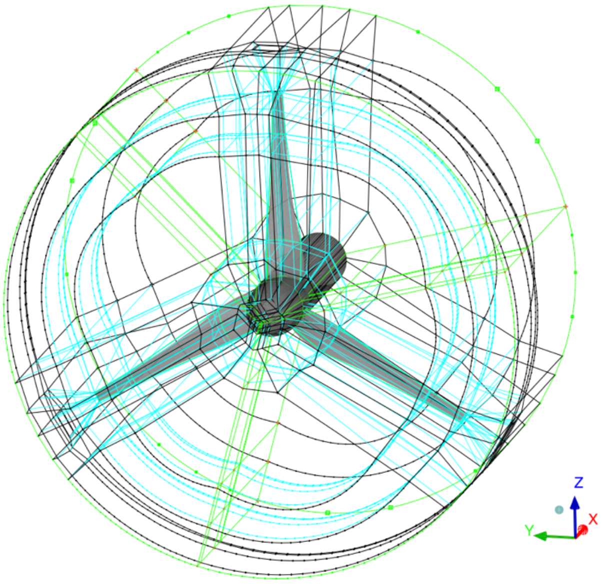

Fig. 1. 5 An example of the blocking topology of the blade-resolved model for the three-bladed rotor.

Afgan *et al*. (2013) and McNaughton (2013) conducted blade-resolved computations for the lab-scale rotor from Bahaj *et al*. (2007). The results showed reasonable agreement with experimental data. In addition, the simulations produced detailed flow behaviours such as the interaction between the blade vortices and the supporting tower. Ouro *et al*. (2017) and Ahmed *et al*. (2017) used the blade-resolved model with LES solver to study the effect of shear flow and freestream turbulence intensity on the hydrodynamic loading on the tidal turbine. Wimshurst *et al*. (2018) conducted the blade-resolved computation to investigate cavitation inception on the blade suction surface. Frost *et al*. (2015) used the blade-resolved model to study the effect of tidal flow directionality on tidal turbine performance. They found that in the presence of stanchion the turbine with a yaw mechanism allowing the turbine to always facing into the flow has better performance compared to the turbine with blades that can rotate through 180 degree to benefit from a strongly bi-directional flow. Tatum *et al*. (2016) used the blade-resolved model to investigate the effect of waves on the tidal turbine performance and found that in-phase wave with long period could lead to fluctuations in power range being over 100%.

Muchala and Willden (2018) conducted the blade-resolved simulation to compare the turbine performance in the presence of bed-mounted cylindrical and elliptical support structures. They found that the cylindrical structure gave higher opposing thrust in the channel and increases the local flow speed around the top half of the rotor, which resulted in higher power and thrust coefficients.

However, the high computational cost of this method makes the investigation of the performance of tidal arrays and corresponding flow physics impractical, especially when the wake recovery and blade surface have to be resolved with sufficient accuracy. Hence, few studies have been conducted to study the tidal array performance. Nuernberg and Tao (2018b) used the BR model to conduct a preliminary study of a multi-row array of 4 turbines, where the dynamic mesh technique (different mesh resolutions in different regions) is adopted to save computational cost. The results showed reasonable agreement with the experimental study of Nuernberg and Tao (2018a).

1.3.6 Porous Disc and Scaled Rotor

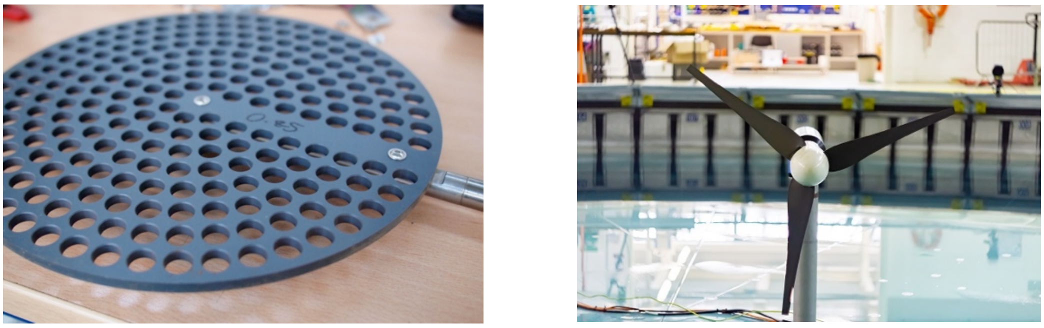

(a) (b)

Fig. 1. 6 (a) An example of the porous disc used for the experimental study (Cooke *et al.* , 2016); (b) An example of the scaled-rotor model from McNaughton *et al.* (2019).

Experimental modelling of the tidal turbine, including porous discs and scaled devices, has become an important way to study the tidal stream power extractions and to evaluate the results from both analytical and numerical studies (Examples shown in Fig. 1.6). Similar to that using a uniform actuator disc in the numerical simulation, the porous disc model can only apply thrust to the flow and result in the non-rotational wake. However, this model can be appropriate when large-scale effects are of interest and has shown to adequately simulate the far wake region behind a tidal turbine (Bahaj *et al.* , 2007). Whelan *et al.* (2009) used a porous disc and a strip to study the effect of free-surface proximity on the tidal turbine and validated their analytical model. In addition, they conducted a scaled rotor experiment to compare against their analytical correction to the conventional BEM theory. Cooke *et al. (*2014*)* used a fence of 8 porous discs to study the array power performance. They showed that the power available was maximized as the porosity of the discs is low (the thrust applied on the flow is high) and the intra-disc spacing was narrow.

For the scaled rotor model, Mycek *et al.* (2014a), Chamorro *et al.* (2013) and Fernandez-Rodriguez *et al.* (2014) conducted experimental studies on a scaled rotor to investigate the effect of different freestream turbulence intensities on the turbine performance. The results showed that the turbulence intensities have minimal effect on the mean power coefficient but have considerable influence on the wake characteristics. Furthermore, Blackmore *et al.* (2016) included the effect of turbulence length scales on the turbine performance and loadings. Stallard *et al.* (2015) and Chen *et al.* (2017) studied the wake characteristics using the scaled rotor testing, which provided details of velocity deficits behind the rotor. Milne *et al.* (2015) and Payne *et al.* (2018) conducted comprehensive analyses of unsteady loadings on turbine blades using the scaled-rotor model.

Experimental studies have also been conducted to understand the flow effects within tidal turbine array. However, the space of the testing facility and the cost associated with experiment often limits the number of turbines and array arrangements that can be tested. Such method is commonly used to validate the analytical and numerical array models. Myers and Bahaj (2012) used the porous discs to model a two-turbine fence and a three-turbine staggered array. Mycek *et al*. (2014b) studied the in-line arrangement of two scaled rotors and demonstrated that the higher turbulence intensity facilitated the wake recovery and resulted in higher power coefficient for the downstream turbine. Stallard *et al*. (2013) and Nuernberg and Tao (2018b) conducted experimental testing on several array arrangements using scaled rotors to understand the wake interactions. McNaughton *et al*. (2020) studied a fence of 2 closely packed turbines with blade tip-tip spacing of 0.25 rotor diameter and found that compared to the single turbine operation, the fence arrangement increased the power coefficient of each turbine by around 26%.

1.4 Tip Correction for Three-dimensional Flow Effects

Blade-Element theory based models, including the conventional BEM model and the RANS-BE model, have been widely used in computing the performance of horizontal axis turbines for wind and tidal stream energy generation. In these models, a key assumption is that the forces on each blade element can be determined through two-dimensional aerofoil characteristics and that there is no radial interaction between the flows through adjacent annular elements. Hence, three-dimensional flow effects are largely ignored. This assumption often leads to reasonable accuracy along the mid-span of the blade (see e.g. Cao *et al*., 2018). However, such a simple treatment of the flow leads to an overprediction of the loads on the outboard sections of the blade, which is due to the unaccounted for three-dimensional pressure equalisation effect and the induced spanwise flow component, and the downwash induced by the shed vortex, as depicted in Fig. 1.7. Micallef *et al*. (2016) experimentally studied the tip vortex generation on horizontal axis turbines and showed how vorticity was shed radially away from the blade tip due to the in-plane spanwise component of flow. Wimhurst and Willden (2018) conducted a detailed numerical analysis on the tip loss mechanism and showed that on the outboard sections of the blade the net force vectors rotates towards the streamwise direction, which results in an anisotropic change of the torque producing and thrust producing forces. These studies have provided detailed information of the three-dimensional flow in the blade tip region.

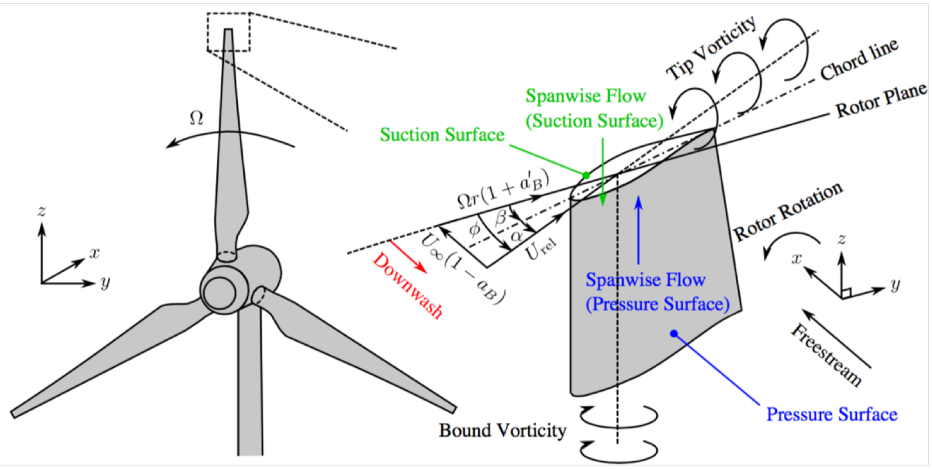

Fig. 1. 7 Schematic diagram of the three-dimensional flow effects on the outboard section of the blade (Wimshurst and Willden, 2018).

Several studies and models have been proposed to account for the three-dimensional effects. One type of the correction model directly modifies the load on the blade sections. For example, Shen *et al*. (2005) introduced a loading correction factor, based on the formulation proposed by Glauert (1935) with an empirical coefficient for the closure. They used it to correct the tangential and axial forces simultaneously. Wimshurst and Willden (2017b) further modified this correction model and recalibrated the empirical coefficients for tangential and axial forces respectively. Another type of the correction model was to correct the induced velocity and hence the angle of attack approaching the blade sections in the tip region. For example, Edmunds *et al.* (2017) considered the effect of tip vortices on the angle of attack approaching the blade section. Based on the lifting line theory, their model computes an extra source term which represents the downwash induced by the tip vortices. Schmitz and Maniaci (2017) proposed an analytical tip-loss factor based on the spanwise distribution of the blade flow angle. This distribution is obtained from the high-fidelity numerical model, which is deemed to resolve the three-dimensional tip vortices and the near-wake expansion and distortion. However, Wimhurst and Willden (2018) pointed out that in the blade tip region, the spanwise flow effect distort the pressure field and rotates the force vectors, which anisotopically alters the lift and drag forces generated on the blade section. Hence, only modifying the angle of attack of the approach flow cannot completely reproduce the three-dimensional blade physics. Zhong *et al.* (2020) proposed a tip-loss model as a summation of two factors, one determined by the downwash and the other determined by rotation. The model is used to correct both the induced velocity and the two-dimensional lift and drag coefficients. Alternatively, Wimhurst and Willden (2017a) replaced the two-dimensional lift and drag data by those extracted from the three-dimensional blade at various spanwise locations to improve the load predictions in the blade tip region.

1.5 Research Objectives

1.5.1 Multi-Rotor Tidal Array Design

In order to achieve commercially viable amount of power, tidal turbines are often deployed in an array configuration. In fact, the interest in the multi-rotor system has also increased in the wind industry (see e.g. Knudsen *et al.*, 2018). The local blockage effect, also known as the constructive interference effect, introduced by Nishino and Willden (2012b) has shown to improve the tidal array performance in both analytical and numerical studies (Nishino and Willden, 2013 and Vogel and Willden, 2017). However, to date, few studies have been conducted to design a short tidal fence for its specific blocked flow condition.

The research in this thesis will provide a numerical method to design multi-rotor tidal array to exploit its specific blocked flow condition and leverage the constructive interference effect to maximize the power efficiency. Experimental study will be conducted to demonstrate the high power efficiency resulted from the design method. The research result will be shown to provide a way for tidal industry to benefit from the constructive interference in the next-generation rotor design and rotor operation.

1.5.2 Three-Dimensional Flow Effects and Tip correction

As the multi-rotor system has become increasingly popular in both wind and tidal industries, the associated computational cost increases due to modelling of multiple devices. Hence, the low-order numerical models such as the RANS-BE model are favored. One major problem of the low-order models is that they are based on the two-dimensional lift and drag data, which makes the models not capable of capturing spanwise flow effect. The inability of incorporating the spanwise flow effect usually results in over-predictions of the torque and thrust in the blade tip region. Shen *et al.* (2005) have developed a function to parameterize the spanwise flow effect as a correction model. Wimshurst and Willden (2017b) have extended the correction model to an anisotropy version. However, these models are mainly semi-empirical and do not incorporate underlying flow physics in the formulation.

The analysis in chapter 6 will reveal the spanwise flow component on both suction and pressure sides of the blade surface, which is the result of the centrifugal force (due to the rotor rotation) and blade tip vortices. A new theoretically based tip correction formulation for use with Blade Element models will be developed based on radial momentum conservation and vortex theory. This model will provide a better correction for the RANS-BE method to accurately model the multi-rotor array performance.

1.6 Thesis Outline

The thesis is outlined as follows:

Chapter 2 briefly summaries the numerical methods used throughout the thesis. The chapter discusses the RANS equations and the turbulence closure, which plays an important role in determining the hydrodynamic performance of the rotor and the wake characteristics. This will be followed by introducing the low-order tidal turbine modelling technique, the blade element (BE) theory, which is embedded in the RANS solver by McIntosh, *et al.* (2011). This method, or the RANS-BE method, has been widely used for investigating tidal turbine design and performance. After this, the high-fidelity three-dimensional blade resolved model, the wall modelling methods and the rotor rotation techniques are discussed.

Chapter 3 provides an evaluation study of the modified RANS-BE design tool. The design result is compared against the high-fidelity blade-resolved model. The blocking topology, mesh convergence and numerical setups are also examined in this chapter.

Chapter 4 adopts the RANS-BE method to design multi-rotor tidal arrays in a two-rotor and a four-rotor configuration. The design flow conditions are matched with the measurement at the FloWave tank at the University of Edinburgh (Sutherland *et al.* , 2017). Three-dimensional rotor geometry is formed based on the sectional hydrofoil profiles and the twist and chord profiles of the designed blade. High-fidelity blade-resolved computations, using a fully structured mesh to resolve the boundary layers on the blade surface, are then conducted to compute the rotor performance. The spanwise distribution of the blade loads and angle of attack from the two models are compared and the discrepancies are discussed.

Chapter 5 discusses the experimental test for investigating the constructive interference effect. The rotor was fabricated according to the design in chapter 4 and was connected to the University of Edinburgh’s nacelle. Both a single turbine and a twin-rotor fence configuration with tip-to-tip spacing of 0.25 rotor diameters were tested at the FloWave facility. The flow velocity and rotor performance were measured and discussed. Blade-resolved computation is conducted to reproduce the experimental result. The simulation result is compared against the experimental result.

Chapter 6 explores the three-dimensional flow field on the blade surface and emphasizes the spanwise flow effect. A new theoretically derived tip correction model is also developed. The new correction model corrects for the spanwise pressure effects resulted from the spanwise flows along the blade, for which the two-dimensional lift and drag data does not account. This additional dimension is added by the correction model to reproduce the loading associated with three-dimensional blade physics.

Chapter 2

Numerical Methods

In this thesis, the Reynolds-Averaged Navier-Stokes (RANS) equations are solved to simulate the fluid flow. Both the finite-volume method based Computational Fluid Dynamics (CFD) solvers OpenFOAM and ANSYS FLUENT (version 15.0) are adopted. FLUENT is used for the rotor design tool, in which the in-house blade-element design code is embedded as a User Defined Function (UDF) for the boundary conditions. OpenFOAM is adopted for the high-fidelity blade-resolved computation. The high level of mesh resolution and high number of mesh cells of the blade-resolved model requires a high computation cost. Due to the open-source nature of the OpenFOAM, more CPU cores can be utilized for the computation without the license limitation. For both OpenFOAM and FLUENT solvers, second-order central differencing is used for the face interpolation of all the Laplacian and gradient terms, while a flux limited form of central differencing with the Sweby (1984) limiter, is used for the convection terms. The SIMPLE algorithm of Patankar (1980) is used for pressure-velocity coupling.

2.1. Reynolds-Averaged Navier-Stokes (RANS) Equations

The Navier-Stokes (NS) equations describe a deterministic process for the fluid particle. For an appropriate set of boundary and initial conditions, it will give a single velocity field $\boldsymbol{u}(\boldsymbol{x}, t)$. However, this deterministically predicted behaviour is extremely sensitive to the slightest variations in boundary and initial conditions due to the chaotic nature of turbulent flows and the non-linearity. In order to capture the motion of the fluid particle, the spatial scale of the turbulence from the smallest dissipative scale (Kolmogorov scale, η) up to the integral length scale $\mathcal{L}$ must be resolved in the numerical mesh cells. In addition, time stepping has to be small enough to allow the motion of fluid particle to be captured by the mesh scale. The method that fully resolves all the turbulence scales is called Direct Numerical Simulation (DNS). However, the computational cost of the DNS method goes up with Re_T^3, where Re_T is Reynolds number for turbulence (Pope, 2000). This limits its application to problems with low Reynolds number.

The incompressible Reynolds Averaged Navier-Stokes (RANS) equations can be obtained by applying statistical time averages to the Navier-Stokes equations. The velocity field is decomposed into an average and a fluctuating velocity component as:

$$\boldsymbol{u}(\boldsymbol{x},t) = \langle \boldsymbol{u}(\boldsymbol{x},t) \rangle + \boldsymbol{u}'(\boldsymbol{x},t), \tag{2.1}$$

where $\langle \cdot \rangle$ indicates the statistical time average process. The RANS equations are shown in Eq. (2.2). Detailed derivation can be found in Pope (2002).

$$\nabla \cdot \langle u_i \rangle = 0 \tag{2.2a}$$

$$\rho \frac{\partial \langle u_i \rangle}{\partial t} + \rho \frac{\partial}{\partial x_j} \langle u_i u_j \rangle = \frac{\partial}{\partial x_j} \left[-\langle p \rangle \delta_{ij} + \mu \left(\frac{\partial \langle u_i \rangle}{\partial x_j} + \frac{\partial \langle u_j \rangle}{\partial x_i} \right) - \rho \langle u_i' u_j' \rangle \right] \tag{2.2b}$$

In Eq. (2.2), ρ is fluid density, $\langle u_i \rangle$ is Reynolds averaged velocity component and u_i' is the fluctuating velocity component ($i, j = 1,2,3$). μ is dynamic viscosity of the fluid. p is pressure and δ_{ij} is the Kronecker delta.

The covariances $\langle u_i' u_j' \rangle$ in Eq. (2.2) are referred as Reynolds stress by convention (even though it is $\rho \langle u_i' u_j' \rangle$ that can be interpreted as stresses). The system of Eq. (2.2) is not closed because it has 4 equations for 10 unknowns (an averaged pressure, 3 averaged velocity components and 6 Reynolds stresses). The closure problem, raised from the non-linearity of the convection term in the Navier-Stokes equations and the non-locality introduced by the pressure, presents a major challenge in predicting mean flow properties of turbulence flows.

2.2. Turbulence Closure

Two types of models are normally considered for turbulence closure: the turbulent-viscosity model and the Reynolds-stress model. The main focus in this thesis is the turbulent-viscosity model, which has been incorporated into most of the commercial CFD codes and has been widely used for wind and tidal rotor computations.

The turbulent-viscosity model is based on the Boussinesq turbulent viscosity (or eddy viscosity) assumption,

$$-\rho\langle u_i' u_j'\rangle + \frac{2}{3}\rho k \delta_{ij} = \rho \nu_T(\boldsymbol{x}, t)\left(\frac{\partial\langle u_i\rangle}{\partial x_j} + \frac{\partial\langle u_j\rangle}{\partial x_i}\right), \tag{2.3}$$

where k is turbulence kinetic energy. ν_T is turbulent viscosity, or eddy viscosity, and is a function of spatial position and time. This assumption mimics the viscous stresses generated in a Newtonian fluid. A detailed discussion of the validity of this assumption can be found in Pope (2002). The determination of ν_T becomes the object of turbulence modelling. The following sections discuss two turbulence models that are used in this thesis.

2.2.1 $k-\omega$ SST model

The $k-\varepsilon$ two-equation model (Launder and Spalding, 1974) is one of the most widely used turbulence models. The transport equations are solved for two turbulence quantities: the turbulence kinetic energy, k, and the turbulence dissipation rate, ε. The turbulence viscosity is then calculated as:

$$\nu_T = C_\mu \frac{k^2}{\varepsilon}, \tag{2.4}$$

where $C_\mu = 0.09$ is model constant. However, the well-known shortcoming of the $k-\varepsilon$ model is its relatively poor accuracy in the near wall region where adverse pressure-gradient is significant (Menter, 1993). One of the most successful alternative model developed to overcome this shortcoming is the $k-\omega$ model introduced by Wilcox (1982), in which transport equations are solved for k and the specific dissipation rate, ω. However, the $k-\omega$ model has a disadvantage that it is sensitive to the freestream turbulence properties.

Menter (1993) introduced the $k-\omega$ SST model which combines the $k-\omega$ and the $k-\varepsilon$ model, using a blending function to switch between the two models. It hence has good accuracy in predicting both flow near the solid boundaries and flow far away from the solid boundaries (freestream flow). This model has been widely used in large-scale wind and tidal turbine computations. For example, it has been used to successfully reproduce the experimental results from the MEXICO rotor test (Bechmann, *et al.*, 2011). One drawback of this model, which will be discussed later, is that due to its fully turbulent nature the model cannot capture the laminar-to-turbulent transition on the blade surface. However, for large-scale wind and tidal rotors, the chord-based Reynolds number is of order 10^7 and so it is reasonable to assume a fully turbulent boundary layer on the entire blade surface. Hence, this model is adopted for large-scale rotor computations in this thesis.

Different commercial CFD codes use different calculations for ω, which leads to different model initialisations. In ANSYS FLUENT (ANSYS, 2013), the ω is calculated as:

$$\omega = {C_\mu}^{3/4} \frac{k^{3/2}}{\mathcal{L}}, \tag{2.5}$$

where $\mathcal{L}$ is a reference length scale. While in OpenFOAM, the ω is calculated as:

$$\omega = \frac{k^{1/2}}{{C_\mu}^{1/4} \mathcal{L}}. \tag{2.6}$$

This is because FLUENT uses a different length scale definition based on the mixing-length model. The turbulence kinetic energy k is:

$$k = \frac{3}{2}(UI)^2, \tag{2.7}$$

where $U = \sqrt{u_i^2 + u_j^2 + u_k^2}$ and I is the turbulence intensity, which is defined as the ratio of the streamwise velocity perturbation to the mean velocity.

For simulations with uniform inflow (i.e. no mean shear flow) and slip boundary condition at domain boundaries, there is no mechanism for turbulence generation and the turbulence intensity decays from the inlet boundary of the computational domain. An artificially large reference length scale is usually used and the turbulence intensity is set higher at the inlet boundary in order to achieve the required turbulence intensity upstream of the rotor or the hydrofoil (Gant and Stallard, 2008; McNaughton, 2013).

2.2.2 $\gamma - \mathrm{Re}_\theta$ model

As mentioned before, the $k - \omega$ SST model cannot capture the boundary layer transition in the blade boundary layer due to its fully turbulent nature. At low chord-based Reynolds number, typically less than 5×10^5, the laminar-to-turbulent boundary layer transition may occur in the attached boundary layer or in the separated shear layer. The latter would lead to either stall if flow remains detached following the separation or a laminar separation bubble if flow reattaches downstream of the separation.

The transitional SST model, or the $\gamma - \mathrm{Re}_\theta$ model, is developed by Langtry (2006) for modelling the laminar-to-turbulent transition. The model is based on the $k - \omega$ SST model and is coupled with two additional transport equations: one for intermittency, γ, and another for momentum-thickness Reynolds number (used for transition onset criteria), Re_θ. This four-equation model has been implemented in most commercial CFD codes and has been widely used for computing external aerodynamic flows (see e.g. Langtry and Menter, 2009 and Lanzafame, *et al.*, 2013). Hence, this model is used for small-scale rotor computations in this thesis.

The initialisations of the two extra quantities γ and Re_θ at the inlet boundary are specified as follows (Langtry, 2006):

$$\gamma = 1\,, \tag{2.8}$$

$$\mathrm{Re}_\theta = \begin{cases} 1173.51 - 589.428T_u + \dfrac{0.2196}{{T_u}^2}, & T_u \leq 1.3 \\ \dfrac{331.5}{(T_u - 0.5658)^{0.671}}, & T_u > 1.3 \end{cases} \tag{2.9}$$

where $T_u = 100I$. For solid boundaries, zero gradient boundary conditions of γ and Re_θ are imposed.

The $\gamma - \mathrm{Re}_\theta$ model demands higher computational cost than the $k - \omega$ SST model. The two additional transport equations for γ and Re_θ require extra time to solve. In addition, finer mesh is required for the $\gamma - \mathrm{Re}_\theta$ model in the chordwise direction of the blade to capture possible transition at any point on the blade surface and in the wall-normal direction to fully resolve the boundary layer. The computational cost would be further increased when the mesh-rotation approach is used to simulate the rotor rotation as the time stepping size depends on the minimum size of the mesh cell at the sliding interface.

2.3 RANS-BE model

The Blade-Element theory coupled with the RANS solver, also known as the RANS-BE method, has been widely used for modelling tidal turbines (see e.g. Schluntz and Willden, 2005). The blade element theory is used to model the rotor blades, on which the viscous effects are resolved in the two-dimensional lift and drag coefficients. The flow filed is numerically simulated by the RANS solver, which enables complex flow conditions such as turbulent flows, shear flows, and flow constraints due to sea bed, sea surface and neighbouring turbines to be considered. The following sections start with an introduction to the conventional simple momentum theory and the blade element theory, where an unbound infinite flow is assumed, followed by the discussion of the RANS-BE method and design tool.

2.3.1 Simple Momentum theory

A method to determine the power extraction in a fluid is the linear momentum actuator disc theory, which gives an upper limit of the power extraction. In this method, the turbine is represented as a uniform actuator disc and the simple momentum theory is used to determine the force acting on the turbine and on the fluid flow. A concept of induction factor is introduced to take into account the induced flow at the disc. The physical presence of the actuator disc reduces the free-stream flow speed, U_∞, by aU_∞ at the disc plane, where a is called the axial flow induction factor. Hence, the streamwise velocity that passes through the disc, U_D, is given as $U_\infty(1-a)$.

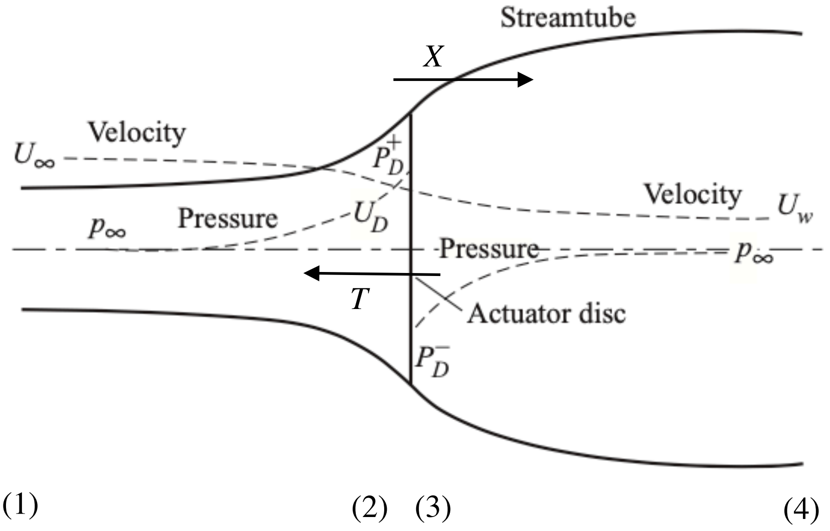

Fig. 2. 1 Schematic diagram of energy extracting actuator disc and stream-tube (Burton *et al.*, 2001).

As shown in Fig. 2.1, four positions are analysed: (1) far upstream of the turbine, referred using subscript ∞; (2) and (3) immediately upstream and downstream of the turbine, referred using subscript D; (4) far wake downstream from the turbine such that the pressure is equalized, referred using subscript w. The fluid flow passing through the disc undergoes a streamwise velocity change of $U_\infty - U_w$ from far upstream to far downstream of the rotor. The rate of change of momentum is then related to the force causing this change as:

$$T - X = (U_\infty - U_w)\rho A U_D, \tag{2.10}$$

where A is rotor disc area and T is force exerted to the flow by the turbine, which can be determined by the pressure difference across the rotor disc as: $(P_D^+ - P_D^-)A$. X is force exerted to the flow due to the core stream-tube expansion. For the unbound infinite flow, X is assumed to be zero, which means that there is no net change of momentum in the bypass flow that surrounds the core stream-tube. Applying Bernoulli equation from positions 1 to 2 and from positions 3 to 4 respectively, the pressure difference is related to the streamwise velocity change as:

$$P_D^+ - P_D^- = \frac{1}{2}\rho(U_\infty^2 - U_w^2). \tag{2.11}$$

Combining Eq. (2.10) and Eq. (2.11), the streamwise velocity far downstream from the turbine is:

$$U_w = U_\infty(1 - 2a). \tag{2.12}$$

The power removed from the fluid flow is then given by:

$$TU_D = 2\rho A U_\infty^3 a(1 - a)^2. \tag{2.13}$$

A power coefficient, C_P, is then defined as:

$$C_P = \frac{Power}{\frac{1}{2}\rho U_\infty^3 A} = 4a(1 - a)^2. \tag{2.14}$$

By differentiating Eq. (2.14), the maximum power coefficient is obtained as 16/27 when $a = 1/3$. Furthermore, a thrust coefficient, C_T, is defined as:

$$C_T = \frac{T}{\frac{1}{2}\rho U_\infty^2 A}. \tag{2.15}$$

A local thrust coefficient, c_x, obtained by normalizing the thrust by the local velocity at the disc, is defined as:

$$c_x = \frac{T}{\frac{1}{2}\rho(1 - a)^2 U_\infty^2 A} = \frac{4(1 - a)}{a}. \tag{2.16}$$

When the C_P is maximized as $a = 1/3$, $c_x = 2$.

It is noted that the simple momentum actuator disc theory only considers the streamwise velocity component so that the swirl and the spanwise velocity components are ignored. In addition, the unbounded infinite flow means that the velocity and pressure far downstream from the rotor will eventually recover to those far upstream, which implies that no energy is removed from the flow. This issue can only be resolved by considering a bounded finite flow, such as the models developed by Garret and Cummins (2007) and Houlsby *et al*. (2008).

2.3.2 Blade Element Momentum (BEM) Theory

Instead of using a uniform actuator disc to represent the turbine, the blade element theory discretises the disc into a series of azimuthally averaged concentric rings and introduces the swirl velocity component. The turbine geometry and its operation conditions are also considered. The force and torque exerted to the flow by the turbine are the source terms for the rate of change of axial and angular momentums. In the conventional BEM theory, the unbounded infinite flow boundary condition is assumed.

In this theory, a rotor with finite number of blades, N, is approximated by a disc divided into many concentric annular rings. A key assumption in this theory is that the velocity component in the spanwise direction is ignored. Hence, the lift and drag forces on a blade element can be calculated from two-dimensional lift and drag polars. Three-dimensional effects are largely ignored. Fig. 2.1(a) shows how a disc is used to discretise a rotor of radius R rotating at angular velocity Ω. At each radial position r with a width δr, the blades have pitch angle β and angle of attack α with incoming flow vector; see Fig. 2.1(b). The axial and circumferential velocity components experienced by the blade element is $(1-a)U_\infty$ and $(1+a')\Omega r$ respectively, where a and a' are the azimuthally averaged axial and tangential induction factors at the disc plane respectively. The incident resultant velocity W resulting from these two velocity components is calculated by:

$$W = \sqrt{(1-a)^2 U_\infty^2 + (1+a')^2 \Omega^2 r^2} \tag{2.17}$$

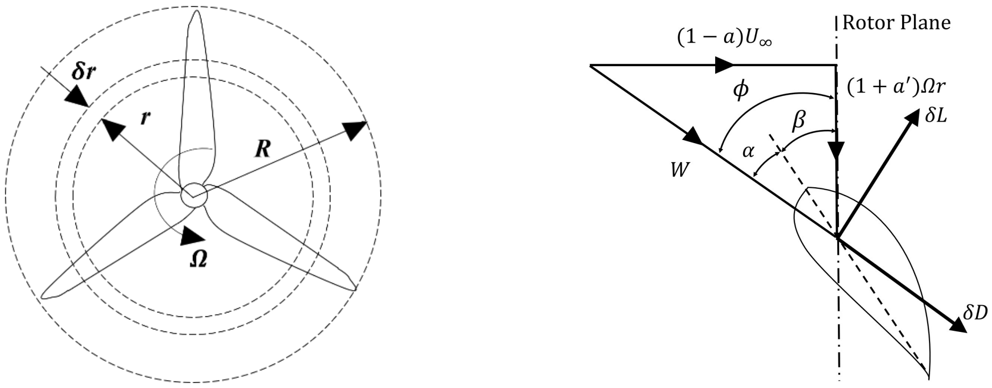

(a) (b)

Fig. 2. 2 Schematic diagrams of (a): rotor discretization; (b): flow vector and lift and drag resolution.

The angle between the relative velocity and rotor plane is ϕ and hence the angle of attack α can be determined by $\alpha = \phi - \beta$. The lift and drag forces produced on the blade elemental ring are calculated as:

$$\delta L = \frac{1}{2}\rho W^2 N c C_L \delta r \tag{2.18}$$

$$\delta D = \frac{1}{2}\rho W^2 N c C_d \delta r, \tag{2.19}$$

where c is chord length of each blade at radius r, and C_L and C_D are the lift and drag coefficient obtained from two-dimensional data at an angle of attack of α. The axial thrust, δT, and torque, δQ, on the blade elemental ring are determined from:

$$\delta T = \delta L \cos\phi + \delta D \sin\phi \tag{2.20}$$

$$\delta Q = (\delta L \sin\phi - \delta D \cos\phi) r. \tag{2.21}$$

Equating the axial thrust to the rate of change of the axial momentum of the air passing through the annular ring, following equation is obtained:

$$\delta L\cos\phi + \delta D\sin\phi = 4\pi r\delta r\rho U_\infty^2 a(1-a) \tag{2.22}$$

Similarly, equating the torque to the rate of change of the angular momentum of the air passing through the annular ring, following equation is obtained:

$$(\delta L\sin\phi - \delta D\cos\phi)r = 4\pi r^3\delta r\rho U_\infty a'(1-a)\,\Omega \tag{2.23}$$

Iterations may be required for solving the above two equations. The total thrust T and torque Q are obtained by integrating δT and δQ over the radius along the blade span respectively. The power coefficient and thrust coefficient are calculated as:

$$C_P = \frac{Q\Omega}{\frac{1}{2}\rho U_\infty^3 A} \tag{2.24}$$

$$C_T = \frac{T}{\frac{1}{2}\rho U_\infty^2 A}, \tag{2.25}$$

where $A = \pi R^2$ is the rotor disc area.

One important assumption in the blade element theory is that there is a sufficient number of blades in each annular ring to interact with the flow passing through, which means all fluid particles undergo the same loss of momentum. When the number of blades is small, some of the fluid particles interacts with the blades while some of them passes between the blades, and hence the azimuthally averaged induction factor, a, becomes different from the induction factor close to the blade, a_B. Fig 2.3 shows an example of azimuthal variation of the induction factor. It can be seen that in the mid-span region of the blade, the variation is negligible while in the outboard region of the blade, significant variation can be observed and the values at the blade location are much larger than those in the between. Further details can be found in Burton *et al.* (2001).

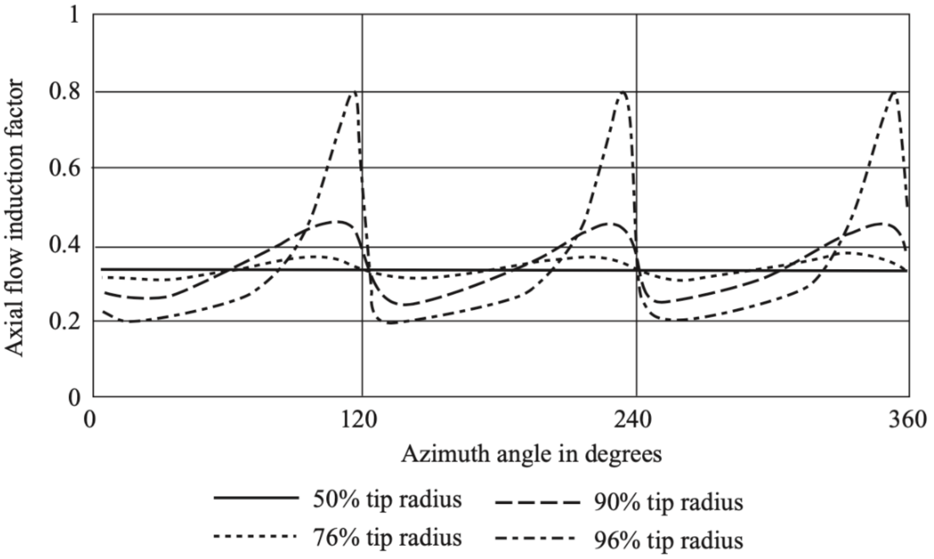

Fig. 2. 3 Azimuthal variation of induction factor (a) for various radial positions for a three-blade rotor at a tip-speed-ratio of 6. The blades are at 120^o, 240^o, and 360^o. (Reproduced from Burton *et al.*, 2001).

In order to correct the discrete blade effect, Glauert correction factor (F) is adopted (Glauert, 1935). This is used to correct the azimuthally averaged induction factor as:

$$a_B = \frac{a}{F} \tag{2.26}$$

The formulation of F is given by:

$$F = \frac{2}{\pi}\cos^{-1}\left[\exp\frac{N(1-\frac{R}{r})}{2\sin\phi}\right]. \tag{2.27}$$

2.3.3 RANS-BE method

Although BEM method has been widely used in wind energies, the analytical momentum equation limits its application to simple flow conditions. Instead, the RANS-BE method, in which the flow field is simulated by the numerical RANS solver, allows complex flow conditions to be considered.

An in-house blade element code developed by McIntosh *et al.* (2011) is embedded in ANSYS FLUENT and has been used in the studies of Schluntz and Willden (2015), Belloni *et al.* (2017) and Wimshurst *et al.* (2018). In this RANS-BE model, the rotor is modelled as an infinitely thin disc, applied with an "fan" boundary condition in ANSYS FLUENT. This boundary condition allows for a pressure jump to be imposed across the disc and a swirl velocity component on the disc to be specified. Instead of using induction factors to calculate the streamwise and swirl velocity components at the blade element, the RANS solver directly passes the local streamwise and the swirl velocities at the rotor disc plane to the blade element code. The pressure jump, Δp, across each disc cell of area δA is then calculated as:

$$\Delta p = \frac{\delta T}{\delta A} = \frac{1}{2}\rho W^2 \sigma (C_L \cos\phi + C_D \sin\phi), \tag{2.28}$$

where solidity σ at local radius r is $Nc/2\pi r$. The torque on a disc cell is equal to the rate of change of angular momentum for the corresponding area, thus:

$$\rho \delta A u_x \Delta u_{\theta,ud} = \frac{1}{2}\rho W^2 \sigma (C_L \sin\phi - C_D \cos\phi) \tag{2.29}$$

where $\Delta u_{\theta,ud}$ is the change in circumferential velocity between the immediately upstream and downstream sides of the rotor. The swirl velocity u_θ at the rotor plane is assumed as:

$$u_\theta = \frac{\Delta u_{\theta,ud}}{2} = \frac{W^2 \sigma (C_L \sin\phi - C_D \cos\phi)}{4u_x} \tag{2.30}$$

This relationship cannot be derived analytically and hence it mimics the assumption in the conventional BEM method. This is one of the key assumptions in the RANS-BE method. With the Glauert correction factor applied, the corrected axial velocity u_x' and swirl velocity u_θ' are then calculated as:

$$u_x' = U_\infty\left(1 - \frac{1 - \frac{u_x}{U_\infty}}{F}\right) \tag{2.31}$$

$$u_\theta' = \frac{u_\theta}{F} \tag{2.32}$$

These two corrected velocities are used to determine the angle ϕ according to $\tan\phi = u_x'/u_\theta'$. Starting from u_x and u_θ computed by the RANS solver, u_x', u_θ', ϕ and F may be iteratively determined. The relative velocity, W, at each disc element may then be obtained by:

$$W = \sqrt{\left[\left(\Omega r - u_\theta'\right)^2 + {u_x'}^2\right]} \tag{2.33}$$

It is noted that unlike the standard approach used in RANS-BE method (see e.g. Malki *et al.*, 2013), in which the forces are applied uniformly across an annular ring, this model calculates the forces on each mesh cell independently, which thus enables azimuthal variations in the flow field to be accounted for.

2.3.4 RANS-BE Design Tool

The design tool is an add-on function that can be turned on and off. When used as a design tool the method can iteratively calculate the optimal blade chord and twist for each annular elemental ring in order to maximise the power coefficient. The inputs to the design tool are the two-dimensional lift and drag data, target tip-speed-ratio and local thrust coefficient. The optimal twist angle of the blade is normally set such that it maintains the angle of attack that corresponds to the maximum lift to drag ratio. The tip-speed-ratio (TSR) is defined as $\Omega R/U_\infty$. The local thrust coefficient, c_x, is given by:

$$c_x = \frac{\delta F_x}{\frac{1}{2}\rho u_x^2 \delta A}, \tag{2.34}$$

where δF_x is the axial force acting on a corresponding annular ring of area δA. The blade chord and thus the blade solidity is adjusted to achieve the requirement of c_x. The design adjustment is executed at each steady RANS iteration. As the global RANS simulation converges, so does the rotor design process. A constant c_x approach is used in the present study following Belloni (2013) who demonstrated that using an optimized radially varied local thrust coefficient only leads to negligible increase in rotor power coefficient. In order to avoid unrealistic large blade root section or to achieve load relief in the blade root region, a relaxation of c_x may be applied.

For the conventional linear momentum actuator disc model, where the flow is unbounded, an optimal value of c_x of 2 can be analytically derived (as discussed in section 2.3.1). For design of the tidal rotor in the bounded flow condition, depending on the blockage ratio, a series of c_x larger than 2 are tested and an optimal c_x value is normally determined based on the trade-off between the power and thrust performance of the rotor. The optimal c_x would result in a high power coefficient at a cost of reasonable thrust coefficient.

2.4 Three-Dimensional Blade-Resolved Model

Blade-resolved model directly resolves the complete three-dimensional rotor geometry and hence the three-dimensional flow effects, flow separations and blade tip vortices can be directly investigated. In this thesis, the numerical computation for the blade-resolved model is conducted using OpenFOAM. The structured mesh with all hexahedral cells are used. Compared to the unstructured mesh, the structured mesh offers a better control of resolutions and a better prediction accuracy for the region near the blade surface (when a similar amount of unstructured mesh cells is used).

Due to different spatial resolution requirements for different regions, the computational domain of the blade-solved model is divided into an inner and an outer domain separately, whereby the nonconformal cells at the interface are joined by a conservative interpolation method through the local Galerkin projection, introduced by Farrell and Maddison (2011). This technique is termed as Arbitrary Mesh Interface (AMI) in OpenFOAM, which is achieved by applying the cyclicAMI boundary condition. The inner domain contains the region around the blade surfaces, which requires high spatial resolutions clustered in the near wall region to resolve or model the boundary layer. This segregated mesh approach allows a refined structured mesh to be fitted around the blade surfaces, without continuing this high resolution through to the outer domain, which would have led to an extremely high number of mesh cells.

2.4.1 Near-Wall Treatments

Wall-bounded turbulent flows are significantly affected by the presence of the wall (see e.g. ANSYS, 2013). When the flow is very close to the wall, the viscous damping reduces the velocity fluctuations in the tangential direction to the wall while the physical presence of the wall reduces the velocity fluctuations in the wall-normal direction. Moreover, in the outer part of the near-wall region, the large gradients in mean velocity produce turbulence kinetic energy, which rapidly augments the turbulence. Hence, the result of the numerical simulations can be significantly impacted by the near-wall modelling.

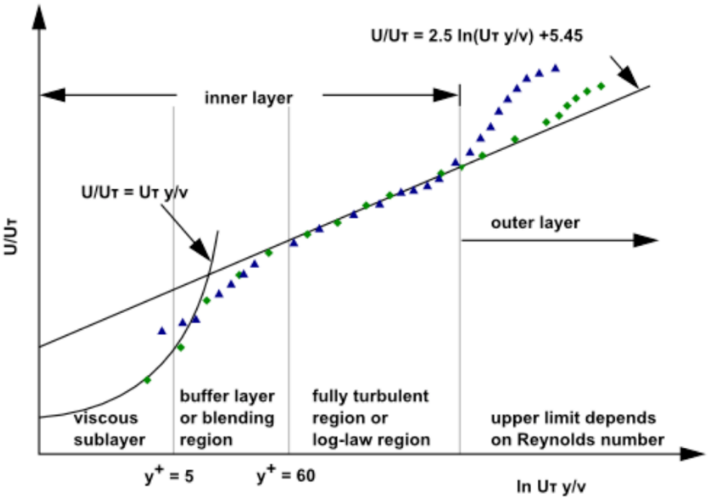

Fig. 2. 4 Subdivisions of the Near-Wall region, plotted in semi-log coordinates. The discrete green diamonds and purple triangles show the experimental results. The black solid lines show the fitted curve. (ANSYS, 2013).

A non-dimensional wall normal distance, y^+, is defined as $\frac{y}{\delta}$, where y is wall normal distance and δ is wall unit, which is defined as $\frac{\sqrt{\tau_w/\rho}}{\nu}$ where τ_w is wall shear stress and ν is kinematic viscosity of the fluid. The $\sqrt{\tau_w/\rho}$ is also called friction velocity (u_τ). Experiments and direct numerical simulations have shown that the near-wall region for the wall-bounded turbulent flows can be subdivided into three layers, as an example shown in Fig. 2.4. In the innermost layer, the viscous force (due to molecular viscosity) dominates, and flow is laminar. This layer is called the ‘viscous sublayer’. In the outer part, the flow is fully turbulent and more importantly the normalised mean flow velocity (normalised by u_τ) can be modelled using a semi-empirical logarithmic function (see e.g. Malalasekera and Versteeg, 2007). This region is also termed as logarithmic layer. In the interim region between the two is the buffer layer where both the turbulent and viscous forces are important.

Two approaches are often used to model the near-wall region for the RANS computation. In one approach, the mesh is resolved all the way to the wall, including the viscous sublayer.

The centroid of the first mesh cell (i.e. the mesh cell adjacent to the wall) is placed inside the viscous sublayer ($y^+ < 5$) with appropriate expansion ratio of the wall normal cell to ensure that there are sufficient inflation layers to resolve the high velocity gradient inside the boundary layer. This is often referred as the wall-resolved approach. It is noted that the turbulence model itself should be valid throughout the near-wall region. One practical difficulty for this approach is that the very small height in the wall normal direction often leads to high aspect-ratio mesh cells on the body surfaces and leads to highly skewed mesh cells if the geometry of the surface is complex, resulting in difficulties for the numerical solver (e.g. unbounded errors). This difficulty becomes more significant with the increasing Reynolds number. When the Reynolds number increases, the velocity gradient increases and hence the first cell height required to sufficiently resolve them becomes even smaller.

In another approach, the centroid of the first mesh cell is placed inside the log-law region of the boundary layer. Instead, the logarithmic wall function is used to bridge the region between the wall and the first mesh cell centroid, providing near-wall boundary conditions for the momentum and turbulence transport equations, rather than to specify those conditions at the wall itself. Using the wall function may reduce mesh cell count and improve the mesh quality, however the numerical accuracy may decrease when the solid boundary has a high curvature or the flow separation occurs. In order to use the wall-function approach with confidence, the first cell has to be placed correctly. The y^+ of the first cell height cannot be too large such that it falls outside the logarithmic layer region, otherwise the flow properties at this first calculation is incorrect. The upper limit of the logarithmic layer depends on the Reynolds number, which may range from several thousand y^+ units for high Reynolds number (e.g. ships, airplanes) to a hundred y^+ units for low Reynolds number (ANSYS, 2013). The accuracy of the wall-function also deteriorates when the y^+ of the first cell height is too small such that it is inside the buffer layer or the viscous sublayer. This would become using the wall function to model the regions that do not follow the logarithmic law.

In this thesis, the wall function approach is adopted for the 20 m diameter full-scale rotor in the evaluation study conducted in Chapter 3 whereas the wall-resolved approach is used for modelling the experimental scale rotor. For the experimental scale rotor, the laminar-to-turbulent transition of the boundary layer is found to occur on the blade surface, which significantly impacts the hydrodynamic performance of the blade. The transitional $\gamma - \mathrm{Re}_\theta$ model is adopted for the turbulence closure. In order to determine the transition point correctly, the model requires y^+ of approximately one with sufficient layers of cells in the boundary layer. Studies from ANSYS (2013) showed that if y^+ is greater than 5 or the wall normal expansion ratio is larger than 1.2, then the transition onset location moves upstream with increasing y^+ and expansion ratio. In addition, the mesh resolution on the blade surface along the chordwise direction is also required to be fine enough to correctly capture the transition.

2.4.2 Multiple Reference Frame

The rotor rotation in the blade-resolved model can be achieved either by physically rotating the mesh region that contains the blades or by using the Multiple Reference Frame (MRF) technique. The mesh-rotation approach can resolve most of the flow physics (with appropriate level of mesh resolution), including the transient phenomena such as flow separations and the blade tip vortices. However, the unsteady nature of this approach requires unsteady RANS simulation to be performed. In this thesis, the computational cost associated with solving the four-equation $\gamma - \mathrm{Re}_\theta$ turbulence closure model and the mesh resolution requirement for the $\gamma - \mathrm{Re}_\theta$ model make the mesh-rotation approach impractical for this study. Instead, the MRF approach, also known as Frozen rotor approach, is adopted for simulating the rotor rotation in the blade-resolved model. The basic idea of the MRF approach is to transform the problem that is unsteady in an inertial (stationary) reference frame to a moving reference frame such that steady-state solutions are possible. In the MRF approach, the mesh remains fixed whilst the governing equations are solved in the moving frame. Specifically, for the study in this thesis, the moving reference frame only has the rotational motion and is referred as 'rotating frame'. When the flow is in the rotating cell zone (i.e. the inner domain), the equations in the rotating frame with angular velocity $\mathit{\Omega}$ are solved; when the flow is in the stationary cell zone (i.e. the outer domain), the angular velocity $\mathit{\Omega}$ becomes zero and the rotating reference frame reduces to the inertial form. At the interfaces between the two, a local frame transformation is performed to enable calculations of fluxes (e.g. diffusion flux) at the boundary.

The underlying theory for the MRF is summarized as follows. Consider a rotating frame with angular velocity $\boldsymbol{\Omega}$. The relationship between the absolute velocity in the inertial frame ($\boldsymbol{u_I}$) and the relative velocity in the rotating frame ($\boldsymbol{u_R}$) is expressed as:

$$\boldsymbol{u_I} = \boldsymbol{u_R} + \boldsymbol{\Omega} \times \boldsymbol{r}, \tag{2.35}$$

and the relationship of the acceleration between the two frames is expressed as:

$$\left[\frac{d\boldsymbol{u_I}}{dt}\right]_{\boldsymbol{I}} = \left[\frac{d\boldsymbol{u_I}}{dt}\right]_{\boldsymbol{R}} + \boldsymbol{\Omega} \times \boldsymbol{u_I} \tag{2.36}$$

Hence, by substituting Eq. (2.35) into Eq. (2.36), the following relationship can be obtained:

$$\left[\frac{d\boldsymbol{u_I}}{dt}\right]_{\boldsymbol{I}} = \left[\frac{d\boldsymbol{u_R}}{dt}\right]_{\boldsymbol{R}} + \frac{d\boldsymbol{\Omega}}{dt} \times \boldsymbol{r} + 2\boldsymbol{\Omega} \times \boldsymbol{u_R} + \boldsymbol{\Omega} \times \boldsymbol{\Omega} \times \boldsymbol{r} \tag{2.37}$$

For constant $\boldsymbol{\Omega}$, the term $\frac{d\Omega}{dt}$ reduces to zero. By substituting the above relationships, the steady and incompressible Navier-Stokes equations for relative velocity in the rotating frame writes:

$$\nabla \cdot \boldsymbol{u_R} = 0 \tag{2.38a}$$

$$\nabla \cdot (\boldsymbol{u_R} \otimes \boldsymbol{u_R}) + 2\boldsymbol{\Omega} \times \boldsymbol{u_R} + \boldsymbol{\Omega} \times \boldsymbol{\Omega} \times \boldsymbol{r} = -\nabla \frac{p}{\rho} + \upsilon \nabla \cdot \nabla \boldsymbol{u_R} \tag{2.38b}$$

Eq. (2.38) can be further developed for absolute velocity by replacing the convected velocity by $\boldsymbol{u_I} - \boldsymbol{\Omega} \times \boldsymbol{r}$:

$$\nabla \cdot \boldsymbol{u_I} = 0 \tag{2.39a}$$

$$\nabla \cdot (\boldsymbol{u_R} \otimes \boldsymbol{u_I}) + \boldsymbol{\Omega} \times \boldsymbol{u_I} = -\nabla \frac{p}{\rho} + \upsilon \nabla \cdot \nabla \boldsymbol{u_I} \tag{2.39b}$$

The governing equations Eq. (2.39), which use the absolute velocity as dependent variable in the rotating reference frame, is known as the absolute velocity formulation, whereas the equations Eq. (2.38), which use relative velocity as dependent variable, is known as the relative velocity formulation. For the blade-resolved computations conducted in OpenFOAM, the absolute velocity formulation Eq. (2.39) is utilized. It's noted that when the angular velocity $\boldsymbol{\Omega}$ reduces to zero for the outer domain, both Eq. (2. 38) and Eq. (2.39) reduces to the inertial form.

At the interface of the multiple reference frames, scalar quantities (e.g. pressure, turbulent kinetic energy) are passed locally whilst for vector quantities, they are converted to the inertial frame first. For the absolute velocity formulation, the velocities are already in the absolute inertial frame and hence no conversion is required.

Compared to the mesh-rotation approach, the MRF approach leads to a dramatic reduction in the computational cost due to its steady nature. The main disadvantage of the MRF approach is that it only provides a steady-state approximation and hence it cannot accurately reproduce unsteady effects such as flow separations and sheared inflows. Since the lab-scale rotor is tested in controlled experimental flow conditions where the shear flow is not significant and the operation conditions are close to the design condition, the blade-resolved computations with MRF approach is deemed to give reasonable approximations.

Chapter 3

Model Evaluation

In this chapter, numerical tools used throughout this thesis are discussed and evaluated. Mesh convergence is discussed, which provides a guideline for the mesh resolution in following chapters. An in-house Blade Element (BE) code written in C programming language developed by McIntosh *et al.* (2011) is embedded in the RANS solver in ANSYS FLUENT as a User Defined Function (UDF). The RANS-BE method is adopted for rotor design. Several modifications to the original code have been made in order to achieve additional functions. The original BE code is based on the unstructured mesh and the interpolation scheme is based on the equally spaced annular rings. In order to take the benefit of the clustered annular ring on the structured mesh, the interpolation scheme is modified. The BE code is also extended to achieve multiple rotor design. A blade-resolved model is then developed and is used to compare with the result from the RANS-BE computations.

Due to the more complex flow physics on the blade surface of the lab-scale rotor, the evaluation in this chapter is based on a 'full' scale rotor of 18 m. The evaluated method will be then applied to the design of lab-scale rotor in the Chapter 4.

3.1 Rotor Design

The RANS-BE model and the design tool are used to design a three-bladed rotor of diameter $D = 20\ \mathrm{m}$ operating in infinitely long tidal arrays. A series of blockage ratios of 0.01, 0.04 and 0.16 are used to investigate the effect of low, moderate and high flow constraints, where the local blockage ratio (B) is defined as:

$$B = \frac{A_D}{A_c} \tag{3.1}$$

where A_D is rotor disc area and A_c is cross-sectional area of the flow passage. A simple uniform free-stream inflow of $2\ \mathrm{m/s}$ is adopted. For the evaluation purpose, the effects of shear and yaw flows are not considered.

3.1.1 Hydrofoil Computation

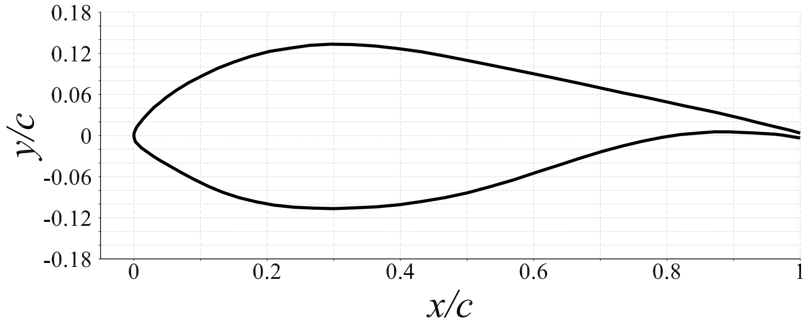

Fig. 3. 1 The geometry of the modified RISØ-A1-24 profile used by Wimshurst and Willden (2016a).

The hydrodynamic characteristic of the blade section is an important input for the RANS-BE method, as the blade forces are highly dependent on the sectional lift and drag coefficients. For this evaluation study, the RISØ-A1-24 profile is adopted for the entire span of the blade. This profile has a maximum thickness to chord ratio of 24% and has good hydrodynamic characteristics such as a high lift-to-drag ratio and a smooth post stall region (Fuglsang and Bak, 2004). Sale *et al.* (2009) and Ahmed (2012) stated that this profile has been widely used in tidal blade design. The trailing edge of the original proprietary RISØ-A1-24 profile is unclear. Hence, a modified version from Wimshurst and Willden (2016a) is utilized, as depicted in Fig. 3.1. Specifically, following the method of Herrig *et al.* (1957) a realistic profile for three-dimensional rotor geometry is obtained by thickening the trailing edge. Wimshurst and Willden (2016a) demonstrated that this method does not significantly affect the hydrodynamic characteristic of the profile.

Depending on the radial position and the estimated chord length of the blade section, the chord-based Reynolds number (Re) varies from 7×10^6 to 14×10^6. Following the study of Wimshurst and Willden (2016a), a chord based Reynolds number of 12×10^6 is chosen for the design process, which is based on the chord length at r/R of 0.7.Since there is insufficient hydrofoil data at Re $= 12 \times 10^6$, two-dimensional steady RANS computations are conducted to compute lift and drag hydrofoil data at this Reynolds number. A validation study is firstly performed on the modified RISØ A1-24 aerofoil at a chord-based Re $= 1.6 \times 10^6$ and a freemstream turbulence instensity of 0.7% to match the conditions in experimental measurements from Bertagnolio et al. (2001).

ANSYS ICEM is adopted for generating the structured mesh. The boundary of computational domain is placed 10-chord around the hydrofoil and 15-chord behind the hydrofoil. The C-type block is fitted around the hydrofoil profile (which is of unit chord) and the wall adjacent mesh cells on the hydrofoil surface are placed such that $y^+ < 1$. The computational domain and the mesh are shown in Fig. 3.2. The $k - \omega$ SST turbulence closure is adopted. A constant inlet velocity at the inlet boundary is set such that the chord-based Re $= 1.6 \times 10^6$. According to Eq. (2.6) and (2.7), a freestream turbulence intensity of 1% and a reference length scale of 50% of the unit chord is used to set the turbulence kinetic energy and the specific dissipation rate at the inlet boundary. These values lead to a 0.7% turbulence intensity one-chord upstream from the hydrofoil. A pressure outlet boundary condition is set for the domain outlet, where zero gradient is specified for all the properties except that the pressure is set as the reference pressure (zero for this case).

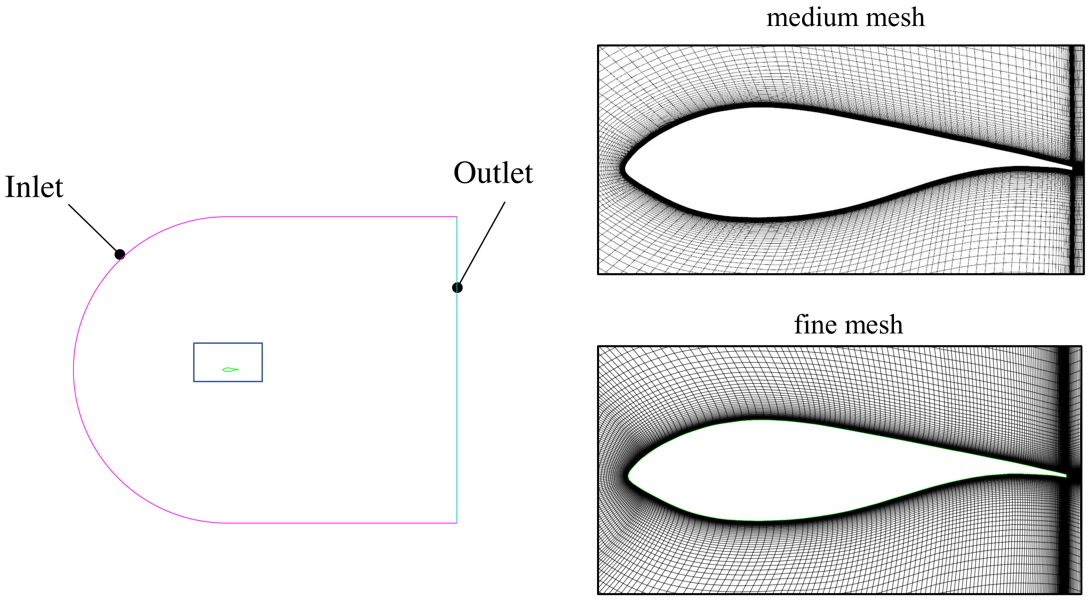

Fig. 3. 2 The computational domain for the 2D hydrofoil study. A C-type blocking topology with all hexahedral cells is fitted around the hydrofoil profile.

Before a comparison between the experimental and numerical results, the numerical errors and uncertainties are evaluated. The uncertainty of the total numerical error can be determined, as proposed in ASME PTC Committee (2009), as the Root Mean Square (RMS) of the uncertainty of the round-off error, the uncertainty of the iterative error and the uncertainty of the discretization error. In order to estimate the discretization error, a series of mesh grids are generated. The total number of mesh cells (N_{cell}) for each mesh and the lift and drag coefficients, for angle of attack of 6^o, are summarized in Table 3.1. Based on the level of agreement between the lift and drag coefficients for the medium and the very fine mesh, the medium mesh is deemed to be sufficiently accurate and is used for further computations. Another reason to choose medium mesh, rather than the fine mesh, is to make the resolution of mesh for the two-dimensional hydrofoil comparable to that for the three-dimensional blade section in the later study.

Table 3.1 Summary of the mesh sensitivity study for the modified RISØ-A1-24 hydrofoil at an angle of attack of 6^o in the experimental condition of Bertagnolio et al. (2001). The change in lift and drag coefficients (ΔC_L and ΔC_D) have been expressed relative to the very fine mesh.

Mesh	N_{cell}	C_L	C_D	ΔC_L[%]	ΔC_D[%]
Coarse	34,726	1.028	0.02048	-1.54	2.45
Medium	51,376	1.042	0.02012	-0.19	0.65
Fine	74,816	1.045	0.01996	-0.10	-0.15
Very Fine	95,228	1.044	0.01999	-	-

The use of double precision for a practical application is enough to guarantee that the round-off error is negligible compared with other sources of numerical errors (see e.g. Roache, 2009). During the SIMPLE iterations, the residuals for the governing equations (normalised by their initial values) reduced by at least 5 orders of magnitude for the velocity components, pressure and turbulence scalars. Compared to the discretization error, the iterative error is assumed negligible and hence the main component of the numerical uncertainty is the discretization error. Because the main purpose of this thesis is not to quantify the numerical uncertainty accurately, following Wimshurst and Willden (2016) and Otto *et al.* (2012), their method to estimate numerical uncertainty for use in practical numerical applications is adopted. Specifically, the greatest difference in the lift and drag coefficients between the medium, fine and very fine meshes is taken as a measure of discretisation error and then multiplied by a proposed factor of safety of 3.0 to estimate the uncertainty. This method is also used to estimate the uncertainty in later studies. Consequently, the uncertainty at angle of attack of 6^o was estimated to be 0.60% in the lift coefficient and 2% in the drag coefficient.

In Section 3.2, the wall function approach is adopted for the blade-resolved model in order to avoid impractically high number of mesh cells (will be discussed in details later). To investigate the limitation of such approach, a comparison is made of a two-dimensional hydrofoil section meshed with wall function approach and the one meshed with wall resolved approach. Following Wimshurst and Willden (2016), for wall function approach, the centroid of the wall adjacent mesh cell on the hydrofoil surface is placed such that $30 < y^+ < 300$.

Fig. 3.3 shows the lift coefficient (C_L), drag coefficient (C_D) and lift to drag ratio (C_L/C_D) as a function of angle of attack (at an increment of 1 degree). At low and moderate angles of attack, both the wall-resolved approach and the wall-function approach give similar results, showing good agreement with the experimental data. Above 8^o, both the two methods predicts delayed separations since the lift coefficient is overpredicted and the drag coefficient is underpredicted. Compared to the wall-resolved approach, the results of the wall-function approach show larger discrepancies between the experimental data. This is likely due to the steady computation adopted and the limitation of the turbulence model. However, in the RANS-BE design process the blade sections are orientated to target the angle of attack corresponding to the maximum lift to drag ratio, which is less than 8^o. Therefore, the numerical hydrofoil data from the two different wall-treatment approaches, is deemed to give reasonably accurate prediction of lift and drag forces on the blade section for the rotor design.

When the Reynolds number is increased to 12×10^6, the slope of the lift coefficient plot increases slightly compared to that at $Re = 1.6 \times 10^6$, with separations delayed and the drag coefficient reduced across all angles of attack. Similar trends can be found in experimental studies of aerofoils with thickness to chord ratios larger than 20% (e.g. NACA 4421 and 4424 wing section data from Abbot and Von Doenhoff (1959)). The maximum lift to drag ratio of 69 occurs at an angle of attack of 6^o.

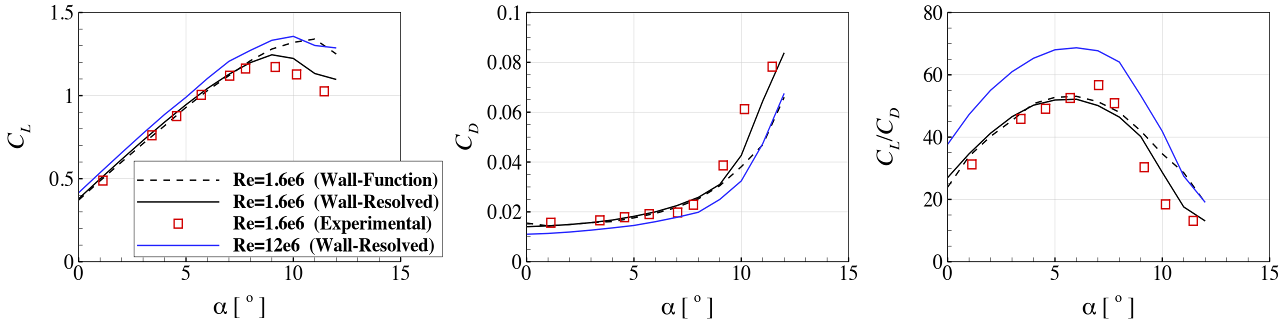

Fig. 3. 3 Sectional Lift coefficient (C_L), drag coefficient (C_D) and lift to drag ratio (C_L/C_D) computed for the RISØ-A1-24 profile.

Due to lack of high Re experimental data to compared with, the accuracy of the numerical results remains a little uncertain. Fuglsang and Bak (2004) report that the RISØ-A1-24 profile is sensitive to leading edge roughness, which infers that this profile can be sensitive to the turbulence intensity in the numerical model. However, by comparison to the experimental result of similar thick profiles, the computed result shows similar qualitatively behaviour.

3.1.2 Computational Domain and Mesh Convergence

The cylindrical computation domain of radius R_0, as shown in Fig. 3.4, is chosen for convenient comparison with results from blade resolved model. The blockage ratio, B, is calculated as: $\pi R^2/\pi R_0^2$. The low blockage ratio of 0.01, the moderate blockage ratio of 0.04 and the high blockage ratio of 0.16 correspond to $R_0 = 10R$, $5R$ and $2.5R$ respectively, where R is the rotor radius, $D/2$. Nishino and Willden (2012b) show that for blockage ratios investigated in the present study, the aspect ratio of the domain has minor effects on the power extraction. The domain extends $10R$ upstream and $20R$ downstream of the rotor plane. The free surface effect is not considered as it is known to only become significant when the blockage is very high, typically, $B > 0.2$ (Consul et al., 2013). A nacelle of diameter $d_{nac} = 3$ m is included in order to simulate the deflection of flows due to blockage. For simplicity, a support structure is not included in the present study.

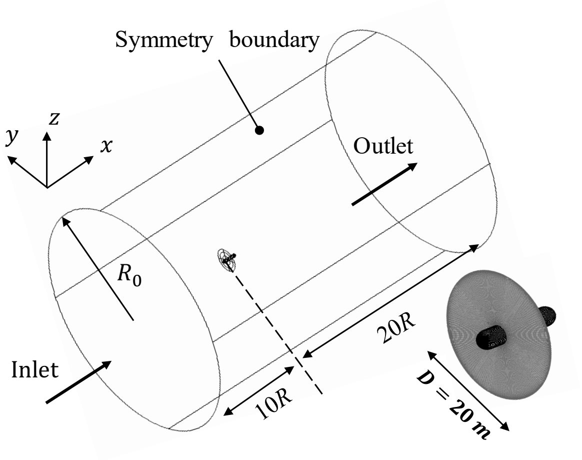

Fig. 3. 4 Schematic diagram of the computational domain of the RANS-BE computation. The streamwise direction is in the x direction.

The uniform inlet velocity U_∞ is $2\ \mathrm{m/s}$. A turbulence length scale of 14 m (0.7 times the rotor diameter of 20 m) is used following Gant and Stallard (2008). As the turbulence naturally decays from the inflow boundary to the rotor plane, a higher inlet turbulence intensity of 0.9% is used to achieve the desired turbulence intensity at 1D upstream from the rotor plane. In order to simulate the constraining effects due to the blockage, symmetry boundary condition is applied on the cylindrical surface

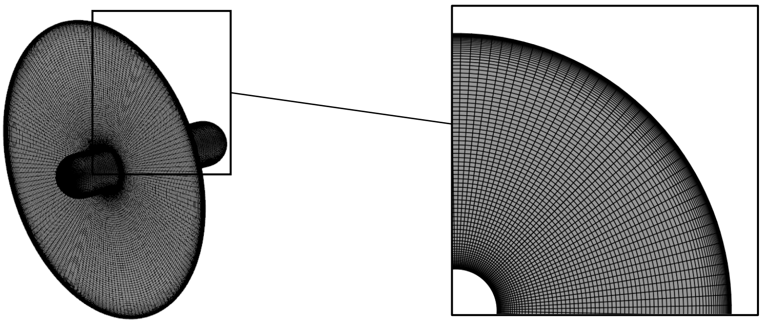

Fig. 3. 5 Structured mesh cells fitted on the rotor disc and on the nacelle. In order to capture the flow interactions, the mesh cells on the rotor disc are clustered around the rotor edges

Table 3. 2 Mesh Sensitivity Study for the RANS-BE design process (For B=0.01, TSR=7, c_x=2).

Mesh	N_{cells}	N_r/N_a	$N_u/N_d/N_l$	C_P	C_T	ΔC_P[%]	ΔC_T[%]
C	0.5 M	41 / 80	35 / 80 / 30	0.477	0.950	0.85	0.53
M	1 M	58 / 116	35 / 80 / 30	0.475	0.947	0.42	0.21
F1	1.8 M	82 / 164	35 / 80 / 30	0.473	0.945	0.00	0.00
F2	7.6 M	116 / 236	70 / 160 / 60	0.473	0.945	-	-

Fully structured hexahedral mesh is created for the whole domain. Fig. 3.5 shows the meshes on the nacelle surface and on the rotor disc. Four meshes of the largest domain ($B = 0.01$) are constructed to investigate the mesh sensitivity. Table 3.2 shows the numbers of nodes used in the upstream (N_u), downstream (N_d) and lateral (N_l) directions (which is the direction as the dash line shown in Fig. 3.4) of the domain and the nodes used to discretise the disc in radial (N_r) and azimuthal (N_a) directions. Sample results of C_P and C_T demonstrate that the Mesh F1, which consists of around 1.8 million cells, is able to achieve a good approximation of the rotor performance at a moderate computational expense.

3.1.3 Design Result

A range of tip-speed-ratios (TSRs), from 5 to 8, and local thrust coefficients, from 1.8 to 3.6, are investigated for design of rotors operating in the three different blockage ratios. Fig. 3.6

shows the contours of the design power and thrust coefficients as a function of TSR and local thrust coefficient. Note that all points represent different optimal rotor for the indicated design cases. Different colormap scale is used for different blockage ratios in order to highlight the optimal power coefficient. For all the three blockage ratios, the power coefficient peaks at TSR=5.5. As the blockage ratio increases, the target local thrust coefficient that results in peak power coefficient increases from $c_x = 1.9$ for $B = 0.01$, to $c_x = 2.1$ for $B = 0.04$, and $c_x = 3.4$ for $B = 0.16$. The peak design power coefficient increases from 0.506 for $B = 0.01$, to 0.531 for $B = 0.04$, and 0.678 for $B = 0.16$. The corresponding thrust coefficient is greater in higher blockage cases in order to utilise the greater pressure jump available across the rotor. For each blockage ratio, there are only small variations of the design power coefficient and thrust coefficient on the tip-speed-ratios.

Fig. 3.7 shows spanwise distributions of the solidity and geometric twist angle along the blade, for the optimal C_P design in each blockage ratio. To demonstrate the effect of TSR, two design results of TSR of 4.5 and 6.5 for B=0.04 are also plotted. It can be seen that as the design TSR increases, the design solidity decreases in order that an optimal resistance is exerted on the flow. The blade geometric twist angle also decreases in order to maintain the design angle of attack. For a given TSR, the design blade solidity increases with the blockage ratio, whereas the design twist angle reduces with the blockage ratio. This is because at their respective optimal local thrust coefficients, the streamwise velocity passing through the rotor decreases as the blockage increases, which means that the blade twist must be reduced so as to maintain the optimal angle of attack in higher blockage case.

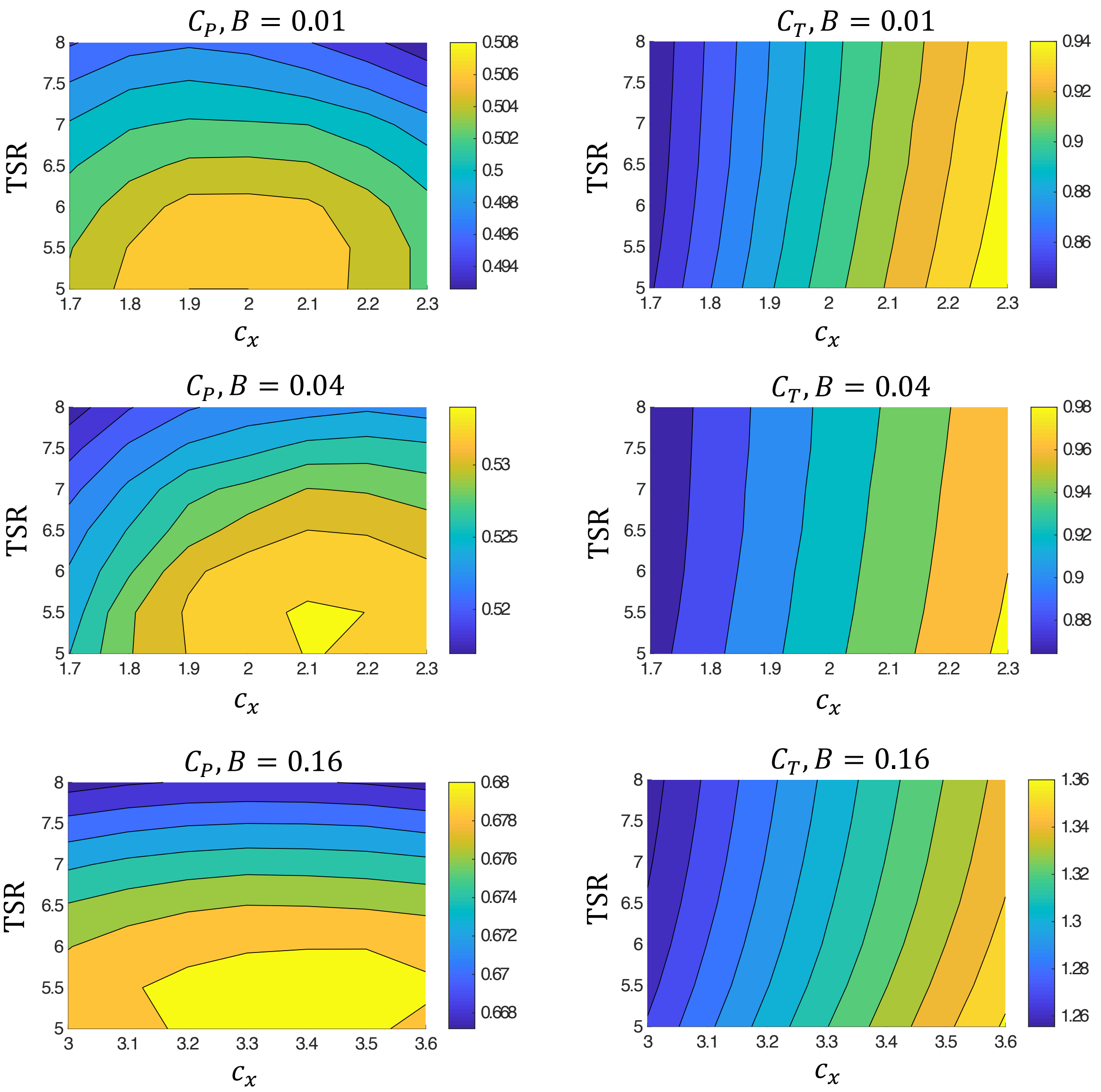

Fig. 3. 6 The contour of the design power and thrust coefficients for different blockage ratios (B), as a function of tip-speed-ratio (TSR) and local thrust coefficients (c_x).

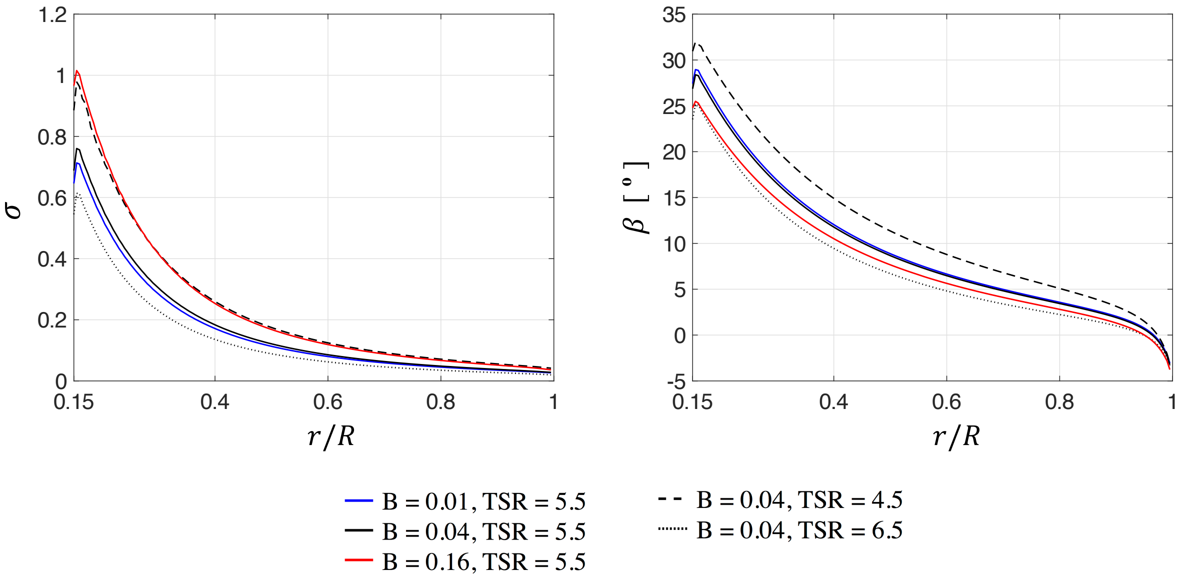

Fig. 3. 7 Blade solidity and twist angle for different rotor designs. The blue, black and red solid lines represent rotors designed for tip speed ratio (TSR) of 5.5 in blockage ratio (B) of 0.01, 0.04 and 0.16 respectively. The black dash and dot lines indicates rotors designed in B = 0.04 for TSR = 4.5 and 6.5 respectively.

Fig. 3.8 shows at different blockage ratios the contour of streamwise velocity, u_x, on the horizontal centre plane for the optimal C_P rotor design. It can be seen that as the blockage ratio increases, there is a significant increase in bypass flow velocity. Schluntz and Willden (2015) showed that: for a given design of rotor, as the blockage ratio increases, the constraining of the bypass region not only leads to greater flow speed but also greater resistance in the bypass, which results in increased flow passing through the turbine and thus greater power. However, in order to achieve the peak power coefficient for that increased blockage ratio, a further adjustment must be made to counter the higher resistance in the bypass region and the thrust applied by the rotor must be increased, achieved by increasing the blade chord. This results in a further increase in flow speed and pressure drop in the bypass region and hence improve the power available to the rotor. Further explanation can be found in Schluntz and Willden (2015).

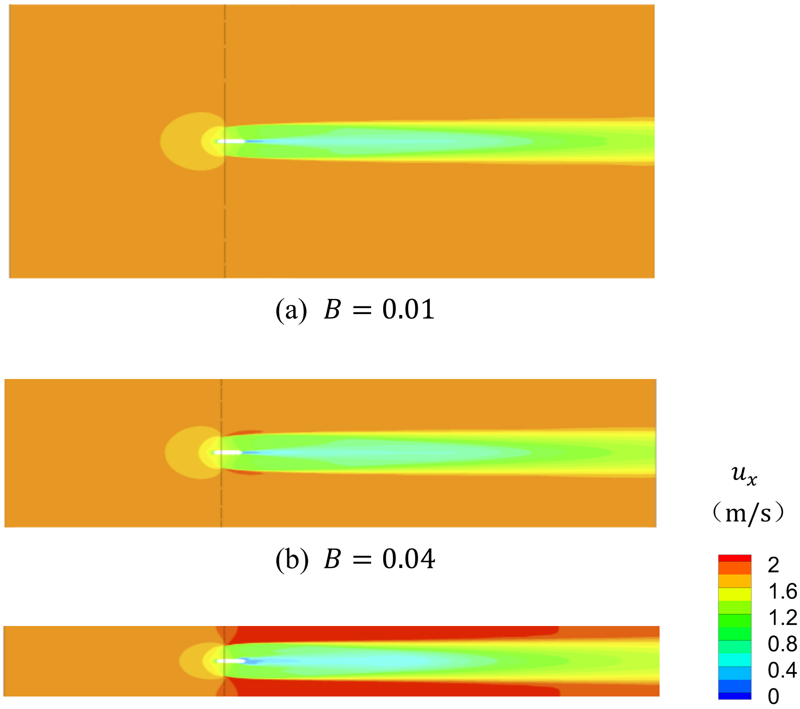

(a) $B = 0.01$

(b) $B = 0.04$

(c) $B = 0.16$

Fig. 3. 8 Contours of streamwise velocity, u_x, on the horizontal centre xy plane for the rotor designed for different blockage ratios.

3.2 Blade-Resolved Computation

The RANS-BE solutions presented thus far inherently neglect the spanwise flow effects due to the assumption of no flow interaction between adjacent rotor radii. Hence, the blade-resolved computation, which directly resolves the complete rotor geometry, is conducted in order to investigate the accuracy of the RANS-BE design tool. The three-dimensional mesh geometry is generated using ANSYS ICEM and the numerical computation is conducted using the OpenFOAM.

The three-dimensional rotor blades are generated using the RISØ-A1-24 profiles with the chord and twist distributions of the optimal rotor design for TSR of 5.5 and $B = 0.04$. The two-dimensional hydrofoil computations give, at the design angle of attack of 6 degrees, the center of pressure, through which aerodynamic force acts, at the location of 35% chord behind the leading edge. Hence, aerofoil sections are aligned based on points located at 35% of the chord. In order to have a realistic blade root section, the blade of r/R from 0.15 to 0.16 is replaced by a cylinder of radius 0.6 m (approximately 1/4 of the maximal chord length). In addition, inboard of $r/R = 0.3$, aerofoil sections are gradually thickened to fit the inserted cylindrical structure. The three-dimensional blade structure is shown in Fig. 3.9. This modification of the blade root sections is based on observations of some commercial full-scale axial tidal turbines that have been already deployed (Tomko, 2016).

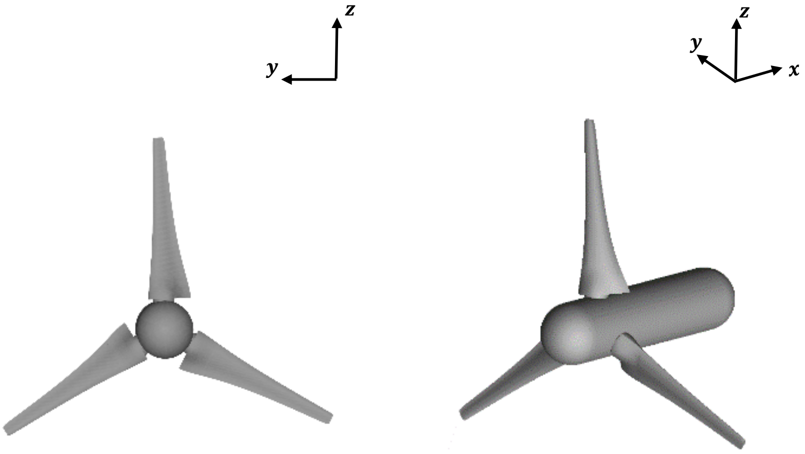

Fig. 3. 9 The front view (left) and the iso-metric view (right) of the full turbine geometry.

3.2.1 Computational Domain and Meshing Strategy

The computational domain takes advantage of symmetry and a 120^o wedge shaped domain is adopted as shown in Fig. 3.10. The entire domain is divided into an inner and an outer domain. A very high spatial resolution is required at the blade surface to capture high velocity gradients while such high resolution is unnecessary for the outer domain. The purpose of using the two separate domains is to exert better control over the mesh to prevent the high resolution in the inner domain from propagating through the entire domain. The inner domain has streamwise length of $0.9R$ and radius of $1.2R$. It contains one blade and the rotating part of the nacelle. The outer domain has upstream length of $10R$, downstream length of $20R$ and radius of R_o, which is $5R$ for $B = 0.04$. It contains the remaining stationary part of the nacelle and domain boundaries.

A fully structured mesh with all hexahedral cells is created. In the inner domain, a C-type blocking topology is adopted to fit the blade within which another C-type block is created at the blade root to fit the root cylinder. A Y-block is created to fit the nose cone of the nacelle. Several slices are created along the spanwise direction of the blade to offer mesh refinement in the root and tip regions. Fig. 3.11(a) shows the blocking topology for the inner domain. Based on the blocking topology, the generated surface mesh is shown in Fig. 3.11(b).

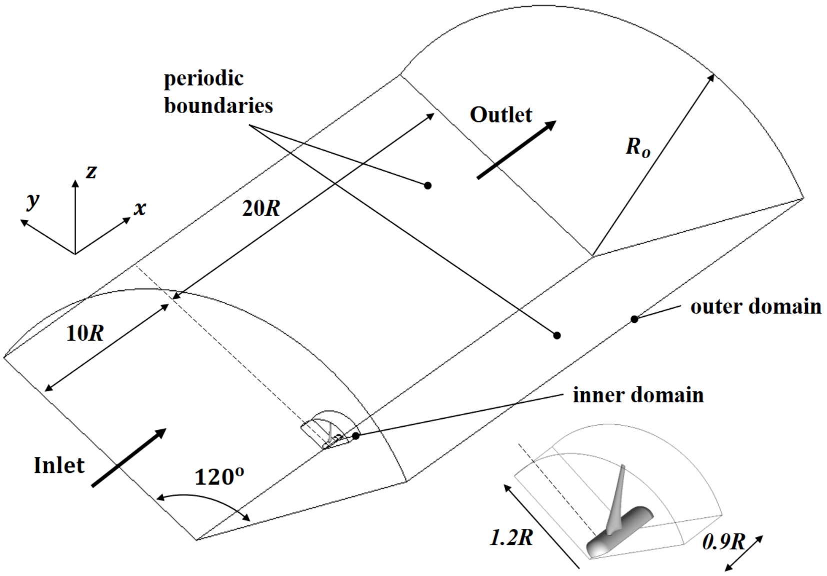

Fig. 3. 10 Schematic diagrams of computation domain and setup for the blade-resolved model.

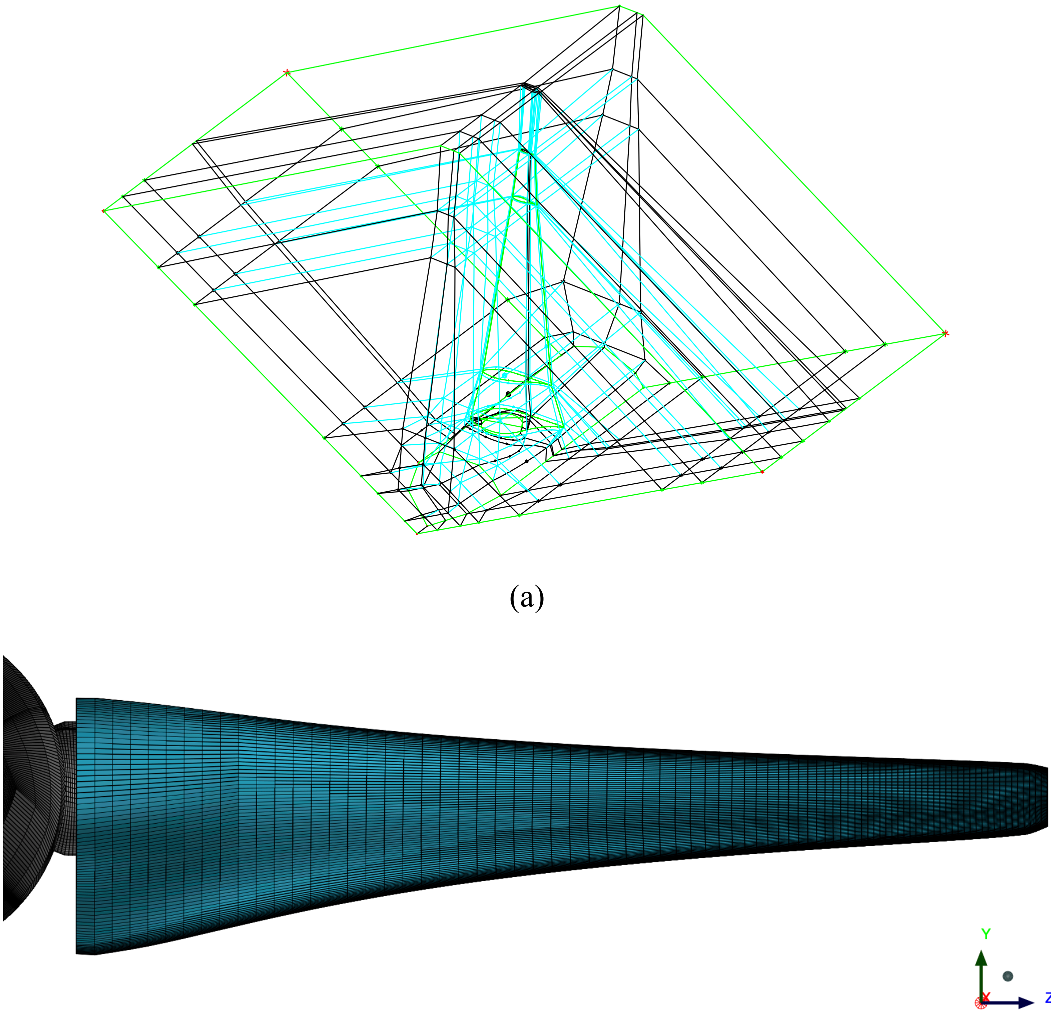

(a)

(b)

Fig. 3. 11 (a) Blocking Topology for the $120\ ^{o}$wedged inner domain; (b) Surface mesh cells on the rotor blade designed for B=0.04 and TSR=5.5.

Due to the high chord-based Reynolds number, it is not practical to place wall-adjacent cells within the viscous sublayer and to explicitly resolve the boundary layer on the blade surface. In addition, the highly twisted blade geometry and the abrupt change of the shape in the blade root region could lead to highly non-orthogonal and skewed mesh cells if the wall-resolved approach was used, to improve which would require significant refinement of the mesh in both the spanwise and chordwise directions, leading to an impractically high number of cells. Therefore, the wall-function approach is adopted. A wall-normal distance of $y^{+}{\sim}35$ is placed for the mesh cells at the blade span of $r/R = 0.7$ and for most of the mesh cells adjacent to the blade surface, y^+ is in the range of [30, 300].

3.2.2 Numerical Scheme and Mesh Sensitivity

In order to make comparisons with the RANS-BE results, the steady RANS equations with $k-\omega$ SST turbulence closure are solved to simulate the fluid flow. The same velocity inlet and pressure outlet boundary conditions as those in the RANS-BE simulation are utilized. Periodic boundary conditions are applied at the side faces of the wedge. The nonconformal cells at the interface between the inner and outer domain are joined by a conservative interpolation method through local Galerkin projection introduced by Farrell and Maddison (2011). This technique is referred as Arbitrary Mesh Interface (AMI) in OpenFOAM, achieved by applying the cyclicAMI boundary condition.

An initial mesh for the blade-resolved model consists of 92 cells in the blade spanwise direction (N_s) and 84 cells in the blade chord-wise direction (N_c) and the cell growth ratio normal to the blade surface, G, is set as 1.2, resulting in a total cell count of around 2.7 million for the inner domain ($N_{cells-inner}$). This initial mesh, referred as coarse mesh, is then selectively refined in chordwise, spanwise and wall normal directions to generate medium and fine meshes. The mesh parameters adopted for the three meshes and the power and thrust coefficients (C_P and C_T) resulted from the three meshes are summarized in Table 3.3. Based on the integrated blade thrust, 15,000 iterations are computed in order for the convergence to a quasi-steady solution. Over these iterations, the residuals for the governing equations reduced by at least 5 orders of the magnitude of velocity components, pressure and turbulence scalars.

Based on the level of agreement between the power and thrust coefficients for the coarse and fine meshes, the coarse mesh was deemed to be sufficiently accurate. Similar to the method adopted in Section 3.1.1, based on the greatest difference in the thrust and power coefficients between the coarse, medium and fine meshes and a factor of safety of 3.0, the uncertainty is estimated to be 0.42% and 0.45% in the power coefficient and thrust coefficient respectively. Therefore, the discretisation error is not expected to significantly impact the integrated loading results.

Table 3.3 Summary of mesh parameters adopted for the mesh sensitivity study.

Mesh	G	N_s	N_c	$N_{cells-inner}$	C_P	C_T	$\Delta C_P[\%]$	$\Delta C_T[\%]$
Coarse	1.2	92	84	2,703,422	0.5109	0.8842	-0.04	0.15
Medium	1.1	112	104	5,302,632	0.5118	0.8848	0.14	0.08
Fine	1.08	132	124	8,532,458	0.5111	0.8855	-	-

3.2.3 Comparison of RANS-BE Results

The spanwise distribution of the blade axial and tangential forces from the blade-resolved simulation is calculated by integrating the wall shear stress and surface pressure on the blade sections along the spanwise direction of the blade. The torque at a radial position of r is then calculated by multiplying of the tangential force and the corresponding radius r. Fig. 3.12 shows the sectional torque and axial thrust distributions along the blade span. The integrated power coefficient and thrust coefficient are 0.511 and 0.884 respectively. Compared to the result from RANS-BE simulations, the power coefficient and the thrust coefficient are 3.8% and 5.2% lower respectively.

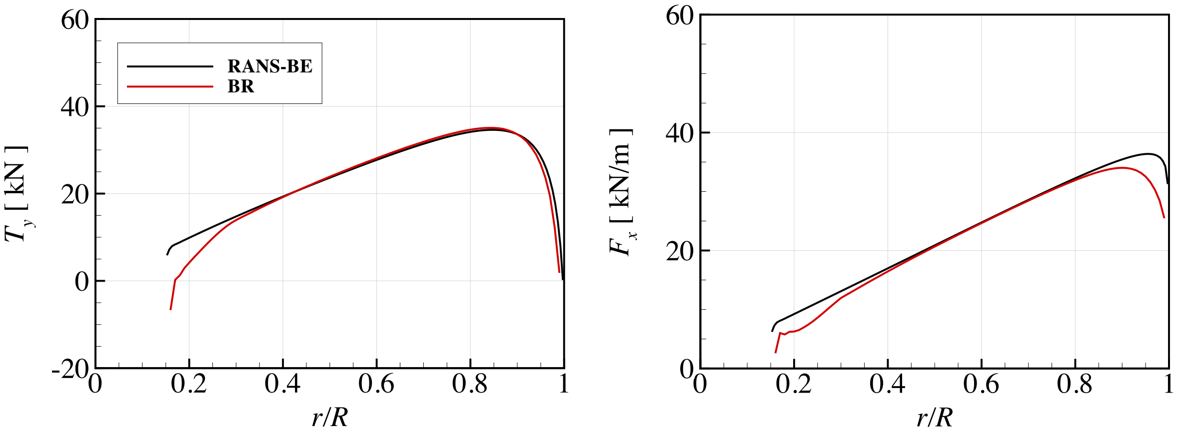

Fig. 3. 12 Comparison of thrust force (F_x) and torque (T_y), per unit span, along the blade from the RANS-BE (black) and blade resolved (BR) simulations.

In Fig. 3.12, the results from the blade-resolved computations show a good agreement with those from the RANS-BE simulation especially in the midspan section of the blade, with relative difference less than 1%. Table 3.4 lists the contribution of inboard, midspan and outboard blade section to the total power and thrust coefficient. In the blade inboard section from $0.15R$ to $0.35R$, there are large differences in both power and thrust coefficients between the two models, with relative error of $28\ \%$ and 24.7% respectively. This is because the modification of the blade root geometry inevitably introduces a bluff structure, which results in an increased drag force resisting the rotation of the blade, as shown in Fig. 3.12. In addition, the RANS-BE design tool does not include any root loss correction model. However, the inboard section only contributes a small part of both power and thrust coefficients, with the structural strength requirement for the design of the inboard section usually being more important than its aerodynamic performance.

Table 3. 4 Contribution of the inboard, midspan and outboard blade section to the total power and thrust coefficients from the RANS-BE model and the Blade Resolved (BR) model.

	$0.15R$ *to* $0.35R$ Inboard	$0.35R$ *to* $0.8R$ Mid-span	$0.8R$ *to* $1R$ Outboard	Total
		Power Coefficient		
RANS-BE	0.0640	0.3145	0.1528	0.531
BR	0.0460	0.3150	0.1501	0.511
Relative Difference	28%	0.2%	1.7%	3.8%
		Thrust Coefficient		
RANS-BE	0.1102	0.5099	0.3124	0.932
BR	0.0830	0.5047	0.2957	0.884
Relative Difference	24.7%	1%	5.4%	5.2%

In the blade tip region, the RANS-BE model gives reasonably good approximation in the torque with a relative difference of 1.7% but performs worse in predicting the axial thrust, giving a relative difference of 5.4%. Even though the Glauert correction model is implemented, it only corrects for the discrete blade number and does not consider other three-dimensional flow effects. The spanwise flow effect becomes significant in the tip region due to the pressure equalisation which forces the flow from the pressure surface to suction surface and generates blade tip vortices. These vortices reduce the pressure difference between the upper and lower surfaces of the blade and therefore change the aerodynamic performance of the tip region of the blade. The tip loss model of Shen *et al.* (2005) accounted for the pressure equalization but its correction coefficients are empirically determined and are isotropic. Wimshurst and Willden (2017) extended this model and introduced an anisotropic correction to axial and tangential forces respectively. However, since the rotor investigated in their study is different from the one designed in the present study, the coefficients may be sub-optimal.

3.3 Summary

An investigation into the impact of local blockage conditions on the design of a single tidal stream rotor and its performance are investigated. Three blockage ratios are studied including: a low blockage ratio of 0.01, a moderate blockage ratio of 0.04 and a high blockage ratio of 0.16. The RISØ-A1-24 profile is adopted for the entire span of the rotor blade. Steady RANS computations are conducted to obtain sectional lift and drag coefficients, which are used as the input to the design process. A series of tidal rotors are designed using the RANS-BE design tool with objective to achieve maximum power coefficient. For all blockage ratios considered, the optimal design tip speed ratio (TSR) is found to be 5.5. The power and thrust coefficients are seen to increase as the blockage ratio increases. The design solidity ratio increases with the blockage ratio in order to utilize the higher pressure difference available across the rotor plane, whilst the design twist angle slightly decreases as the blockage ratio increases in order to maintain the optimal angle of attack along the rotor blade span.

Blade resolved computations are conducted to evaluate the RANS-BE design tool. Good agreements in power and thrust coefficients are observed, with relative differences of 3.8% and 5.2% respectively. Further investigation of the thrust and torque distributions along the blade are then conducted. The results show a good agreement in the midspan of the blade between the two methods (with errors less than 1%). The primary differences in thrust and torque distributions are found in the root section of the blade, which is mainly due to the practical geometry modification and the steady computation conducted, and in the tip region of the blade, which is thought due to the deficiencies of the implemented Glauert tip correction model.

Chapter 4

Lab-Scale Rotor Design and Performance

In Chapter 3, the modified and enhanced numerical design tool are evaluated for the rotor of diameter 18 m. In this chapter, a similar design procedure is adopted and is used to design multi-rotor tidal array to exploit its specific blocked flow condition and leverage the constructive interference effect to maximize the power efficiency.

Garrett and Cummins (2007) have shown that the peak power coefficient for an idealized turbine operating in a blocked flow, increases by $(1-B)^{-2}$ above the well-known Betz limit of 0.593. The blockage ratio, B, is defined as the fraction of a flow passage occupied by the swept area of a turbine and has been shown to be an important factor in the performance of a tidal stream rotor. Constraining the flow expansion results in accelerated flow in the bypass flow region that surrounds the core stream-tube. According to the Bernoulli equation, due to this higher flow in the bypass region than that in the far upstream of the rotor, when pressure is equalized in far wake downstream from the rotor, the pressure does not recovery to the pressure in the far upstream, which leads to a higher pressure gradient across the turbine than that in a unconstrained flow condition and this enables a higher level of thrust to be applied by the turbine. Both analytical and numerical models have shown that turbine performance can be increased in blocked flows (see e.g. Nishino and Willden, 2012a; Wimshurst and Willden, 2016a).

Several studies have been conducted to investigate flow interactions in a tidal turbine array. Nishino and Willden (2012b) studied a tidal array partially spanning a much wider flow passage and introduced the concept of the local blockage effect, also known as the constructive interference effect, due to the laterally close-packed turbine configuration. They showed that tidal array performance increases when the intra-array spacing reduces to an optimal value that achieves the required local blockage to maximize constructive interference effects, but then decreases as the spacing is further reduced due to an array-scale choking effect. Nishino and Willden (2013), Hunter et al. (2015) and Vogel and Willden (2017, 2018) numerically investigated the constructive interference effect and showed increased tidal array performance. Olczak et al. (2016) and Gebreslassie et al. (2015) showed numerically that the lateral closely spaced configuration can achieve a performance increase, but may also affect the performance of downstream turbines. Experimentally, Nuernberg and Tao (2018) and Stallard et al., (2013) investigated interactions between tidal turbine wakes and found faster wake recovery downstream of the array.

Schluntz and Willden (2015) used the RANS-BE method to design full-scale rotors of 10-meter diameter to exploit the constructive interference effect. However, their focus was mainly on design of a single rotor within an infinitely long cross-stream array of turbines. To date, few studies have been conducted to design a short tidal fence for its specific blocked flow condition.

The present study adopts the RANS-BE method to design a lab-scale multi-rotor arrays consisting four 1.2m diameter rotors in support of an experimental campaign conducted at the FloWave facility at the University of Edinburgh. The structure of this chapter is as follows. Section 4.1 discusses the design conditions, which is based on the FloWave Ocean Energy Research Facility at the University of Edinburgh, and the rotor parameters for the design process. Section 4.2 discusses two-dimensional hydrofoil modifications and performances. Section 4.3

presents the numerical setup, the meshing strategy and the design results for the multi-rotor array. High-fidelity blade-resolved computations are conducted in Section 4.4 and comparisons against the RANS-BE design result are presented.

4.1 Design Conditions

A rotor design for an array of four 1.2 m diameter lab-scale tidal turbines was developed in support of an experimental campaign being conducted at the FloWave Ocean Energy Research facility at the University of Edinburgh through a UKCMER SuperGen and Wave Energy Scotland Flex Fund project. The rotors are designed to be deployed in a close-packed configuration to exploit constructive interference effects. The aim of the design process is to maximize the array power production. The flow dynamics between the device-scale and the array-scale are directly resolved in the RANS solver. Turbine thrust is adjusted through the specification of the local thrust coefficient, c_x, as defined in Eq. (2.34), to balance these two-scale effects and optimize the array performance.

The diameter and depth of the FloWave tank are of 25 m and 2 m respectively. The current is generated by 28 drive units, each of these contains a 5-bladed impeller. The circular shape of the FloWave tank means that estimation of the effective width for defining blockage conditions is not straightforward. Recirculation regions near the sides of the tank mean that the effective width is significantly less than the tank diameter, and the effective width may also vary with turbine thrust due to the interaction between the array thrust, bypass flow and the recirculation regions. As a result, a conservative estimate of the effective width of 16 m is used based on the observation of the recirculation regions in the tank. This assumption is explored further in later sections.

A uniform streamwise flow speed of 0.8 m/s is used for rotor design since the most detailed analysis of flow in the tank was performed at this value (Sutherland *et al.*, 2017). The vertical variation of the streamwise velocity at the rotor plane (at the height of 1 m) is small, with only a 12.5% decrease to 0.7 m/s at the bottom region of the tank (at the height of 0.1 m). Hence, for simplicity the shear profile is not simulated. The streamwise Freestream Turbulence Intensity (FTI) which is used to quantify the magnitude of turbulence is defined as:

$$\mathrm{FTI} = \frac{\sqrt{\langle u'^2 \rangle}}{u} \tag{4.1}$$

where u' is the streamwise velocity perturbation and u is the mean velocity value. The distribution of the measured streamwise turbulence intensity at this flow speed is centred around 7.08%, varying bewteen 5% to 10% (Sutherland *et al.*, 2017). The turbulence intensity is chosen as 7.08%.

The rotor diameter of 1.2 m is chosen to be reasonably large compared to the depth of 2 m of the tank, helping to increase the chord-based Reynolds number and ensure a significant constructive interference effect, whilst not affecting the free surface. The design Tip-Speed-Ratio (TSR) of 7 is chosen to be relative high compared to other tidal rotors (see e.g. Schluntz and Willden, 2015) due to the conservative estimation of the effective width (if the effective width is higher, the TSR for optimal performance is likely to be reduced). The diameter of the nacelle and rotor nose is chosen as 0.15 m in order to accommodate the turbine generator and instrumentation.

A summary of the design conditions is listed in Table 4.1. Based on the design TSR, inflow velocity and an estimated chord length at $r/R = 0.7$ of the blade, the chord-based Reynolds number at 70% span is 2×10^5.

Table 4. 1 Summary of design conditions

Inflow velocity (U_∞)	0.8 m/s
Freestream Turbulence Intensity (FTI)	7.08 %
Number of blades (N)	3
Rotor diameter (d)	1.2 m
Nose diameter	0.15 m
Design Tip-Speed-Ratio (TSR)	7
Chord-based Reynolds number ($\mathrm{Re}_{0.7R}$)	2×10^5
Tank depth (h)	2 m
Estimated effective tank width (w)	16 m

4.2 Hydrofoil Study

The Wortmann FX-84-W-140 profile is selected as the blade section in the design process. The profile, which is originally designed for use on small wind turbines, has a maximum thickness-to-chord ratio of 14.1% and has good hydrodynamic characteristics at Reynolds number of order 10^5. The FX-84-W series consist of a family of profiles with thickness-to-chord ratio ranging from 9.7% to 21.8%, meaning that the blade could be easily modified for further structural enhancement at the blade root or performance improvement at the blade tip without profile compatibility concerns.

4.2.1 Hydrofoil Modifications

The theoretical FX-84-W-140 hydrofoil has a sharp trailing edge, which is not realistic for the manufacturing process. In addition, in this lab-scale rotor design case where the chord length near the blade tip is estimated to be 20 – 30 mm, any small modification in the hydrofoil trailing edge would lead to a large geometry change, altering its hydrodynamic performance. Hence, it is necessary to incorporate this attribute and minimize the uncertainty in the design process.

The thickness of the trailing edge of the turbine blade δ_0 is set to 0.25 mm (for practicality and safety concerns) and is maintained along the entire blade span. Depending on the chord length at different blade spanwise positions, modifications of the baseline FX-84-W-140 hydrofoil are generated with different trailing edge thickness to chord ratios (δ_0/c). The chord lengths near the blade tip and root region are approximated to be 20 mm and 120 mm, which corresponds to a $\delta_0/c_{tip} = 0.0125$ and $\delta_0/c_{root} = 0.0021$ respectively. Two trailing edge thickened hydrofoils with δ_0/c_{tip} and δ_0/c_{root} are investigated, as discussed in later sections. The hydrodynamic characteristics of intermediate hydrofoil sections along the blade span with different δ_0/c are obtained through linear interpolation.

In the wind energy industry, blunt trailing edge modification has been considered to improve the aerodynamic performance of thick aerofoils for use near the root section of the turbine blades (see e.g. Standish and van Dam, 2003). Typically, there are two manners to create blunt trailing edge aerofoils, either by truncating the rear portion of the baseline aerofoil or by using a thickening function to symmetrically add thickness to both sides of the camber line over a portion of the aerofoil. Which thickening method outperforms the other still remains an open question, especially for transitional $Re \approx 10^5$. Hence, both methods are investigated in the present study.

The hydrofoil outlined in red in Fig. 4.1 shows the baseline FX-84-W-140 hydrofoil with unit chord length. The thickening function used follows Xu *et al.*, 2014:

$$
\begin{aligned}
&x = x_0, y = y_0 && 0 \leq x \leq x_t \\
&x = x_0, y = y_0 \pm 0.5\delta_0 \left(\frac{x - x_t}{c - x_t}\right)^n && x_t < x \leq c,
\end{aligned}
\tag{4.2}
$$

where (x_0, y_0) are the coordinates of the baseline hydrofoil, x_t is location of maximum thickness, c is chord length and (x, y) are the coordinates of the thickened hydrofoil. n is chosen as 2 here to ensure a smooth transition of geometry shape (Xu *et al.*, 2014).

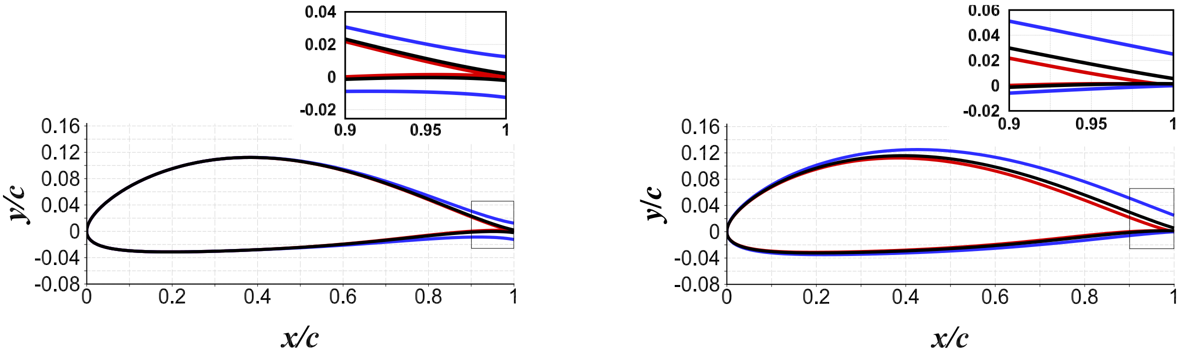

(a)

(b)

Fig. 4. 1 The baseline FX-84-W-140 profile is shown in red. (a): The thickened profiles obtained from the thickening equation, Eq. (4.2), where the TF-0125 is shown in blue the TF-0021 is shown in black. (b): The truncated profiles obtained through the truncation method where the TR-0125 is shown in blue and the TR-0021 is shown in black.

Fig. 4.1(a) shows the modified hydrofoils, generated through the thickening equation Eq. (4.2), with $\delta_0/c_{tip} = 0.0125$ (in blue) and $\delta_0/c_{root} = 0.0021$ (in black), which are denoted TF-0125 and TF-0021 respectively. Fig. 4.1(b) shows the modified hydrofoils obtained via the truncation method. Specifically, in order to achieve $\delta_0/c = 0.0125$ and 0.0021, the hydrofoil is truncated aft 93.6% and 98.1% of the baseline FX-84-W-140 hydrofoil respectively. The hydrofoils are then rescaled to a common unit chord length, which are referred as TR-0125 and

TR-0021 respectively. It can be seen that the truncation method increases the hydrofoil maximum thickness to chord ratio and alters its camber line.

4.2.2 Numerical Method Evaluation

Due to a lack of available experimental data for the FX-84-W-140 hydrofoil, the FX 63-137 aerofoil with a similar thickness-to-chord ratio (13.7%) is investigated in order to validate the low Reynolds number blunt trailing edge hydrofoil computations. The original FX 63-137 aerofoil has a sharp trailing edge but its coordinates are not analytically smooth. Selig and McGranahan (2004) used a modified smooth version that has a blunt trailing edge in their experiment, as shown in Fig. 4.2, which is used in the validation study.

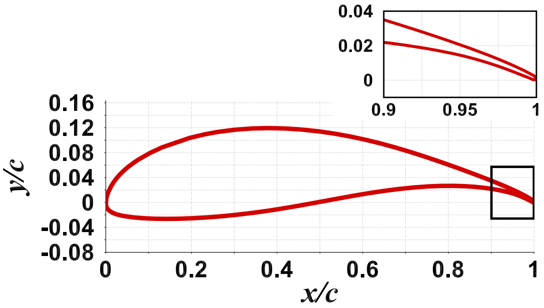

Fig. 4. 2 The FX 63-137 profile used for validation of the numerical tool.

Steady RANS computations using the $k-\omega\,SST$ and $\gamma-Re_\theta$ turbulence closure models are conducted using OpenFOAM. As discussed in Chapter 2, the $k-\omega\,SST$ model assumes a fully turbulent flow and hence a fully turbulent boundary layer on the blade surface (Menter *et al.*, 2003), while the transitional model, using $\gamma-Re_\theta$ correlation to predict the intermittency and the transition onset criteria, allowing a free transition from laminar to turbulent flow (Langtry and Menter, 2009).

The inlet turbulence is set such that the freestream turbulence intensity decays to around 0.1% to match the experimental condition using a reference length scale of half of the chord length. The inviscid-viscous boundary layer code XFOIL (Derla, 1989) is also used for comparison, in which the transition is estimated by e^N method. In this study, N is set to the default value of 9, which corresponds to a smooth hydrofoil surface in a very low freestream turbulence intensity. The Reynolds number for computations is 2×10^5.

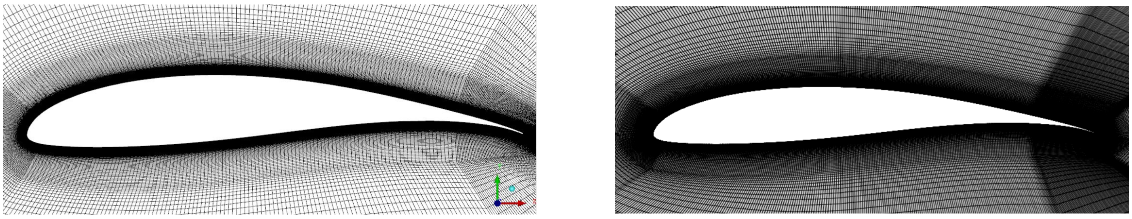
(a) (b)

Fig. 4. 3 (a) coarse (b) fine mesh adopted for the FX 63-137 profile.

Table 4.2 Summary of the mesh sensitivity study for the modified FX 63-137 at an angle of attack of 6^o in the experimental condition of Selig and McGranahan (2004).

Mesh	N_{cell}	C_L	C_D	ΔC_L[%]	ΔC_D[%]
Coarse	77,316	1.3561	0.01816	-0.04%	0.72%
Fine	121,600	1.3567	0.01803	-	-

A mesh sensitivity study is conducted based on $\gamma - Re_\theta$ correlation turbulence closure model at angle of attack 6°. An initial mesh, referred as coarse mesh, with O-type blocking topology is fitted around the hydrofoil, with 284 cells on each of the upper and lower surface. The wall adjacent cells are placed such that $y^+ < 1$ with a wall-normal expansion factor of 1.08, as shown in Fig. 4.3. This very high resolution is adopted because the transitional $\gamma - Re_\theta$ model can be more sensitive to mesh resolution than the fully turbulent $k - \omega\ SST$ model. The far-field boundary is located ten chord lengths away from the hydrofoil. Due to the high resolution of the initial mesh, only one further mesh refinement is conducted. The refined mesh is referred as the fine mesh. The total number of mesh cells and the the lift and drag coefficients are summarized in Table 4.2. Based on the level of agreement between the lift and drag coefficients for the coarse and fine mesh, the coarse mesh is deemed to be sufficiently accurate and is used for further computations. The numerical uncertainty at angle of attack of 6^o, following the method adopted in Chapter 2, is estimated to be 0.12% and 2.16% for the lift and drag coefficients respectively.

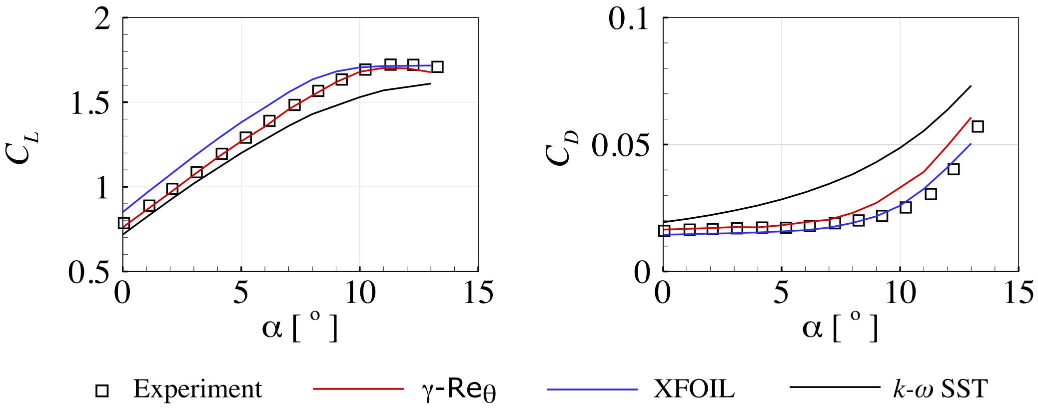

Fig. 4. 4 The lift (C_L) and drag (C_D) coefficients for the FX 63-137 profile at $\mathrm{Re} = 2 \times 10^5$ and freestream turbulence intensity of 0.1%, obtained from numerical simulation with different turbulence models, XFOIL and experimental results of Selig and McGranahan (2004).

Fig. 4.4 shows the computed lift coefficient (C_L) and drag coefficient (C_D) from different computations and the experimental study (Selig and McGranahan, 2004). When the angle of attack (α) is between 0 and 10 degrees, the lift coefficients computed by the $\gamma - Re_\theta$ model are in good agreement with the experimental results. The $k - \omega$ SST model under-predicts the lift curve while the XFOIL over-predicts the lift curve. Beyond $\alpha = 10°$, the $\gamma - Re_\theta$ model well captures the onset of stall but slightly under-predicts the lift coefficients. The $k - \omega$ SST model predicts a delayed stall and largely under-predicts the lift coefficients while the XFOIL shows a good agreement. As for the drag coefficient, the $\gamma - Re_\theta$ model well predicts the value at low and moderate angle of attacks, and it over-predicts the value beyond $\alpha = 8^o$. The $k - \omega\ SST$ model significantly over-predicts the value for all angles of attack due to its assumption of a turbulent boundary layer throughout. The XFOIL code slightly under-predicts the value at low angle of attacks but generally it gives the best predication of drag coefficients over the angles of attack investigated among the three models.

In the rotor design process, the blade is twisted such that it should achieve an angle of attack approximately corresponding to the maximum lift-to-drag ratio, which is normally at a moderate angle and less than the stall angle. Although the XFOIL code can give reasonably good prediction of lift and drag coefficients, the complex fluid physics may not be resolved in the simple coupling of the boundary layer equation and the potential flow equation (the underlying equations solved in the XFOIL). Following the procedure adopted in the existing commercial wind rotor design process (see e.g. Bak *et al*., 2013), the more reliable $\gamma - Re_\theta$ model is deemed to give reasonably accurate predictions of lift and drag coefficients for the design process and is used for further computations.

4.2.3 Effect of Blunt Trailing Edge

In order to study the effect of the trailing edge modifications on the hydrodynamic performance of the hydrofoil, the lift and drag polars of the baseline FX-84-W-140 hydrofoil (sharp trailing edge), the TF-0125 and the TR-0125 are computed, as shown in Fig. 4.5. The chord-based Reynolds number is 2×10^5 and the turbulence intensity is chosen as 0.1%. Compared to the baseline hydrofoil, when the angle of attack is between 0 and 10 degrees, the TF-0125 shows increased lift coefficients whereas the TR-0125 shows decreased lift coefficients. Both the TF-0125 and the TR-0125 show similar drag coefficients between 0 and 10 degrees, which are slightly higher than those of the baseline hydrofoil. Correspondingly, the TF-0125 results in the highest lift to drag curve when the angle of attack is between 0 and 10 degrees. The optimal angle of attack for the TF-0125 is 7 degrees which leads to the highest lift-to-drag ratio of 56.3.

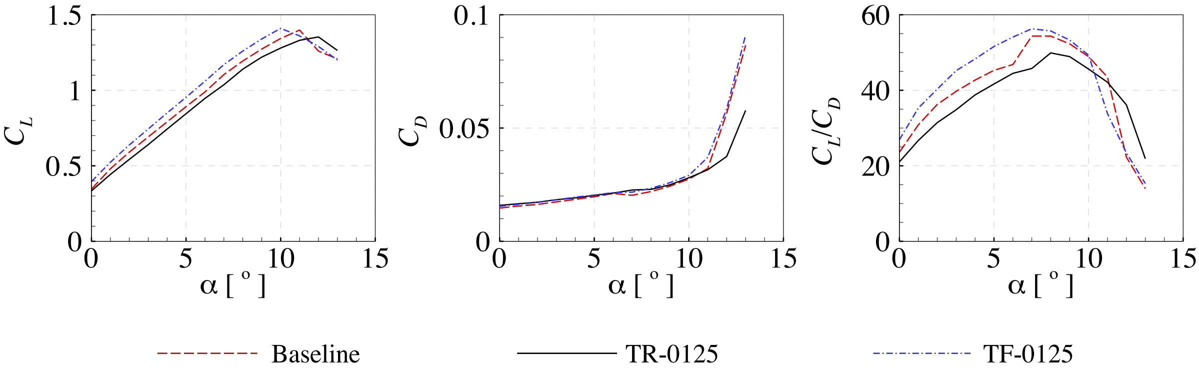

Fig. 4. 5 Lift (C_L) and drag (C_D) coefficients and lift-to-drag ratios (C_L/C_D) for the baseline FX 84-140 profile (red dash line), the TR-0125 (black lines) and TF-0125 (blue lines) at $\mathrm{Re} = 2 \times 10^5$ and freestream turbulence intensity of 0.1%.

Fig. 4.6 shows the static pressure coefficient (C_{pre}) and the wall shear stress (τ_w) distribution on the suction surfaces of the hydrofoils at $\alpha = 7^o$, where the static pressure coefficient is defined by normalising the static pressure with the undisturbed dynamic pressure,

$$C_{pre} = \frac{p - p_{ref}}{\frac{1}{2}\rho u_{ref}^2} \tag{4.3}$$

where p_{ref} and u_{ref} are undisturbed far-upstream pressure and velocity respectively. In Fig. 4.6, laminar separation bubbles followed by turbulent flow reattachment are observed in all cases. For the baseline hydrofoil, τ_w becomes negative at $x/c \approx 0.37$, which indicates the occurrence of the laminar separation bubble. Correspondingly, the C_{pre} distribution exhibits a local plateau. At $x/c \approx 0.54$, τ_w decreases dramatically (a large increase in its magnitude), which indicates the laminar to turbulent transition happens in the separated shear layer. At $x/c \approx 0.6$, τ_w starts to recover to a positive value, which corresponds to the turbulent boundary layer reattachment. After $x/c \approx 0.85$, τ_w decreases to approximately zero, which indicates that at this range of Reynolds number, the trailing edge turbulent separation may occur even at the optimal angle of attack (of maximum lift-to-drag ratio).

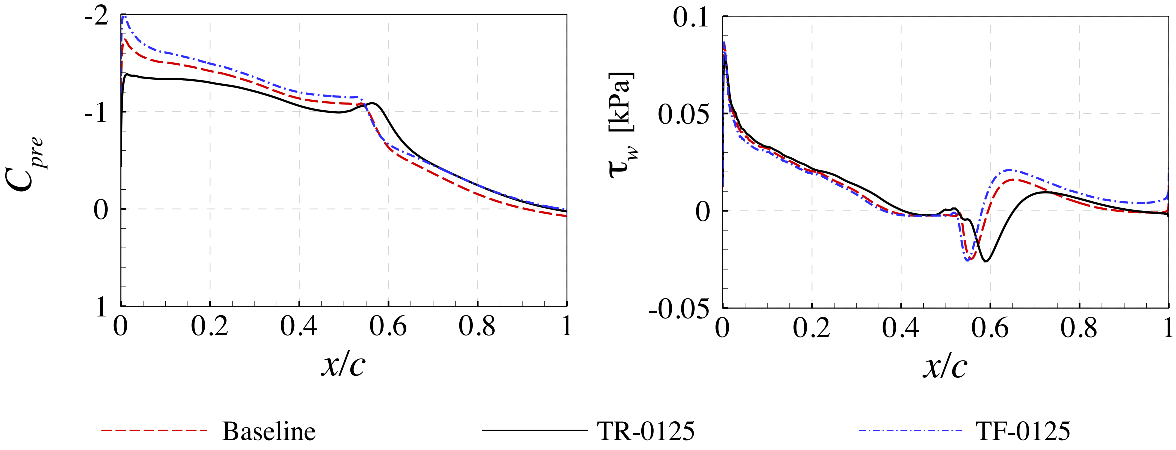

Fig. 4. 6 Suction surface pressure coefficient (C_{pre}) and wall shear stress (τ_w) distributions for the baseline FX 84-140, the TR-0125 and the TF-0125 hydrofoils, at $\alpha = 7^o$.

For the TF-0125 hydrofoil, before the flow reattachment, the τ_w distribution displays similar features as that for the baseline hydrofoil except that the whole τ_w distribution is slightly shifted towards the leading-edge. However, after the flow reattachment, the value of τ_w becomes greater than that for the baseline hydrofoil, reducing the likelihood of trailing edge flow separation for the TF-0125 (the separation on the blade surface happens when the wall shear stress becomes negative). One potential explanation for the benefit of the blunt trailing edge could be that the presence of bluntness introduces vortices shed away from the hydrofoil surface, which results in the near wake region acting as off-surface pressure recovery process that reduces the adverse pressure gradient at low angle of attacks (Standish and van Dam, 2003). As can be seen in Fig. 4.7, small recirculation zones behind the trailing edges are observed in the two blunt hydrofoil cases, which are absent in the baseline case. As a result, compared to the baseline hydrofoil, the TF-0125 provides an increase in lift at low angles of attack. However, due to a higher wall shear stress which yields a higher frictional force, the TF-0125 also experiences an increase in drag.

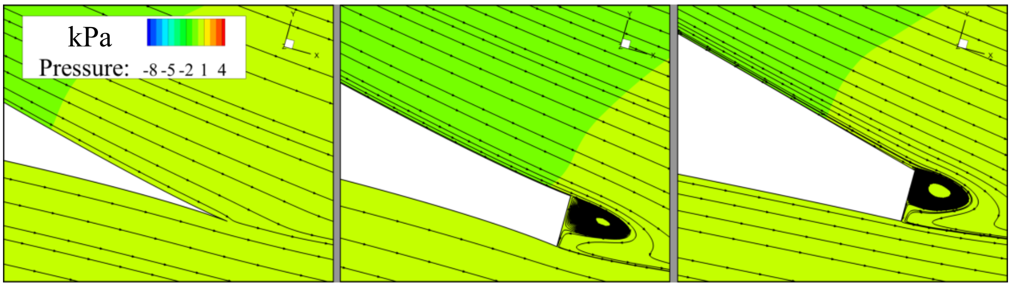

(a) (b) (c)

Fig. 4. 7 The pressure distribution (kPa) and the streamlines around the trailing edge of (a) the baseline sharp-trailing edge FX 84-140 (b) the TF-0125 and (c) the TR-0125.

The TR-0125 hydrofoil combines the effects of a blunt trailing edge and increased thickness-to-chord ratio. As can be seen from Fig.4.6, the suction peak of the TR-0125 is much less negative than that of the TF-0125 and the baseline cases, which leads to decreases in lift. This difference has also been observed in other studies, which may be explained by that the truncation method increases the radius of curvature of the leading edge in relation to the chord length (Chen and Agarwal, 2012; Thomareisa and Papadakis, 2017).

In summary, the thickening function method introduces a blunt trailing edge and a recirculation regions, which acts as off-surface pressure recovery to mitigate adverse pressure gradient and leads to a more negative pressure distribution (greater suction) on the suction surface. This results in increased lift coefficients among the linear region, and for the thickness of the blunt trailing edges investigated here, it only leads to slightly increased drag coefficients. As a result, a higher maximum lift-to-drag ratio is obtained. The truncation method not only leads to the blunt trailing edge but also introduces increased maximum thickness-to-chord ratio. This makes it difficult to differentiate the favourable effects of the blunt trailing edge from the often-adverse effects of increased thickness. Compared to the baseline hydrofoil, the truncated version results in hydrodynamic performance degradation. Therefore, the thickening function method is used hereafter to blunt the baseline FX-84-W-140 hydrofoil.

4.2.4 Effect of Turbulence Intensity

The measured freestream turbulence intensity (FTI) in the FloWave tank is approximately $7.08\ \%$ at a mean flow velocity of 0.8 m/s (Sutherland *et al.*, 2017). This turbulence intensity is then renormalized by the approximated relative velocities local to the rotating blade at the tip and root regions (at the design tip-speed-ratio of 7) to give blade-relative turbulence intensities of 0.5% and 5.5% respectively for the TF-0125 and TF-0021 hydrofoils studied.

Fig. 4.8 shows the computed lift and drag polars of the TF-0125 and TF-0021 hydrofoils at 1.5% and 5.5% respectively. At 1.5% FTI the lift coefficients are slightly increased compared to 0.1% FTI in the linear region while 5.5% FTI decreases the slope of the lift coefficient curves, resulting in a decreased maximum lift coefficient and delayed stall. At the relatively low FTI of 1.5%, the drag coefficients decrease whereas when FTI increases to a high level of 5.5% the drag coefficient increases significantly. The optimal angle of attack decreases from 7 degree to 6 degree when FTI increases to 1.5% and 5.5%.

In order to understand the flow physics on the blade surface when FTI increases, Fig. 4.9

shows the distributions of C_{pre} and τ_w on the suction surfaces of the TF-0125 at $\alpha = 0^o$, 3^o and 7^o respectively. As α increases, the occurrence of the laminar-to-turbulent transition moves towards the leading edge. Compared to low FTI of 0.1%, the separation bubble length is significantly reduced in the 1.5% FTI case and is completely eliminated at 5.5% FTI which has fully attached laminar-to-turbulent transition where the transition point is close to the leading edge. At 1.5% FTI, the reduction of separation bubble length reduces the plateau in the suction surface, as shown in the Fig. 4.9, which reduces the pressure drag. This reduction mitigates the effect of the increased friction drag due to the larger portion of the turbulent boundary layer compared to the lower 0.1% FTI case, resulting in an overall decrease in the drag force. At 5.5% FTI, however, the transition happens close to the leading edge and a majority (>70%) of the boundary layer becomes turbulent. The wall shear stress becomes more significant, resulting in a large increase in the drag coefficient.

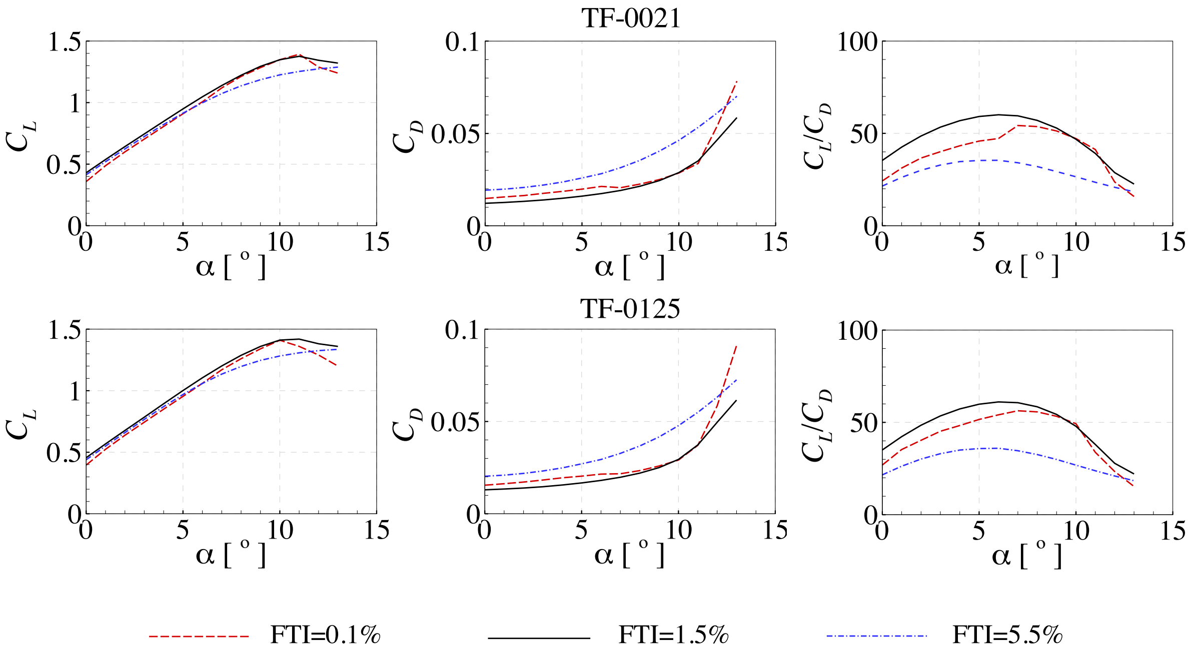

Fig. 4. 8 Lift (C_L) and drag (C_D) coefficients and lift-to-drag ratios (C_L/C_D) for the TF-0021 and TF-0125 at Reynolds number of 2×10^5 and freestream turbulence intensities (FTI) of 0.1%, 1.5% and

5.5%.

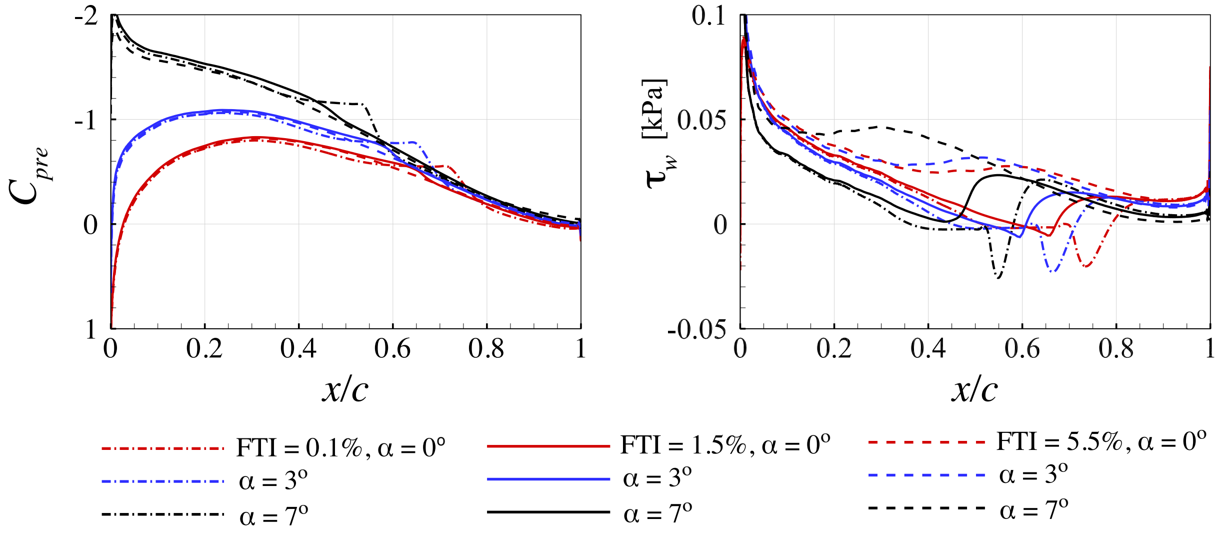

Fig. 4. 9 Pressure coefficient (C_{pre}) and the wall shear stress (τ_w) distributions on the suction surface of the TF-0125 at different angle of attacks and at different freestream turbulence intensities (FTI).

Fig. 4.10 plots the distributions of C_{pre} and τ_w on the suction surface of the TF-0021 and TF-0125 at $\alpha = 0^o$, 3^o and 7^o when $\text{FTI} = 1.5\%$. It can be found that with larger trailing edge thickness (TF-0125), the effect of the off-surface pressure recovery is stronger at each angle of attack, which leads to higher suction pressure (more negative value) and more positive wall shear stress (mitigating flow separation) around the trailing edge and hence higher lift and drag coefficients as indicated in Fig. 4.8. It is also interesting to find that when separation bubbles appear at low angle of attack (0^o and 3^o), the effect of the blunting trailing edge thickness to the pressure and wall shear stress is only restricted to the flow reattachment region (the region after the separation bubbles) whereas when there is no separation bubble (attached transition occurs) at high angle of attack (7^o), this effect becomes significant to the whole suction surface. The separation bubble acts as a discontinuity to restrict the effect of blunt trailing edge to the aft part of the suction surface.

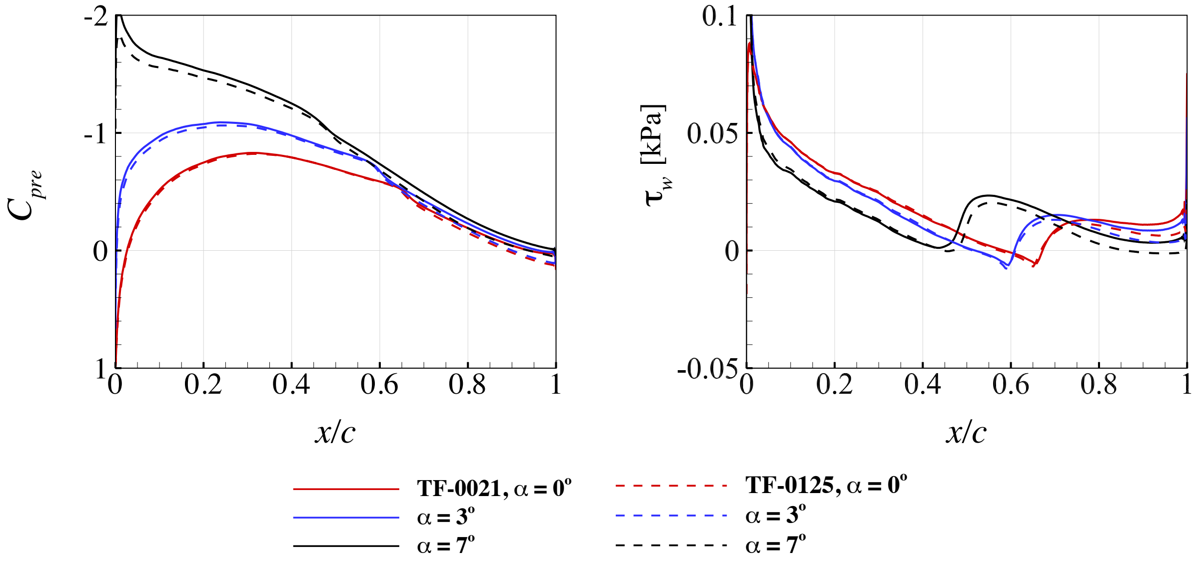

Fig. 4. 10 The pressure coefficient (C_{pre}) and the wall shear stress (τ_w) distributions on the suction surface of the TF-0021 and TF-0125 at different angles of attack. The freestream turbulence intensity is at 1.5%.

In summary, at the Reynolds number of 2×10^5 encountered by the lab-scale rotor, the flow physics of laminar-to-turbulent boundary layer transition on the blade could vary significantly with different levels of freestream turbulent intensity along the blade span. Thus it is important to incorporate these different hydrodynamic characteristics into the design process. Hence, the six lift and drag polars, as shown in Fig. 4.8, are used as input to the design process. This high-fidelity data is supplemented with lift and drag data for angles of attack in the range $[-10^o, -1^o]$ and $[14^o, 35^o]$ computed using XFOIL to save computational costs. Since for the design process, the blade sections are twisted such as to maintain an angle of attack corresponding to the maximum lift-to-drag ratio, which is 6°, the XFOIL extended range of lift and drag data is only used for transient numerical iterations and forms no part of the final solution. The lift and drag coefficients for hydrofoils with δ_0/c between 0.125 and 0.021, experiencing different turbulent intensities between 1.5 % and 5.5% (the lowest and highest estimated values), are obtained through two-dimensional interpolation of the computed data.

4.3 Rotor Design and Results

4.3.1 Computational Domain

Fig. 4.11 (a) shows a side-by-side array configuration of four rotors in estimated 2 m by 16 m target domain. In the design process, by taking advantage of symmetry, a twin-rotor design domain containing two rotors in a 2 m by 8 m domain is used, as shown in Fig. 4.11 (b). This domain considers an inboard-array rotor 1 and an outboard-array rotor 2 with a symmetry plane providing a mirror image of the two rotors. It is noted that the symmetry plane mirroring the rotor assumes a counter-rotating turbine array. Hunter (2016) found that counter-rotating discs resulted in increased wake mixing, but it only led to a small increase in array power coefficient by 0.25%. Hence, the symmetry plane is used here only to take advantage of symmetry of the array configuration without explicitly considering the influence of rotational direction of the rotors.

Even though the inboard-array rotor 1 and outboard-array rotor 2 experience different flow constraints due to the presence of side boundaries and neighbouring rotors, it is of interest to investigate how important these differences are in array design and performance. Hence, a further simplified single-rotor design domain containing only one rotor in a 2 m by 4m domain, also shown in Fig. 4.11 (c), is considered. This domain considers only one rotor with a symmetry plane mirroring the rotor, which is equivalent to two rotors facing a local blockage constraint that lies somewhere between the blockage experienced by the inboard-array rotor 1 and the outboard-array rotor 2, as considered in the twin-rotor design domain. The global blockage of the two cases is equivalent. This single rotor domain will be used to design the rotor for the four-rotor array configuration. The inter-rotor spacing (tip-to-tip spacing of the rotor blade) is chosen as $d/4 = 0.3$ m, following the study by Schluntz and Willden (2015).

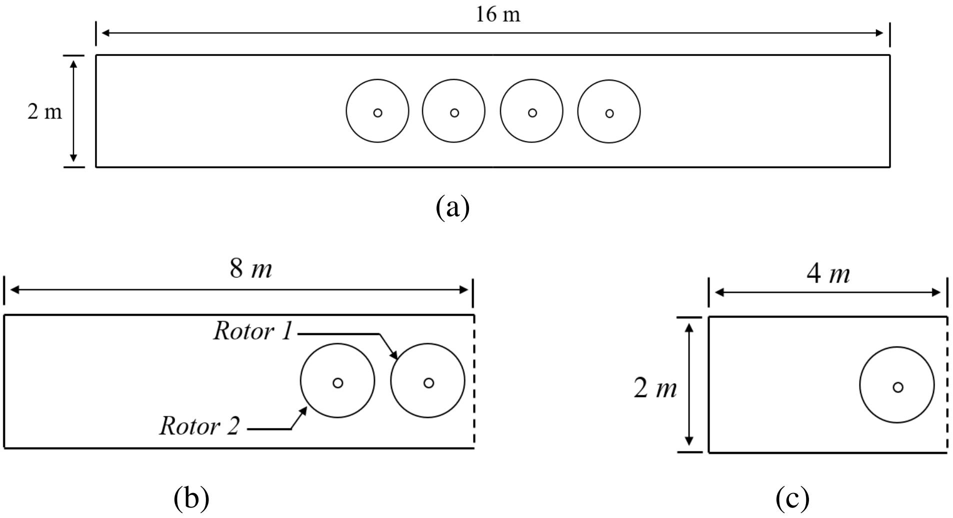

Fig. 4. 11 Schematic diagrams of (a): An array of four turbines in a side-by-side configuration; (b): a twin-rotor design domain which takes advantage of the symmetry about the centre of the four turbine array, in which Rotor 1 indicates the inboard-array rotor while rotor 2 indicates the outboard-array rotor; (c): a further simplified single-rotor design domain which represents an averaged blockage condition of the rotor 1 and rotor 2 in (b).

4.3.2 Meshing and Numerical Scheme

A fully structured mesh is used for both single-rotor and twin-rotor design domains, offering good control over mesh resolution. Fig. 4.12 (a) illustrates the mesh topology of the twin-rotor domain, in which the region behind the discs until 3d downstream is particularly refined to resolve the near wake region sufficiently. Fig. 4.12 (b) shows the cut-plane of the structured mesh around the two discs, where clustered fine resolution is adopted around the disc edges to capture the flow interactions. The nacelle is explicitly modelled. The mesh structure for the single-rotor design domain is the same as the twin rotor design domain except that only one rotor included. The mesh resolution follows those in section 3.1.2.

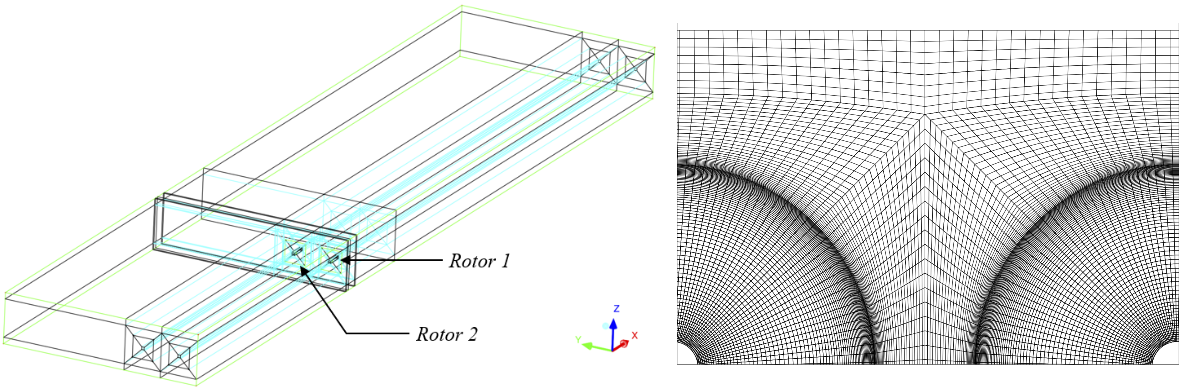

(a) (b)

Fig. 4. 12 (a): Blocking topology for generating a structured mesh of the computational domain of the twin-rotor design domain case; (b): a slice through the mesh at the rotor plane showing the structured mesh of the rotor discs where the mesh is refined at the rotor edges.

A uniform inflow speed of 0.8 m/s is applied at the domain inlet. A reference turbulence length scale is chosen as $0.7D$ following the recommendations from Gant and Stallard (2008), which results in a turbulence length scale of 0.84 m in this study. The turbulence intensity at the inlet is set as 8% and it decays to 7.05% one diameter upstream of the rotor plane, as shown in Fig. 4.13. At the domain outlet, the pressure outlet boundary condition is applied. Symmetry boundary conditions are used for the top, bottom and two side walls.

The $k-\omega$ SST turbulence closure model is used for the steady RANS computation. The laminar-to-turbulence transition may be significant on the blade surfaces, but in the low-order design process the blades are approximated by a disc. Hence, the $k-\omega$ SST fully turbulent model is sufficient to predict the mean flow field around the disc edges and is less computationally expensive. In order to evaluate this assumption, a simulation of the design case at TSR = 7 is conducted using the $\gamma-\mathrm{Re}_\theta$ turbulence model. The differences in C_P and C_T between the two models are found to be less than 0.2%.

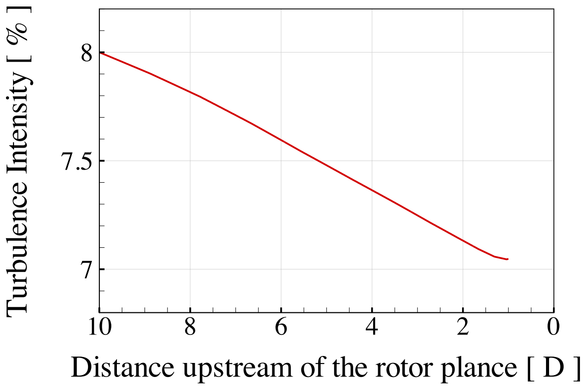

Fig. 4. 13 Decay of turbulence intensity from $10D$ upstream to $1D$ upstream of the rotor .

4.3.3 Single-Rotor Design

A design condition of maintaining a constant c_x is used in the present study. Note that power coefficient (C_p) and thrust coefficient (C_T) investigated here are only for an individual rotor even though the simulation represents a side-by-side two turbine array. Fig. 4.14 shows that by varying the c_x with an interval of 0.1, the optimal c_x of 3.0 is found for the single-rotor design case at the design TSR $= 7$. The peak design C_p is 0.610 with corresponding design C_T of 1.237. For the range of c_x investigated the design C_T increases almost linearly, changing by 7.3%, as the c_x increases from 2.7 to 3.3 while the design C_p varies by less than 2%. The result shows that for the two-rotor array, a range of rotors with different target thrust can be designed without too significant reduction in array performance.

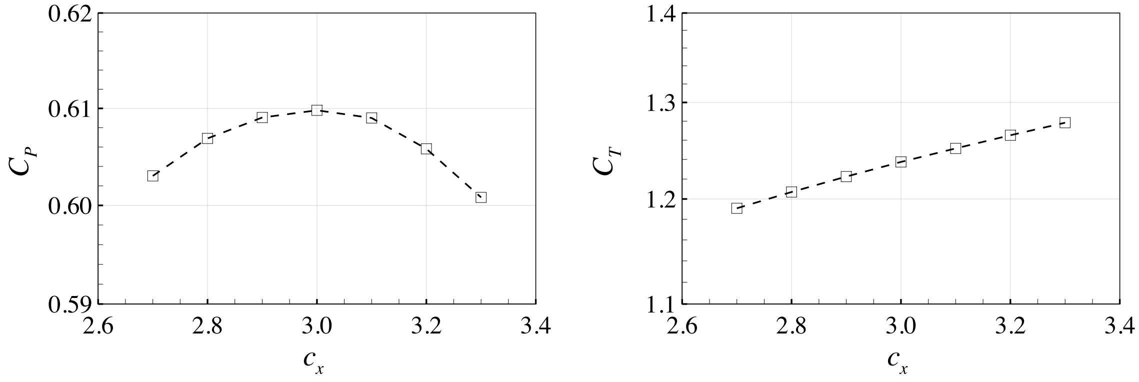

Fig. 4. 14 Design power coefficient (C_P) and thrust coefficient (C_T) as a function of the design local thrust coefficient (c_x) for the single-rotor design domain. The tip-speed-ratio is fixed at 7.

Fig. 4.15 shows the design chord and twist distributions for the designed blade when $c_x = 3.0$. The red lines show the design result achieved using a constant c_x throughout the blade, however, this leads to an unrealistically large chord distribution around the blade root, which may cause problems when connecting the blade to the nacelle structure. A modification is made by using a constant c_x for the blade span of r/R in the range of [0.3, 1] whereas for the inboard blade a linear relaxation are imposed for span of $r/R < 0.3$ to avoid an unrealistically large blade chord design. Specifically, c_x imposed at blade root ($r/R = 0.125$ for this study) is half of the constant value at $r/R = 0.3$, and linear interpolation is used to assign c_x over the intermediate range of [0.125, 0.3]. This root profile modification is incorporated in each iteration of the design process. Due to the uncertainty in the tip region in which the three-dimensional flow effects are not adequately resolved, a linear extrapolation is used for both the chord and the twist distributions for $r/R > 0.9$. This is a conservative approach to tip modification as it increases the local twist and therefore decreases the angle of attack in the tip region. Unlike the modifications around the blade root, these tip profile modifications are applied directly to the design result due to a lack of a generalised spanwise-flow correction model.

Re-simulating the modified version of the rotor designed for constant $c_x = 3.0$, yields a power and thrust coefficient of 0.602 and 1.201, slightly decreases from the original design with minor differences of 1.3% and 0.9% for power and thrust coefficients respectively. These decreases are mainly due to the modifications in the tip region.

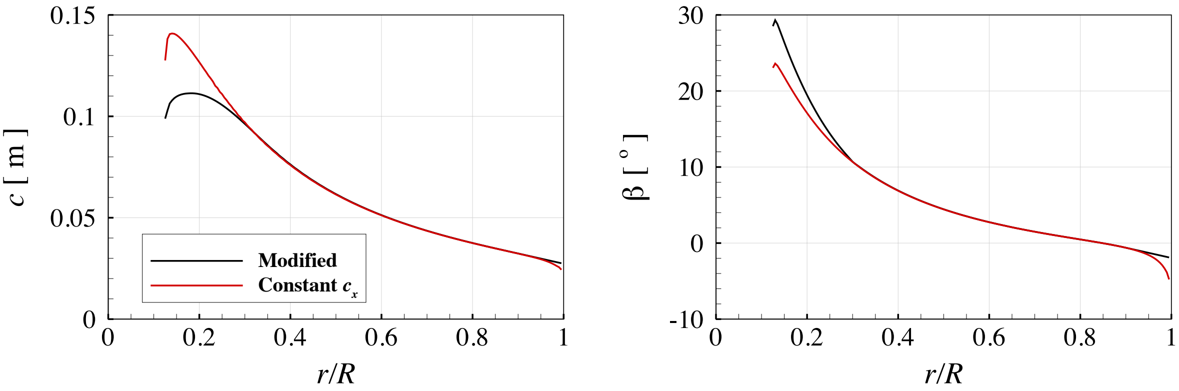

Fig. 4. 15 Spanwise chord and twist angle distributions required to achieve a spanwise constant $c_x = 3$, and the modified approach with relaxation in the root region and linearization in the tip region.

4.3.4 Twin-Rotor Design

In order to find the optimal power coefficient for the twin-rotor array, the design c_x is varied individually for the two rotors. As shown in Fig. 4.12 (a), rotor 1 corresponds to the rotor close to the symmetry plane, representing the inboard-array rotor while rotor 2 corresponds to the outboard-array rotor. The tip speed ratio is fixed at 7 for both rotors. Performance contour plots, Fig. 4.16 and Fig. 4.17, show the results of design power and thrust coefficients for rotor 1, rotor 2 and the average of the two. For convenience of comparison, the total array power is represented by the average, since the greater the average power across the rotor, the greater is the total array power.

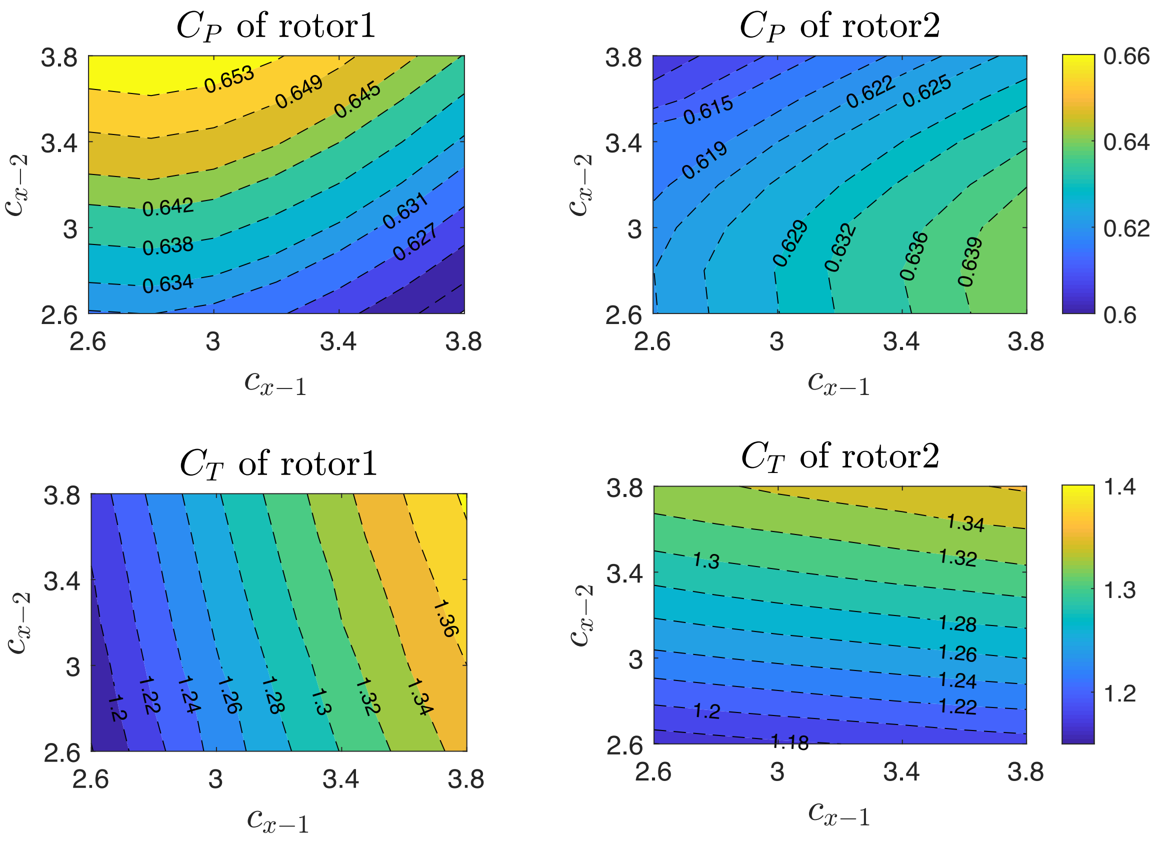

Fig. 4. 16 Design power coefficient (C_P) and thrust coefficient (C_T) for rotor 1 and rotor 2, as a function of the local thrust coefficients of rotor 1 (c_{x-1}) and rotor 2 (c_{x-2}) when varied individually.

As shown in Fig. 4.16, for either rotor 1 or rotor 2, when the neighbouring rotor is designed at higher thrust, the rotor itself achieves a higher C_P at a higher C_T. For example, if c_{x-1} is fixed at 3.0, then as c_{x-2} increases, the design C_P of rotor 1 increases with increased C_T while the design C_P of rotor 2 decreases. A similar trend can be found when c_{x-2} is fixed while c_{x-1} varies. When the neighbouring rotor is designed at a fixed c_x, either rotor 1 or 2 peaks its design power coefficient at $c_x = 2.8$.

Across the range of c_x investigated, the C_P of rotor 1 increases as c_{x-1} decreases and c_{x-2} increases, while the C_P of the rotor 2 increases as c_{x-1} increases and the c_{x-2} decreases. Hence, the average array C_P (average of C_P of rotor 1 and rotor 2) is affected by this competing factor. As shown in Fig. 4.17, the average array C_P is maximised at a value of 0.635

when $c_{x-1} = 3.4$ and $c_{x-2} = 3.6$ with corresponding average array C_T of 1.331. In fact, the array C_P shows negligible difference (less than 0.2%) when the c_{x-1} and c_{x-2} are both in the range of 3.2 to 3.6. It is noted that for the whole range of c_{x-1} and c_{x-2} investigated, even though the C_P for individual rotors 1 and 2 vary by up to 7% and 6.5% respectively, the array C_P varies only within 2%.

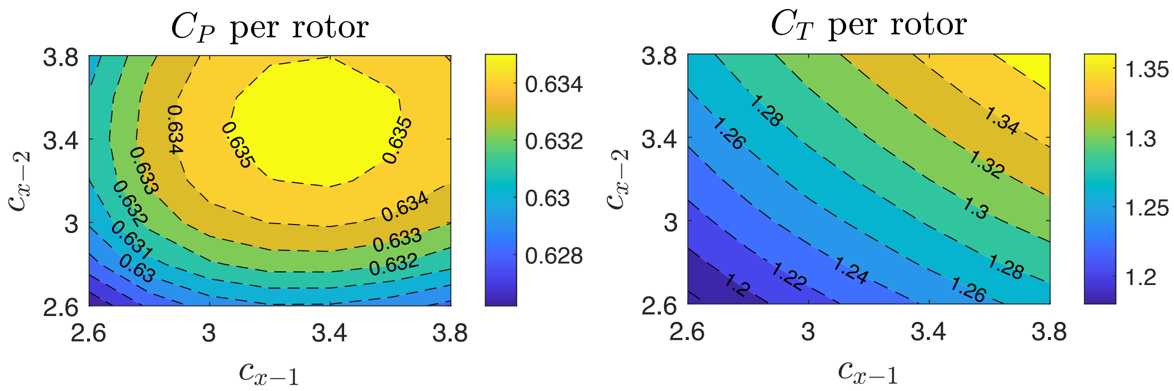

Fig. 4. 17 The array (average of rotor 1 and rotor 2) power coefficient (C_P) and thrust coefficient (C_T) as a function of the local thrust coefficients of rotor 1 (c_{x-1}) and rotor 2 (c_{x-2}) when values shown are varied individually.

Fig. 4.18 plots the modified version of chord and twist profiles for rotors resulting from the maximum array C_P design, i.e. $c_{x-1} = 3.4$ and $c_{x-2} = 3.6$. Compared to the rotor design in the single-rotor domain (where $c_x = 3.0$ with modifications), the rotor 1 and rotor 2 have blades of larger chord and less twist, which is not surprising as they are designed for higher local thrust coefficient. It is noted that the differences of the profiles between these three rotors are small. The small differences in design means that the rotors will likely have similar performance when operates in the four-rotor array configuration.

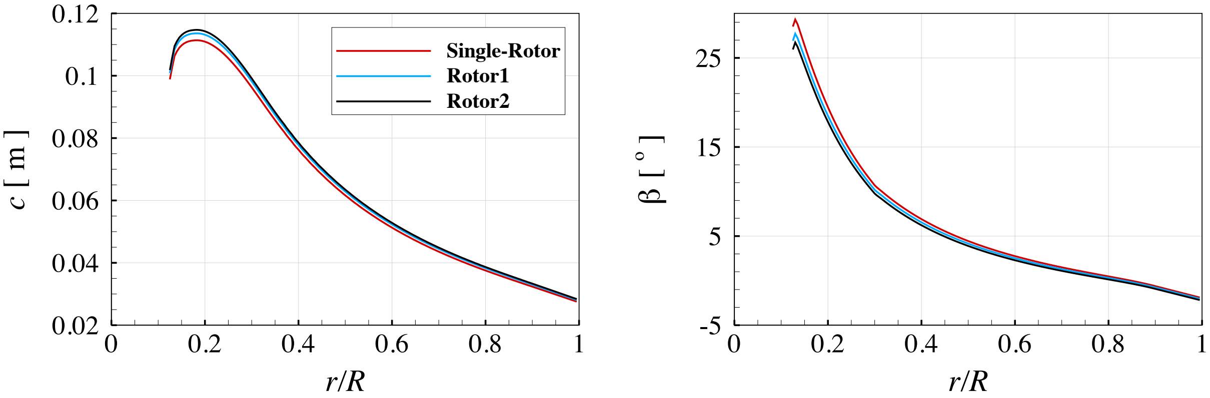

Fig. 4. 18 Spanwise chord (left) and twist angle (right) distributions along the blade for the optimal rotor designed in the single-rotor design domain with $c_x = 3$, and for the two rotors designed in the twin rotor design domain with $c_{x-1} = 3.4$ and $c_{x-2} = 3.6$.

4.3.5 Comparison of The Two Design Results

The rotor designed in the single-rotor design domain, referred to rotor S in the following discussion, is set into operation in the four-rotor array configuration, i.e. the twin-rotor design domain. As can be seen from the Table 4.3, when the rotor S operates at its design TSR of 7, the inboard (IB) and outboard (OB) rotors achieve a C_P of 0.637 and 0.626 respectively. Compared to the rotors designed for the twin-rotor design domain, the difference in array C_P is less than 1%. This indicates that even though the rotors at IB and OB positions experience different flow constraints, a single rotor design from a simplified domain that has blockage of an intermediate level can achieve similar array power compared to the optimal design for these two positions. In addition, the average thrust achieved by the rotor S is 5% less than those achieved by the twin-rotor design due to its smaller chord distributions. Hence, the rotor design from the single-rotor design domain is chosen for the later studies.

Similar streamwise flow fields are observed for the two design cases, as shown in Fig. 4.19. The flow speed is accelerated significantly between the rotor discs. It is noted that the two-rotor array has faster wake recovery than the four-rotor array.

Table 4. 3 Summary of the power (C_P) and thrust (C_T) coefficients of the individual rotor and the entire array (Average). Twin-Design refers to the optimal design in the twin-rotor design domain while the Single-Design refers to the single rotor design operating at inboard-array (IB) and outboard-array (OB) positions.

	TSR		C_P			C_T		
	IB	OB	IB	OB	Average	IB	OB	Average
Twin-Design	7	7	0.646	0.624	0.635	1.331	1.331	1.331
Single-Design	7	7	0.637	0.626	0.631	1.242	1.233	1.237

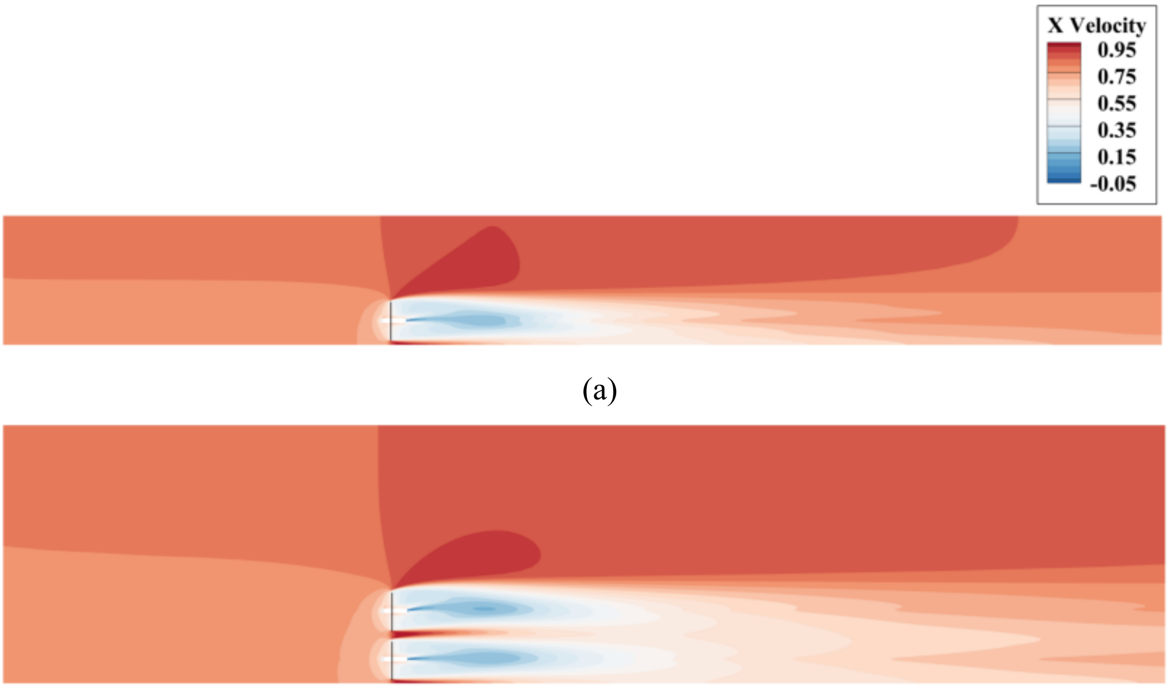

(a)

(b)

Fig. 4. 19 Contours of streamwise velocity on the horizontal centre xy plane for the rotor designed in the (a): single-rotor and (b): twin-rotor case respectively. The short black lines indicate the position of the rotor discs.

4.4 Blade Resolved Computation

High-fidelity blade-resolved computations are conducted in this section to identify the three-dimensional effects ignored in the design process. Although in Chapter 3 a blade-resolved computation has been conducted to evaluate the RANS-BE design result, the rotor scale is different. In the present lab-scale rotor design, the rotor diameter is of 1.2 meters and the chord-based Reynolds number is of order 10^5. As can be seen from section 4.2, the laminar-to-turbulent transition in the boundary layer on the suction surface of the blade and the effect of the turbulence intensity make the flow physics on the blade surface more complex compared to the rotor investigated in Chapter 3. In addition, as can be seen in section 4.4.1 below, the root section of the lab-scale rotor is treated differently compared to the rotor in Chapter 3. Hence the blade-resolved computation is necessary to evaluate the design result from the RANS-BE model.

4.4.1 Three-Dimensional Blade Geometry

The modified rotor in the single-rotor design domain desined for TSR=7 and $c_x = 3$ is adopted for the blade-resolved computation. The three-dimensional blade geometry is formed by aligning the hydrofoil sections through the hydrodynamic centre of pressure, through which the hydrodynamic force acts. At the design angle of attack of 6°, the centre of pressure of the 2D hydrofoil section is located at 0.35 chords aft of the leading edge (with slight variations across hydrofoil sections at the blade root to tip). Hence, the hydrofoil sections are aligned based on a centre of pressure line located at 35% of the chord.

When blade element theory is used to design a wind rotor blade the solidity is sufficiently low to make the alignment of the local sections of little importance. However, for this higher solidity design we choose to incurve each hydrofoil along an annular path so that it better follows the annular control volume in which it has been designed. To follow this theory, the hydrofoil profile at radial position r is projected onto a cylindrical surface with the same radius r while the chord length is maintained after the projection. An illustration is shown in Fig. 4.20.

Consider a blade section at radial position r with chord length c. After the projection, it should also have a length of c, as the two blue lines in Fig. 4.20 show. For example, if we consider a point P_0 on the blade section with a coordinate of (x_0, y_0, z_0), after the projection, the projected section OP also has a length of y_0. Hence, the coordinate of $P(x, y, z)$ can be determined by $(x_0, r\cos\theta, r\sin\theta)$, where $\theta = \frac{\pi}{2} - \frac{y_0}{r}$.

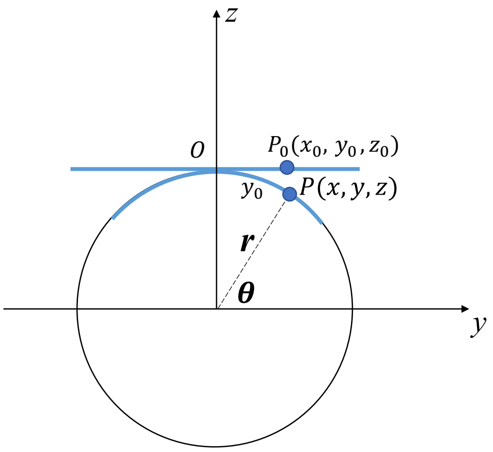

Fig. 4. 20 Schematic diagram of the projection process. The blue lines are of the same length, where P_0 is the point on the original profile and P is the projected point on an arc of radius r.

Fig. 4.21 (a) shows the aligned and projected hydrofoil sections according to the modified chord and twist distributions (black lines in Fig. 4.15). The full three-dimensional turbine geometry is shown in Fig. 4.21 (b).

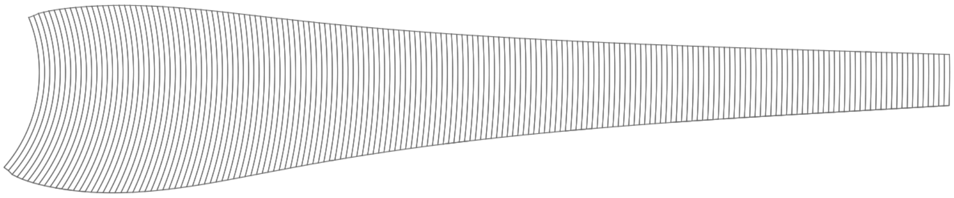

(a)

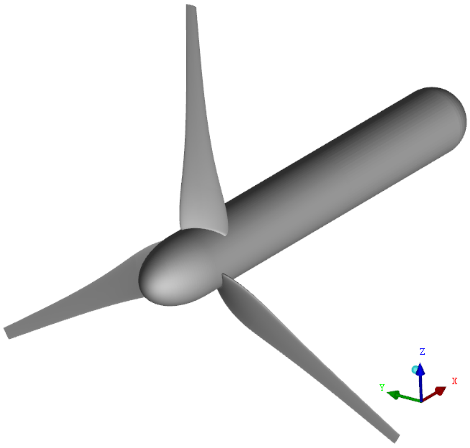

(b)

Fig. 4. 21 (a): Hydrofoil sections are curved and aligned along the location of 0.35 chord behind the leading edge; (b): Iso-metric view of the three-dimensional turbine geometry.

4.4.2 Meshing and Numerical Scheme

The blade resolved simulation conducted only considers one blade in a $120°$ wedge domain with periodic boundary conditions. Even though this one-third domain cannot take into account the aspect ratio of the rectangular domain and non-centred position of the turbine, it can provide an efficient investigation of the mesh convergence and key features for relatively low computational cost. In the next section, the rectangular domain will be discussed and the results will be compared against experimental measurement. The radius of the wedge domain is set such that it matches the global blockage ratio of the single-rotor design domain, which is the ratio of the rotor area to the cross-sectional area of the domain and is calculated as 0.14.

The computational domain is divided into separate inner and outer domains, as shown in Fig. 4.22. The non-conformal interface between the inner and outer domains is coupled together the Arbitrary Meshing Interface (AMI) boundary condition. The block topology for the inner domain is similar to that adopted in Section 3.2.1, as shown in Fig. 4.23 (a). In order to model the laminar-to-turbulent boundary layer transition on the blade surface, shown to be significant in the 2D hydrofoil study, the $\gamma - \mathrm{Re}_\theta$ turbulence closure model is used. Due to the fine mesh requirement of this model, the wall function approach cannot be used and the boundary layer on the blade surface has to be fully resolved with $0.001 < y^+ < 1$, as suggested by the validation result by ANSYS (2013). The chordwise resolution has to be fine enough to capture the transition and potential separation bubbles. Meanwhile, the spanwise resolution also has to be fine enough in order to avoid mesh cells with high non-orthogonality and high aspect ratio. Fig. 4.23 (b) shows the mesh cells on a slice through the blade section at r/R of 0.7. In addition, the spanwise resolution in blade root and tip regions are refined in order to resolve the three-dimensional effects, as shown in Fig. 4.23 (c) and (d).

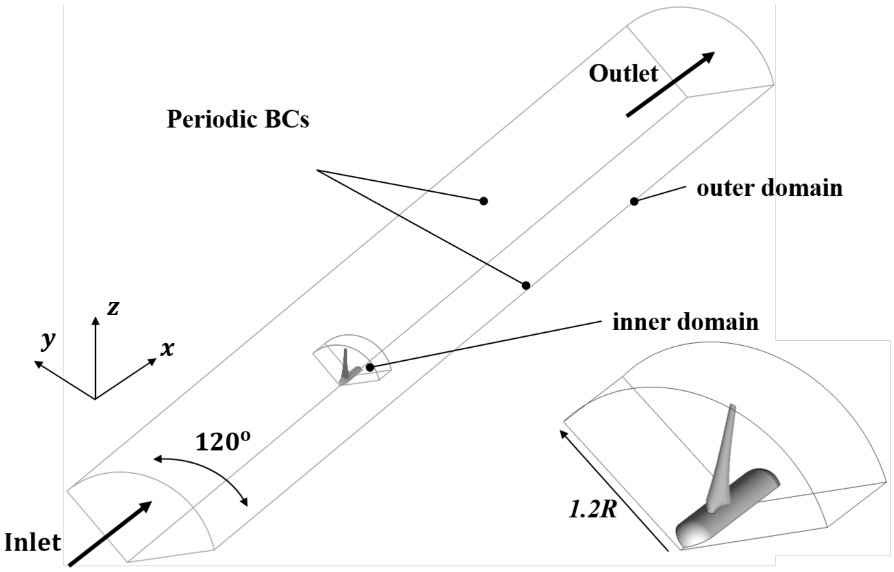

Fig. 4. 22 Schematic diagrams of the 120^o wedged computation domain and setup for the blade-resolved model.

]

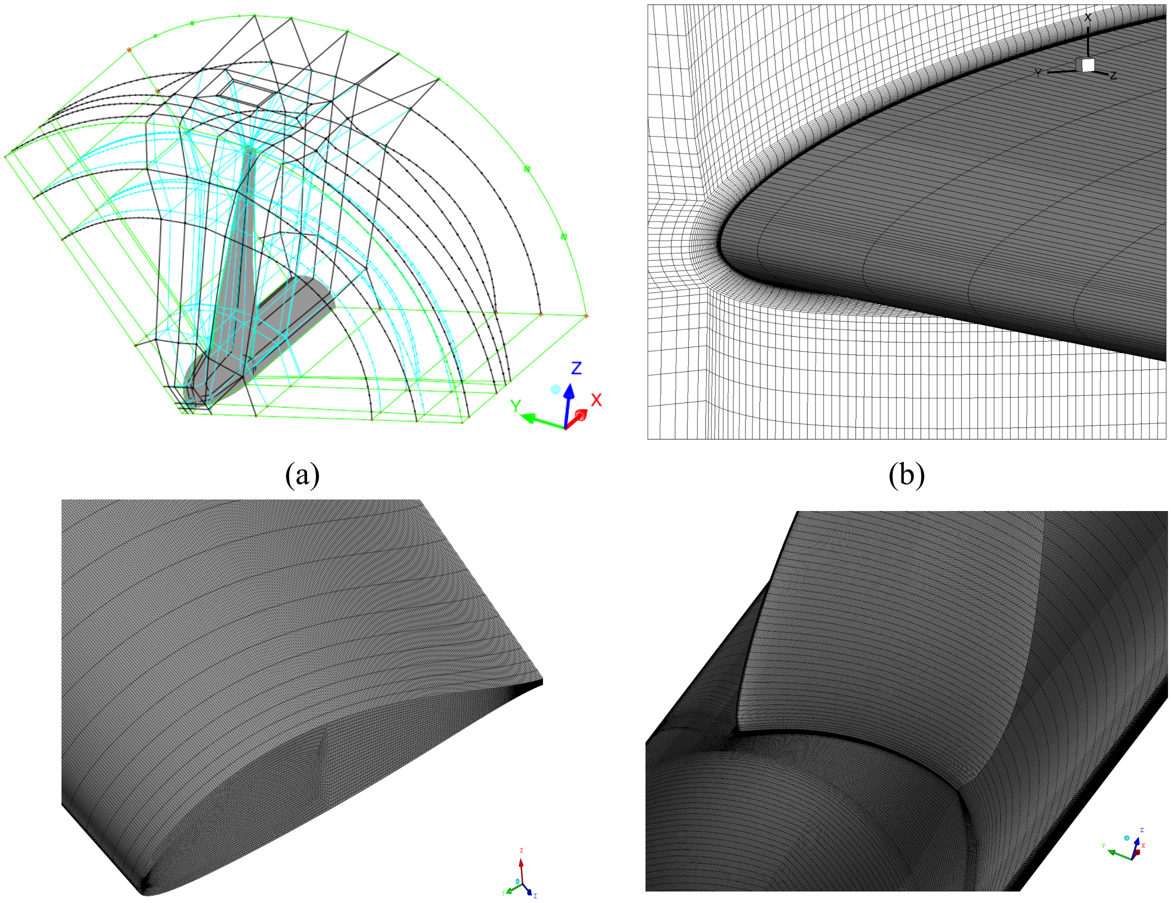

(a) (b)

(c) (d)

Fig. 4. 23 (a) Block topology of the inner domain for the blade-resolved model; (b) Mesh cells on a slice through the blade at $r/R = 0.7$; (c) Surface mesh cells in the blade tip region; (d) Surface mesh cells in the blade root region.

A summary of the mesh resolution adopted for the blade surface is given in Table 4.4. $y_{wall-0.7R}$ refers to the absolute wall adjacent cell height at spanwise position of $r/R = 0.7$, G the cell growth ratio normal to the wall, N_c the number of cells in the chordwise direction on each of the suction and pressure sides of the blade, N_s the number of cells in the spanwise (radial) direction and $N_{cells-1/3}$ the total number of cells in the wedged inner domain. It is noted that the fine mesh resolution requirement from the turbulence model, and the mesh quality criteria such as non-orthogonality and constrained aspect ratio, along with solving the four-equation $\gamma - \mathrm{Re}_\theta$ turbulence model itself, results in the computational cost of the blade-resolved simulations very high. Hence, to save computational cost, the initial mesh, M1, is only further refined once to produce the refined mesh M2. Based on the level of agreement between the power and thrust coefficients for the M1 and M2 mesh, the M1 mesh is deemed to be sufficiently accurate and is used for further computations. The numerical uncertainty, following the method adopted in Chapter 2, is estimated to be 0.51% and 0.06% for the power and thrust coefficients respectively. Therefore, the discretisation error is not expected to significantly impact the integrated loading results.

Table 4. 4 The parameters adopted for the M1 and M2 mesh. The change in power and thrust coefficients (ΔC_L and ΔC_D) have been expressed relative to the M2 mesh.

Mesh	$Y_{wall-0.7R}$ [m]	G	N_c	N_s	$N_{cells-1/3}$	C_P	C_T	ΔC_P[%]	ΔC_T[%]
M1	1.5e-6	1.1	254	147	9,811,522	0.580	1.2108	-0.17	-0.02
M2	1.5e-6	1.08	360	206	18,041,862	0.581	1.2111	-	-

The same numerical setups as those in the RANS-BE design process are used for the blade-resolved computation. At the inlet, a uniform velocity profile of 0.8 m/s is applied. The turbulent intensity (k) and specific dissipation rate (ω) are specified the same as those in the RANS-BE design process to maintain the turbulence intensity of 7% one diameter upstream the rotor plane. The γ and Re_θ at the inlet boundary are set according to Eq. (2.8) and Eq. (2.9). The pressure outlet boundary condition is applied for the outlet. The symmetry boundary condition is applied for the top cylindrical surface and the periodic boundary conditions are applied to the side surfaces. Multiple Reference Frame (MRF) approach is used to simulate the rotor rotation.

4.4.3 Computation Results

The blade resolved (BR) computation is conducted when TSR=7. Fig. 4.24 shows the distributions of the torque and axial force per unit span along the blade, which are obtained by integrating the surface pressure distributions and wall shear stress in the chord-wise direction. Negligible differences can be found between the results of the two meshes. Hence, the parameters in mesh M1 are deemed to be sufficient for further blade resolved computations.

The integrated power and thrust coefficients from the BR model are 0.58 and 1.21 respectively while those from the RANS-BE design process are 0.61 and 1.23 respectively. As can be seen from Fig. 4.24, in the mid-span of the blade, the torque and axial thrust distributions predicted by the RANS-BE and BR models are in great agreements. Slight differences are found in the blade root region while the major differences in torque and thrust distributions between the two models occur in the tip region. For the torque distribution the two results start to deviate at $r/R = 0.8$ while for the thrust distribution deviation starts at $r/R = 0.85$.

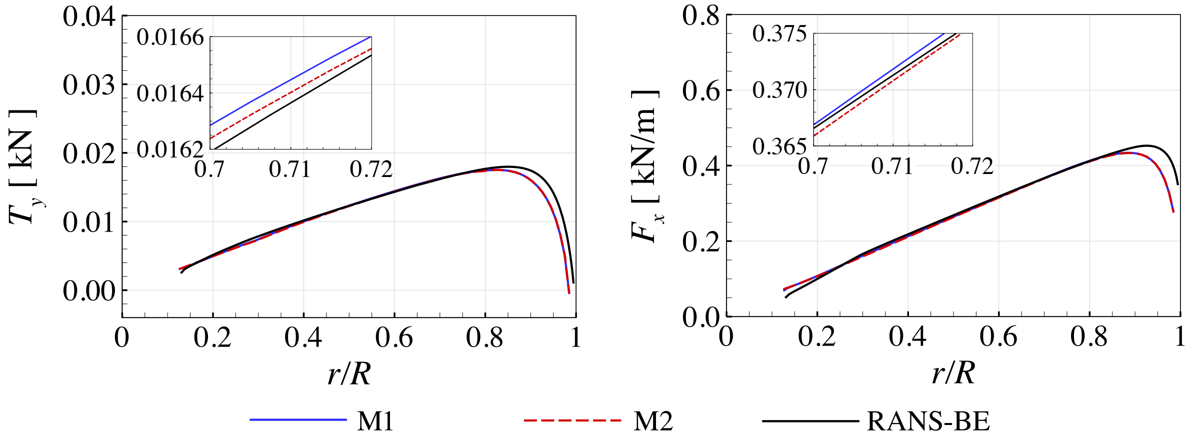

Fig. 4. 24 Torque and axial force and per unit span at tip speed ratio of 7. M1 and M2 refer to meshes using the parameters outlined in Table 4. RANS-BE refers to the result from the RANS-BE design.

In the blade tip region, the implemented Glauert tip correction model only corrects for the effect of having a discrete number of blades but does not consider other three-dimensional and spanwise flow effects. Spanwise flow effects becomes significant in the tip region due to the pressure equalization which forces the flow underneath the blade to swirl to the upper surface, generating blade tip vorticity. The shed vorticity induces a downwash which decreases the angle of attack in the blade tip region. Meanwhile the spanwise pressure gradient introduced by the vorticity accelerates the flow radially. The study by Wimshurst and Willden (2018) showed that this spanwise flow acceleration altered the pressure distribution of the blade surface and caused the torque-producing force drops off faster than the thrust-producing force. These three-dimensional flow effects are not captured and corrected in the RANS-BE model, which contributes to the differences in force distributions between the two models. Several tip loss models that account for the pressure equalization are available (see e.g. Shen *et al.*, 2005), however, the correction coefficients are empirically determined and are rotor specific without generalizations. In addition, the laminar to turbulent transition phenomenon in three-dimensional boundary layer can be significantly different from the that in the two-dimensional case (Saric, *et al.*, 2003), which adds an additional complexity for analysing tip flow effects.

4.4.4 Angle of Attack Extraction from Three-Dimensional Blade

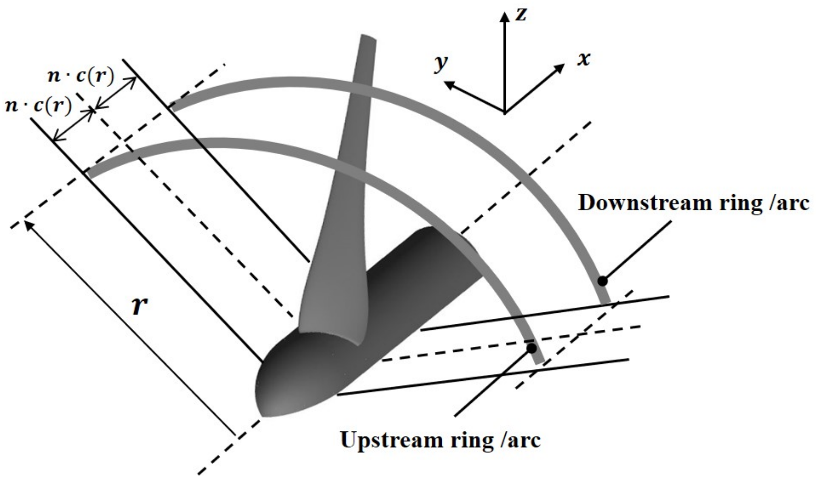

Fig. 4. 25 Schematic diagram of the Azimuthal Average Technique for extracting angle of attack from the blade-resolved model.

The extraction of angle of attack from the blade-resolved model is not straightforward. Due to the wake induction and the flow field distortions from the physical presence of the blade, the relative velocity is challenging to extract. Several methods have been proposed in the literature to extract the distribution of angle of attack along the 3D blade, such as Average Azimuthal Technique (AAT) based on the annular average values of the axial velocity (Johansen and Sørensen, 2004), inverse blade element momentum method (Guntur, *et al.*, 2011), line average method (Jost *et al.*, 2018) based on bound circulation. Rahimi *et al.* (2018) compared different methods for extracting the angle of attack from three-dimensional CFD computations and found that all the methods mentioned above gave good agreement in the mid-span of the blade while strong discrepancies was observed in the blade tip and root regions where three-dimensional flow effects are predominant. They also mentioned that in the blade and tip regions, the location of the sampling points could lead to very different results.

In this chapter, the Average Azimuthal Technique (AAT) is examined. An illustration of the AAT method is shown in Fig. 4.25, where two annular sampling rings at radial position r are placed upstream and downstream with a distance of $nc(r)$ to the rotor plane, where $c(r)$ is the local chord length of the blade section at radial position r and n is an coefficient to adjust the sampling location to a multiple chord-length distance. The azimuthally averaged axial velocities ($\bar{u}_x$) and swirl velocities ($\bar{u}_\theta$) at the two sampling rings are calculated by integrating the axial velocity, u_x, and swirl velocity, u_θ, over the entire ring and averaging them by the area of the ring respectively. The $\overline{u_x}$ and $\overline{u_\theta}$ at the rotor plane are then assumed to be the average of these two sampling rings. The inflow angle $\phi(r)$ and the relative velocity $W(r)$ to the blade section are calculated as:

$$\phi = \tan^{-1}\left(\frac{\bar{u}_x}{\Omega r - \bar{u}_\theta}\right), \tag{4.4}$$

$$W = \sqrt{\bar{u}_x^2 + (\Omega r - \bar{u}_\theta)^2}\,, \tag{4.5}$$

where Ω is angular velocity of rotation.

To correct for the effect of a discrete number of blade, the Glauert correction model is used. This is because the azimuthally averaged flow field cannot represent well the flow field approaching the blade tip, as discussed in Section 2.3.1. The axial and swirl induction factors (a and a') are computed using the $\bar{u}_x$ and $\bar{u}_\theta$ as:

$$a = \frac{U_\infty - \overline{u_x}}{U_\infty}, \tag{4.6}$$

$$a' = -\frac{\bar{u}_\theta}{\Omega r}. \tag{4.7}$$

The induction factors that are local to the blade sections (a_B and a'_B) are then computed according to the Glauert correction F as:

$$a_B = \frac{a}{F}, \tag{4.8}$$

$$a'_B = \frac{a'}{F}. \tag{4.9}$$

Finally, the Glauert corrected ϕ and W that are computed as:

$$\phi^{'} = \tan^{-1}\left[\frac{U_\infty(1 - a_B)}{\Omega r(1 + a'_B)}\right], \tag{4.10}$$

$$W^{'} = \sqrt{[U_\infty(1 - a_B)]^2 + [\Omega r(1 + a'_B)]^2}\,. \tag{4.11}$$

The angle of attack, α,is then computed as:

$$\alpha = \phi^{'} - \beta\,. \tag{4.12}$$

Fig. 4.26 plots the result of $\bar{u}_x$ sampling and computed angle of attack at different streamwise sampling distance, with Glauert correction F applied. Even though the $\bar{u}_x$ upstream and downstream of the rotor plane varies with the streamwise sampling distance, the averaged $\bar{u}_x$ at the rotor plane corresponds well when r/R is in the range of [0.3, 0.75].

Along the blade span form r/R of 0.35 to 0.9, the angle of attack determined from the three sampling distances is close to the design angle of attack of 6 degrees. The major difference of the $\bar{u}_x$ at the rotor plane between the three sampling distances is in blade tip and root regions. In the blade root region, the local chord length has a relatively large value and hence the streamwise sampling distance, $nc(r)$, scales significantly with the value of n. It is noted that for the sampling distance of $3c$, the $\bar{u}_x$ at downstream of the rotor plane is negative in the blade root region, which means the sampling point is in the separation region, as shown in Fig. 4.27. By averaging this velocity in separation region may not give a good representation of the

$\bar{u}_x$ at the rotor plane. In addition, due to the wake expansion, the velocity sampled with large streamwise distance upstream and downstream of the rotor plane may not belong to the same streamtube. Hence, the sample distance should ideally be close the rotor plane. Schluntz and Willden (2014) demonstrated that local flow field distortions become significant when the distance is less than one chord length and so sampling distances less than one chord length are not investigated in the present study. Therefore, a sampling distance of one local chord length is deemed to be appropriate for determining the angle of attack for the blade-resolved model.

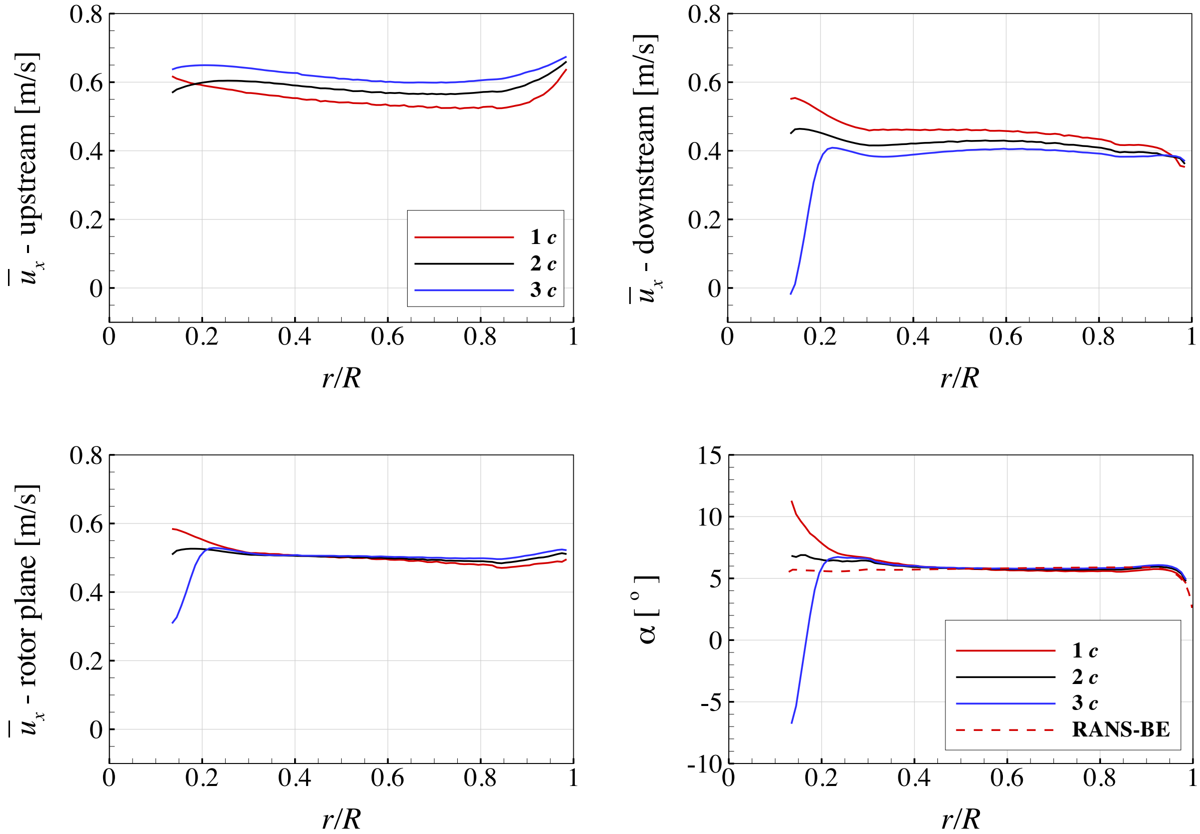

Fig. 4. 26 Averaged axial velocity ($\bar{u}_x$) at upstream and downstream of the rotor plane and at the rotor plane, computed based on different streamwise sampling distances.

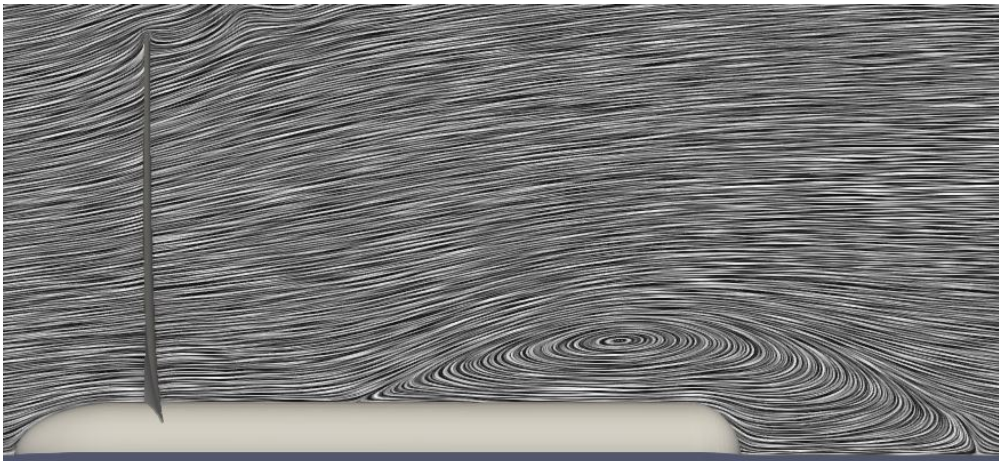

Fig. 4. 27 Streamwise velocity visualization on a slice through three-dimensional flow field from the blade-resolved model.

It is worth noting that due to the sensitivity of the angle of attack to the streamwise sampling distance, the accuracy of the angle of attack in the blade root region remains a little uncertain. In addition, even though the computed angle of attack on the outboard sections is relatively insensitive to the sampling distance, the accuracy of the AAT method also remains a little uncertain when it is used to determine the angle of attack in the blade tip region where the flow field is highly distorted due to the shed vortices and other three-dimensional effects. Moreover, as will be discussed in next chapter, the correction of angle of attack becomes less important for determining the blade load in the blade tip region. The three-dimensional spanwise flow effect modifies the pressure distribution on the blade surface in the tip region and hence the hydrodynamic characteristics of the three-dimensional blade section become significantly different from the two-dimensional blade section.

4.5 Summary

The FX-84-W-140 hydrofoil is chosen for the blade sections of the lab-scale rotor. Both truncation and thickening function methods are investigated for thickening the trailing edge of the blade for practicality and safety reasons. The steady RANS computations are conducted to study the effect of the thickening methods. Compared to the baseline hydrofoil, the thickening function method leads to a more negative pressure distribution (greater suction) on the suction surface while the truncation method results in hydrodynamic performance degradation. Hence, the thickening function method is used to blunt the trailing edge of the blade sections. The study also reveals that at Reynolds number of 2×10^5, the laminar-to-turbulent boundary layer transition occurrs and hence the drag coefficients may vary significantly with different levels of freestream turbulent intensity along the blade span. At a very low turbulence intensity at 0.1%, the transitional separation bubble occurs on the suction surface of the hydrofoil, which introduces relatively large pressure drag; at a moderate turbulence intensity at 1.5%, the higher turbulence level mitigates the separation bubble but introduces higher skin-friction drag; at a high turbulence intensity at 5.5%, the effect of the skin-friction dominates, and the overall drag coefficient increases.

An in-house RANS-BE simulation and design tool is used to design the multi-rotor array for the experimental study, with the purpose of maximizing the power output by exploiting constructive interference effect. The local thrust coefficient and tip-speed-ratio are varied to search for an optimal power output. Two design cases are considered. The first case considers a simplified domain of designing a rotor operating in a side-by-side two-rotor array. This rotor design is then used for operating in a four-rotor array. The second case considers designing of two rotors individually for outboard and inboard positions of the four-rotor array. The simulation result shows that compared to the two rotors designed for the four-rotor array, the single rotor design operating in the four-rotor array achieves only around 1% lower total array power, while the total array thrust is reduced by around 5%.

High fidelity blade-resolved computations are conducted to evaluate the rotor design and identify the discrepancies. The radial loading distributions from the RANS-BE design model shows good agreement in the blade mid-span region with those from the blade-resolved model. Discrepancies are observed in the blade root and tip regions, primarily due to the three-dimensional flow effects that are not fully resolved in the RANS-BE model.

Chapter 5

Experimental Test and Numerical Analysis

5.1 Experimental Test

In this chapter, experimental result is discussed and is shown to demonstrate the high power efficiency resulted from the design method. The blade design in Chapter 4 is utilized for the experimental study. The blades are fabricated on a CNC machine by an external company. The design of the rotor hub, connectors, printed circuit board (PCB), blade-root-bending-moment load cells and other mechanical parts are done by Dr. James McNaughton. Blades are fabricated using Aluminium 6082-T651, which has a high maximum yield strength, and are hard anodised with a thickness of 30μ m for the purpose of preserving model life and protecting from impact damage. In addition, Aluminium 6082-T651 has good machineability so that the blade can be fabricated with a high tolerance. The blades are mounted onto the platforms of the rotor hub by screws, as shown in Fig. 5.1. The blade-root-bending-moment load cells are designed to measure the flapwise and edgewise loads on each individual blade. A customized PCB is housed in the nose section, as shown in Fig. 5.1, which is used to connect the strain gauges with amplifiers.

The rotor part is connected to the drive trains and turbine nacelle of the University of Edinburgh. As described in Payne *et al.* (2017 and 2018), the nacelle is originally designed for a rotor of 1.2 meters diameter with similar loads and is controlled and monitored by the equipment in the FloWave facility where the experimental study is conduced. A servo motor with a drive is used to control the rotational speed of the turbine by varying the torque. A thrust and torque transducer and a servo motor shaft encoder is equipped inside the nacelle to monitor and measure the thrust, torque, rotational speed, power production and blade position of the rotor.

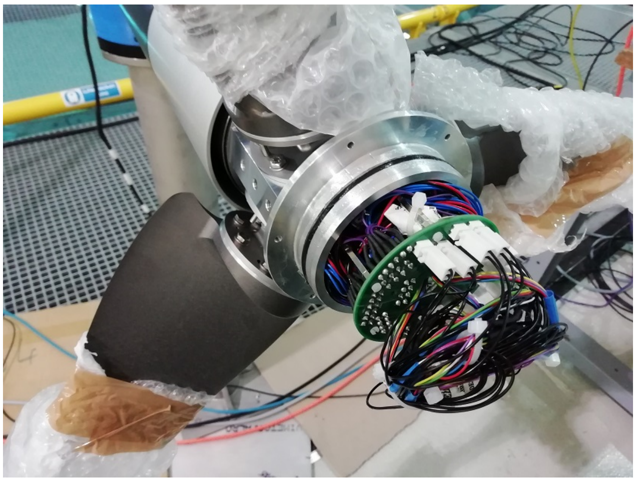

Fig. 5. 1 Photo of rotor section of the turbine, where the nose cone and cover are removed to expose the interior printed circuit board for connecting strain gauges with amplifiers and connection of blades to the rotor (McNaughton *et al*., 2019).

5.1.1 Test Set Up and Data process

The tests were performed in February 2019 at FloWave at the University of Edinburgh. The tank has a circular shape with a diameter of 25 meters and a depth of 2 meters. A flow speed of 0.8 m/s was used throughout the test since this value was studied with most details by Sutherland *et al.* (2017). Flow field measurements were taken using a Nortek Vectrino+, an Acoustic Doppler Velocimeter (ADV), positioned at hub height. The ADV uses four beams to sample three velocity components over a control volume of the order 1 cm^3. A series of flow measurements at various locations were taken with the turbines operating at a constant rotational speed of 77.5 rpm or 8.116 rad/s (referred as Ω^*), which corresponds to a tip-speed-ratio of 6.1. The ADV measurements were sampled at 100 Hz.

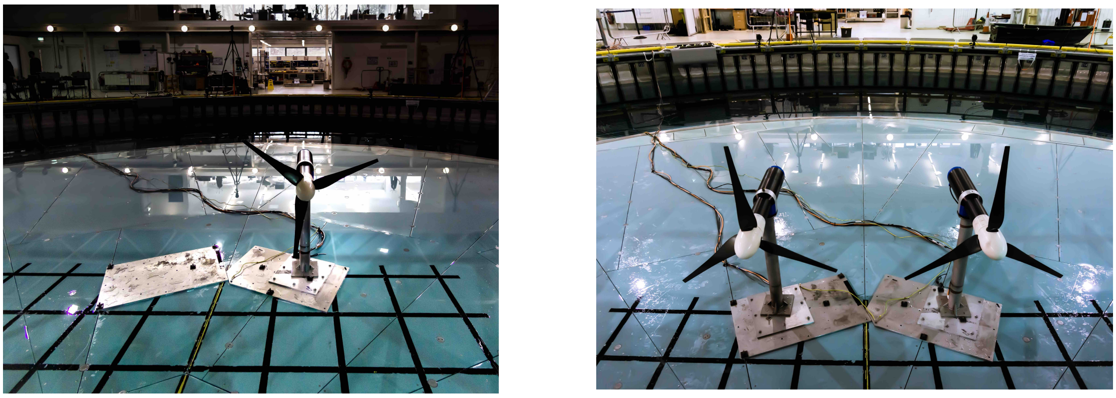

(a) (b)

Fig. 5. 2 Photos of the two configurations tested in the experiment. (a): a single turbine (North) installed; (b) two turbines (North and South) equally spaced either sided of the centreline with a tip-to-tip spacing of $0.25D$.

Two configurations, single turbine and twin turbines, were tested. For the single turbine configuration, only the north turbine was installed, while for the twin turbine configuration, both the north and south turbines were installed, as shown in Fig. 5.2. The two turbines were placed equally either side of the centreline of the tank, with a tip-to-tip spacing, s, of $0.25d$, which was same as the tip-to-tip spacing used in the rotor design. This leads to a local blockage ratio of 0.37, which is calculated by $\frac{A}{(s+d)h}$, referring to the ratio of the area of a single turbine to the cross-sectional area of local flow passage. For both configurations, the thrust and power of the turbine were recorded at various rotational speeds. The turbine load data were sampled at 256 Hz. For each configuration at each tip-speed-ratio, the test lasted five minutes and so the five-minute averaged power and thrust data combined with the five-minute averaged flow measurement give a data point of power and thrust coefficient respectively.

In order to remove the noise in the measured data, the raw data is pre-processed before computing the five-minute average. The method for data pre-processing from McNaughton *et al.* (2020) is summarised in the followings. In order to measure the velocity field at the hub height, the ADV is supported by a support pole. Vortex induced vibrations (VIV) were observed during the testing and are of a peak frequency of 18.5 Hz. For the ADV measurement of the flow velocity, two filtering processes are applied. Firstly, the correlation of the ADV signals was monitored and when it started to drop off seeding was added to the tank. According to the Vectrino's instrument quality metrics, a correlation of 90% and a signal-to-noise ratio of 10dB were used to remove data outliers. The removed data points are then replaced by the linear interpolated data points. Secondly, in order to deal with the high frequency data points associated to the VIV, a Finite Impulse Response (FIR) filter is applied using a pass band of 15Hz, stop band of 20Hz and attenuation of 40 dB. For the turbine performance measurements, including the thrust and torque data from the transducer and the rotational speed data from the motor's encoder, two stages of filtering are applied. Firstly, a Hampel filter is used, which replaces any data point that is greater than 2.5 standard deviations with the median of the six neighbouring data points on either side. Secondly, the high frequency components that are not associated to the lower harmonics of blade rotating and rotor interactions are treated with the FIR filter with a pass and stop band frequency of 6 and 12 times the rotor rotational frequency (i.e. two and four times the blade-passing frequency) and an attenuation of 40 dB. The processed flow measurement and turbine performance data points are then averaged with a five-minute window. The analysis of the sensitivity of experimental data to the averaging period, conducted by McNaughton *et al.* (2020), shows that the torque signal is the most sensitive to the averaging period, with 2% difference between the 150 and 300 second averaging periods, with other variables (the rotational speed and thrust of rotor and the flow velocity) demonstrating less than 1% variation.

5.1.2 Flow Measurement

Before the investigation of the turbine performances, it is important to understand the flow field approaching the turbines. Fig. 5.3 shows the averaged streamwise velocity upstream of the rotors, along the centerline of the rotors respectively. The velocity is normalized by U_0, which is the averaged velocity 2D upstream of the North turbine operating at the rotational speed of Ω^*. A case of free wheeling, in which no torque was exerted on the shaft of the North turbine, was also tested to represent an extreme case of low torque and high thrust. It can be seen in Fig. 5.3 that the flow is decelerated as it approaches the turbines, and this becomes more significant for the free wheeling case where the turbine exerts a maximum thrust to the flow. Fig. 5.3 also shows that when the turbine operates at the rotational speed of Ω^*, the normalized velocity only shows little variation from 2D to 3D upstream of the rotor, which implies that the streamwise velocity at 2D upstream of the rotor is sufficient to represent the free-stream velocity for this case.

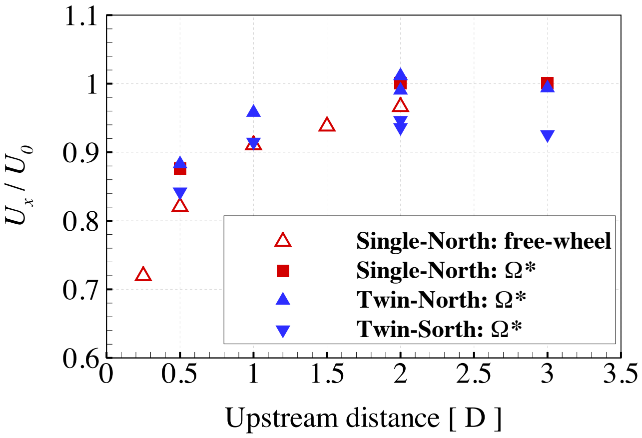

Fig. 5. 3 Normalized averaged streamwise velocity on the centre-line upstream of rotor plane.

Two data points were recorded at the location of 2D upstream of the rotor for the twin configuration. As shown in Fig. 5.3, there is slight difference between two measurements, which can be resulted from various reasons such as the difference in tank flow controls and in environmental conditions. This indicates that in order to get the performance coefficients of the rotor accurately, it is important to measure the flow field data and rotor performance concurrently.

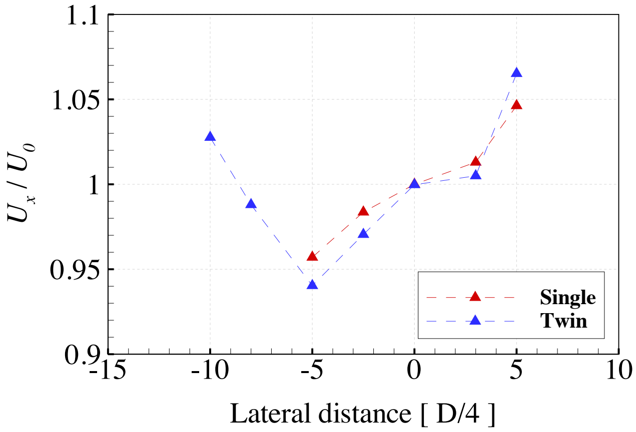

Fig. 5. 4 Normalized averaged streamwise velocity at various lateral locations at 2D upstream of the rotor plane. The position of North turbine is at the lateral distance of 0, and due to the tip-to-tip spacing of $D/4$, the position of South turbine is at the lateral distance of -5D/4 (basically $1.25D$ from the North turbine).

It is also worth noting that in Fig. 5.3, the mean flow velocity in front of the North and South turbines shows noticeable difference. To understand this lateral asymmetry further, a series of measurements at the cross-section plane at 2D upstream of the rotors were taken for the both configurations at the rotational speed of Ω^*, as shown in Fig. 5.4. The mean flow velocity at 2D upstream of the North turbine is close to 0.8 m/s for both configurations while that at 2D upstream of the South turbine is lower. For the single and twin configuration, the mean flow velocity in front of the South turbine position is around 4% and 6% lower than that in front of the North turbine respectively. This means that when the two turbines operate at the same rotational speed, their tip-speed-ratios will be different. In order to deal with this, rpm-to-flow-speed transfer functions are proposed by McNaughton *et al.* (2020), which relate the rotational speed of the rotor (measured in rpm) to the upstream stream velocity. Specifically, a series of upstream velocities (2D upstream of the rotor) and corresponding rotational speeds of the rotor are recorded respectively for North and South turbine in the twin configuration. A linear least-square regression is then fitted to the data, which provides two functions to obtain the upstream velocity for a given rotational speed for North and South turbine respectively. For the single configuration, the same approach is adopted, which yields another transfer function. These three transfer functions are used to determine the reference upstream velocity for a given rotational speed when tip-speed-ratios and performance coefficients are computed.

5.1.3 Rotor Performance

This section highlights the constructive interference effect demonstrated by the experiment. Fig. 5.5 shows the power and thrust coefficients for the single and the twin configurations. The averaged power and thrust coefficients from the two rotors are represented for the twin configuration. Due to the difficulties in maintaining the rotational speed of the rotor at lower values, the limiting rotational speed is 75 rpm. For the single rotor configuration, the power coefficient peaks around tip-speed-ratio of 6, which is less than the design tip-speed-ratio of 7. This is as expected since the rotor is originally designed for a four-rotor fence in a domain with width of 16 meters and height of 2 meters, the global blockage is of 0.14, which is calculated as the ratio the total rotor area to the cross-section area of the domain. Even though the effective width of the FloWave tank remains unknown, the global blockage ratio for the single rotor configuration, which could vary from 0.045 to 0.075 if the width of tank is assumed as 25 m to

15 m, is less than the design case. The optimal thrust that the rotor could apply is less in a less constrained flow condition. Hence, in order to achieve a thrust close to the level of the optimal thrust in a lower global blockage ratio, the rotor designed for a higher global blockage ratio should operate at a lower tip-speed-ratio. This is also demonstrated in the configuration of twin rotors, where the optimal tip-speed-ratio shifts close to 7 when the global blockage ratio is increased and becomes closer to the design blockage ratio.

The most important finding, as shown in Fig. 5.5, is that the presence of a closely placed second turbine leads to an increase in performance of 26% around the maximum C_P point, while the thrust is increased by 7.7%. Moreover, as the power coefficient for the single rotor decreases significantly when the tip-speed-ratio is over 7, it is clear that the twin configuration achieves more than 26% power gains. This demonstrates that the performance of the turbine can be significantly increased in a closely packed configuration when the local blockage ratio is high.

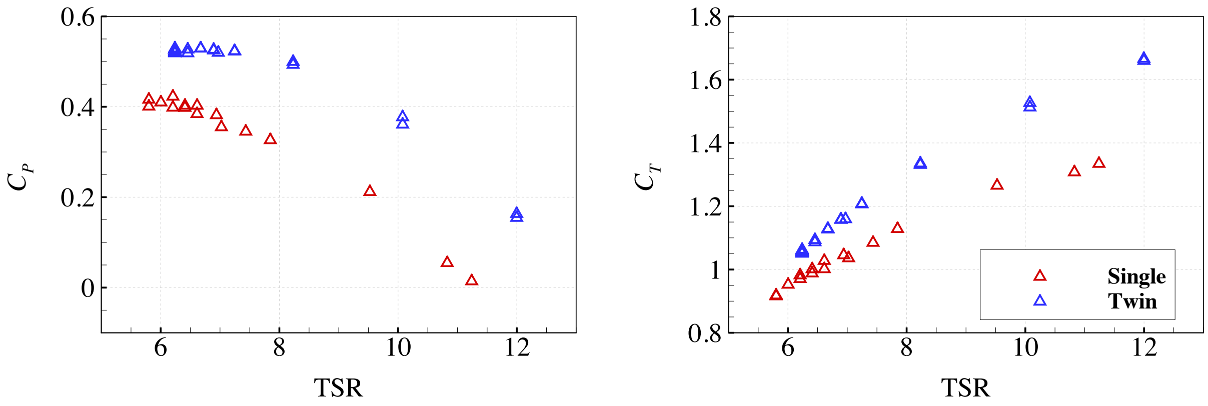

Fig. 5. 5 Power coefficient (C_P) and thrust coefficient (C_T) as a function of tip-speed-ratio for the single and the twin configurations. The reference upstream velocities are obtained through the rpm-to-flow-speed transfer functions.

5.2 Numerical Analysis

The numerical computations were conducted before the experiment test. The purpose of the numerical study was to provide the guidance of the performance of the rotors and to have some understandings of the flow field and blade loadings. The configuration of twin rotors is adopted for the studies in following sections.

5.2.1 Computational Domains

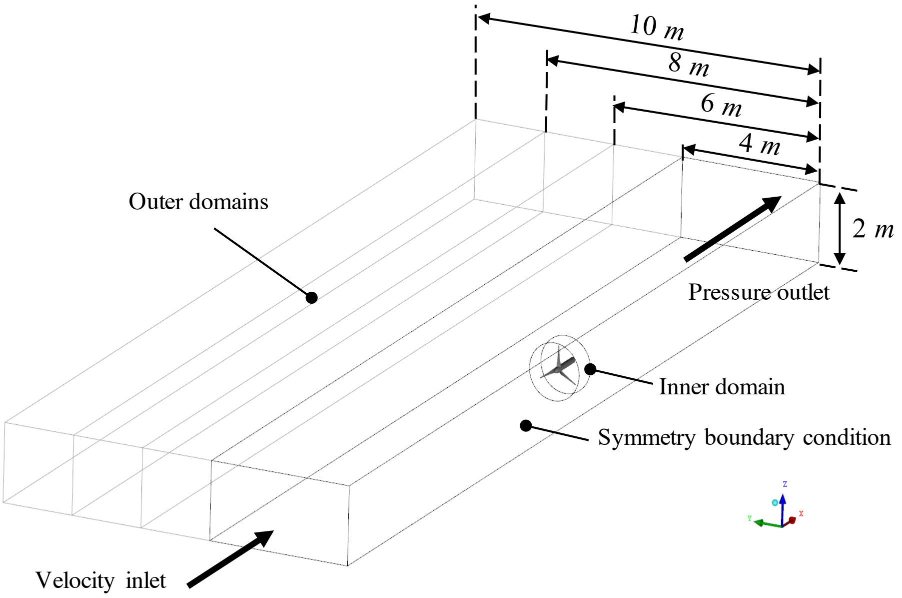

Fig. 5. 6 Diagram of the half-width computational domain. A series of computational domains with width of 4, 6, 8 and10 m were investigated. A symmetry boundary condition is applied at the side wall to mirror the half domain.

As discussed in section 4.1, the effective width of the tank remains unknown due to the circular shape of the tank, the recirculation regions at the sides of the tank and the interactions between the wake and the recirculation regions. Hence, a series of square computational domains with different global blockage ratios are considered, as shown in Fig. 5.6. In domains with similar blockage ratios (with other flow conditions being the same), the same rotor operating at the same tip speed ratio will produce similar thrust on the flow. Hence, by matching the thrust coefficient from the experimental test and from the numerical simulations, the effective blockage ratio of the tank may be estimated. The computational domains are of width varying from 4, 6, 8 to 10 m (which are referred as. 2-by-4, 2-by-6, 2-by-8 and 2-by-10 respectively in later sections), which is equivalent to simulating the configuration of twin rotors in domains with width of 8, 12, 16 and 20 m respectively. For each computational domain, the steady RANS computations are conducted using OpenFOAM (v5.0) for various operating tip-speed-ratios. The $\gamma - \mathrm{Re}_\theta$ turbulence closure model is adopted to capture the possible laminar-to-turbulent boundary layer transition on the blade surface. The MRF is used to simulate the rotor rotation.

5.2.2 Numerical Setups

A uniform streamwise velocity of $0.8\ \mathrm{m/s}$ is set at the inlet. The shear profile is not significant as studied in Suntherland et al. (2017), and for simplicity it is not simulated in the steady computation. The turbulence scalars such k, ω, γ and Re_θ are set as the same as the case with 120^o wedged domain in Section 4.4.2, to achieve a freestream turbulence intensity of around 7% $1D$ upstream of the rotor. The pressure boundary condition is applied for the outlet. Although some asymmetry of the freestream velocity was found ahead of the two turbines in the experimental study, this asymmetry is difficult to be parameterized in the steady RANS simulations. Hence, the computational domain treats the twin turbines as seeing the same flow and a symmetry boundary condition is used along the centreline. It is worth noting that this simplified half domain with a symmetry plane simulates a counter-rotation of the two rotors, while in the experiment, the two rotors rotate in the same direction (counter-clockwise). The performance of the rotor array and the flow field surrounding the rotors would be different for the two different rotating configurations. However, from the comparison shown later in section 5.2, the numerical simulation gives a reasonable agreement with the experimental measurement. Hence, considering the high computational cost for the blade-resolved model, the simplified half domain is adopted. The symmetry boundary condition is applied for the top, bottom and the far-end side of the computational domain.

The inner domain contains the nose section and the three blades. Fig. 5.7 shows the blocking topology for the inner domain, which is formed by copying and rotating the one-third wedged shape domain studied in section 4.3.1. The mesh parameters are set according to the M1 mesh as listed in Table 4.3. The total cell count for the inner domain is around 30 million. Each simulation takes on average 110 hours on 128 CPUs (around 14000 CPU hours).

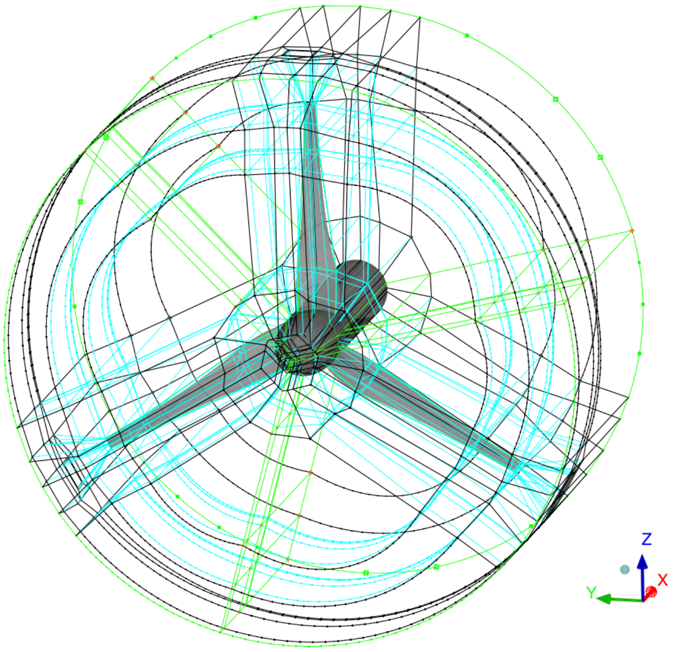

Fig. 5. 7 Blocking topology for the inner computational domain.

A trial run of unsteady RANS simulation for the rotors operating in the 2-m-by-4-m domain and at a tip-speed-ratio of 7 was also tested. Sliding mesh approach was used to simulate the rotor rotation, in which the inner domain is physically rotated relative to the stationary outer domain. The result from the steady simulation was used as an initial value for the flow field. However, in addition to the large number of the mesh cells resulted from the wall-resolving approach and four-equation turbulence model, the time stepping size is also limited by the smallest mesh size at the interface of the inner and outer domains. These factors lead to a computational time of around 55 hours on 128 CPUs for five degrees of rotor rotation, which indicates that the estimated computational time for one revolution of the rotor rotation would be over 4000 hours (around 0.5 year) on 128 CPUs. Even though the flow field was initialized by the result of the steady simulation, several revolutions may be required for each simulation, which makes the unsteady numerical study impractical.

5.2.3 Rotor Performance and Comparisons

The power coefficient (C_P) and thrust coefficient (C_T) obtained from the steady RANS simulations are shown in Fig. 5.8. It is noted for the thrust coefficient, the axial forces from the three blades and from the nose cone are considered. For the 2-by-4 domain in which the rotor is designed, the power coefficient peaks at TSR=7 as expected. The C_P curve is very flat, with slight variations over the tip-speed-ratios from 6 to 7.5. As the global blockage ratio decreases, i.e. the computational domain becomes wider, the optimal tip-speed-ratio at which the power coefficient peaks shifts to a lower value and the entire C_P curve shifts to lower values and shows larger variations over the tip-speed-ratios. When the flow becomes less constrained, it decreases the resistance in the bypass flow and allows higher mass flow to be diverted into the bypass region (for a given operating tip-speed-ratio), leading to less mass flow through the rotor

(Schluntz and Willden, 2015). The shift in the optimal TSR occurs since for a domain with lower global blockage ratio, the turbine designed for a higher blockage ratio applies too much thrust to the flow (compared to the optimal thrust in this lower-blockage domain). When the turbine operates at a lower TSR, a lower thrust is applied which is closer to the optimal thrust for the lower-blockage domain. The thrust coefficient shows an approximately linear relationship with the tip-speed-ratio. As expected, for a given tip-speed-ratio, the thrust is higher when the global blockage ratio is higher.

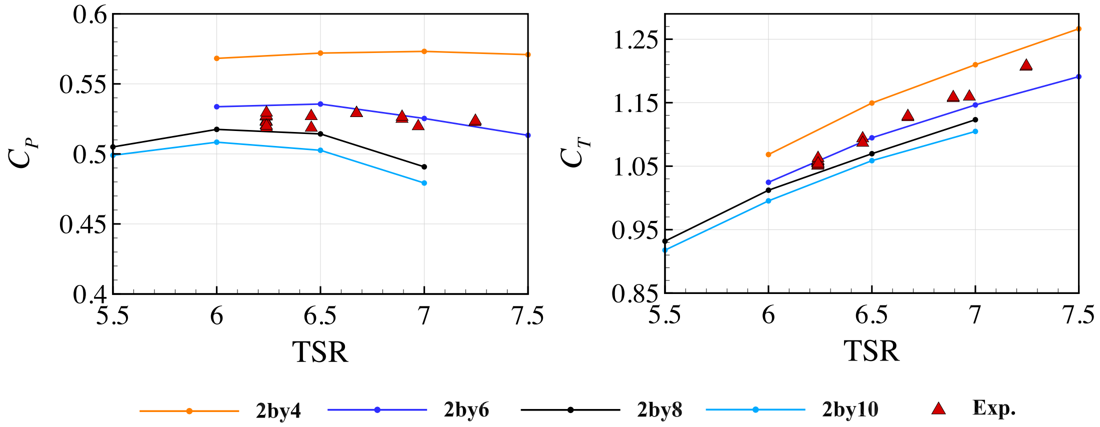

Fig. 5. 8 The power coefficient (C_P) and thrust coefficient (C_T) from the experimental measurements (Exp.) and numerical simulations. An envelope of performance curves is obtained from a series of square computational domains with a height of 2 m and widths of 4, 6, 8 and 10 m respectively (2by4, 2by6, 2by8 and 2by10 respectively).

It is noted that even though the blade-resolved model gives a close approximation to the experimental case, the vertical shear, the effect of unsteady flow behaviours and the effect of the supporting structure and circular shape of the test facility are ignored in the blade-resolved model (even these effects on integrated power prediction are justified to be small), which may cause a few percent difference to the C_P and C_T. Hence, the information on the accuracy of C_P and C_T remains unknown. However, it can be seen in Fig. 5.8 that the experimental result falls in the envelope of the numerical results.

5.2.4 Flow Field and Comparisons

Fig. 5.9 shows the contour of the streamwise velocity, u_x, around the two rotors on horizontal (xy) cut-plane at the hub height. The figure is formed by mirroring the half 2-by-6 domain. The two rotors operate at a same tip-speed-ratio of 6.1. An acceleration of the streamwise velocity between the two rotors can be observed. The map of flow velocities measured in the experiment and those extracted from Fig. 5.9 are shown in Fig. 5.10. The relative errors of the streamwise velocity and the velocity magnitude are presented above and below the flow vectors respectively. The length of the arrow indicates the relative velocity magnitude.

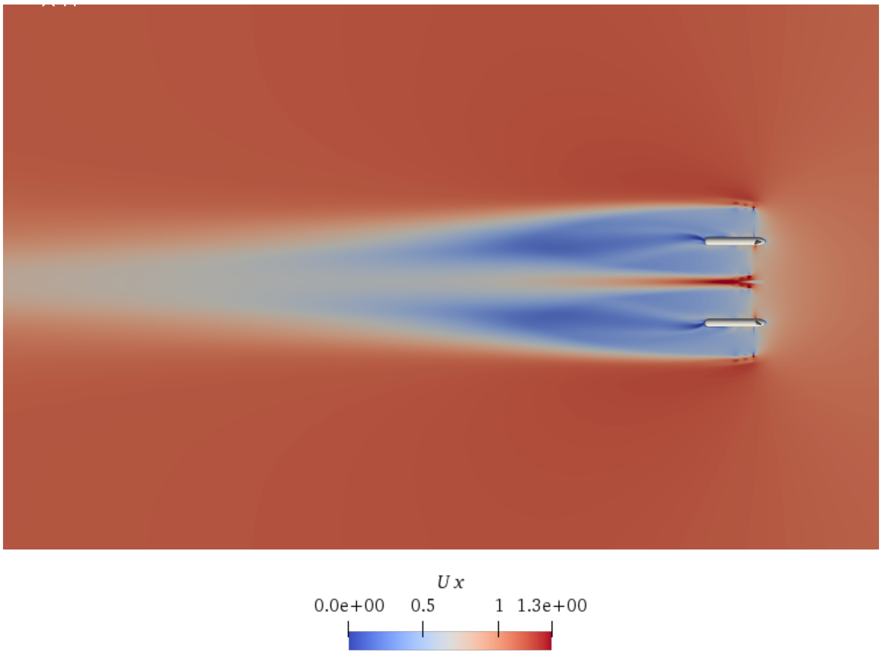

Fig. 5. 9 Contour of streamwise velocity on a cut-plane through the computational domain at the hub height. Zoomed into the region around the rotor array.

In Fig. 5.10, due to the circular shape of the tank and the recirculation regions near the sides of the tank, the velocity vectors from the experimental measurement contract inward towards the centreline of the tank upstream of the rotors whereas expands more outward towards the sides of the tank downstream of the rotors. All the velocity vectors from the experiment measurement at the $1.25D$ lateral position have greater magnitude, which likely due to the acceleration induced by the recirculation vortices in the tank. For the wake at 2D downstream from the rotors, the experimental measurements show significantly greater expansion.

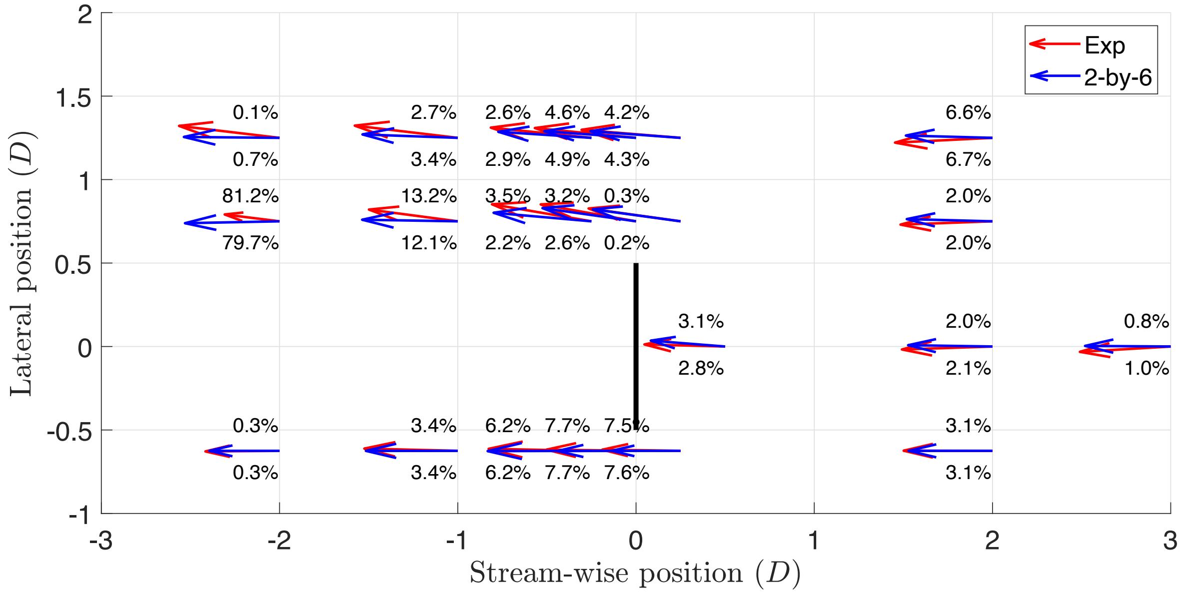

Fig. 5. 10 Flow field vectors measured in the experiment (Exp) and in the 2-by-6 numerical domain, at the hub height. The length of the arrow shows the relative magnitude of the velocity. The tip-speed-ratio is 6.1. The values above the arrows show the relative error of the streamwise velocity while the values below the arrows represent the relative error of the velocity magnitude. The solid black line indicates the North turbine position (The South turbine is positioned at a stream-wise position of 0 and a lateral position of -1.25D).

For the velocity vectors between the rotors and close to the rotor plane, the relative errors are relatively large, around 7%. This is likely due to the different rotating configurations. The symmetry boundary condition in the numerical study leads to a counter-rotating configuration of the two rotors while the two rotors rotate in the same direction in the experiment. However, for the $1D$ and $2D$ downstream of the rotor plane, the effect of the different rotating configuration seems to become less significant since the relative errors decrease.

Overall, the steady RANS computations compare well to the experimentally measured mean turbine performance and flow field, especially before the 1D downstream from the rotor plane. The difference can be to due to several factors. Firstly, the idealised square domain cannot simulate the recirculation regions near the sides of the tank, which tends to contract the velocity vector in the mainstream inwards towards the centreline before the rotor plane and expand the velocity vector outwards after the rotor plane. Secondly, the unresolved unsteady effects around the blades and the nacelle in the numerical simulation can contribute to the differences at downstream positions. Finally, the unresolved shear flow profile due to the uniform inflow assumption and the different direction of the rotor rotation might also contribute the differences.

Fig. 5.11 shows the streamwise velocity profile along the horizontal coordinates at different streamwise positions, extracted for the 2-by-6 domain at hub height with rotors operating at tip-speed-ratio of 6.1. The downstream positions are only investigated up to 2D. Since the convergence study of the blade-resolved model was only conducted for the blade loading distributions, and it is well known that the accuracy of the far wake profile is sensitive to the mesh resolution (see e.g. Batten *et al.*, 2013). For the blade-resolved model in this thesis, the main interest is to study the rotor performance and blade loading distribution, which is not sensitive to the far wake characteristics, and hence the computational domain is not particularly refined in the far wake region. As the flow approaches the rotor plane, the flow velocity in the bypass region is accelerated due to the reduction in flow velocity approaches the rotors. For the downstream positions from the rotor up to $1D$, the flow velocity between the two rotors gets accelerated. It’s noted that until the 2D downstream from the rotor, the wake profile from the two rotors is not mixed to an array scale but is still at the device scale.

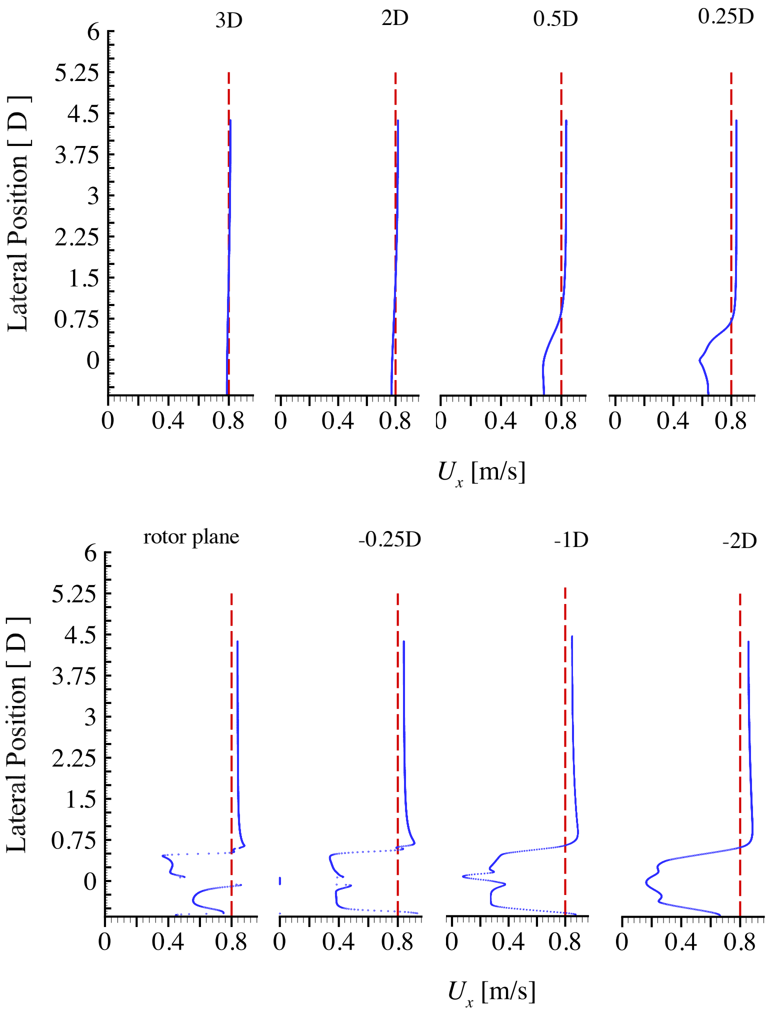

Fig. 5. 11 Streamwise velocity profile at various streamwise locations, extracted at the hub height. The positive sign indicates the upstream positions and the negative sign indicates the downstream positions.

5.3 Summary

Experimental result shows that significant power increase can be achieved through a closely packed side-by-side configuration. By taking the effect of increased local blockage ratio, the rotor is shown to have a 26% increase in power coefficient around the maximum power points at the expense of 7.7% increase in thrust. The rotor design shows a superior power performance in the experimental study, achieving a maximum average power coefficient of 0.53 for the twin configuration.

The high-fidelity blade-resolved computations are conducted to determine the effective width of the tank and to reproduce the experimental result. Due to the high computational cost of the unsteady simulation resulted from the mesh resolution and the four-equation transitional turbulence model, the steady RANS solver is adopted. Overall, the comparison shows that numerical simulation can give reasonable predictions of the performance of the turbines and the flow field around the turbines. The major differences are due to the idealised computational domain, the unresolved unsteady effects, the upstream turbulence fluctuations and the loading variations during the rotor revolutions. In addition, the uniform flow assumptions and the direction of rotor rotation might also contribute to the differences.

Chapter 6

Blade Surface Flow Analysis and Tip Correction

As discussed in Chapter 4, the major difference of blade load distributions between the RANS-BE model and the blade-resolved model is in the blade tip region. This is because in the RANS-BE model, the forces on each blade element are assumed to be determined through two-dimensional aerofoil characteristics and there is no radial interaction between the adjacent elements. Hence, three-dimensional flow effects are largely ignored. This assumption often leads to reasonable accuracy along the mid-span of the blade. However, such a simple treatment of the flow leads to an overprediction of the loads on the outboard sections of the blade, which is due to the unaccounted-for three-dimensional flow effects. The following sections 6.1 to 6.4 explore three-dimensional flow field on the blade surfaces and emphasizes the spanwise flow component due to the spanwise flow effects.

A new anisotropic tip correction is developed in section 6.5, which is fundamentally different from the existing correction models. The aerodynamic model of the rotating blade uses a circulation model for the bound vortex and trailing vortex sheet that is similar to that found in lifting line theory. In a similar manner to lifting line theory, we consider the velocities induced by the trailing vortex sheet at the location of the bound vortex which is located along the blade's centre of pressure line. In classical lifting line theory, the focus is on the velocities induced perpendicular to the bound vortex. This leads to the idea of an induced downwash, being a velocity component in the plane of the local blade section. This downwash changes the effective angle of attack of the flow to the blade leading to aerodynamic modification of the lift distribution at each position along the blade span. Similar analysis leads to the classical Glauert correction and leads to the specification of a spanwise varying correction factor which is used to modify the velocity induction factor and thereby the velocity component normal to the rotor plane. This acts to alter the angle of attack seen by the local blade section through which the blade's sectional lift and drag coefficients are then modified.

In the new tip correction model, we consider the influence of the trailing vortex sheet on the flow induced in the spanwise direction along the blade. This induced flow is therefore in the direction aligned with the bound vortex and perpendicular to the local blade section. Therefore, its influence cannot be accounted for by an induced downwash and modification of the approach flow and angle of attack in the local blade section. Fundamentally, this is a three-dimensional flow effect and should not be able to be accounted for using modification of approach flows to two-dimensional blade sections. We instead seek to use the radial component of the momentum equation to develop a relationship. This additional dimension is included in the correction model to reproduce the loading associated with three-dimensional flow physics.

6.1 The Numerical Simulations

The analyses in this chapter are based on the numerical simulations conducted at three blockage ratios (B) of 0.05, 0.14 and 0.42. These three blockage ratios are selected to represent respectivrly low, moderate and high blockage ratios that tidal rotor may experience during operations. At each blockage ratio, both the RANS-BE and the blade-resolved simulations are conducted for design and several off-design tip-speed-ratios. The rotor S, designed in section 4.3.3, is adopted. The computational domains for the two models are shown in Fig. 6.1. The cylindrical domain is selected in order to save the computational cost and to isolate the effect of blockage. 120^o wedge domain is adopted for the blade-resolved model to take advantage of azimuthal periodicity. The mesh resolutions follow the study in section 4.4.2. For the blade-resolved model, $y^+ < 1$ is maintained on the blade surface.

Steady RANS computations are conducted for both simulations. The transitional $\gamma - \mathrm{Re}_\theta$ turbulence closure is adopted for both models. The inflow condition is the same as the rotor design condition, where the uniform inflow velocity is 0.8 m/s and the freestream turbulence intensity is maintained as 7 % one diameter upstream of the rotor plane. The standard velocity inlet and pressure outlet boundary conditions are applied to the domain inlet and outlet boundaries respectively. The symmetry boundary condition is applied to the cylindrical surface. For the blade-resolved simulation, the periodic boundary condition is applied to the side faces. The computational domain is divided to inner and outer domains with Multiple Reference Frame (MRF) adopted to simulate the rotor rotation.

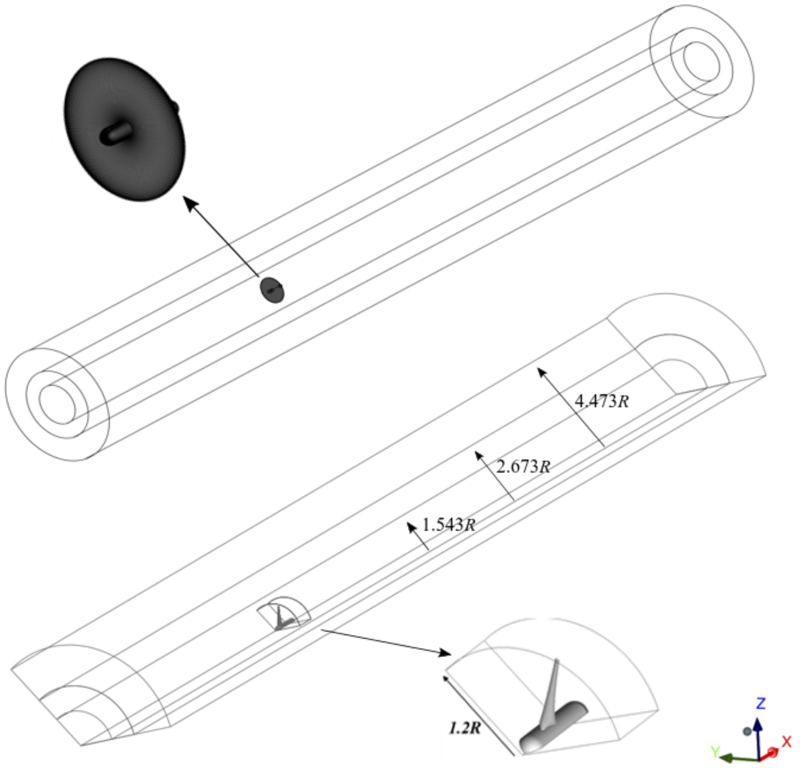

Fig. 6.1 Computational domains for the RANS-BE and the blade-resolved model.

6.2 The Effect of Blockage and Tip-Speed-Ratio on Angle of Attack

The Azimuthal Average Technique (AAT) as discussed in section 4.4.4 is used to extract spanwise distribution of angle of attack from the blade-resolved model. Fig. 6.2 shows the distributions of angle of attack for different TSRs when $B = 0.14$. Greater angles of attack are observed in the blade root region, especially for low $\mathrm{TSR} = 6$ where the angles of attack are over 10^o. However, it is noted that in the three-dimensional flow cases, the angle of attack that triggers the trailing edge separation may be higher than that in the 2D hydrofoil study due to the radial velocity component induced by the blade rotation and the corner separation (see e.g. Bangga *et al.*, 2017). It is noted that the angle of attack in the blade root region determined using the AAT approach is sensitive to the streamwise sampling distance, as studied in section

4.4.4, thus its accuracy remains a little uncertain. At $\mathrm{TSR} = 7$, in which the operating condition is similar to the design condition (recall that the rotor is designed in a non-centred square domain with blockage ratio of 0.14 and TSR of 7), the angles of attack along the majority of the blade span (from r/R of 0.3 to 0.9) are close to the design angle of attack of 6^o. Fig. 6.2 also shows that as TSR increases, the angle of attack across the entire span decreases. This agrees with the analysis of the velocity triangle in blade element model, in which for a given upstream velocity, increase in the rotational speed reduces the flow angle approaching the blade section and thus the angle of attack.

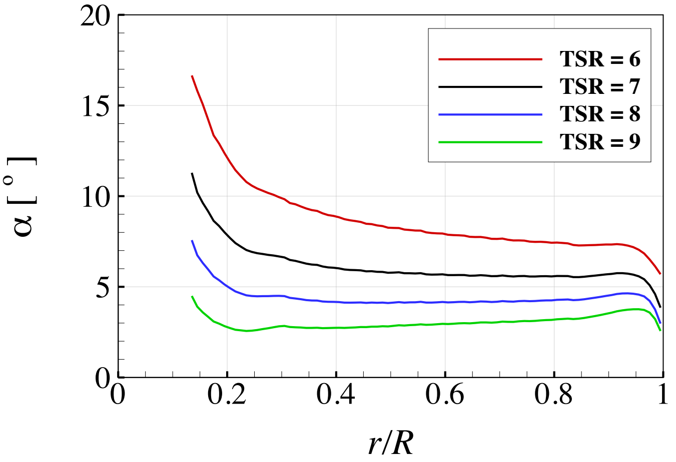

Fig. 6. 2 Distributions of the angle of attack along the blade span for $B = 0.14$, extracted from the blade-resolved model.

Fig. 6.3 plots skin friction lines on the suction surface of the blade and spanwise distributions of angle of attack for different blockage ratios. The skin friction lines are obtained by calculating the streamlines of the wall shear stress. The shaded red area indicates the flow separation region, determined by negative chordwise wall shear stresses. It is noted that the skin friction lines begin to curve radially outwards before the separation occurs. For a given TSR, the angles of attack across the entire blade span increase as the blockage ratio increases. This is due to that the increase of blockage ratio results in higher resistance in bypass flow region, which diverts more flow into the rotor plane. Following the velocity triangle in the blade element analysis, the rise of the axial flow rate increases the flow angle approaching the blade section and hence increases the angle of attack. As a result, there is greater area of flow separation on the blade suction surface when the turbine operates in lower TSR and higher blockage ratio.

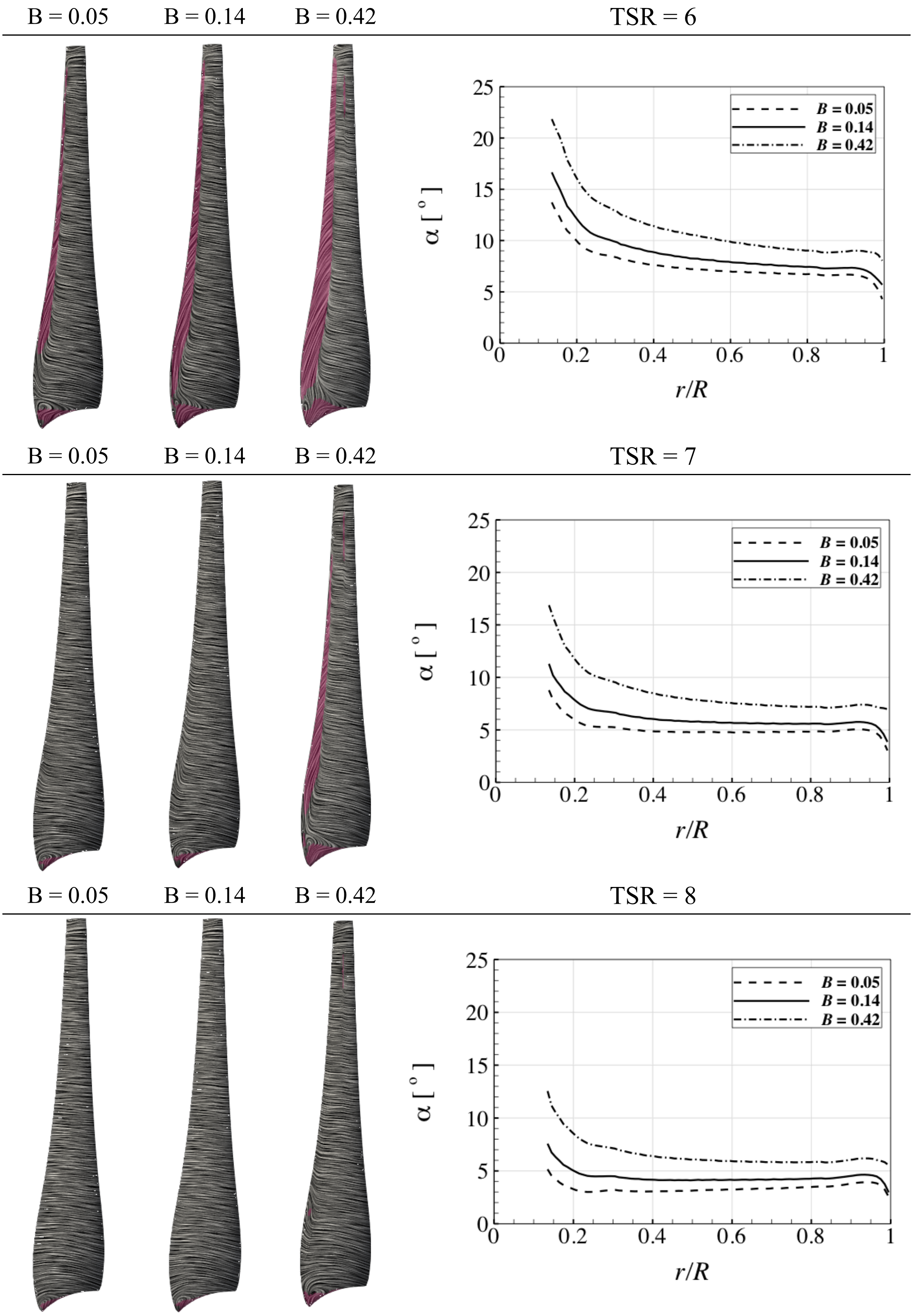

Fig. 6. 3 Plots of skin friction lines on the suction surface of the blade and distributions of angle of attack across the blade span. The shaded red areas indicate the flow separation region where the chordwise wall shear stress is smaller than zero.

6.3 Blade Load Analysis

Fig. 6.4 plots the spanwise distributions of the torque per unit span (T_y) and axial thrust per unit span (F_x) from the RANS-BE and the blade-resolved simulations for different blockage ratios. For $B = 0.05$ and $B = 0.14$, the distributions of the torque and axial thrust from the two models show good agreement in the mid-span of the blade. At TSR=6, the flow separation on the mid-span of the blade (seen in Fig. 6.3) seems to have minor effect on the torque and thrust distributions. For $B = 0.42$, the RANS-BE model under-predicts the torque and thrust in the mid-span of the blade, especially for TSR $= 6$ and TSR $= 7$ where large discrepancies in the torque distributions are observed. It is noted that from both the RANS-BE and blade-resolved model, the torque distributions for TSR $= 6$ and TSR $= 7$ are very similar. For $B = 0.42$, the torque distributions for different tip-speed-ratios vary in a smaller range compared to the other two cases.

In the blade root region, the difference in the thrust distribution is more significant than that in the torque distribution. This is because when the tangential force is multiplied by the radius to yield the torque, the difference in tangential force is offset by the small radius in the blade root region and hence the difference in torque is reduced. The RANS-BE model under-predicts the thrust in the blade root region due to lack of the correction model to resolve the three-dimensional flow effects such as the flow separations. For example, as shown in Fig. 6.3, when $B = 0.42$ and TSR $= 6$, a large area of corner separation and blade surface flow separation is observed. As a result, the torque and thrust distributions show large discrepancy in the blade root region.

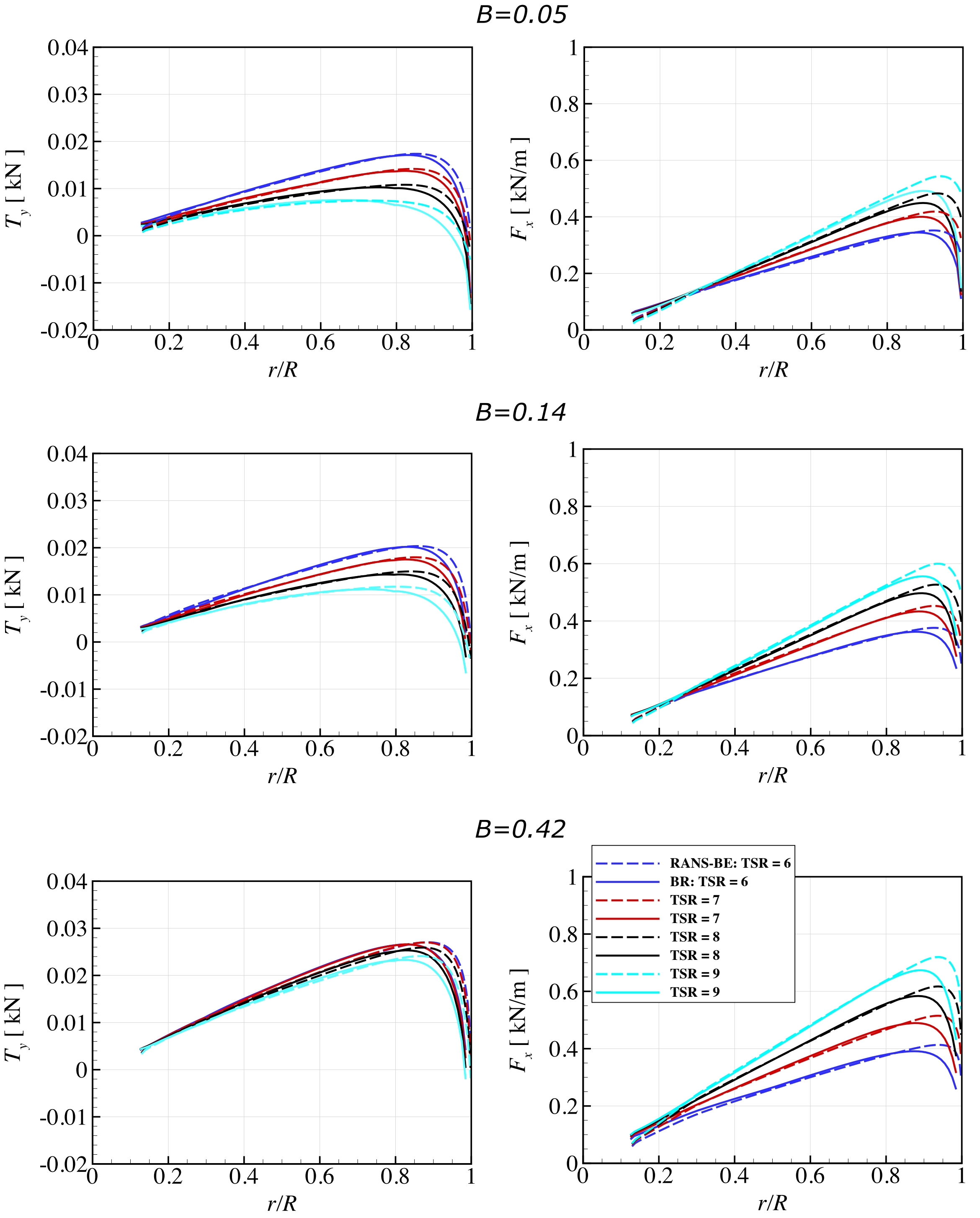

Fig. 6. 4 Torque per unit span (T_y) and axial thrust per unit span (F_x) from the RANS-BE and blade-resolved simulations for each blockage ratio (B) and tip-speed-ratio (TSR).

In the blade tip region, significant difference in the torque and thrust distribution is observed for all cases. Due to the lack of correction model to resolve the three-dimensional flow effects in the blade tip region, the RANS-BE model overpredicts both the torque and thrust. As the tip-speed-ratio increases, these discrepancies start at a more inboard position. For example, at $B = 0.14$, for $\mathrm{TSR} = 7$ the torque distributions from the two models start to deviate significantly at $r/R = 0.8$ while for $\mathrm{TSR} = 8$ they start to deviate at a more inboard position of $r/R = 0.75$. This can be resulted from that as the tip-speed-ratio increases, the chord-based Reynolds number for the blade section, turbulence intensity relative to the blade section and the associated laminar-to-turbulent transitional physics become different. In addition, the higher tip-speed-ratio leads to a greater resistance to the flow, resulting in a greater stream-tube expansion and hence leads to greater spanwise flows in the blade tip region. The blade-resolved model is able to directly resolves these effects while the RANS-BE model is highly dependent on the two-dimensional lift and drag data.

Table 6.1 summaries the percentage difference in the integrated power and thrust coefficients. The integrated power and thrust are derived from integrating the torque (then multiplied by angular velocity) and thrust distributions respectively. Across all the cases investigated, the percentage difference is less than 8%. The discrepancy in the power coefficient is less than that in the thrust coefficient. It is noted that the percentage difference is smallest for $B = 0.42$. However, it is clear that for $B = 0.42$ the torque and thrust distribution shows large discrepancy between the two models. This is due to that the disagreement of the load distribution in the mid-span of the blade offsets the discrepancy in the outboard region. For example, for $B = 0.42$ and TSR = 6, the percentage difference in power and thrust coefficients are the smallest. However, their torque and thrust distributions show the largest discrepancies. It is the under-prediction of the RANS-BE model in the mid-span of the blade offsets its over-prediction in the blade tip region, resulting in a smallest difference in the integrated value. This indicates that investigating only the integrated power and thrust coefficients may not be enough for accessing the accuracy of the prediction of loading distributions for a model. Hence, in later sections when the load distribution is compared, the Root Mean Square (RMS) error between the distributions, rather than the integrated quantities, is used as a metric to access the accuracy.

Table 6. 1 Percentage difference (%) in the integrated power coefficient (C_P) and thrust coefficient (C_T) between the blade-resolved model and RANS-BE model at each blockage ratio and tip-speed-ratio.

	TSR = 6	TSR = 7	TSR = 8	TSR = 9
$B = 0.05$				
C_P	3.20	3.67	4.48	6.82
C_T	1.42	3.21	3.89	5.63
$B = 0.14$				
C_P	3.33	3.96	4.76	7.31
C_T	2.31	2.92	3.71	4.64
$B = 0.42$				
C_P	1.59	2.75	3.70	4.47
C_T	0.40	1.50	2.63	3.68

Without the three-dimensional flow effects, the two-dimensional hydrofoil section would give similar performance to the three-dimensional blade section, as the blade load distributions in the mid-span region show. However, there is a large discrepancy in the blade tip region between the two models. In order to further investigate this discrepancy, Fig. 6.5 shows the chordwise distribution of the static pressure coefficient (C_{pre}) on slices through the three-dimensional blade at different spanwise positions (at the design condition of $B = 0.14$ and TSR $= 7$). The chordwise distribution of the static pressure coefficient for the two-dimensional hydrofoil sections at corresponding spanwise locations, over a range of angles of attack, is also shown for comparison. It is noted that these distributions for the two-dimensional cases are re-simulated according to the blade-relative turbulence intensity and the chord-based Reynolds number for different spanwise locations.

At $r/R = 0.8$, the pressure distribution from the three-dimensional blade show close agreement with that from the two-dimensional hydrofoil section at the design $\alpha = 6^o$. At $r/R = 0.9$, the pressure distribution from the three-dimensional blade generally matches with that from two-dimensional simulation at $\alpha = 6^o$. A slight reduction in the suction peak is observed. As it moves further towards the blade tip, at $r/R = 0.95$ and $r/R = 0.98$, the pressure distribution from the three-dimensional blade shifts to a two-dimensional case with lower angle of attack. This agrees with the spanwise distribution of angle of attack plotted in Fig. 6.3, in which the angle of attack is decreased as the blade tip is approached. However, more importantly, the pressure distribution from the three-dimensional blade in the blade tip region is distorted and it does not match with the distribution from the two-dimensional case at any angle of attack. This distortion of the pressure field rotates the force vectors on the outboard sections of the three-dimensional blade, which anisotopically alters the lift and drag forces generated on the blade section and thus the torque and thrust distributions (Wimshurst and Willden, 2018). As a result, the discrepancy in the blade load in the tip region cannot be fully resolved by only correcting the angle of attack in the blade element model.

It is noted that changing only the angle of attack will also alter the lift and drag anisotropically unless the lift-to-drag ratio is constant, so this is an additional anisotropic alteration. It is also noted that on the suction surface of the blade, the separation bubble presented in the two-dimensional case is absent for the three-dimensional blade. This may be due to the rotational effect and the resulted centrifugal force, which introduces a radial flow component and it mitigates the separation. This may be also due to the difference in transitional physics between the two-dimensional and three-dimensional flows (see e.g. Demekhin *et al.*, 2007).

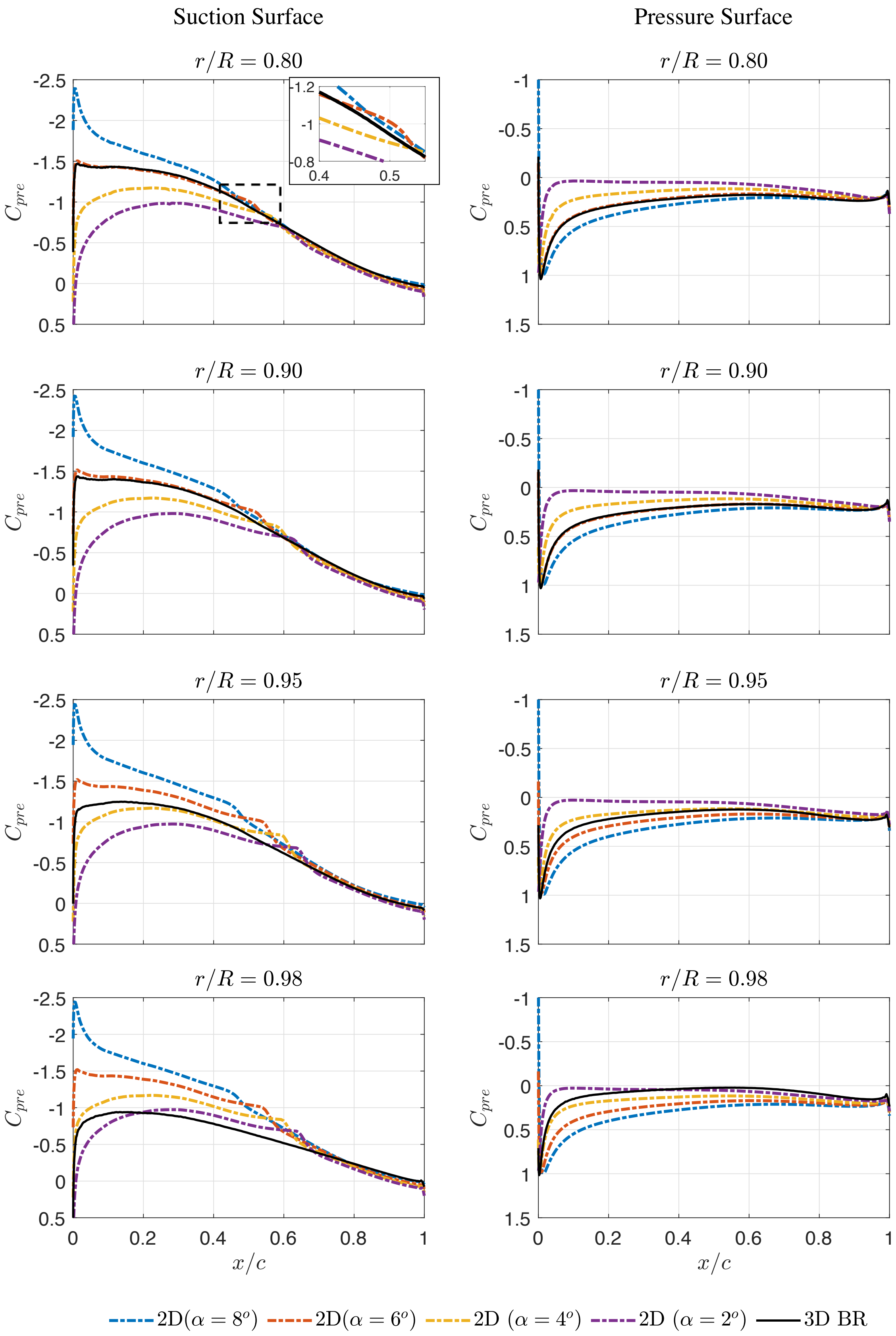

Fig. 6. 5 Chordwise distribution of the pressure coefficient from the three-dimensional (3D) blade-resolved model at $B = 0.14$ and TSR $= 7$ and from two-dimensional (2D) numerical simulations at different angle of attack (α).

6.4 Extraction of Blade Spanwise Flow

As shown in Fig. 6.5, the distortion of the pressure field on the blade sections largely impact the load in the blade tip region, which is difficult to be resolved in the two-dimensional hydrofoil characteristics. The distortion is primarily due to the pressure equalization in the blade tip region. The static pressure tends to equalise in the blade tip region between the suction and pressure surfaces, rolling up the flow and inducing the blade tip vortex. On the pressure side of the blade (with higher pressure), the pressure equalization process stretches and accelerates the flow towards the blade tip, which introduces a spanwise velocity component moving outboard towards the blade tip. The flow being stretched from the pressure surface is rolled up onto the suction surface, inducing a spanwise velocity component moving inboard towards the blade root.

Before investigating the spanwise or the radial flow on the blade surface, the boundary layer thickness has to be determined. However, the boundary layer thickness may vary with both chordwise and spanwise positions. For simplicity, the chordwise dimension is reduced since the spanwise flow and its radial variation is of main interest in this chapter. At a particular spanwise location, the flow field is qualitatively represented by that at a single point which has a chordwise position of the centre of pressure (CoP), along which the blade sections are aligned. A more plausible approach is to investigate the chordwise-averaged flow field, however, in practice it involves more complex post-processing steps. As can be seen later, the flow field sampled at the single point, CoP, is adequate for the qualitative study.

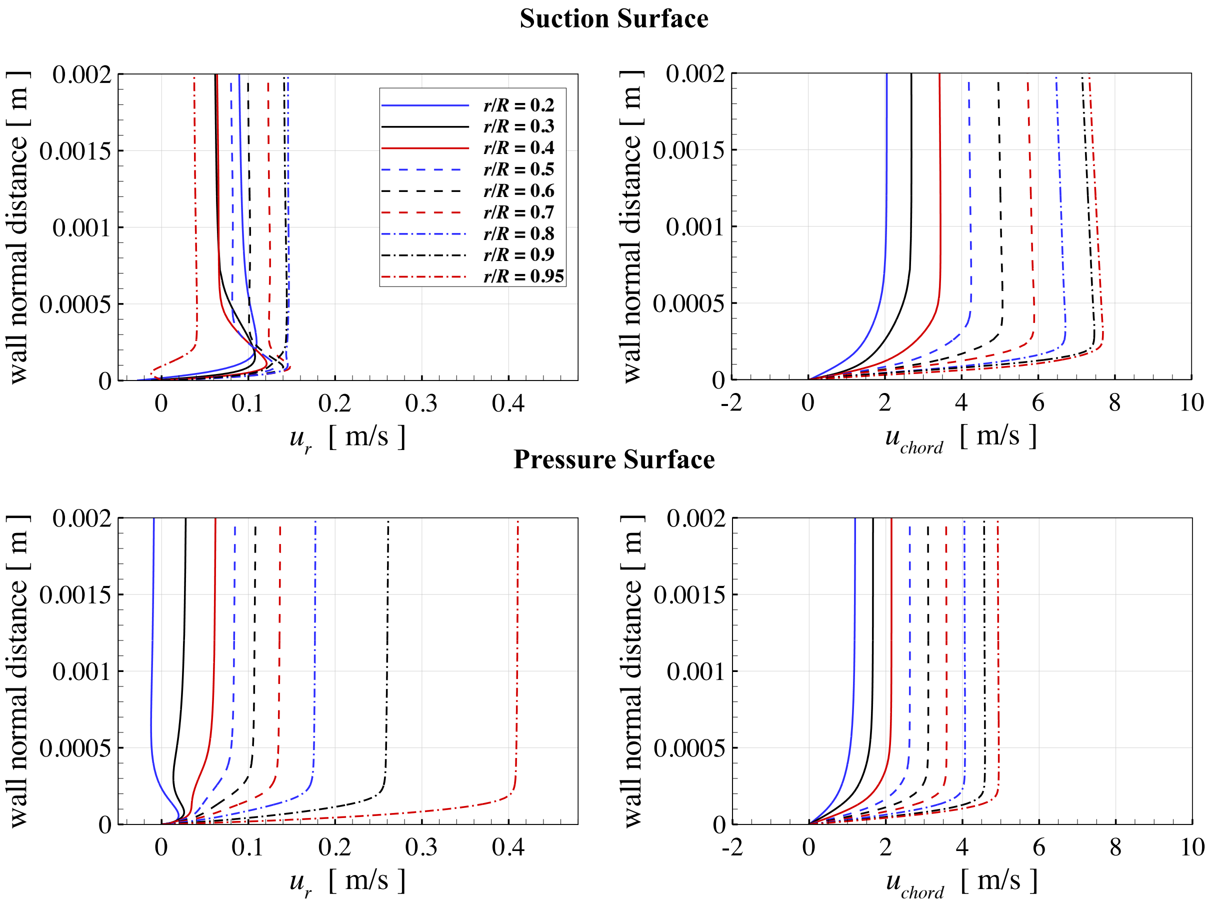

Suction Surface

Pressure Surface

Fig. 6. 6 Chordwise (u_{chord}) and spanwise (u_r) velocity profile on the blade surfaces sampled along the centre of pressure line at various spanwise positions, normal to the blade surfaces.

Fig. 6.6 shows the chordwise (u_{chord}) and spanwise (u_r) velocity profile on the blade surface sampled along the CoP line at various radial positions (for $B = 0.14$ and TSR $= 7$). The chordwise velocity, on both the suction and pressure surfaces, scales with the radial position. The boundary layer thickness decreases as the blade tip is approached. At the same radial position, the chordwise velocity on the suction side has greater magnitude than that on the pressure side. This agrees with lift generating process in which the velocity on the suction side is greater.

The spanwise velocity is more complex. For $r/R < 0.4$, the corner separation on the suction surface leads to a higher spanwise velocity. This also can be seen from Fig. 6.3, where the skin friction lines around the blade root tend to curve radially. The spanwise velocity on the pressure surface has a negative value at $r/R = 0.2$, which implies that radially the flow moves inward towards the blade root. This is reasonable since in the blade root region, the blade section has large chord length and large curvature (small radius). The attached flow on the pressure side tends to follow the curvature and has a radial velocity component moving towards the blade root. For r/R in the range of [0.4, 0.7], the spanwise velocity on suction and pressure sides has similar magnitude and increases with the radial position as a result of centrifugal force due to the blade rotation. In the outboard region of the blade, $r/R > 0.7$, without the effect of the pressure equalization the spanwise velocity would increase steadily with the radial position as that in the mid-span of the blade. However, the spanwise velocity on the pressure surface is accelerated while on the suction surface it is reduced significantly.

Fig. 6.7 shows the clear trend of the spanwise velocity along the CoP line. The velocity is sampled at an increment of r/R of 0.01 along the CoP line and at a wall normal distance of 0.001 m above the blade surface. In the blade root region, the corner separation on the suction surface induces a greater spanwise velocity. For r/R in the range of [0.3, 0.7], the radial velocities on the pressure and suction surfaces are similar, increasing at almost a constant rate. On the outboard sections of the blade, there is a significant increase in radial velocity on the pressure surface and a significant reduction in radial velocity on the suction surface. For TSR=6, it is noted that the flow separation on the suction surface across the mid-span region, as shown in Fig. 6.3, contributes to a greater radial velocity.

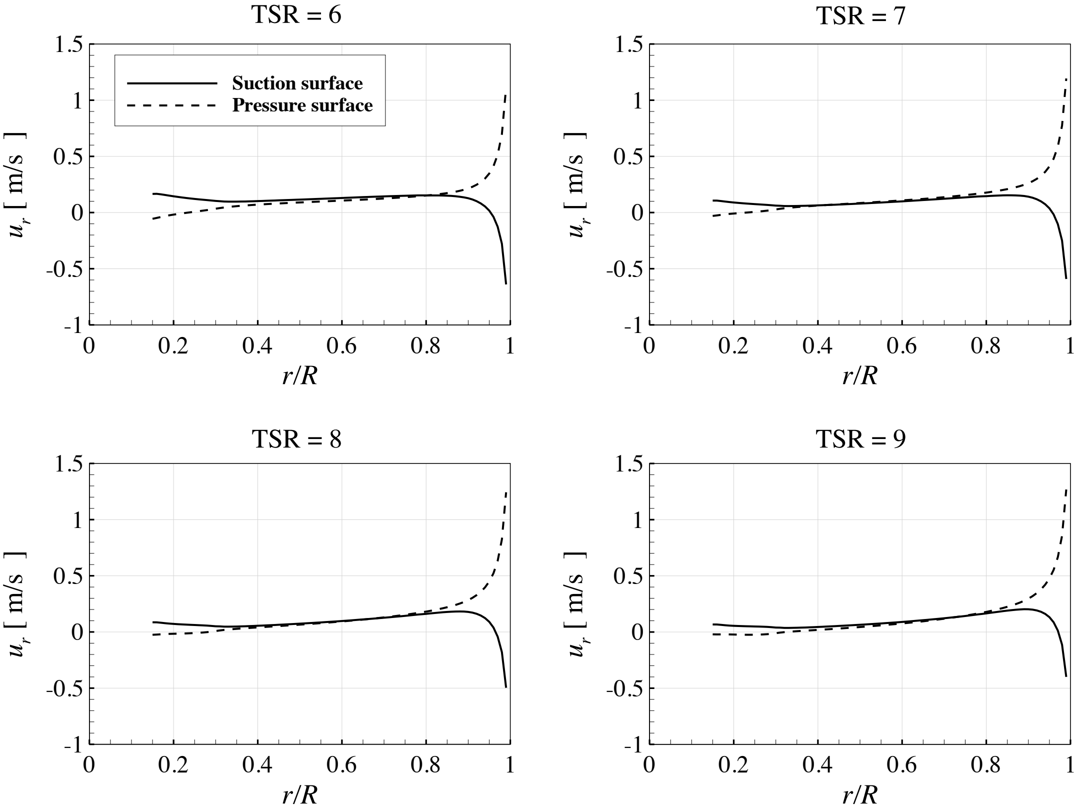

Fig. 6. 7 The radial (spanwise) velocity component sampled along the centre of pressure line on the blade suction and pressure surfaces when $B = 0.14$. The free-stream flow speed is 0.8 m/s.

6.5 Tip Correction for Spanwise Flow Effects

Having examined the pressure field and spanwise velocity on the blade suction and pressure surfaces, it is clear that the pressure equalization process in the blade tip region modifies significantly the hydrodynamic performance of the outboard section of the blade. This section provides a theoretically derived tip correction model to account for this spanwise pressure effect.

6.5.1 Radial Momentum Conservation and Spanwise Pressure Gradient

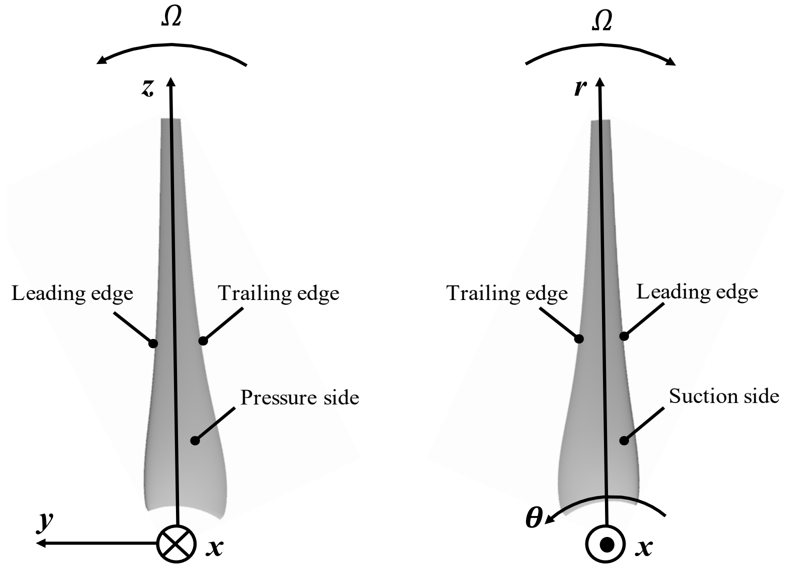

Fig. 6. 8 The cylindrical coordinate system local to the blade. TE indicates trailing edge of the blade whereas LE indicates leading edge of the blade.

The flow is assumed to be steady, incompressible and inviscid, which is reasonable for attached flow on the blade surface when the angle of attack is small. The steady and inviscid assumptions are also used in vortex theory and lifting line method for computing blade performance of the turbine. In cartesian coordinate, the momentum conservation may be expressed as:

$$(\boldsymbol{u} \cdot \boldsymbol{\nabla})\boldsymbol{u} = -\frac{1}{\rho}\boldsymbol{\nabla} p \tag{6.1}$$

where $\boldsymbol{u}$ is the velocity vector, p is the pressure field and ρ is the fluid density. Eq. (6.1) is applied off of the blade surface and hence body forces are absent. It is noted that under steady and inviscid assumptions, Eq. (6.1) is not applicable in regions of flow separation.

To facilitate the analysis of spanwise flow (i.e. radial flow component) on the blade surface, Cartesian coordinate $\boldsymbol{x} = (x, y, z)$ is transformed into a cylindrical coordinate, as shown in Fig. 6.8, where the Cartesian coordinate $\boldsymbol{x} = (x, y, z)$ and the cylindrical coordinate (x, r, θ) are related by:

$$\begin{aligned} x &= x \\ y &= r\sin\theta \\ z &= r\cos\theta, \end{aligned} \tag{6.2}$$

where $-\infty < x < \infty$, $0 \leq r < \infty$ and $0 \leq \theta < 2\pi$.

In order to transform the gradient operator from the Cartesian system into the cylindrical system, the cylindrical basis vectors are expressed as:

$$\begin{aligned} \hat{\boldsymbol{e}}_x &= \frac{\partial \boldsymbol{x}}{\partial x} = (1,0,0) \\ \hat{\boldsymbol{e}}_r &= \frac{\partial \boldsymbol{x}}{\partial r} = (0, \sin\theta, \cos\theta), \\ \hat{\boldsymbol{e}}_\theta &= \frac{1}{r}\frac{\partial \boldsymbol{x}}{\partial \theta} = (0, \cos\theta, -\sin\theta). \end{aligned} \tag{6.3}$$

It is noted that $\hat{\boldsymbol{e}}_r$ and $\hat{\boldsymbol{e}}_\theta$ change with θ and as a consequence:

$$\begin{aligned} \frac{\partial \hat{\boldsymbol{e}}_r}{\partial \theta} &= \hat{\boldsymbol{e}}_\theta \\ \frac{\partial \hat{\boldsymbol{e}}_\theta}{\partial \theta} &= -\hat{\boldsymbol{e}}_r. \end{aligned} \tag{6.4}$$

The derivatives with respect to the cylindrical coordinates are then obtained by differentiating through the Cartesian coordinate as:

$$
\begin{gathered}
\frac{\partial}{\partial x} = \nabla_x \\
\frac{\partial}{\partial r} = \frac{\partial \boldsymbol{x}}{\partial r} \cdot \frac{\partial}{\partial \boldsymbol{x}} = \hat{\boldsymbol{e}}_{\boldsymbol{r}} \cdot \boldsymbol{\nabla} = \nabla_r \\
\frac{\partial}{\partial \theta} = \frac{\partial \boldsymbol{x}}{\partial \theta} \cdot \frac{\partial}{\partial \boldsymbol{x}} = r\hat{\boldsymbol{e}}_\theta \cdot \boldsymbol{\nabla} = r\nabla_\theta.
\end{gathered}
\tag{6.5}
$$

The gradient operator for the cylindrical system then writes:

$$
\boldsymbol{\nabla} = \nabla_x \hat{\boldsymbol{e}}_{\boldsymbol{x}} + \nabla_r \hat{\boldsymbol{e}}_{\boldsymbol{r}} + \nabla_\theta \hat{\boldsymbol{e}}_\theta = \frac{\partial}{\partial x} \hat{\boldsymbol{e}}_{\boldsymbol{x}} + \frac{\partial}{\partial r} \hat{\boldsymbol{e}}_{\boldsymbol{r}} + \frac{1}{r} \frac{\partial}{\partial \theta} \hat{\boldsymbol{e}}_\theta.
\tag{6.6}
$$

By expressing the velocity vector in the cylindrical system as:

$$
\boldsymbol{u} = u_x \hat{\boldsymbol{e}}_{\boldsymbol{x}} + u_r \hat{\boldsymbol{e}}_{\boldsymbol{r}} + u_\theta \hat{\boldsymbol{e}}_\theta,
\tag{6.7}
$$

the left-hand-side (LHS) term in Eq. (6.1) is expressed as:

$$
\begin{aligned}
(\boldsymbol{u} \cdot \boldsymbol{\nabla})\boldsymbol{u} &= \left(u_x \frac{\partial}{\partial x} + u_r \frac{\partial}{\partial r} + \frac{u_\theta}{r} \frac{\partial}{\partial \theta} \right) \cdot (u_x \hat{\boldsymbol{e}}_{\boldsymbol{x}} + u_r \hat{\boldsymbol{e}}_{\boldsymbol{r}} + u_\theta \hat{\boldsymbol{e}}_\theta) \\
&= \left(u_x \frac{\partial u_x}{\partial x} + u_r \frac{\partial u_x}{\partial r} + \frac{u_\theta}{r} \frac{\partial u_x}{\partial \theta} \right) \hat{\boldsymbol{e}}_{\boldsymbol{x}} \\
&+ \left(u_x \frac{\partial u_r}{\partial x} + u_r \frac{\partial u_r}{\partial r} + \frac{u_\theta}{r} \frac{\partial u_r}{\partial \theta} - \frac{u_\theta^2}{r} \right) \hat{\boldsymbol{e}}_{\boldsymbol{r}} \\
&+ \left(u_x \frac{\partial u_\theta}{\partial x} + u_r \frac{\partial u_\theta}{\partial r} + \frac{u_\theta}{r} \frac{\partial u_\theta}{\partial \theta} + \frac{u_\theta u_r}{r} \right) \hat{\boldsymbol{e}}_\theta,
\end{aligned}
\tag{6.8a}
$$

and the right-hand-side (RHS) term is expressed as:

$$
-\frac{1}{\rho} \boldsymbol{\nabla} p = \frac{\partial p}{\partial x} \hat{\boldsymbol{e}}_{\boldsymbol{x}} + \frac{\partial p}{\partial r} \hat{\boldsymbol{e}}_{\boldsymbol{r}} + \frac{1}{r} \frac{\partial p}{\partial \theta} \hat{\boldsymbol{e}}_\theta.
\tag{6.8b}
$$

It's noted that the terms $\frac{u_\theta u_r}{r}$ and $\frac{u_\theta^2}{r}$ in Eq. (6.8a) are resulted from Eq. (6.4). The radial momentum conservation is then:

$$
\frac{\partial p}{\partial r} = -\rho \left(u_x \frac{\partial u_r}{\partial x} + u_r \frac{\partial u_r}{\partial r} + \frac{u_\theta}{r} \frac{\partial u_r}{\partial \theta} - \frac{u_\theta^2}{r} \right).
\tag{6.9}
$$

6.5.2 Decomposition of Radial Velocity

We decompose the radial velocity into two components. The first component results from blade rotational effects, and is referred to as u_c (c stands for centrifugal), whilst the second, referred to as u_Γ, results from the velocity induced by the shedding of bound circulation. We postulate that the variation of radial velocity and its gradients drive radial pressure gradients on the suction and pressure surfaces of the blade, which lead to additional loads that distort the spanwise blade loading distributions that might be assumed or calculated in the absence of three-dimensional flow effects.

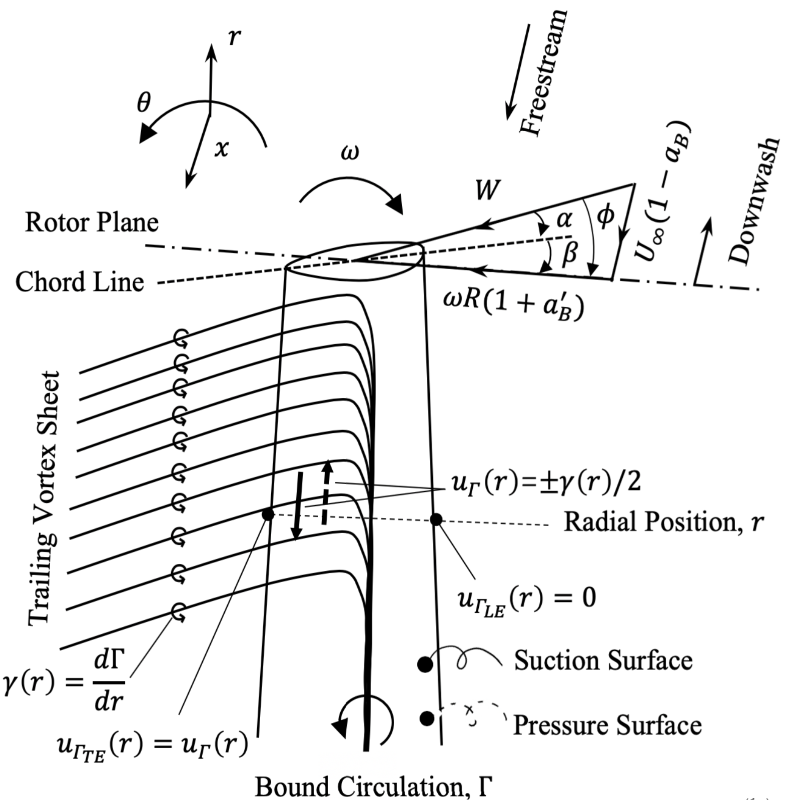

Fig. 6. 9 Schematic diagram of three-dimensional flow effects on the blade surfaces.

As shown in Fig. 6.7, along the mid-span of the blade, where velocities induced by shed circulation should be minimal, the radial flow velocity increases steadily from inboard to outboard on both the suction and pressure surfaces of the blade. u_c increases similarly on both blade surfaces and therefore the resulting radial pressure changes should be matched between suction and pressure surfaces. Hence, there should be little effect on blade loading from the centrifugally induced component of radial velocity. Hence, we assume that radial flow modifications to the spanwise loading distribution along the blade are independent of the centrifugally induced radial blade flow, and we do not study the form of the expression for u_c further in this thesis.

The shedding of bound circulation along the blade span is a necessary consequence of the variation in spanwise lift and resultant circulation distributions. The shedding of circulation to form the tip vortex is normally modelled as inducing a downwash type velocity in the plane of the blade section, and its effects are modelled through the Glauert model for rotating turbines. However, whilst a trailing vortex induces a velocity component in the plane of the blade it also induces spanwise velocity components towards the blade tip on the suction surface and towards the blade root on the pressure surface. It is these velocities that we refer to as u_Γ and which we will relate to the pressure gradient along the blade leading to a new correction for spanwise loading distributions.

For a bound circulation along the blade, $\Gamma(r)$, the rate at which circulation is shed from the blade is given by the strength of the trailing vortex sheet , $\gamma(r) = d\Gamma/dr$. The vortex sheet induces a velocity locally on either side of itself equal to half of its strength, and so we relate the changes in the bound circulation distribution to the radial flows induced along the blade through:

$$u_\Gamma(r) = \pm\frac{1}{2}\frac{d\Gamma}{dr} \,, \tag{6.10}$$

for the suction and pressure surface respectively, as depicted in Fig. 6.9. Since the bound circulation is shed as we move towards the blade tip ($d\Gamma/dr < 0$), u_Γ on the suction surface is negative and acts inwards from the blade tip, reducing the total radial velocity, whereas u_Γ on the pressure surface is positive, increasing the total radial velocity. Note that in the expression for u_Γ in Eq. (6.10) we neglect the radial velocities induced by the vortices shed from other radial positions and consider the radial velocity to be dominated by the vortex shed at that radial location along the blade span.

The Kutta–Joukowski theorem allows us to relate the bound circulation to the lift per unit span (L') of the blade section through:

$$L' = \rho W \Gamma \,, \tag{6.11}$$

where W is the velocity relative to the blade section. Hence, for a given lift distribution the radial velocity distribution, $u_\Gamma(r)$, resulting from shed circulation may be calculated with ease.

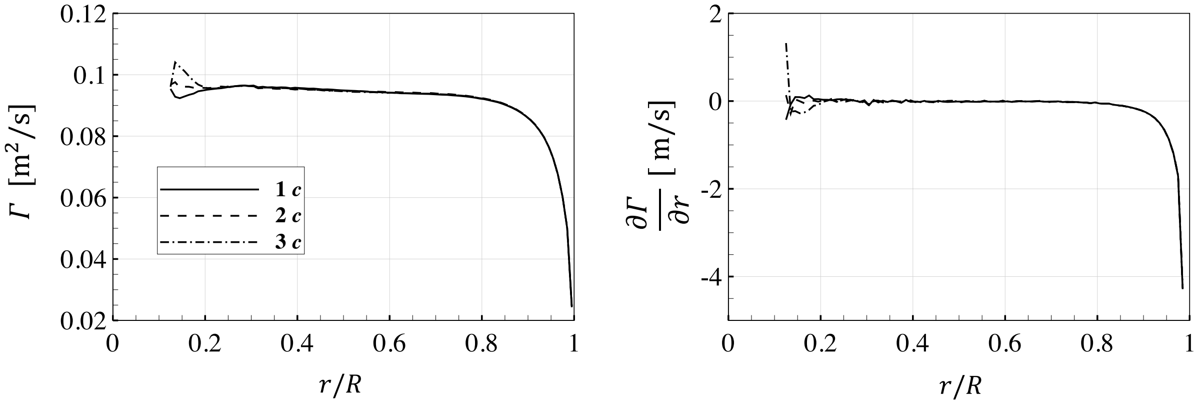

Fig. 6. 10 Spanwise distributions of bound circulation and the corresponding spanwise derivatives, computed using the AAT method with different streamwise sampling distances from the blade-resolved model, for $B = 0.14$ and $\mathrm{TSR} = 7$.

The determination of Γ for blade-element based model is straightforward. The lift force can be directly computed from the input of the two-dimensional lift data and the relative velocity approaching a blade section. Instead, the determination of Γ for the three-dimensional blade-resolved model is not straightforward. In order to compute the lift force on the blade section, the angle of attack has to be determined. As discussed in section 4.4.4, the Average Azimuthal Technique (AAT) is adopted to determine the angle of attack. The W in Eq. (6.11) is determined using the relative velocity triangle based on the azimuthally averaged streamwise velocity through the rotor plane and the azimuthally averaged tangential velocity. Fig. 6.10 shows the spanwise distribution of Γ and $\frac{\partial \Gamma}{\partial r}$ across the blade span computed using the AAT method from the blade-resolved result. The partial derivative is approximated using second-order difference method. It can be seen that the distribution is insensitive to the sampling distance in the AAT method except for that in the blade root region. Both the lift and streamwise velocity are affected by the separations in the blade root region, which makes the determination of Γ near the blade root difficult. To be consistent with the study of the angle of attack in section 4.4.4, the one-chord sampling distance is adopted for further studies.

6.5.3 Correction Formulation

Eq. (6.9) describes the spanwise pressure gradient along the blade that we seek to evaluate in order to develop a correction to account for three-dimensional effects, with which the loading distribution otherwise derived from two-dimensional data can be corrected.

First consider the three components of flow velocity in the cylindrical frame relative to the blade; u_θ is dominated by the rotation of the blade and may be approximated by $u_\theta \approx \Omega r$, i.e. neglecting swirl induced velocities $\Omega r a'_B$. Modern wind and tidal turbines operate at tip-speed-ratios in the region of 5 to 10 and so u_θ may be an order of magnitude in excess of u_x, the axial component of flow speed, except in regions close to the blade root where r/R is small (note $u_x \leq U_\infty$ due to axial flow induction). Further note that the radial component of velocity, u_r is nearly an order of magnitude smaller than the free-stream flow speed except in the region of the blade tip where the flow velocities may be comparable (see Fig. 6.7). So that, away from the blade root we expect $u_\theta \gg u_x \gtrsim u_r$.

We next consider the terms that contribute to the pressure gradient in Eq. (6.9). The final term is associated with centrifugal effects and has only weak dependency on induced flows as u_θ is dominated by Ωr. Hence, this term will provide a similar contribution to the pressure gradient on both the suction and pressure surfaces of the blade, and hence will yield little net contribution to blade loads in the tip region. For the remaining terms it is clear that all spatial gradients of the radial velocity, u_r, may be non-negligible in the presence of the blade. $\partial u_r/\partial r$ is associated with the slow radial expansion of the stream-tube as the flow decelerates (axially) through the rotor and is small except in the tip region due to localized effects. $\partial u_r/\partial x$ is associated with flow shearing and will be small except for within the blade boundary layers; in the current analysis we concentrate on inviscid effects and hence take $\partial u_r/\partial x$ to be small everywhere. $\partial u_r/\partial\theta$ is associated with the development of radial flow as the fluid moves across the blade chord and we observe that this may be non-negligible particularly in the tip region, see Fig. 6.3.

Coupled with the prior observation that $u_\theta \gg u_x \gtrsim u_r$, we expect the second and third terms to dominate the contributions to the radial pressure gradient that can lead to spanwise loading modifications due to radial effects. We study these two components further below by evaluating their contributions along the blade surface. We first though consider an approximation to the circumferential gradient term to aid in its evaluation.

We write the radial velocity as the sum of a centrifugally induced component and a component arising from the change in circulation, i.e. $u_r = u_\Gamma + u_c$, and hence write:

$$\frac{u_\theta}{r}\frac{\partial u_r}{\partial\theta} = \frac{u_\theta}{r}\frac{\partial(u_\Gamma + u_c)}{\partial\theta} = \frac{u_\theta}{r}\frac{\partial u_\Gamma}{\partial\theta} + \frac{u_\theta}{r}\frac{\partial u_c}{\partial\theta} \tag{6.12}$$

The velocity component associated with centrifugal effects, u_c, varies with radial position but is assumed not to vary in the circumferential direction and hence $\partial u_c/\partial\theta \sim 0$. As our interest is in the contribution of terms to pressure differences on either side of a blade, we again note that the $\partial u_c/\partial\theta$ term cannot contribute to such pressure differences and resulting forces as it will take similar values on both suction and pressure surfaces of the blade. We next consider the $\partial u_\Gamma/\partial\theta$ term and note that the radial flow due to changes in circulation will develop over the chord length of the blade; we assume that $u_\Gamma \sim 0$ at the blade leading edge and develops to the value u_Γ by the blade trailing edge, as shown in Fig. 6.11. Eq. (6.12) for the suction surface then becomes:

$$\frac{u_\theta}{r}\frac{\partial u_r}{\partial \theta} \approx \frac{u_\theta}{r}\frac{\partial u_\Gamma}{\partial \theta} \approx \frac{u_\theta}{r}\frac{\Delta u_r}{\Delta \theta} = \frac{\Omega r}{2c}\cdot\frac{d\Gamma}{dr} \tag{6.13}$$

in which u_θ is approximated by Ωr, u_Γ is replaced by $\frac{1}{2}d\Gamma/dr$ and the approximation $r\Delta\theta = c$ is used, where c is the chord length at radial position r, as it is representative of the distance over which u_Γ develops. On the pressure surface this term evaluates to the same magnitude but is negative as the velocity induced by the vortex sheet is in the opposite direction.

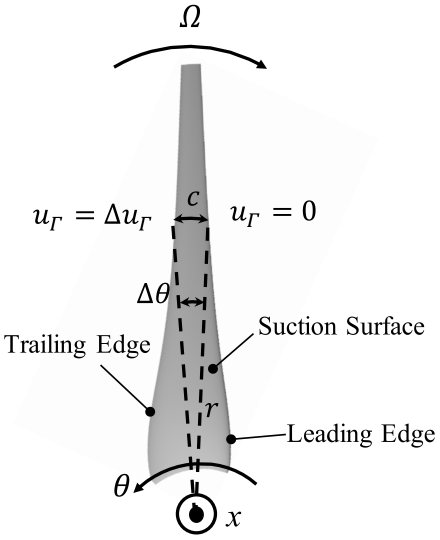

Fig. 6. 11 Schematic diagram for the assumption of the chordwise change of the circulation induced velocity.

We return to considering the magnitude of the second and third terms on the right-hand side of Eq. (6.9). To analyse the $u_r\frac{\partial u_r}{\partial r}$ term we choose not to decompose u_r into components, u_c and u_Γ, as u_c is not readily calculable and instead analyse u_r as a whole based on the radial velocity component extracted from numerical simulations. Fig. 6.12 plots the distribution of the term $\frac{\Omega r}{2c}\frac{d\Gamma}{dr}$ and $u_r\frac{\partial u_r}{\partial r}$, along the span of the blade, in which first order differentiation is used to estimate the derivatives. The term $u_r\frac{\partial u_r}{\partial r}$ on both the suction and pressure surfaces is observed to be very much smaller in magnitude than the $\frac{\Omega r}{2c}\frac{d\Gamma}{dr}$ term. When we consider that it is the difference in the value of a term between suction and pressure surfaces that is important, it becomes clear that the $u_r \frac{\partial u_r}{\partial r}$ term will make negligible contribution to the spanwise loading modification relative to the $\frac{\Omega r}{2c}\frac{d\Gamma}{dr}$ term. It is noted that it may not be appropriate to compare the term ($u_r \frac{\partial u_r}{\partial r}$) directly evaluated from RANS simulation results with the term evaluated based on the inviscid flow theory and other approximations. However, as the u_c is not readily calculable, decomposing u_r into components, u_c and u_Γ, would lead to difficulties in the further analysis. The main purpose of the comparison analysis shown in Fig. 6.12 is to justify that, considering the magnitude of the $u_r \frac{\partial u_r}{\partial r}$ term and difference between the terms for suction and pressure surface, it is reasonable to drop the $u_r \frac{\partial u_r}{\partial r}$ term in Eq. (6.9).

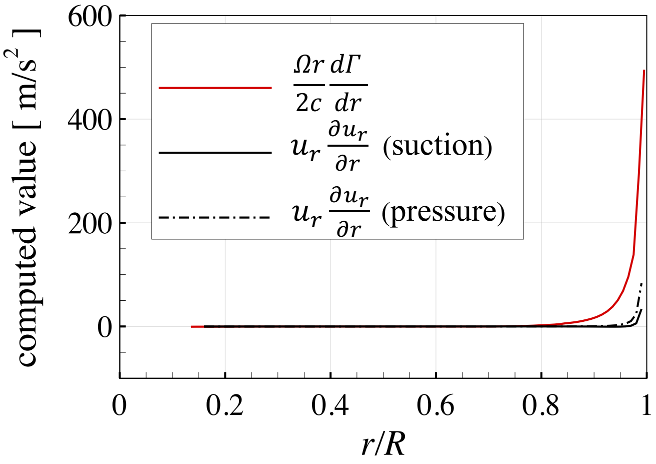

Fig. 6. 12 Numerically computed values of different terms in the radial momentum conservation.

Following the above, we therefore approximate the radial pressure gradient (or the component of the gradient that will lead to differential forces between suction and pressure surface) as:

$$\frac{\partial p}{\partial r} = \mp\rho \frac{\Omega r}{2c} \cdot \frac{d\Gamma}{dr}, \tag{6.14}$$

where $-/+$ refers to suction and pressure surfaces respectively. We next integrate this expression to develop radial pressure distributions. These are similar in form for suction and pressure surfaces and subject to an arbitrary constant pressure at the blade root which we take to be the same for both surfaces. For simplicity, only the suction surface pressure distribution is analysed, and the magnitude of the pressure difference between the two surfaces is accounted for by closure parameters introduced later. The pressure due to spanwise flow effects, p_{Γ}, on the suction surface at radial position r is then:

$$p_{\Gamma} = p_{\Gamma 0} + \int_{0}^{r} -\rho \frac{\Omega r}{2c} \cdot \frac{d\Gamma}{dr} dr, \tag{6.15}$$

where $p_{\Gamma 0}$ is the value of p_{Γ} at the blade root. The additional loading due to p_{Γ} is assumed to act over the blade surface, and so by multiplying by the local chord, we develop a force per unit span with which the two-dimensional sectional aerofoil data, L' and D', can be modified:

$$F_{\Gamma} \propto c p_{\Gamma}. \tag{6.16}$$

Two empirically calibrated closure parameters, g_L and g_D, which are assumed constant along the blade span, are then used to determine the modification to the lift and drag as:

$$F_{\Gamma,L}(r) = g_L c(r) p_{\Gamma}(r) = g_L c \int_{0}^{r} -\rho \frac{\Omega r}{2c} \cdot \frac{\partial \Gamma}{\partial r} dr + g_L c p_{\Gamma 0} \tag{6.17}$$

$$F_{\Gamma,D}(r) = g_D c(r) p_{\Gamma}(r) = g_D c \int_{0}^{r} -\rho \frac{\Omega r}{2c} \cdot \frac{\partial \Gamma}{\partial r} dr + g_D c p_{\Gamma 0} \tag{6.18}$$

The closure parameters should necessarily be a function of the aerofoil geometry and of the blade's twist distribution. The modified lift and drag per unit span, L^* and D^* respectively, are then:

$$L^*(r) = L'(r) + F_{\Gamma,L}(r) \tag{6.19}$$

$$D^*(r) = D'(r) + F_{\Gamma,D}(r) \tag{6.20}$$

which result in modified thrust, F_x, and torque, T_x per unit span:

$$F_x = L^* \cos\phi + D^* \sin\phi \tag{6.21}$$

$$T_y = (L^* \sin\phi - D^* \cos\phi) r \tag{6.22}$$

For model implementation purposes it is also useful to note the expressions for the modified non-dimensional lift and drag coefficients, C_L^* and C_D^*, per unit span:

$$C_L^* = C_L + \frac{F_{\Gamma,L}}{\frac{1}{2}\rho W^2 c} = C_L + g_L \frac{2p_\Gamma}{\rho W^2} \tag{6.23}$$

$$C_D^* = C_D + \frac{F_{\Gamma,D}}{\frac{1}{2}\rho W^2 c} = C_D + g_D \frac{2p_\Gamma}{\rho W^2} \tag{6.24}$$

6.5.4 Circulation Distribution

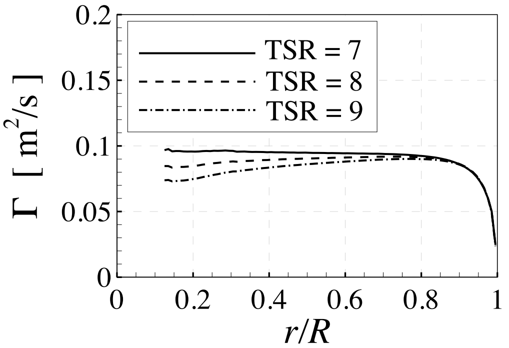

Fig. 6. 13 Bound circulation distribution computed from the blade-resolved model, for $B = 0.14$.

Fig. 6.13 shows the bound circulation distribution along the blade span for $B = 0.14$, computed from the blade-resolved simulations. At the design condition, $\text{TSR} = 7$, the bound circulation remains approximately constant for $r/R \leq 0.8$, after which it starts to decrease significantly as the bound circulation is shed in the blade tip region. As the tip-speed-ratio is increased, we observe additional shedding of bound circulation over the inboard sections of the rotor blade. The results for lower tip-speed-ratios are not presented, as for $\mathrm{TSR} \leq 6$ the flow separates on the suction surface over the mid-span region of the blade. In deriving the new loading model, we made inviscid flow assumptions and hence do not expect the model to be valid for such cases.

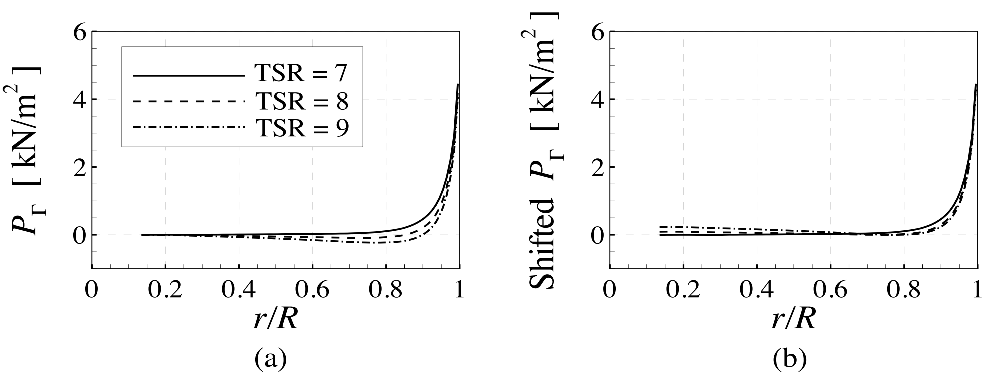

Fig. 6. 14 (a) Integrated spanwise pressure, P_Γ, numerically computed according to the bound circulation; (b) Shifted integrated spanwise pressure obtained by subtracting its minimum respectively.

Fig. 6.14 (a) shows the suction surface distribution of the pressure contribution due to spanwise flow effects, which is computed according to Eq. (6.15), where a first-order approximation is used to compute the derivative and trapezoidal integration is used to evaluate the integral. The spanwise pressure on the suction surface increases significantly in the blade tip region as shown in Fig. 6.14(a), which is consistent with the effect of pressure equalization, increasing the pressure (reducing the suction) on the suction surface. Similarly, on the pressure surface the spanwise pressure in the blade tip region tends to be negative, leading to a decreased pressure, as the spanwise induced flow due to shedding, u_Γ, is in the opposite direction from that on the suction surface. $P_{\Gamma 0}$ is set to zero in Fig. 6.14 (a). In practice, the true value of $P_{\Gamma 0}$ is difficult to know and may be different for different cases. When P_Γ is zero there are no net spanwise effects due to shedding of bound circulation and hence the two-dimensional lift and drag data can be a good representation of the real three-dimensional blade physics. Outboard of this point circulation shedding leads to significant spanwise flow effects for which the correction model can account for. Inboard of this point the circulation shedding leads to only small spanwise flow effects which are not as important as the viscous effects that dominate the root region. Hence P_{Γ} is shifted at which P_{Γ} is minimum, as shown in Fig. 6.14 (b). The correction model is only be applied in the region outboard of where $P_{\Gamma} = 0$. In order to avoid the sensitivity to numerical fluctuations in the blade root region, the minima at $r/R \geq 0.3$ is used to shift the P_{Γ}.

6.5.5 Static Correction model

The static correction model in this section discusses an approach of using the P_{Γ} distribution to correct the final result of the load distributions from the two-dimensional model to match with those from the three-dimensional model. The additional sectional forces, $F_{\Gamma,L}$ and $F_{\Gamma,D}$, due to the spanwise pressure, are added onto the two-dimensional sectional lift and drag force, as described in Eq. (6.19) and (6.20). The two closure parameters g_L and g_D are calibrated to achieve a good match in thrust and torque distributions between the two models. As discussed before in section 6.3, the difference in the integrated power and thrust between the two models may not be a good criterion for calibration. In the present study, the calibration is conducted to minimise the sum of normalized Root-Mean-Square (RMS) error in the thrust and torque distributions. The RMS error in the thrust and torque distributions between the three-dimensional model and corrected two-dimensional model is firstly calculated, which is then normalized respectively by the RMS error in those between the three-dimensional model and original two-dimensional model with only the Glauert tip correction applied. The RMS error is calculated for the blade outboard sections where r/R is in the range of [0.6, 0.99]. Since the correction model is only be applied in the region outboard of where $P_\Gamma = 0$, which is beyond $r/R = 0.6$ in the present study. The difference in further inboard blade sections is not taken into account when RMS error is computed.

Fig. 6.15 (a) and 6.15 (b) shows contours of the normalized RMS error in the thrust and torque as a function of g_L and g_D, for $B = 0.14$ and TSR = 7. Fig. 6.15 (c) shows contour of the sum of the two normalized RMS errors. When g_L and g_D are zero, there is no correction applied to the sectional lift and drag force and the normalized RMS error in the thrust and torque distributions both are one and the sum of the two RMS errors is two, which are used as benchmark values of the RMS error. The RMS errors are reduced when g_L is negative, which means that the correction model reduces the lift force as it approaches the blade tip and when g_D is positive, which means that the correction model increases the drag force in the blade tip region. This is in agreement with the three-dimensional blade physics observed before.

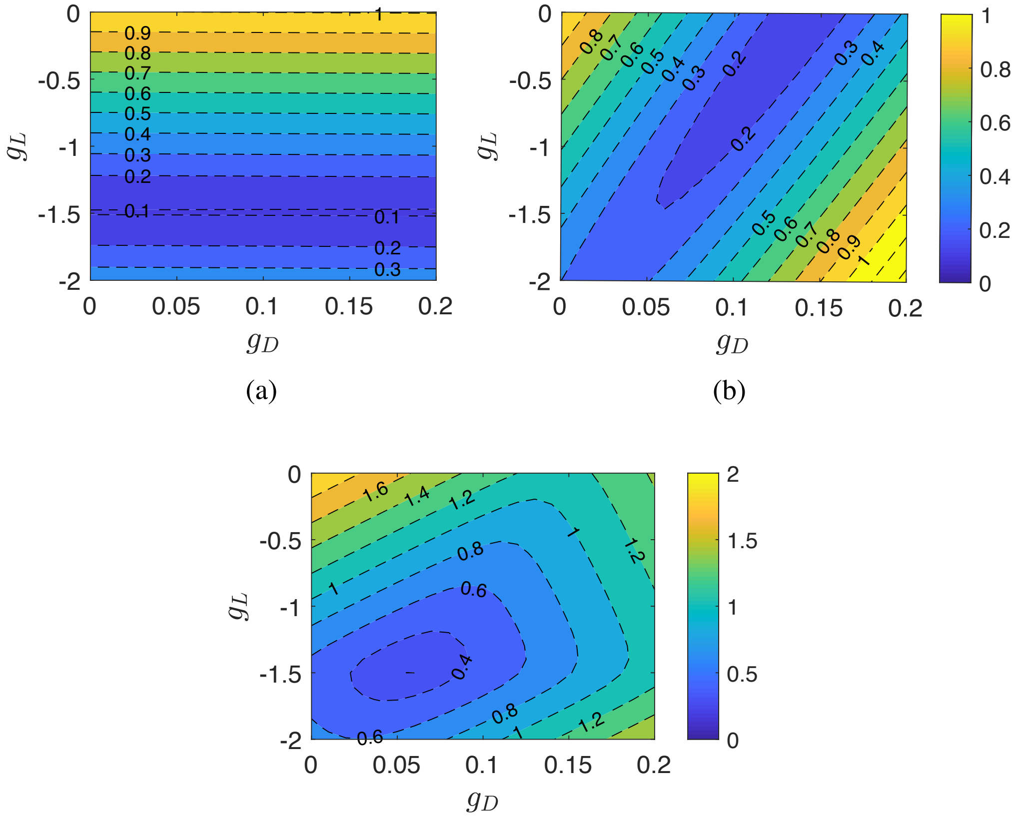

(a) (b)

(c)

Fig. 6. 15 Contours of the normalized RMS error in (a) thrust distribution, (b) torque distribution and (c) the sum of the thrust and torque errors, as a function of g_L and g_D, for $B = 0.14$ and TSR = 7.

As shown in Fig 6.15, the RMS error in the thrust distribution show negligible sensitivity to g_D and is only sensitive to g_L, while the RMS error in the torque distribution is sensitive to both g_L and g_D, Increasing the magnitude of g_L and g_D, the normalized RMS errors in the thrust and torque distributions are firstly decreased to a minimum value and then increased. The sum of the two RMS errors is minimized to 0.30 when $g_L = -1.50$ and $g_D = 0.06$. Compared to the benchmark value of 2, adding the new correction model to the original RANS-BE model (with only the Glauert tip correction model applied) improves the result by 85%. As for the integrated power and thrust, adding the new correction model reduces the difference to 0.2% and 0.3% respectively.

Fig. 6.16 and Fig. 6.17 show the distributions of lift, drag, thrust and torque on the blade outboard sections, where the sensitivity of the distributions to g_L and g_D are visualized. For Fig. 6.16, g_D is fixed at the optimal value of 0.06 and g_L deviates $\pm 50\%$ from its optimal value. For Fig. 6.16, g_L is fixed at the optimal value of -1.5 and g_D deviates $\pm 50\%$ from its optimal value. Compared to the three-dimensional blade-resolved model, the original RANS-BE model over-predicts the lift force and under-predicts drag force in the blade tip region. Hence, the correction model has to reduce the lift force and increase the drag force, which is in agreement with the sign of g_L and g_D. It is noted that when $r/R < 0.8$, the two-dimensional lift data show great agreement with the three-dimensional result, whereas the two-dimensional drag data has slightly greater magnitude. This is likely due to that the separation bubble does not present in the mid-span of the three-dimensional rotating blade, as indicated in Fig. 6.5. However, this mismatch in drag force when $r/R < 0.8$ only lead to slight difference in the thrust and torque distributions.

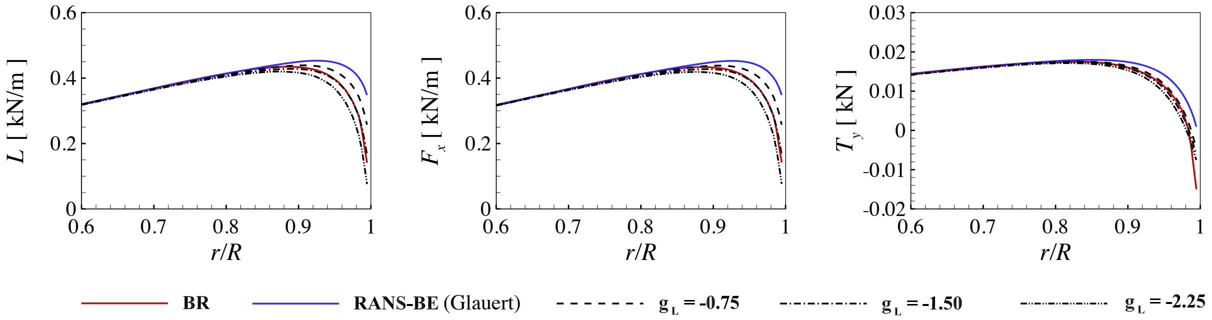

Fig. 6. 16 Distributions of the lift, thrust and torque over the outboard sections of the blade, for $B = 0.14$ and $\mathrm{TSR} = 7$. g_D is set as 0.06 for the static tip correction model.

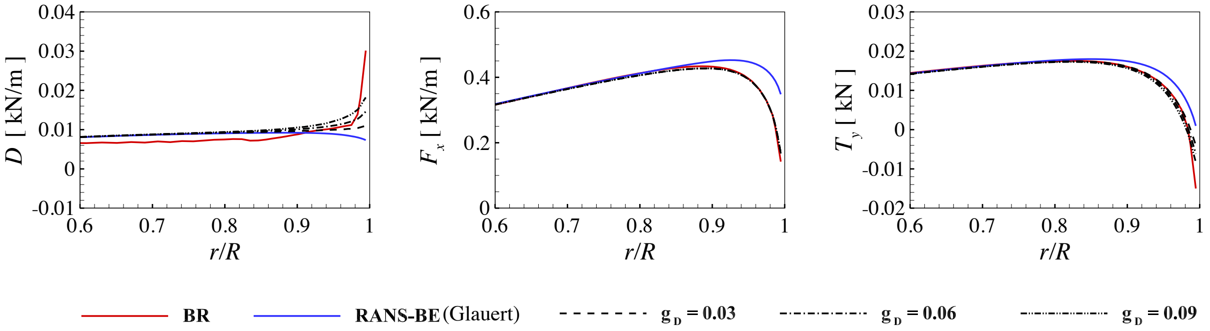

Fig. 6. 17 Distributions of the sectional drag, thrust and torque over the outboard sections of the blade, for $B = 0.14$ and $\text{TSR} = 7$. g_L is set as -1.5 for the static tip correction model.

Following the above calibration approach for $\text{TSR} = 7$, g_L and g_D are re-calibrated for $\text{TSR} = 8$ and $\text{TSR} = 9$ respectively at $B = 0.14$. The bound circulation distribution used for the correction formulation is computed from the blade-resolved model at corresponding tip-speed-ratio respectively. The calibrated distributions are shown in Fig. 6.18. The minimum RMS error in the sum of the thrust and torque distributions is 0.31 when $g_L = -2.0$ and $g_D = 0.08$ for $\text{TSR} = 8$, and is 0.45 when $g_L = -2.6$ and $g_D = 0.12$ for $\text{TSR} = 9$. Compared to the benchmark value of 2, adding the new correction model improves the total RMS error by 85% and 77.5%. There is dependence of the closure parameters on the tip-speed-ratio. Moreover, it is noted that the minimum RMS error achieved by the new correction model for $\text{TSR} = 9$ is slightly larger than other two cases. For $\text{TSR} = 9$, the discrepancies of thrust and torque in the blade tip region between the BR and the original RANS-BE model are over a greater blade outboard span, especially for the torque distribution where the discrepancy starts at $r/R = 0.75$, as shown in Fig. 6.18. As discussed before, this is likely due to the effect of increased chord-based Reynolds number resulted from the higher tip-speed-ratio, which is not parametrized in the two-dimensional lift and drag data in the RANS-BE model. In addition, the different transitional physics adds an extra complex when the Reynolds number is different.

The mismatch of the lift and drag data due to these flow physics may not be corrected by the spanwise flow correction model developed in this study. For $\mathrm{TSR} = 9$, the bound circulation starts to shed at $r/R = 0.87$ (which is close to the reflection point of P_Γ distribution from the three-dimensional model as shown in Fig. 6.14) and correspondingly the distributions are only corrected after $r/R = 0.87$, which leaves the discrepancies of the thrust and torque over r/R in the range of $[0.75, 0.87]$ uncorrected and hence leads to relatively large RMS errors. However, in terms of the integrated power and thrust, for $\mathrm{TSR} = 8$ the relative differences are less than 1% whereas for $\mathrm{TSR} = 9$ the relative difference in power is 2.48% and in thrust is 0.97%.

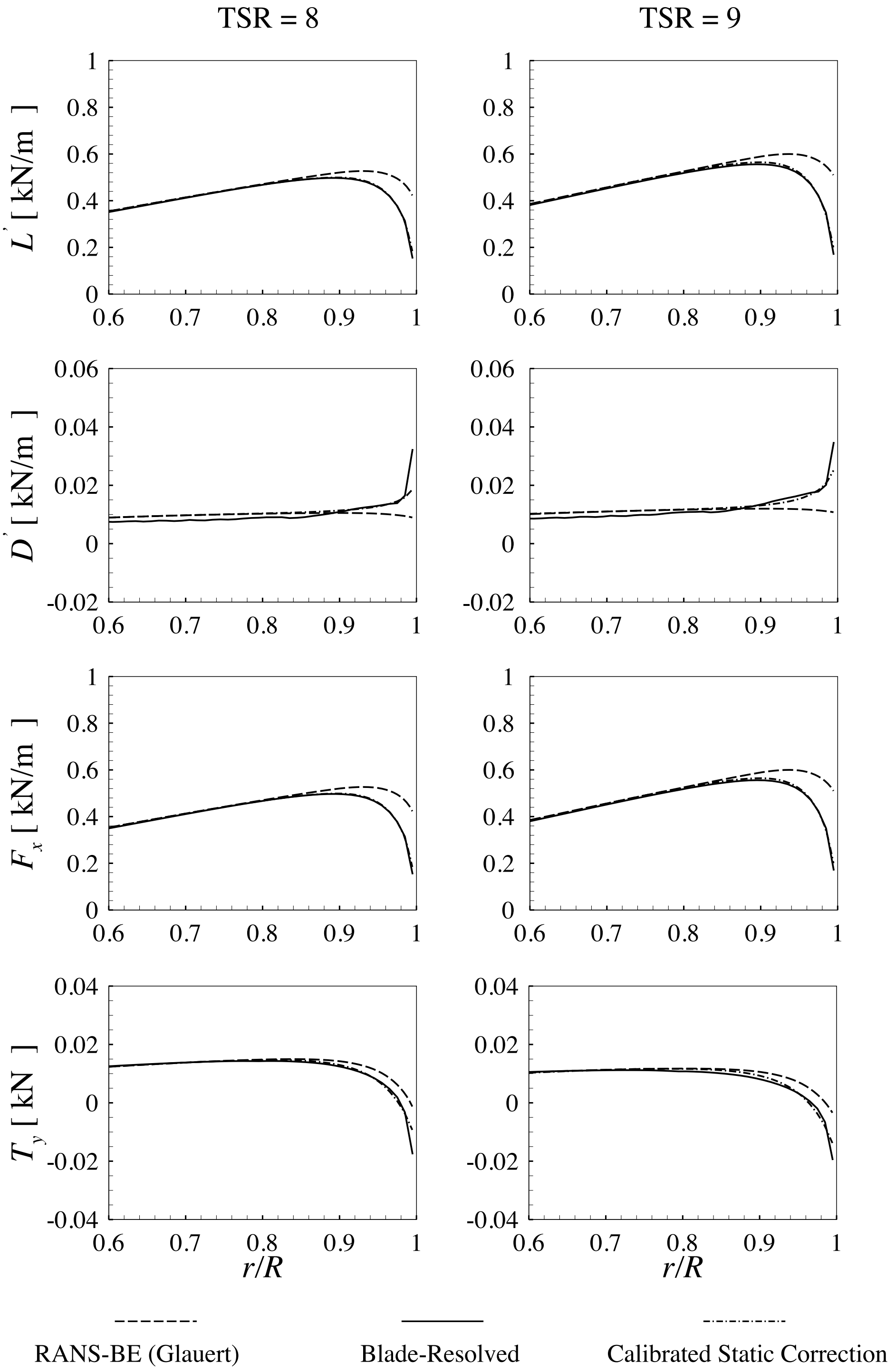

Fig. 6. 18 Distributions of bound circulation and the sectional lift, drag, thrust and torque along the blade span, for $B = 0.14$. $g_L = -1.9$ and $g_D = 0.1$ are calibrated for TSR=8, and $g_L = -2.6$ and $g_D = 0.12$ are calibrated for TSR=9.

The closure parameters calibrated for $B = 0.14$ at each tip-speed ratio are then used in the correction model for $B = 0.05$ and $B = 0.42$. The corrected thrust and torque distributions are shown in Fig. 6.19. It is noted when the rotor operates in a higher blockage ratio of 0.42, flow separation occurs on a large portion of the suction surface of the blade at $\mathrm{TSR} = 7$. This is due to that for a given tip-speed-ratio, the mass flow rate passes through the rotor plane is increased as the blockage ratio increases (Schluntz and Willden, 2015). This leads to the greater angle of attack approaching the blade sections and flow is more likely to separate. Hence, the case of $B = 0.42$ and $\mathrm{TSR} = 7$ is excluded for the present study.

The closure parameters calibrated for $B = 0.14$ give good correction results for $B = 0.05$ and $B = 0.42$, as shown in Fig. 6.19, which indicates that the closure parameters have negligible blockage dependence. Relatively large RMS errors in both thrust and torque distributions are observed for $B = 0.05$ and $\mathrm{TSR} = 9$. As discussed before, this is likely due to the unparameterized Reynolds number effects in the two-dimensional lift and drag data. In terms of the integrated power and thrust, across almost all the cases shown in Fig. 6.19, the relative errors are less than 1%, except for $B = 0.05$ and $\mathrm{TSR} = 9$, where the relative errors in the torque and thrust are 1.44% and 1.81%.

As shown in the study above, the calibrated static correction model anisotropically reduces the lift force and increases the drag force in the blade outboard sections, which enables the thrust and torque to be matched with good agreement across the outboard blade span. However, the static correction model relies on the bound circulation distribution computed from the high-fidelity blade-resolved model as an input, which limits its application. In the next section, a dynamic correction model is discussed, in which at each iteration of the RANS-BE simulation the bound calculation is computed from its own lift distribution. Since in the dynamic correction model the bound circulation is iteratively computed and thus the closure parameters may be expected to be different from those calibrated in the static correction model.

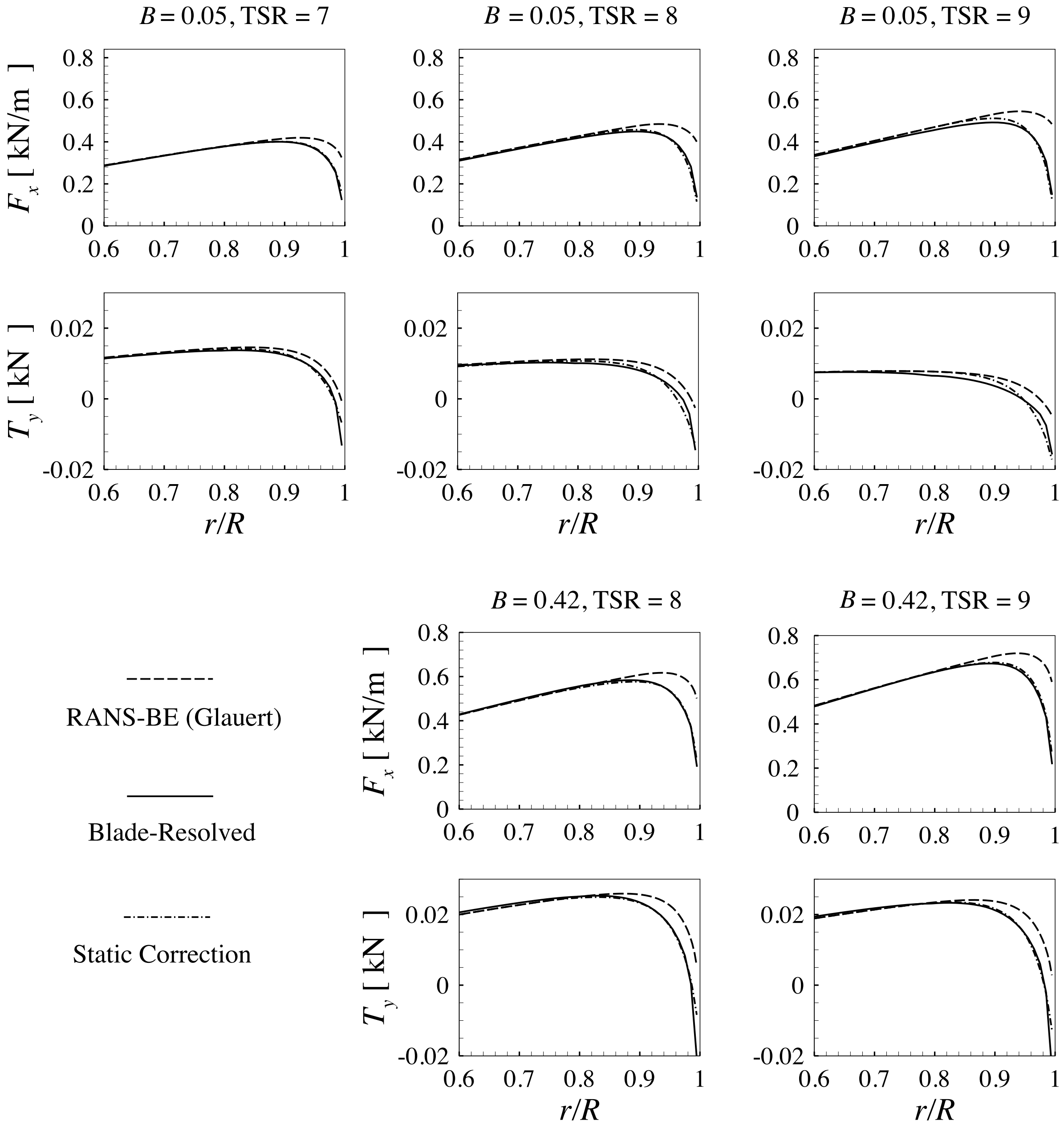

Fig. 6. 19 Distributions of bound circulation and the sectional lift, drag, thrust and torque along the blade span. The calibrated parameters for $B = 0.14$ are applied to the static correction model for $B = 0.05$ and $B = 0.42$, where $g_L = -1.5$ and $g_D = 0.06$ for $\mathrm{TSR} = 7$, $g_L = -1.9$ and $g_D = 0.1$ for $\mathrm{TSR} = 8$, and $g_L = -2.6$ and $g_D = 0.12$ for $\mathrm{TSR} = 9$.

6.5.6 Dynamic implementation into RANS-BE model

Fig. 6.19 shows the flow chart for implementing the correction model, Eq. (6.23) and Eq. (6.24), iteratively in the RANS-BE model. It is noted that the new tip correction is applied in addition to the Glauert tip correction model. At each iteration, the streamwise and swirl (tangential) velocities, u_x and u_θ, from the RANS solver are passed into the blade element code, in which the two-dimensional lift and drag coefficients are determined from the blade-relative incident velocity and the angle of attack, which is the same as discussed in Chapter 2. The new correction model is then applied to modify the two-dimensional coefficients to account for the spanwise pressure effect. In contrast to the static correction model, the bound circulation is computed from the lift and the blade-relative velocity in the RANS-BE model itself. The first-order difference method and the trapezoidal integration are used to numerically approximate the derivative and integration terms respectively when computing $F_{\Gamma,L}$ and $F_{\Gamma,D}$. As discussed before, the value of $p_{\Gamma 0}$ is set as zero at first and the computed P_Γ is shifted at which P_Γ is minimum. The correction model is only be applied in the region outboard of where $P_\Gamma = 0$. In order to avoid the sensitivity to numerical fluctuations in the blade root region, the minima at $r/R \geq 0.3$ is used to shift the P_Γ.

The closure parameters are determined by studying a grid of g_L and g_D values and finding a pair of values that minimise the sum of the normalized RMS errors in the thrust and torque for a given tip-speed-ratio, which is the same as the calibration method used in the static correction. Fig. 6.21 shows the contour of the sum of the two RMS errors as a function of g_L and g_D for $B = 0.14$ and TSR $= 7$. The RMS error is minimized to 0.23 when $g_L = -1.8$ and $g_D = 0.1$. Compared to the benchmark value of 2, the calibrated dynamic correction model improves the result by 89%.

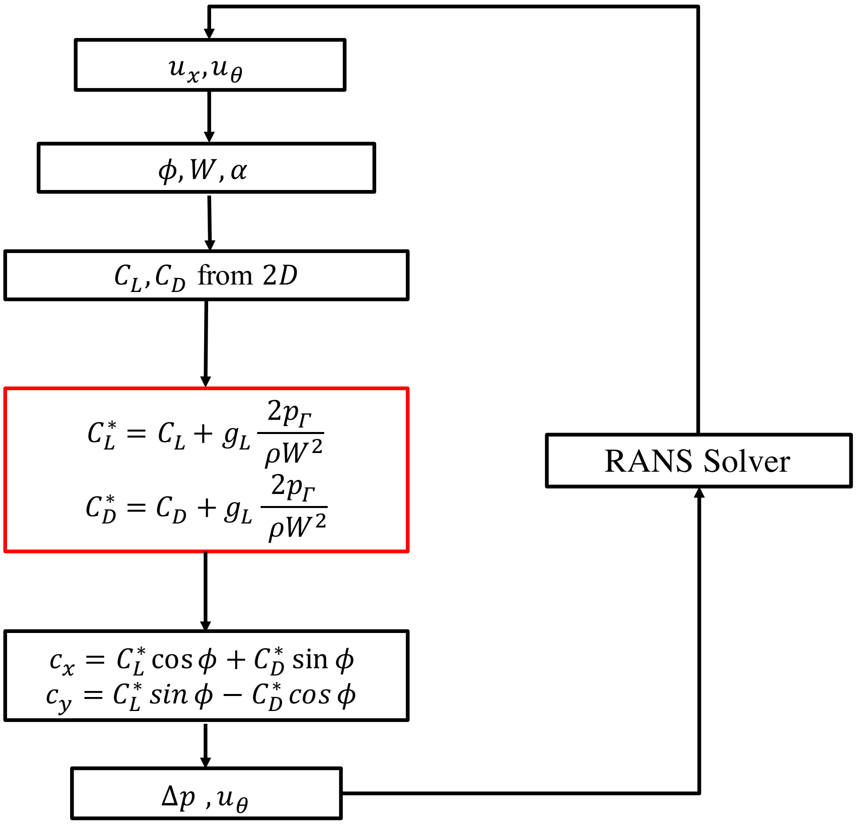

Fig. 6. 20 Flow chart of the implementation of the dynamic correction model into the RANS-BE model.

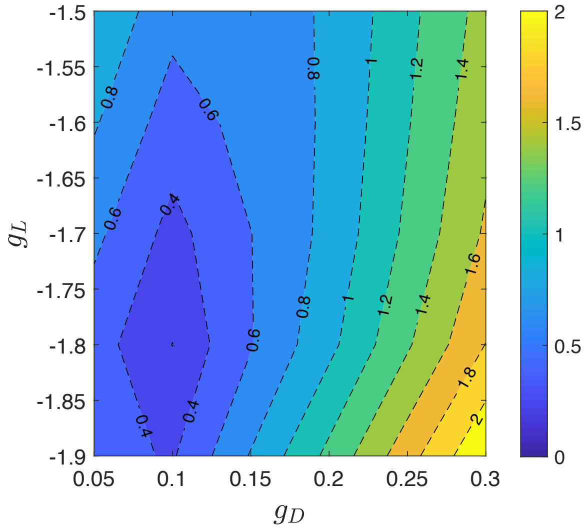

Fig. 6. 21 Contours of the sums of normalized RMS errors in the thrust and torque distributions, for the dynamic correction model, as a function of g_L and g_D, when $B = 0.14$ and $\mathrm{TSR} = 7$.

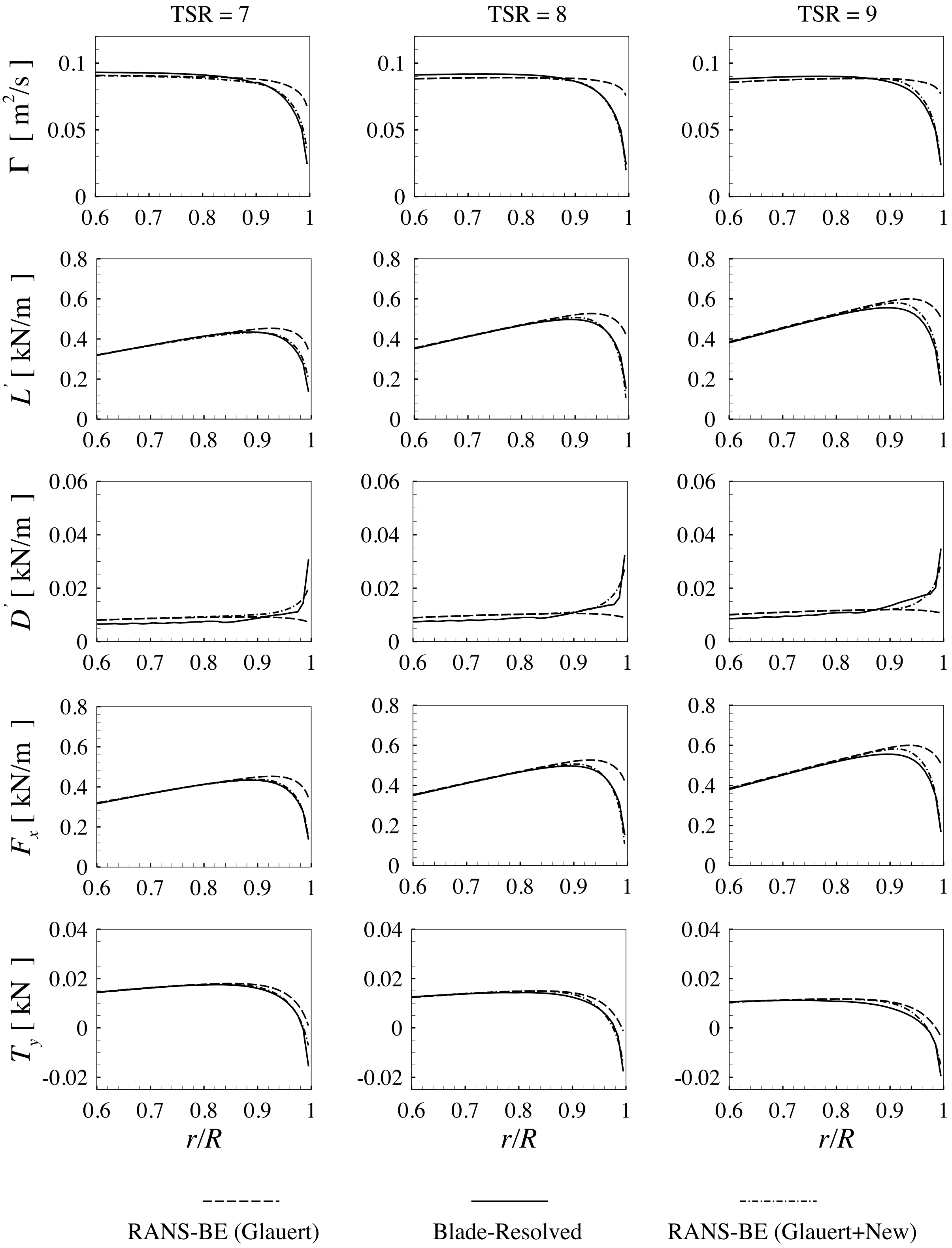

Fig. 6. 22 Distributions of bound circulation and the sectional lift, drag, thrust and torque along the blade span, for $B = 0.14$. $g_L = -1.9$ and $g_D = 0.1$ are used in the new correction model for the three tip-speed-ratios.

Following the same approach, the optimal g_L and g_D are calibrated as -1.9 and 0.1 for both $\mathrm{TSR} = 8$ and $\mathrm{TSR} = 9$ when $B = 0.14$. It is interesting to note that the closure parameters show slight dependence on the tip-speed-ratio. As shown in Fig. 6.21, $g_L = -1.9$ and $g_D = 0.1$, even they are not the optimal parameters for $\mathrm{TSR} = 7$, achieve a total RMS error of 0.36, which still improves the result by 82%. Hence, it may be reasonable to use the $g_L = -1.9$ and $g_D = 0.1$ for the dynamic correction model for all the three tip-speed-ratios.

It is noted that there is a dependence of closure parameters on the tip-speed-ratio in the static correction method, whilst this is not the case in the dynamic correction method. Inherently, the closure parameters are applied to different circulation distributions in the two methods. In static correction method, the circulation distribution is extracted from three-dimensional simulations, whilst in the dynamic correction method, the circulation distribution is derived in the RANS-BE method in an iterative way and is based on the two-dimensional lift data.

Fig. 6.22 shows the bound circulation and the sectional lift, drag, thrust and torque distributions when $g_L = -1.9$ and $g_D = 0.1$. The dynamic correction model largely reduces the bound circulation in the blade tip region and enables the corrected bound circulation to be matched with good agreement with three-dimensional cases. Similar to what is observed in the static correction model, the dynamic correction model reduces the lift and increases the drag in the blade tip region. This dynamic anisotropic approach enables the blade thrust and torque to be closely matched with the three-dimensional blade physics. In terms of the integrated power and thrust, the relative error in the integrated power is 0.72%, 1.12% and 3.66% for TSR = 7, 8 and 9 respectively, and the relative error in the integrated thrust is 0.53%, 0.97% and 1.84% for these three tip-speed-ratios respectively. For TSR=9, similar to that in the static correction model, the correction model starts to correct the lift and drag distributions at a more outboard position than where the distributions from the two- and three-dimensional models start to deviate, which results in a portion of the thrust and torque distributions (and also the bound circulation distribution) remains uncorrected. As discussed before, this might be due to the unparameterized Reynolds number effect and the different two- and three-dimensional transitional physics, which inherently cannot be corrected by the new implemented tip correction model.

Based on $g_L = -1.9$ and $g_D = 0.1$ calibrated for $B = 0.14$, these closure parameters are applied to the cases when $B = 0.05$ and 0.42, as shown in Fig. 6.22. The relative errors of the integrated power and thrust are listed in table 6.2. The maximum relative error is less than 2%. The dependence of the closure parameters on the blockage ratio is slight, at least for the three blockage ratios investigated. As shown in Fig. 6.22, for $B = 0.05$ at $\mathrm{TSR} = 8$ and 9, the thrust and torque distributions are slightly over-corrected, with the thrust and torque at $r/R > 0.95$ being smaller than those from the three-dimensional model. For $B = 0.42$, the thrust and torque distributions are slightly under-corrected. Overall, based on g_L and g_D calibrated at $B = 0.14$, the corrected thrust and torque distributions show good agreement with those from the three-dimensional model across different blockage ratios.

It is noted that in Table 6.2 the relative errors of the integrated thrust and power for $B = 0.14$, where the parameters are calibrated, is the greatest among the three blockage ratios investigated. This is because, as discussed before, the RMS error between the distributions, rather than the relative error in the integrated quantities, is used to access the accuracy of the tip correction model. This avoids the over-correction of the thrust and torque in the extreme tip regions (e.g. $r/R > 0.95$), which would offset and reduces the errors in integrated thrust and torque, thus not reflecting the true accuracy of how close the distributions are.

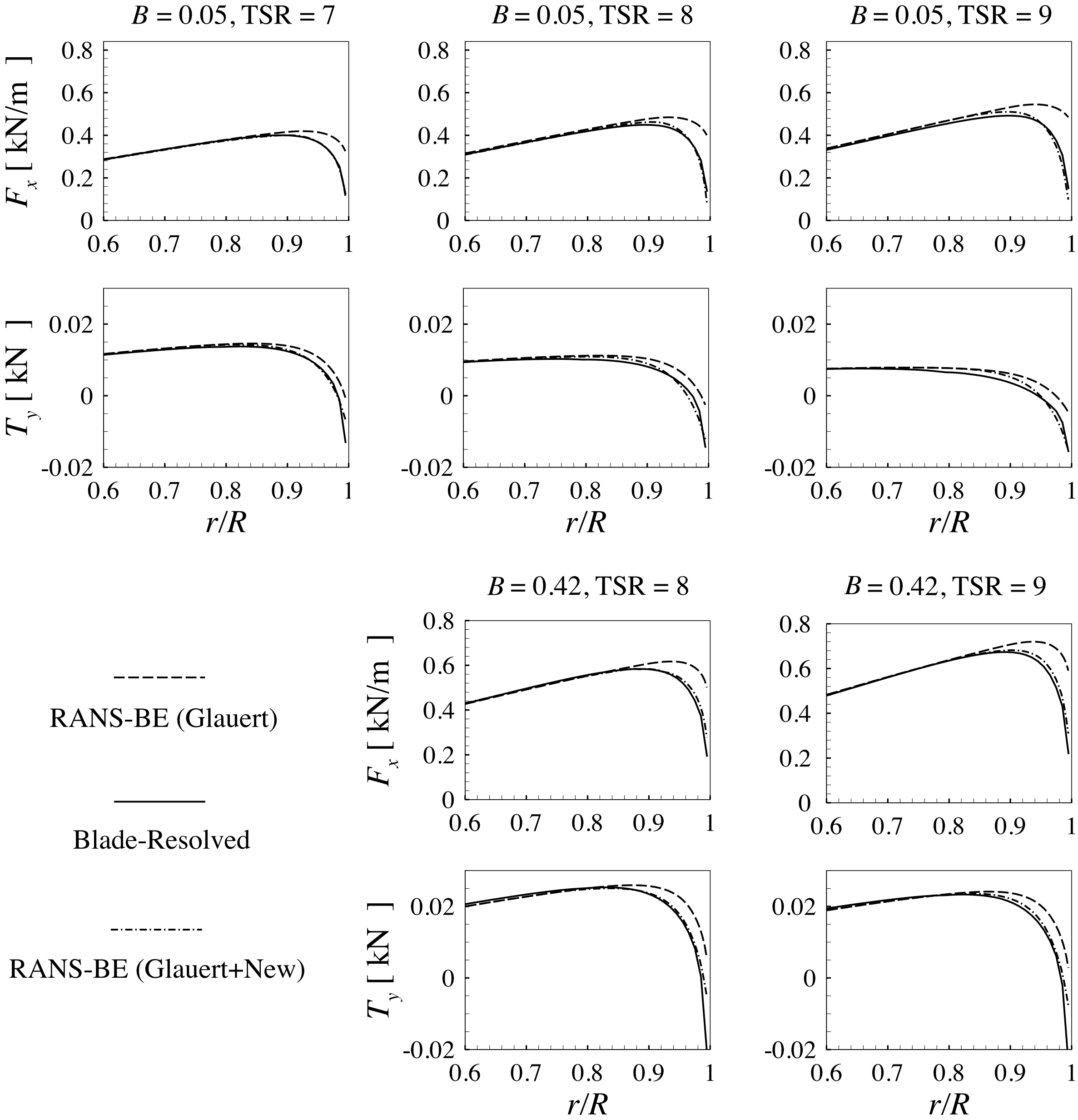

Fig. 6. 23 Spanwise distributions of the sectional thrust (F_x) and torque (T_y) along the blade span, with $g_L = -1.9$ and $g_D = 0.1$ used in the new correction model.

Table 6.2 Percentage difference (%) in the integrated power coefficient (C_P) and thrust coefficient (C_T) between the blade-resolved model and the RANS-BE model with both Glauert and the new tip correction model applied, with $g_L = -1.9$ and $g_D = 0.1$ for all the cases.

	TSR = 7	TSR = 8	TSR = 9
$B = 0.05$			
C_P	0.51	1.02	1.88
C_T	0.48	1.07	1.03
$B = 0.14$			
C_P	0.72	1.12	3.66
C_T	0.53	0.97	1.84
$B = 0.42$			
C_P	-	0.92	1.85
C_T	-	0.81	1.31

6.5.7 Limitations

The tip correction model developed in this chapter has a limited range of applicability. Firstly, the steady and inviscid assumption involved in the development of the correction model restricts its application to operational conditions where the flow is attached on the blade surfaces and the unsteady flow effects are minor. Hence, conditions where the flow separates at the trailing edge of the blade suction surface, the flow is highly sheared across the rotor plane and/or oscillating flow fluctuates across the rotor plane, are inappropriate for the current tip correction model. Secondly, the tip correction model is developed to account for the spanwise flow effects. The mismatch of lift and drag characteristics between the two- and three-dimensional model due to the Reynolds number effect, turbulence intensity and laminar-to-turbulent transitional physics cannot be corrected by the current model. Hence, a set of two-dimensional lift and drag data, which resolves the leading order effects among these, may have to be used in the RANS-BE model. In addition, the closure parameters are calibrated only for the lab-scale rotor designed in the Chapter 4. The universality of the parameters and their dependence on the rotor geometry have not been examined.

6.6 Summary

In this chapter, a series of computations for the rotor, which is numerically designed in Chapter 4, are conducted for different blockage ratios and operating tip-speed-ratios. Both the RANS-BE model and the high-fidelity blade-resolved model are investigated and compared. The effect of the blockage ratio and the tip-speed-ratio on the angle of attack approaching the blade sections are also investigated. When the flow separation on the blade surface is moderate, the thrust and torque distributions from the RANS-BE is shown to agree well with the blade-resolved model in the mid-span region of the blade. The difference in the distributions is primarily in the blade tip region. The pressure field of the two-dimensional hydrofoil section and that extracted from the three-dimensional blade are compared, which demonstrates that the three-dimensional pressure field is distorted in the blade tip region and it cannot be represented by the two-dimensional data at any angle of attack. Detailed blade surface flow analysis is then conducted to understanding the spanwise flow. The boundary layer thickness on the blade surface is identified first and the spanwise velocity on the blade surface is determined. The significantly accelerated spanwise velocity on the pressure surface and the largely reduced spanwise velocity on the suction surface are observed. The spanwise flow largely modifies the pressure field on blade tip sections, resulting in the discrepancies in thrust and torque between the two models.

To account for the three-dimensional spanwise flow effects along rotating blades, a theoretically derived tip correction model is developed. The correction formulation, based on inviscid assumption and the radial component of the governing equations, directly considers spanwise pressure gradient on the blade surface and relates it to the shedding of bound circulation. The radial flow is decomposed into two components: one that is due to rotational effects, which are assumed to be the same on both pressure and suction surfaces and hence do not contribute to blade load generation, and another that is due to the shedding of bound vortices, as a result of circulation reduction towards the blade tip. The latter induces spanwise flows on the pressure and suction surfaces moving outboard towards the blade tip and inboard towards the blade root respectively. Two closure parameters are introduced, which requires the empirical calibration.

Two tip correction models are proposed to implement the correction formulation. The static model relies on the bound circulation from the high-fidelity three-dimensional model and uses it to modify the sectional lift and drag force from the final result of the RANS-BE model. The corrected thrust and torque are then obtained by resolving the corrected lift and drag force. The dynamic model is implemented in the iteration process of the RANS-BE model and the bound circulation is iteratively computed from the RANS-BE model itself. It is noted that the both correction model is added in addition to the Glauert tip correction model. The results show that this anisotropic correction model can significantly improve the blade thrust and torque predictions on the outboard sections. The use of the new model permits anisotropic modification of the thrust and torque that result from decreasing lift and increasing drag as the blade tip is approached, in agreement with computational observations from three-dimensional blade physics. The dynamic correction model, with the calibrated parameters of $g_L = -1.9$ and $g_D = 0.1$, shows minor dependence on the investigated tip-speed-ratios and blockage ratios.

The model achieves an overall good agreement with three-dimensional blade physics across all the cases investigated. Even though the universality of the parameters for different rotor geometries have not been examined, it can be a good correction model for this rotor.

Chapter 7

Conclusions and Future Work

This chapter presents a summary of the main conclusion drawn in this thesis and a discussion of future work.

7.1 Conclusions

7.1.1 Lab rotor design and experimental performance

Truncation and thickening function methods were investigated first for thickening the trailing edge of the blade for practical and safety reasons. The truncation method not only led to a blunt trailing edge but also increased the thickness-to-chord ratio. The numerical study using RANS showed that the truncation method degraded the hydrodynamic performance. Hence, the thickening function method was preferred in blunting the trailing edge of the blade. The numerical study also showed that at the lab-scale blade Reynolds number of 2×10^5, the laminar-to-turbulent boundary layer transition occurred, which could significantly affect the drag force. The different level of turbulent intensities could result in different transition physics. For the FX-84-W-140 hydrofoil studied, at a very low turbulence intensity of 0.1%, a transitional separation bubble occurred on the suction surface of the hydrofoil causing relatively large pressure drag; at a moderate turbulence intensity of 1.5%, the higher turbulence level mitigated the separation bubble but caused higher skin-friction drag with a overall reduction in the drag coefficient. At a turbulence intensity of 5.5% the skin-friction effect dominated, and the overall drag coefficient increased.

An in-house blade-element theory embedded RANS solver was used to design rotors for multi-rotor array operations, exploiting constructive interference effects to maximize the hydrodynamic power efficiency. Two design cases were considered: the first considered a rotor in a side-by-side two-rotor array; the second considered two in-situ rotors in a four-rotor array. Differences in average array power of the two design approaches were within 1%. High fidelity blade-resolved computations were conducted to evaluate the rotor design. Radial loading distributions from the RANS-BE model showed good agreement in the blade mid-span region with those from the blade-resolved model. Discrepancies were observed in the blade root and tip regions, primarily due to three-dimensional flow effects that are not resolved in the RANS-BE model.

Two rotors were fabricated and tested experimentally in a two-rotor fence configuration at FloWave at the University of Edinburgh. The rotor array achieved superior power efficiency in the experimental study. Experimental results showed that the average power coefficient of the twin-rotor fence increases by 26% around the design point compared to that of the single rotor. Blade-resolved computations were conducted and shown to reproduce the experimental results well. Across most of the operational tip-speed-ratios, the relative error of the power and thrust coefficients between the numerical and experimental results were less than 5%. Mapping of the flow velocities around the turbine also showed reasonable agreement with the experimental result.

7.1.2 Spanwise Flow effect and tip correction

The comparison between the reduced order RANS-BE model and the high-fidelity blade resolved model showed a large discrepancy of blade load distribution in the blade tip region. A new tip correction formulation for use with blade-element models was developed based on radial momentum conservation and vortex theory and was used to correct for the pressure effects resulting from spanwise flows along the blade.

The radial flow was decomposed into two components: one that was due to rotational effects, which were assumed to be the same on both pressure and suction surfaces and hence did not contribute to blade load generation, and another that was due to the shedding of bound circulation, as a result of circulation reduction towards the blade tip. The latter induced spanwise flows on the pressure and suction surfaces moving outboard towards the blade tip and inboard towards the blade root respectively. The model related the velocity induced by shedding of bound circulation to the radial pressure gradient along the blade. The analytical formulation, closed with appropriately calibrated empirical coefficients, is used to anisotropically modify the lift and drag forces on blade sections within the framework of the Blade Element Momentum model.

With the new correction model applied, in addition to the Glauert tip correction to account for finite blade number, the new model was found to significantly improve the prediction of the thrust and torque on outboard sections where spanwise flow effects were significant. For $B = 0.14$, with two empirical coefficients calibrated as: $g_L = -1.9$ and $g_D = 0.1$, the appropriate formulation of the model reduced the relative errors of the integrated thrust and power to less than 4% for the tip-speed-ratios investigated. The empirical coefficients calibrated for $B = 0.14$ were then applied to cases with $B = 0.05$ and $B = 0.42$. Slight over-corrections were observed for both thrust and torque distributions in the lower blockage ratio of 0.05 while under-corrections were observed for those in the higher blockage ratio of 0.42. However, the dependence of the empirical coefficients on the blockage ratio was slight.

7.2 Future Work

The unsteady flow physics around the blades have not been studied due to the high computational cost required by the unsteady simulations. Although the steady simulation with the multiple reference frame technique showed a good approximation to the experimental conditions, the real tidal environments are extremely harsh with waves and turbulence producing large unsteady loads on turbines. By leveraging some super-computing facilities with more CPU cores available, the unsteady simulation with mesh-rotation technique can be used to analyse unsteady flow physics and to understand how unsteady flows, waves and turbulence develop unsteady rotor loading, and how this loading can be incorporated in engineering design tools.

RANS model was used throughout the study to maintain a reasonable level of computational cost. However, RANS model may not be sufficient at studying far wake properties and unsteady effects. Unsteady large eddy simulations may be exploited to explore the unsteady flow physics given the increasing computational power everyday.

The tip correction model in this thesis was calibrated specifically for the lab-scale rotor designed in this thesis. In order to study and parametrise the dependency of the closure parameters on blade shape and scale, more rotors need to be analysed, as the current dataset is very limited. Ideally, the rotors are of a variety of scale and blade geometries. Some possible candidates can be the rotor studied in the Model Experiments in Controlled Conditions (MEXICO) experiments and National Renewable Energy Laboratory (NREL) rotors, which have been widely studied both experimentally and numerically. Both reduced order RANS-BE and blade-resolved simulations can be conducted for these rotors in different blockage ratios and in different tip-speed-ratios around their design conditions. The similar procedure can be carried out to optimize the two closure parameters and hence the dependency can be understood.

Reference

Abbott, I. H., & Von Doenhoff, A.E. (1959). *Theory of wing sections, including a summary of airfoil data*. Courier Corporation.

Abolghasemi, M. A., Piggott, M. D., Spinneken, J., Viré, A., Cotter, C. J., & Crammond, S. (2016). Simulating tidal turbines with multi-scale mesh optimisation techniques. *Journal of Fluids and Structures*, **66**, 69-90.

Adcock, T. A., Draper, S., Houlsby, G. T., Borthwick, A. G., & Serhadlıoğlu, S. (2013). The available power from tidal stream turbines in the Pentland Firth. *Proceedings of the Royal Society A: Mathematical, Physical and Engineering Sciences*, **469(2157)**, 20130072.

Afgan, I., McNaughton, J., Rolfo, S., Apsley, D. D., Stallard, T., & Stansby, P. (2013). Turbulent flow and loading on a tidal stream turbine by LES and RANS. *International Journal of Heat and Fluid Flow*, **43**, 96-108.

Allsop, S., Peyrard, C., Thies, P. R., Boulougouris, E., & Harrison, G. P. (2017). Hydrodynamic analysis of a ducted, open centre tidal stream turbine using blade element momentum theory. *Ocean Engineering*, **141**, 531-542.

Althaus, D. (1996). *Niedriggeschwindigkeitsprofile: Profilentwicklungen und Polarenmes sungen im Laminarwindkanal des Instituts für Aerodynamik und Gasdynamik der Universität Stuttgart; mit Diagrammen und einer 3, 5"-Diskette für IBM-PC und k -ompatible Rechner*. vieweg.

Ansys Inc. (2013). ANSYS FLUENT theory guide. *Canonsburg, PA, Release 15.0*.

Ahmed, M.R. (2012). Blade sections for wind turbine and tidal current turbine applications - current status and future challenges. *International Journal of Energy Research*, **36(7)**, 829-824.

Ahmed, U., Apsley, D. D., Afgan, I., Stallard, T., & Stansby, P. K. (2017). Fluctuating loads on a tidal turbine due to velocity shear and turbulence: Comparison of CFD with field data. *Renewable Energy*, **112**, 235-246.

ASME PTC Committee. (2009). Standard for Verification and Validation in Computational Fluid Dynamics and Heat Transfer: ASME V&V 20. *The American Society of Mechanical Engineers (ASME).*

Baba-Ahmadi, M. H., & Dong, P. (2017). Validation of the actuator line method for simulating flow through a horizontal axis tidal stream turbine by comparison with measurements. *Renewable Energy*, **113**, 420-427.

Bahaj, A. S., Molland, A. F., Chaplin, J. R., & Batten, W. M. J. (2007). Power and thrust measurements of marine current turbines under various hydrodynamic flow conditions in a cavitation tunnel and a towing tank. *Renewable energy*, **32(3)**, 407-426.

Bai, L., Spence, R. R., & Dudziak, G. (2009, September). Investigation of the influence of array arrangement and spacing on tidal energy converter (TEC) performance using a 3-dimensional CFD model. In *Proceedings of the 8th European wave and tidal energy conference, Uppsala, Sweden* (pp. 654-660).

Bak, C., Zahle, F., Bitsche, R., Kim, T., Yde, A., Henriksen, L. C., ... & Natarajan, A. (2013). The DTU 10-MW reference wind turbine. In *Danish Wind Power Research 2013*.

Bangga, G., Lutz, T., Jost, E., & Krämer, E. (2017). CFD studies on rotational augmentation at the inboard sections of a 10 MW wind turbine rotor. *Journal of Renewable and Sustainable Energy*, 9(2), 023304.

Baratchi, F., Jeans, T. L., & Gerber, A. G. (2017). Actuator line simulation of a tidal turbine in straight and yawed flows. *International journal of marine energy*, **19**, 235-255.

Batten, W. M., Harrison, M. E., & Bahaj, A. S. (2013). Accuracy of the actuator disc-RANS approach for predicting the performance and wake of tidal turbines. *Philosophical Transactions of the Royal Society A: Mathematical, Physical and Engineering Sciences*, **371(1985)**, 20120293.

Belloni, C.S. (2011). Flow field and performance analysis of bidirectional and open-centre ducted tidal turbines. In *Proceedings of the 9th European Wave and Tidal Energy Conference*.

Belloni, C.S. (2013). *Hydrodynamics of ducted and open-centre tidal turbines*. Doctoral dissertation, University of Oxford, UK.

Belloni, C. S. K., Willden, R. H. J., & Houlsby, G. T. (2017). An investigation of ducted and open-centre tidal turbines employing CFD-embedded BEM. *Renewable Energy*, **108**, 622-634.

Bertagnolio, F., N. Sørensen, J. Johansen, & P. Fuglsang (2001). Wind turbine airfoil catalogue. Technical Report Risø-R-1280(EN), Risø National Laboratory, Roskilde, Denmark.

Blackmore, T., Myers, L. E., & Bahaj, A. S. (2016). Effects of turbulence on tidal turbines: Implications to performance, blade loads, and condition monitoring. *International Journal of Marine Energy*, **14**, 1-26.

Bonar, P. A. J., Chen, L., Schnabl, A. M., Venugopal, V., Borthwick, A. G. L., & Adcock, T. A. A. (2019). On the arrangement of tidal turbines in rough and oscillatory channel flow. *Journal of Fluid Mechanics*, **865**, 790-810.

Bryden, I. G., Naik, S., Fraenkel, P., & Bullen, C. R. (1998). Matching tidal current plants to local flow conditions. *Energy*, **23(9)**, 699-709.

Bryden, I., & Melville, G. T. (2004). Choosing and evaluating sites for tidal current development. *Proceedings of the Institution of Mechanical Engineers, Part A: Journal of Power and Energy*, **218(8)**, 567-577.

Burton, T., Sharpe, D., & Jenkins, N. (2001). *Wind Energy Handbook*. John Wiley & Sons.

Cao, B., Willden, R. H. J., & Vogel, C. R. (2018, October). Effects of blockage and freestream turbulence intensity on tidal rotor design and performance. In *Proceedings of the 3rd International Conference on Renewable Energies (RENEW), Lisbon* (pp. 127-136).

Chen, X., & Agarwal, R. (2012). Optimization of flatback airfoils for wind-turbine blades using a genetic algorithm. *Journal of aircraft*, **49(2)**, 622-629.

Chen, Y., Lin, B., Lin, J., & Wang, S. (2017). Experimental study of wake structure behind a horizontal axis tidal stream turbine. *Applied energy*, **196**, 82-96.

Chamorro, L. P., Hill, C., Morton, S., Ellis, C., Arndt, R. E. A., & Sotiropoulos, F. (2013). On the interaction between a turbulent open channel flow and an axial-flow turbine. *Journal of Fluid Mechanics*, **716**, 658-670.

Churchfield, M. J., Li, Y., & Moriarty, P. J. (2013). A large-eddy simulation study of wake propagation and power production in an array of tidal-current turbines. *Philosophical Transactions of the Royal Society A: Mathematical, Physical and Engineering Sciences*, **371(1985)**, 20120421.

Coles, D. S., Blunden, L. S., & Bahaj, A. S. (2016). Experimental validation of the distributed drag method for simulating large marine current turbine arrays using porous fences. *International journal of marine energy*, **16**, 298-316.

Coles, D. S., Blunden, L. S., & Bahaj, A. S. (2017). Assessment of the energy extraction potential at tidal sites around the Channel Islands. *Energy*, **124**, 171-186.

Cooke, S., Willden, R. H. J., Byrne, B. W. & Stallard, T. (2014). An experimental investigation of blockage in a short fence array of tidal turbines, in '*Proceedings of the 1st International Conference on Renewable Energies Offshore (RENEW)*', Lisbon, Portugal.

Cooke, S. (2016). *Enhanced array design for tidal power generation* (Doctoral dissertation, University of Oxford).

Consul, C.A., Willden, R.H.J, & McIntosh, S. C. (2013). Blockage effects on the hydrodynamic performance of a marine cross-flow turbine. *Phil. Trans. R. Soc. A*, **371(1985)**, 20120299.

Culley, D. M., Funke, S. W., Kramer, S. C., & Piggott, M. D. (2016). Integration of cost modelling within the micro-siting design optimisation of tidal turbine arrays. *Renewable Energy*, **85**, 215-227.

Demekhin, E. A., Kalaidin, E. N., Kalliadasis, S., & Vlaskin, S. Y. (2007). Three-dimensional localized coherent structures of surface turbulence. I. Scenarios of two-dimensional–three-dimensional transition. *Physics of fluids*, **19(11)**, 114103.

Divett, T., Vennell, R., & Stevens, C. (2013). Optimization of multiple turbine arrays in a channel with tidally reversing flow by numerical modelling with adaptive mesh. *Philosophical Transactions of the Royal Society A: Mathematical, Physical and Engineering Sciences*, **371(1985)**, 20120251.

Draper, S. (2011). *Tidal Stream Energy Extraction in Coastal Basins*. PhD thesis, University of Oxford.

Drela, M. (1989). XFOIL: An analysis and design system for low Reynolds number airfoils. In *Low Reynolds number aerodynamics* (pp. 1-12). Springer, Berlin, Heidelberg.

Edmunds, M., Williams, A. J., Masters, I., & Croft, T. N. (2017). An enhanced disk averaged CFD model for the simulation of horizontal axis tidal turbines. *Renewable energy*, **101**, 67-81.

EEL Energy. (2017). EEL ENERGY, There is no planet B. Retrieved June 27, 2017, from http://www.eel-energy.fr/en/video/.

Farrell, P.E., & Maddison, J.R. (2011). Conservative interpolation between volume meshes by local Galerkin projection. *Computer Methods in Applied Mechanics and Engineering*, **200(1)**, 89-100.

Fernandez-Rodriguez, E., Stallard, T. J., & Stansby, P. K. (2014). Experimental study of extreme thrust on a tidal stream rotor due to turbulent flow and with opposing waves. *Journal of Fluids and Structures*, **51**, 354-361.

Fleming, C. F. (2011). Design and analysis of a bi-directional ducted tidal turbine. In *Proceedings of the 9th European Wave and Tidal Energy Conference, 2011*.

Fleming, C. F., & Willden, R. H. (2016). Analysis of bi-directional ducted tidal turbine performance. *International Journal of Marine Energy*, **16**, 162-173.

Flumill. (2012, October 31). Testing of full scale facility. Retrieved June 27, 2017, from http://www.flumill.com/News%20archive/Testing_of_full_scale_facility/news-11.html.

Frost, C., Morris, C. E., Mason-Jones, A., O'Doherty, D. M., & O'Doherty, T. (2015). The effect of tidal flow directionality on tidal turbine performance characteristics. *Renewable Energy*, **78**, 609-620.

Funke, S. W., Farrell, P. E., & Piggott, M. D. (2014). Tidal turbine array optimisation using the adjoint approach. *Renewable Energy*, **63**, 658-673.

Fuglsang, P., & Bak, C. (2004). Development of the Risø wind turbine airfoils. *Wind Energy*, **7(2)**, 145-162.

Gant, S. & T. Stallard (2008, July). Modelling a tidal turbine in unsteady flow. In *International Offshore and Polar Engineering Conference, Vancouver*, Canada, pp. 473–479.

Garrett, C., & Cummins, P. (2005). The power potential of tidal currents in channels. *Proceedings of the royal society A: mathematical, physical and engineering sciences*, **461(2060)**, 2563-2572.

Garrett, C., & Cummins, P. (2007). The efficiency of a turbine in a tidal channel. *Journal of fluid mechanics*, ***588***, 243-251.

Gebreslassie, M. G., Tabor, G. R., & Belmont, M. R. (2015). Investigation of the performance of a staggered configuration of tidal turbines using CFD. *Renewable Energy*, **80**, 690-698.

Glauert, H. (1935). Airplane propellers. In *Aerodynamic theory* (pp. 169-360). Springer, Berlin, Heidelberg.

Herrig, J., J. Emery, & J. Erwin (1951). *Effect of section thickness and trailing edge radius on the performance of NACA 65-series compressor blades in cascade at low speeds*. Technical Report RM L51 J16, NASA.

Houlsby GT, Draper S, Oldfield M (2008). Application of linear momentum actuator disc theory to open channel flow. *Technical report no. 2296-08*, *University of Oxford*, Oxford, UK.

Hunter, W., Nishino, T., & Willden, R.H.J (2015). Investigation of tidal turbine array tuning using 3D Reynolds-averaged Navier–Stokes simulations. *International Journal of Marine Energy*, **10**, 39-51.

Jacobs, C. T., Piggott, M. D., Kramer, S. C., & Funke, S. W. (2016). On the validity of tidal turbine array configurations obtained from steady-state adjoint optimisation. *arXiv preprint arXiv:1601.08091*.

Karsten, R. H., McMillan, J. M., Lickley, M. J., & Haynes, R. D. (2008). Assessment of tidal current energy in the Minas Passage, Bay of Fundy. *Proceedings of the Institution of Mechanical Engineers, Part A: Journal of Power and Energy*, **222(5)**, 493-507.

Knudsen, T., Filsoof, O. T., Hovgaard, T. G., Grunnet, J. D., Neto, J. X. V., & Wisniewski, R. (2018, August). Multi-rotor wind turbine control challenge-A benchmark for advanced control development. In *2018 IEEE Conference on Control Technology and Applications (CCTA)* (pp. 1615-1622). IEEE.

Langtry, R. B. (2006). *A correlation-based transition model using local variables for unstructured parallelized CFD codes*. PhD Thesis, Stuttgart, Germany.

Launder, B. E., & Spalding, D. B. (1974). The numerical computation of turbulent flows. *Computer Methods in Applied Mechanics and Engineering*, *3*(2), 269-289.

Lavaroni, L., Watson, S. J., Cook, M. J., & Dubal, M. R. (2014). A comparison of actuator disc and BEM models in CFD simulations for the prediction of offshore wake losses. In *Journal of Physics: Conference Series* (Vol. 524, No. 1, p. 012148). IOP Publishing.

Malki, R., Masters, I., Williams, A. J., & Croft, T. N. (2014). Planning tidal stream turbine array layouts using a coupled blade element momentum–computational fluid dynamics model. *Renewable Energy*, 63, 46-54.

Marine Current Turbines Ltd. (2013). SeaGen-S. Retrieved June 22, 2017, from http://www.marineturbines.com/SeaGen-Products/SeaGen-S.

Masters, I., Malki, R., Williams, A. J., & Croft, T. N. (2013). The influence of flow acceleration on tidal stream turbine wake dynamics: A numerical study using a coupled BEM–CFD model. *Applied Mathematical Modelling*, **37(16-17)**, 7905-7918.

McAdam, R. A., Houlsby, G. T., & Oldfield, M. L. G. (2013a). Experimental measurements of the hydrodynamic performance and structural loading of the Transverse Horizontal Axis Water Turbine: Part 1. *Renewable energy*, **59,** 105-114.

McAdam, R. A., Houlsby, G. T., & Oldfield, M. L. G. (2013b). Experimental measurements of the hydrodynamic performance and structural loading of the transverse horizontal axis water turbine: Part 2. *Renewable energy*, **59**, 141-149.

McIntosh, S. C., Fleming, C. F., & Willden, R. H. (2011). Embedded RANS-BEM tidal turbine design. In *Proceedings of the 9th European wave and tidal energy conference, Southampton*.

McNaughton, J. (2013). *Turbulence Modelling in the near-field of an axial flow tidal turbine using Code Saturne*. Ph. D. thesis, University of Manchester.

McNaughton, J., Cao, B., Vogel, C. R., & Willden, R. H. J (2019). Model scale testing of multi-rotor arrays designed to exploit constructive interference effects. In *Proceedings of the 13th European Wave and Tidal Energy Conference (EWTEC), Naples*.

McNaughton, J., Cao, B., Nambiar, A., Davey, T., Vogel, C.R., & Willden, R.H.J (2020). Constructive interference effects for tidal turbine arrays. *Journal of Fluid Mechanics(submitted)*.

Micallef, D., Ferreira, C. S., Sant, T., & Bussel, G. V. (2016). Experimental and numerical investigation of tip vortex generation and evolution on horizontal axis wind turbines. *Wind Energy*, **19(8)**, 1485-1501.

Milne, I. A., Day, A. H., Sharma, R. N., & Flay, R. G. J. (2015). Blade loading on tidal turbines for uniform unsteady flow. *Renewable Energy*, **77**, 338-350.

Molland, A. F., Bahaj, A. S., Chaplin, J. R., & Batten, W. M. J. (2004). Measurements and predictions of forces, pressures and cavitation on 2-D sections suitable for marine current turbines. *Proceedings of the Institution of Mechanical Engineers, Part M: Journal of Engineering for the Maritime Environment*, **218(2)**, 127-138.

Muchala, S., & Willden, R. H. (2018). Influence of support structures on tidal turbine power output. *Journal of Fluids and Structures*, **83**, 27-39.

Mycek, P., Gaurier, B., Germain, G., Pinon, G., & Rivoalen, E. (2014a). Experimental study of the turbulence intensity effects on marine current turbines behaviour. Part I: One single turbine. *Renewable Energy*, **66**, 729-746.

Mycek, P., Gaurier, B., Germain, G., Pinon, G., & Rivoalen, E. (2014b). Experimental study of the turbulence intensity effects on marine current turbines behaviour. Part II: Two interacting turbines. *Renewable Energy*, **68**, 876-892.

Myers, L. E., & Bahaj, A. S. (2012). An experimental investigation simulating flow effects in first generation marine current energy converter arrays. *Renewable Energy*, **37(1)**, 28-36.

Nishino, T., & Willden, R.H.J. (2012a). Effects of 3-D channel blockage and turbulent wake mixing on the limit of power extraction by tidal turbines. *International Journal of Heat and Fluid Flow*, **37**, 123-135.

Nishino, T., & Willden, R.H.J. (2012b). The efficiency of an array of tidal turbines partially blocking a wide channel. *Journal of Fluid Mechanics*, **708**, 596-606.

Nishino, T. & Willden, R. H. J. (2013), 'Two-scale dynamics of flow past a partial cross-stream array of tidal turbines', *Journal of Fluid Mechanics,* **730**, 220–244.

Nuernberg, M., & Tao, L. (2018a). Experimental study of wake characteristics in tidal turbine arrays. *Renewable energy*, **127**, 168-181.

Nuernberg, M., & Tao, L. (2018b). Three dimensional tidal turbine array simulations using OpenFOAM with dynamic mesh. *Ocean Engineering*, **147**, 629-646.

Olczak, A., Stallard, T., Feng, T., & Stansby, P. K. (2016). Comparison of a RANS blade element model for tidal turbine arrays with laboratory scale measurements of wake velocity and rotor thrust. *Journal of Fluids and Structures*, **64**, 87-106.

OpenHydro Group Ltd. (2017, April 05). Commissioning the first cape sharp tidal turbine. Retrieved Jun 22, 2017, from http://capesharptidal.com/commissioning/.

Orbital Marine Power Ltd. (2019). Can Orbital become part of a new wave of super-major energy players?. Retrieved Dec 21, 2020, from: https://www.crowdcube.com/explore/blog/investing/can-orbital-become-part-of-a-new-wave-of-super-major-energy-players

Otto, W., D. Rijpkema, & G. Vaz (2012). Viscous–flow calculations on an axial marine current turbine. In *Proceedings of the ASME 2012 31st International Conference on Ocean, Offshore and Artic Engineering, OMAE 2012*, Rio de Janeiro, Brazil.

Ouro, P., Harrold, M., Stoesser, T., & Bromley, P. (2017). Hydrodynamic loadings on a horizontal axis tidal turbine prototype. *Journal of Fluids and Structures*, **71**, 78-95.

Ouro, P., Harrold, M., Ramirez, L., & Stoesser, T. (2019). Prediction of the wake behind a horizontal axis tidal turbine using a LES-ALM. In *Recent Advances in CFD for Wind and Tidal Offshore Turbines* (pp. 25-35). Springer, Cham.

Patankar, S. V. (1980). *Numerical Heat Transfer and Fluid Flow*. Washington DC (USA): Hemisphere Publishing Corporation.

Payne, G. S., Stallard, T., & Martinez, R. (2017). Design and manufacture of a bed supported tidal turbine model for blade and shaft load measurement in turbulent flow and waves. *Renewable energy*, **107**, 312-326.

Payne, G. S., Stallard, T., Martinez, R., & Bruce, T. (2018). Variation of loads on a three-bladed horizontal axis tidal turbine with frequency and blade position. *Journal of Fluids and Structures*, **83**, 156-170.

Roache, P. J. (2009). Fundamentals of verification and validation. hermosa publ..

Pope, S.B. (2001). *Turbulent Flows*. The Edinburgh Building, Cambridge, UK: Cambridge University Press.

Pugh, D. T. (1996). *Tides, surges and mean sea-level (reprinted with corrections)*. John Wiley & Sons Ltd.

Sale, D., Jonkman, J., & Musial, W. (2009). *Hydrodynamic optimization method and design code for stall-regulated hydrokinetic turbine rotors* (No. NREL/CP-500-45021). National Renewable Energy Lab.(NREL), Golden, CO (United States).

Schluntz, J. O. (2014). *Tidal turbine array modelling* (Doctoral dissertation, University of Oxford).

Schluntz, J., & Willden, R.H.J. (2015). The effect of blockage on tidal turbine rotor design and performance. *Renewable Energy*, **81**, 432-441.

Schmitz, S., & Maniaci, D. C. (2017). Methodology to determine a tip-loss factor for highly loaded wind turbines. *AIAA Journal*, ***55*(2)**, 341-351.

Selig, M. S., & McGranahan, B. D. (2004). Wind tunnel aerodynamic tests of six airfoils for use on small wind turbines. *J. Sol. Energy Eng.*, **126(4)**, 986-1001.

Serhadlioglu, S. (2014). *Tidal stream resource assessment of the Anglesey Skerries and the Bristol Channel* (Doctoral dissertation, Oxford University, UK).

Shen, W. Z., Mikkelsen, R., Sørensen, J. N., & Bak, C. (2005). Tip loss corrections for wind turbine computations. *Wind Energy: An International Journal for Progress and Applications in Wind Power Conversion Technology*, **8(4)**, 457-475.

SIMEC Atlantis Energy. (2017). AR1500 tidal turbine. Retrieved June 23, 2020, from: https://simecatlantis.com/services/turbines/.

Sorensen, J. N., & Shen, W. Z. (2002). Numerical modeling of wind turbine wakes. *J. Fluids Eng.*, **124(2)**, 393-399.

Stallard, T., Collings, R., Feng, T., & Whelan, J. (2013). Interactions between tidal turbine wakes: experimental study of a group of three-bladed rotors. *Philosophical Transactions of the Royal Society A: Mathematical, Physical and Engineering Sciences*, ***371*(1985)**, 20120159.

Stallard, T., Feng, T., & Stansby, P. K. (2015). Experimental study of the mean wake of a tidal stream rotor in a shallow turbulent flow. *Journal of Fluids and Structures*, **54**, 235-246.

Standish, K. J., & Van Dam, C. P. (2003). Aerodynamic analysis of blunt trailing edge airfoils. *Journal of Solar Energy Engineering*, ***125*(4)**, 479-487.

Stansby, P. K. (2006). Limitations of depth-averaged modeling for shallow wakes. *Journal of Hydraulic Engineering*, **132(7)**, 737-740.

Sufian, S. F., Li, M., & O'Connor, B. A. (2017). 3D modelling of impacts from waves on tidal turbine wake characteristics and energy output. *Renewable energy*, **114**, 308-322.

Sutherland, G., Foreman, M., & Garrett, C. (2007). Tidal current energy assessment for Johnstone strait, Vancouver island. *Proceedings of the Institution of Mechanical Engineers, Part A: Journal of Power and Energy*, **221(2)**, 147-157.

Sutherland, D. R., Noble, D. R., Steynor, J., Davey, T., & Bruce, T. (2017). Characterisation of current and turbulence in the FloWave Ocean Energy Research Facility. *Ocean Engineering*, **139**, 103-115.

Sweby, P. K. (1984), 'High resolution schemes using flux limiters for hyperbolic con- servation laws', SIAM Journal on Numerical Analysis 21, 995–1011.

Tatum, S. C., Frost, C. H., Allmark, M., O'doherty, D. M., Mason-Jones, A., Prickett, P. W., ... & O'Doherty, T. (2016). Wave–current interaction effects on tidal stream turbine performance and loading characteristics. *International Journal of Marine Energy*, **14**, 161-179.

Tomko, E. (2016). *Development of Electricity Generation and Sensor Systems for a Hydropower Propagating Wave Turbine* (Doctoral dissertation, Worcester Polytechnic Institute).

Turnock, S. R., Phillips, A. B., Banks, J., & Nicholls-Lee, R. (2011). Modelling tidal current turbine wakes using a coupled RANS-BEMT approach as a tool for analysing power capture of arrays of turbines. *Ocean Engineering*, **38(11-12)**, 1300-1307.

Vogel, C. R., & Willden, R. H. J. (2017). Multi-rotor tidal stream turbine fence performance and operation. *International journal of marine energy*, **19**, 198-206.

Vogel, C. R., & Willden, R. H. J. (2018). Designing multi-rotor tidal turbine fences. *International Marine Energy Journal*, **1**, 61-70.

Vogel, C. R., Willden, R. H. J., & Houlsby, G. T. (2018). Blade element momentum theory for a tidal turbine. *Ocean Engineering*, **169**, 215-226.

Vortex Hydro Power (2017). Technology - How it Works. Retrieved June 27, 2017, from http://www.vortexhydroenergy.com/Technology/Works.html.

Walters, R. A., Tarbotton, M. R., & Hiles, C. E. (2013). Estimation of tidal power potential. *Renewable Energy*, **51**, 255-262.

Wilcox, D. C. (1988). Reassessment of the scale-determining equation for advanced turbulence models. *AIAA journal*, *26*(11), 1299-1310.

Wimshurst, A. & Willden, R.H.J. (2016). Computational analysis of blockage designed tidal turbine rotors. In *Proc. 2nd International Conference on Renewable Energies Offshore*, Lisbon.

Wimshurst, A., & Willden, R. H. J. (2017a). Extracting lift and drag polars from blade-resolved computational fluid dynamics for use in actuator line modelling of horizontal axis turbines. *Wind Energy*, **20(5)**, 815-833.

Wimshurst, A., & Willden, R.H.J. (2017b). Analysis of a tip correction factor for horizontal axis turbines. *Wind Energy*, **20(9)**, 1515-1528.

Wimshurst, A., & Willden, R. H. J. (2018). Computational observations of the tip loss mechanism experienced by horizontal axis rotors. *Wind Energy*, **21(7),** 544-557.

Wimshurst, A., Vogel, C., & Willden, R. (2018). Cavitation limits on tidal turbine performance. *Ocean Engineering*, **152**, 223-233.

Whelan, J., Thomson, M., Graham, J. M. R., & Peiro, J. (2007, September). Modelling of free surface proximity and wave induced velocities around a horizontal axis tidal stream turbine. In *Proceedings of the 7th European Wave and Tidal Energy Conference*.

Xu, H., Shen, W., Zhu, W., Yang, H., & Liu, C. (2014). Aerodynamic analysis of trailing edge enlarged wind turbine airfoils. In *Journal of Physics: Conference Series* (Vol. 524, No.1, p. 012010). IOP Publishing.

Zhong, W., Shen, W. Z., Wang, T., & Li, Y. (2020). A tip loss correction model for wind turbine aerodynamic performance prediction. *Renewable Energy*, **147**, 223-238.